ERRATA

Page 15, line 20, charges should read changes
24, line 21, lami ar should read laminar
55, line 5, moving should read using
68, line 9, insert (6) at the end of the line
69, line 6, Table 29 should read Table 30
79, line 18, insert 5461 at beginning of line
86, line 13, for fig. 21 read fig. 22
86, lines 14 and 15, delete "with corresponding fringes numbered"
86, line 15, for fig. 22 read fig. 21
93, line 10, read gradients for gardients
93, line 14, for by Wilkie[28], read by Wilkie[28])
112, At top of diagram under Direction of shift for density increase, insert arrow pointing to the right
152, line 22, insert of 162.1, 139.2 and 113.0 p.s.i.a.
168, Table 20, for Centre line 2.217
Onset point 2.875
read Centre line 2.875
Onset point 2.217
176, Fig. 65 right hand side,
read position of strong shock wave in fig. 60a
and position of weak shock wave in fig. 60a
181, line 19, for 1.03 read 1.13
213, line 22, delete "of the regions"
222, line 20, for increased read decreased
241, line 11, read $\frac{T_o}{T} = 1 + \left(\frac{\gamma - 1}{2}\right) M^2$

Appendix, Page I, line 17, insert ± 0.001 cms.

AN INTERFEROMETRIC STUDY OF FLOW SEPARATION IN NOZZLES

by

J.E.P. MILES B.Sc.

A Thesis submitted for the
Degree of Doctor of Philosophy in the Faculty
of Engineering of the University of London

Department of Chemical Engineering,
Imperial College of Science and
Technology,
London, S.W.7.

June, 1963.

ABSTRACT:

The separation of the boundary layer in a two dimensional convergent-divergent nozzle, discharging to atmosphere, has been investigated using an interferometer in conjunction with pressure measurements.

It is shown that the variation in pressure rise across the separating boundary layer with Mach number is the same as that for separation over steps and wedges in wind tunnels. It is also shown that the position of transition in the boundary layer relative to the point of separation is the prime factor in determining the flow pattern at separation.

Stable turbulent separation is obtained throughout the range of Mach numbers investigated by making the boundary layers turbulent artificially.

The interferometric studies indicate that separation of the boundary layers is accompanied by separation of the boundary layers on the adjacent glass walls.

The flow pattern in the region of reverse flow under the separated layer is complex, the reverse flow being entrained from the atmosphere.

The shape of the velocity profiles in the turbulent regions of the boundary layer are shown to be dependent on the Reynolds and Mach numbers of the flow.

The flow upstream of the shock waves causing separation is not isentropic as the entropy change between the reservoir and a given point in the divergence increases with increase of the reservoir pressure.

ACKNOWLEDGEMENTS

The author would like to take this opportunity of thanking all the members of the Staff of the Chemical Engineering Department for their assistance and forbearance, without which it would not have been possible to complete this work.

While it is impossible to thank everybody individually he would particularly like to express his gratitude to Professor D.M.Newitt,. F.R.S. for his supervision and encouragement during the course of this work. He is also indebted to Mr. R.P. Fraser O.B.E. and Dr. P. Eisenklam for their invaluable advice and interest.

He would also like to thank:-

Dr. N. Dombrowski for his many helpful suggestions on photographic procedure.

Mr. G.K. Adams of the Explosives Research and Development Establishment, Waltham Abbey, for the loan of the Mach-Zehnder interferometer.

Mr. E.S. Brett and his workshop staff for their co-operation in making much of the apparatus.

Mr. J.A. Fenner for his continued patience and experience in maintaining the diesel compressor in working order.

The Ministry of Supply, Directorate of Guided Weapons Research and Development, for financial assistance in this research.

CONTENTS

Page

Appendices

LIST OF FIGURES

List of figures continued.

List of figures continued.

List of figures continued.

List of figures continued.

List of figures continued.

List of figures continued

List of figures continued

LIST OF TABLES.

List of tables continued.

List of tables continued.

NOMENCLATURE

a speed of sound

a_o stagnation speed of sound

A area

A direction number, defined by A-B=D and A+B=P, in section 5 and appendix 2

A_{eff} effective area of nozzle, $A_{eff} = (W - 2\delta^+)(D - 2\delta_c^+)$

A_t throat area

B direction number defined by A-B=D and A+B=P

C_p heat capacity of air at constant pressure

C_p' pressure coefficient equal to the ratio of the one dimensional isentropic static pressure to the measured static pressure

C_{pk} kink pressure coefficient $C_{pk} = \frac{2}{\gamma M^2}\left(\frac{p_k}{p_o} - 1\right)$

C_{pp} peak pressure coefficient $C_{pp} = \frac{2}{\gamma M^2}\left(\frac{p_p}{p_o} - 1\right)$

C_{ps} separation pressure coefficient $C_{ps} = \frac{2}{\gamma M^2}\left(\frac{p_s}{p_o} - 1\right)$

d upstream influence defined in fig 5

D breadth of nozzle

D direction of the stream measured from an arbitrary datum in section 5 and appendix 2

f one of the parameters used by Crocco[43] to define the boundary layer

$$f = (\delta_c - \delta_c^+ - \delta_c^{++})\,\delta_c / (\delta_c - \delta_c^+)^2$$

h half width of the nozzle throat

h_h heat transfer coefficient at the nozzle wall

$$h_h = \frac{q}{(T_{wad} - T_w)}$$

H boundary layer shape factor $H = \frac{\delta^+}{\delta^{++}}$

I Momentum flux in the boundary layer $I = \int_0^\delta \rho u^2 \cdot \cdot \, dy.$

k coefficient of thermal conductivity

K one of the parameters used by Crocco[43] to define the boundary layer $K = \delta_c - \delta_c^+ - \delta_c^{++} / \delta_c - \delta_c^+$ (section 4)

K Gladstone Dale constant, $n_r - 1 = K$, where n_r is the refractive index

m mass flow in the boundary layer, $m = \int_0^\delta \rho u \, dy$

$\bar{m}$ reduced mass flow, $\bar{m} = m a_o$

M Mach number based on the local speed of sound

$\overset{\circ}{M}{}^+$ Mach number based on the stagnation speed of sound $\overset{\circ}{M}{}^+ = \frac{V}{a_o}$

M^+ Mach number based on the speed of sound at $M = 1$, $M^+ = \frac{V}{a_t}$

n index in the relationship $\frac{Vy}{V} = \left(\frac{y}{\delta}\right)^{\frac{1}{n}}$

n' expansion index, $p/\rho^{n'} = \text{constant}$

p static pressure

p_a atmospheric pressure

p_k kink pressure, defined in fig 5.

p_c onset pressure, the free stream pressure just upstream of the region in which separation takes place, defined in fig 6 for nozzle separations

p_p peak pressure, defined in figs 8 & 9

p_s separation pressure, the pressure at which the boundary layer just separates

p_T plateau pressure, defined in fig 4.

P_o stagnation or reservoir pressure

P pressure number defined by $P = 1000 - 0$

q heat conducted through the nozzle wall

R_o Reynolds number at the onset point, based on the distance from the leading edge or from the nozzle throat and the free stream conditions at the onset point

R_t Reynolds number based on the distance from the point of transition in the boundary layer

R Radius of the convergent section

$\mathfrak{R}$ universal gas constant

S fringe shift in units of no flow fringe spacing

S' no flow fringe spacing

ΔS entropy change, $S = C_p \ln \left(\frac{T}{T_o}\right)^{\frac{1}{\gamma}} \left(\frac{\rho_o}{\rho}\right)^{\frac{\gamma-1}{\gamma}}$

T temperature

T_a atmospheric temperature

$\bar{T}$ mean temperature of the boundary layer defined by the relationship $m = \frac{p\bar{u}\delta}{\mathfrak{R}\bar{T}}$

T_o stagnation temperature

T_t temperature at the point where $M = 1$

T_{wad} adiabatic wall temperature

T_w wall temperature

u velocity in the x direction

u velocity in the boundary layer at position y from the surface in section 4.

$\bar{u}$ mean flow velocity in the boundary layer, defined by $\bar{u} = \frac{I}{m} \int u e x$.

y distance perpendicular to the nozzle axis.

y when referring to the boundary layer, distance perpendicular to the wall

v velocity in the y direction

V velocity

Vy velocity in the boundary layer a distance y from the surface.

w limit for the difference in glass thickness in the two beams of the interferometer for white light fringes to be obtained.

W width of nozzle.

x distance along the nozzle axis

x' ratio of the half width of the throat to the convergence radius, $x' = \frac{h}{R}$

Z number of fringes in the absence of dispersion

α Mach angle

α section 8, upper limit to the refractive index that can be measured interferometrically

γ ratio of heat capacity at constant pressure to that at constant volume, for air $\gamma = 1.4$

δ boundary layer thickness

δ^+ boundary layer displacement thickness

$$\delta^+ = \int_0^\delta \left(1 - \frac{\rho u}{\rho_{ex} u_{ex}}\right) dy$$

δ_o^+ boundary layer displacement thickness at the onset point.

δ_g^+ boundary layer displacement thickness on the glass walls of the nozzle.

δ^{++} boundary layer momentum thickness $\delta^{++} = \int_0^\delta \frac{\rho u}{\rho_{ex} u_{ex}} \left(1 - \frac{u}{u_{ex}}\right) dy$

θ deflection angle

λ_p peak wavelength of the light transmitted by the filter.

χ half band width of the source

μ viscosity

ρ density

$\bar{\rho}$ mean density in the boundary layer defined by the relationship $m = \bar{\rho} \bar{u} \delta$

ρ_a atmospheric density.

ρ_t density at the point where $M = 1$

ρ_y density at distance y from the surface in boundary layer.

σ Prandtl number $\sigma = \frac{C_p \mu}{k}$

ϕ Velocity potential defined by $\phi\, x,y = \int_{\text{ref point}}^{xy} (u\,dx + v\,dy)$ for irrotational flow.

w angular opening of the scource, $w = \frac{\text{width of scource}}{\text{focal length of collinating lens}}$

Subscripts.

eff. refers to values calculated from the effective area A_{eff} of the nozzle.

ex. refers to quantities at the free stream edge of the boundary layer

i refers to incompressible quantities.

SECTION 1. Introduction

One of the most important contributions to modern fluid dynamics was the introduction of the boundary layer concept by Prandtl in 1904[1]. The underlying principle of the concept is that, for fluids of low viscosity, the viscous stresses are small compared with the other terms in the equation of motion, except in thin layers adjacent to solid boundaries. These boundary layers result from the high velocity gradients occurring as the fluid is brought to rest at the walls. Thus the boundary layer concept leads to a model in which the flow pattern is treated as though the fluid were inviscid. These results are then utilized to obtain the boundary layer flow where viscous effects are taken into account.

It has been found that there is good agreement between experimental results and theory based on this model, provided the boundary layer is not subject to large pressure gradients. Under these conditions the boundary layer flow is mainly dependent on the pressure gradients established by the external flow, and the free streamlines are displaced from the wall by an amount equal to the boundary layer displacement thickness. When the thickness of the boundary layer is small compared with the other

significant dimensions, the presence of the boundary layer can be ignored and the entire flow assumed to be inviscid. This leads to great simplification and often represents the flow adequately.

When the boundary layer is subjected to large adverse pressure gradients, viscous effects within it modify the external flow. In supersonic flow the boundary layer is often subject to large pressure gradients, induced by the presence of shock waves. The pressure gradients are transmitted through the subsonic parts of the boundary layer resulting in the propagation of compression and expansion waves, which modify the original shock pattern. With strong shock waves, the associated large pressure gradients cause the boundary layer to separate from the wall.

With the advent of supersonic flight, the study of flow separation from a solid body has received a great deal of attention. It is considered as a scourge to many technical devices which depend on the properties of viscous fluids for successful operation, as it often limits the usefulness of these devices. For example, the maximum lift of an aerofoil and the maximum compression ratio of an axial flow compressor are limited by the onset of this

phenomenon.

Attention was first drawn to the problem of separation in supersonic flow by Ferri[2], who observed boundary layer separation near the trailing edge of an aerofoil, in a region where the inviscid flow theory would predict a favourable pressure gradient in which separation would not normally be expected. Further observations[3.4.5.6.] established the significance of interaction between a shock wave and a boundary layer, the experiments carried out by Fage and Sargent[3] were confined to the problem of interaction of a shock wave with a turbulent boundary layer on the flat wall of a supersonic wind tunnel, while Ackeret, Feldmann and Rott[4], and Liepmann[5] examined shock wave interaction on a curved surface. The results showed that the flow pattern at interaction depended critically on the state of the boundary layer. These results may be compared with those of Prandtl[7], who found that the effect of flow separation on the low speed drag of a bluff body in an incompressible fluid was dependent on the state of the boundary layer flow. As a result of this and other work[8.9.10.11.12], the physical nature of the phenomenon has been understood and the effects of Mach number and Reynolds number are established.

A number of theoretical analyses have been attempted[13 14 see references in 15] but none of these have treated the flow in the separated region in detail and often simplifying assumptions such as the neglect of heat transfer effects are made.

The work described above has been concerned mainly with the field of external flow around an object. Little previous work has been carried out on flow separation in nozzles, and insufficient data are available to compare separation in nozzle flow where the Mach number is constantly changing and that in external flow where it is constant.

It is the object of the present research to obtain data on the separation of boundary layers in an over expanded nozzle, and also to investigate the effect on separation of artificially altering the state of the boundary layer.

An interferometric technique has been employed to study separation in a small two dimensional nozzle with a straight divergence of 10° half angle. From interferograms of the flow in conjunction with pressure measurements, calculations have been made of, the pressure rise associated with separation, the flow pattern in the region

under the separated layer, the boundary layer velocity profiles, and the density distribution throughout the flow field. The state of the boundary layer has been determined from shadowographs and from the boundary layer velocity profiles.

The pressure rise associated with separation has been found to vary with Mach number in a manner similar to that for separation over steps and wedges etc. in wind tunnels. As the position of separation moves down the nozzle towards the exit, three distinct types of separation occur. Initially near the throat, separation is assymmetric with low pressure gradients. On moving down the nozzle it remains assymmetric but the associated pressure gradients increase, until it becomes finally symmetrical. Comparison of these results with the work carried out in wind tunnels show that the three types of separation correspond to separation of laminar, transitional and turbulent boundary layers.

It has been found that by fixing fine wires to the convergent section walls and causing the boundary layer to become turbulent upstream of the throat, stable turbulent separation is obtained throughout.

The flow pattern in the region under the separated

layer has been found to be complex, consisting of a number of vortices.

Measurements of the boundary layer velocity profiles were carried out only for the turbulent regions downstream of the throat. It was found that the shape of the profiles was dependent on the Reynolds number and Mach number, and that they did not correspond to a one seventh power law profile.

The range of Mach numbers over which separation has been studied was smaller than expected. Calculation has shown that this effect was due to departures from isentropic flow, the entropy at a given point in the nozzle increasing with resevoir pressure. Good agreement has been found between the velocity distribution measured in the throat of the nozzle and that derived from the two dimensional flow equation. Satisfactory agreement has been found between the Mach numbers calculated from interferograms and those obtained by Mach angle measurements.

SECTION 2. Flow Characteristics of Boundary Layer Separation induced by Shock Waves.

In many aeronautical problems where the flow is supersonic, such as the flow past wings and the flow through engine intakes and in nozzles, shock waves interact with the boundary layers on the surfaces. In such circumstances a major deviation of the actual flow pattern from that predicted by inviscid flow theory is caused by the combination of viscous drag in the boundary layer and the strong adverse pressure gradient applied by the shock wave. An example is given in fig. 1. Here an oblique shock wave is generated by a wedge placed on a flat plate. In the absence of a boundary layer a shock wave would be generated in the corner, fig. 1a. However the actual conditions observed experimentally, fig. 1b., are very different. Compression of the flow near the wall takes place gradually, generating a compression fan which coalesces into a shock wave in the main stream above the wall. The boundary layer has also separated from the wall causing a region of separated flow to be formed at the corner. The important difference between the flow patterns is in the rise of pressure upstream of the obstacle. In the actual case some mechanism exists

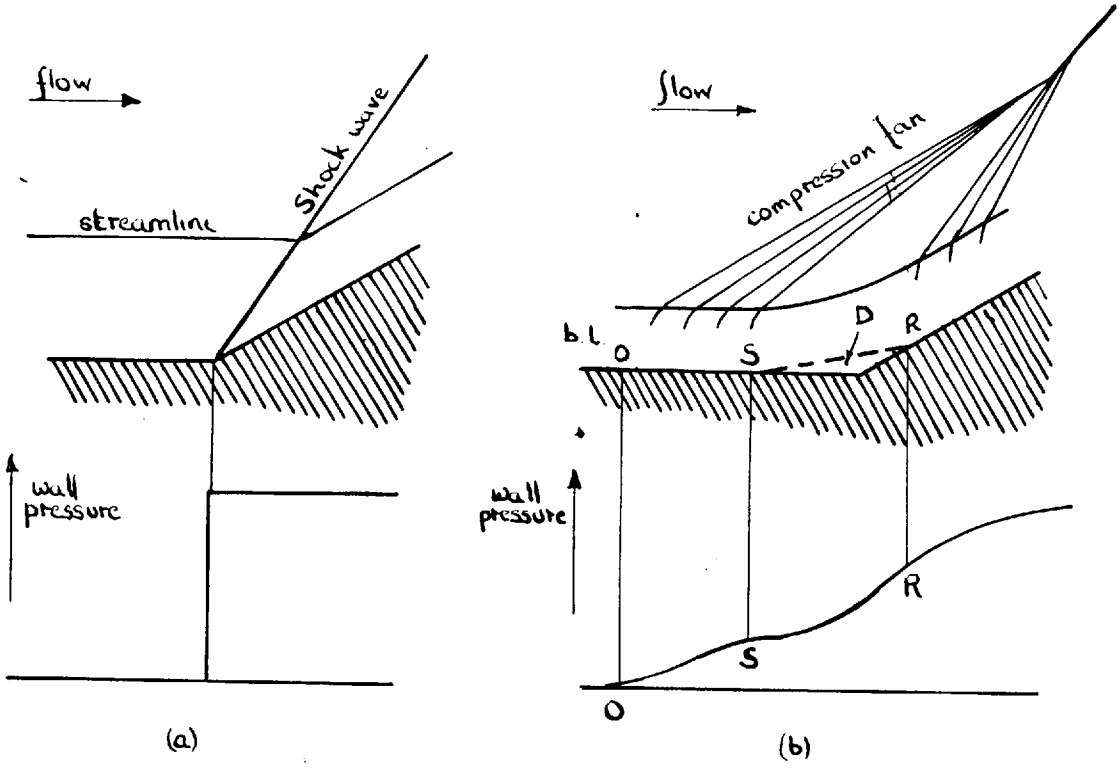

O. Onset point
S Separation position
R Reattachment position
D Region of revered flow.
b.l. Boundary layer

Fig 1. Flow patterns on a wedge, (a) in the absence and (b) in the presence of a boundary layer.

whereby the pressure can be propagated upstream and separation take place. Before any mechanism is suggested the flow of viscous fluids past solid bounderies will be considered.

When a viscous fluid flows over a solid surface, the fluid in immediate contact with the walls must be at rest, otherwise infinite velocity gradient and shear stress would exist at the interface. The viscous drag at the interface is transmitted throughout the whole of the fluid, and sets up a velocity gradient. At progressively greater distances from the surface, the effect of drag decreases until at some point, for practical purposes, it can be considered negligible. Thus viscous effects can be confined to a region close to the surface; this region is the boundary layer.

When the main stream is supersonic, the velocity in the boundary layer varies from supersonic to zero at the wall. Therefore the boundary layer can be divided into two regions, an inner region of subsonic flow and an outer one of supersonic flow. The streamlines in subsonic and supersonic streams expand and contract respectively when retarded by an applied positive pressure gradient. Therefore the widths of the inner and outer regions of the

boundary layer increase and decrease respectively on encountering a pressure rise.

Consider the boundary layer in fig. 2, when it is subjected to a pressure rise retarding the flow. The effect of the pressure rise on any fluid particle is dependent on its energy. Thus fluid in the mainstream and in the high velocity regions of the boundary layer will continue to flow on, while the flow direction of that in the low velocity regions close to the wall will be reversed, causing the flow to separate and a region of reversed flow to be formed.

The flow pattern shown in fig. 2 can also be considered to be the result of a viscous stream meeting a second stream at higher pressure flowing in the opposite direction. On moving upstream the second or reversed stream flows into the separated stream and mixes with it, retarding it and increasing its pressure. The mixing process associated with the energy transfer between the two streams, causes the reversed stream to be continuously removed. However on moving upstream the reversed flow region gets progressively narrower and viscous forces become progressively more effective in preventing the replacement of mixed fluid, and the wall pressure falls. The process continues until at the

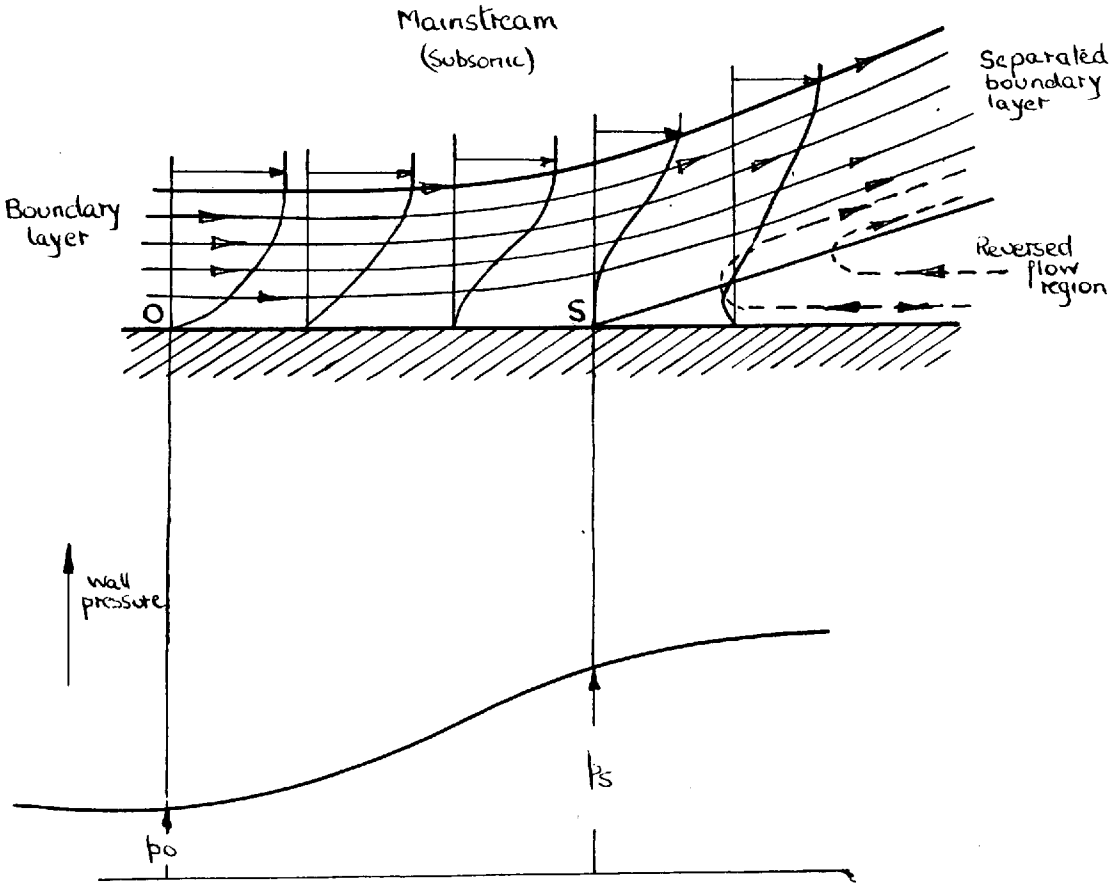

Fig 2. The process of separation of a boundary layer when the mainstream is subsonic.

separation position S all the reversed flow has been absorbed and the wall pressure is equal to the separation pressure. Upstream of the separation point the pressure continues to fall as pressure energy is utilized to retard and compress the boundary layer, until at O the onset point, the pressure has fallen to the undisturbed free stream or onset pressure.

The flow pattern obtained experimentally over a wedged shaped obstacle placed on a flat plate is shown in fig 3. Compression of the boundary layer and mainstream through the pressure rise associated with the corner at B takes place over the region of interaction OBQ.

The fluid in the region of reversed flow moves upstream and mixes with the separated layer in the manner already described. As the mixing process causes the pressure of the subsonic regions of the boundary layer to rise, they increase in width compressing the fluid in the supersonic regions of the boundary layer. The pressure rise associated with the deflection and compression of the supersonic regions is probagated along Mach lines into the mainstream forming a compression fan which finally coalesces into a shock wave.

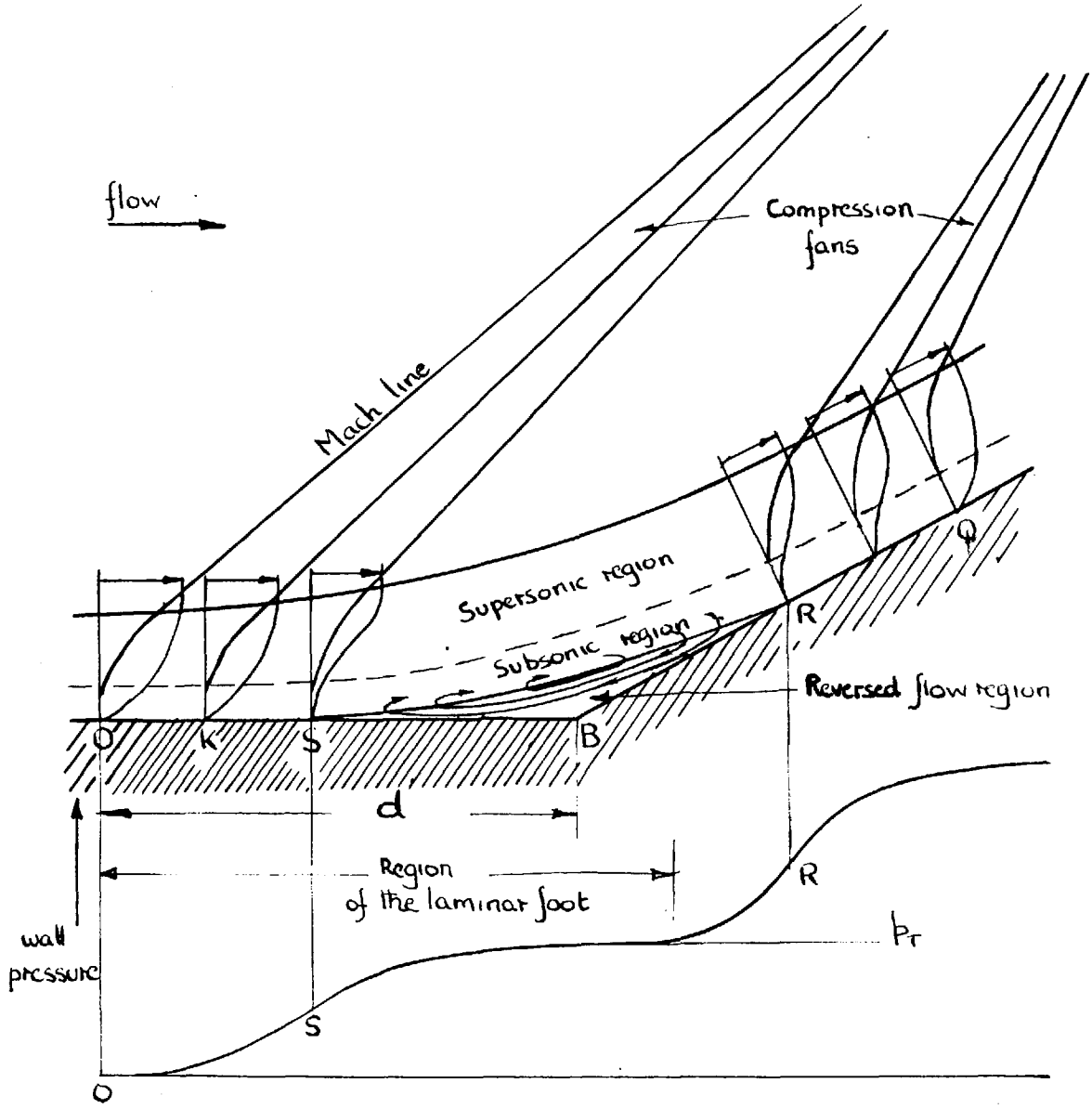

Fig 3. Flow pattern for the separation of a laminar boundary layer over a wedge

At some point downstream of the wedge apex, the separated layer meets the wedge wall and is deflected to flow parallel to it; reattachment of the flow takes place. At the point Q, the end of the region of interaction, the boundary layer is flowing parallel to the wall at a pressure which will depend on the original free stream pressure and the angle through which the flow has been deflected. When the separated layer flows into the region of increasing pressure associated with reattachment, the fluid in the low velocity regions of this layer has insufficient energy to surmount the pressure barrier and its flow direction is reversed. At the same time the subsonic regions are compressed, deflecting and retarding the supersonic regions and the mainstream. On moving downstream towards the reattachment point the region of reversed flow gets narrower and viscous forces become progressively more effective in preventing the removal of reversed fluid, and the wall pressure rises. At the reattachment point the flow of reversed fluid ceases and the wall pressure continues to rise as uniform flow is established in the boundary layer, until at Q the boundary layer is flowing undisturbed at the new free stream pressure.

The stream reversed at reattachment flows forward along the wedge wall and causes separation. The flow adjusts itself so that there is equilibrium between the fluid reversed at reattachment and that removed by the mixing process at separation. When the reversed flow region is wide, the wall pressure is constant as the viscous forces acting on the fluid at the wall are low.

In view of the importance of mixing between the separated layer and the reversed stream, marked differences would be expected between the pressure gradients and extent of the region of interaction, associated with laminar and turbulent boundary layers. Such differences have been observed experimentally[8,9].

The effect of transition from a laminar to a turbulent flow is shown in fig. 4, the wall pressure profile for a completely laminar interaction is shown together with one in which the boundary layer is laminar at separation, but turbulent at reattachment.

When a boundary layer becomes turbulent the velocity distribution charges due to the increased rate of energy transfer, resulting in a large reduction in the extent of the low velocity regions. Therefore when the turbulent layer reattaches in fig. 4, the amount of

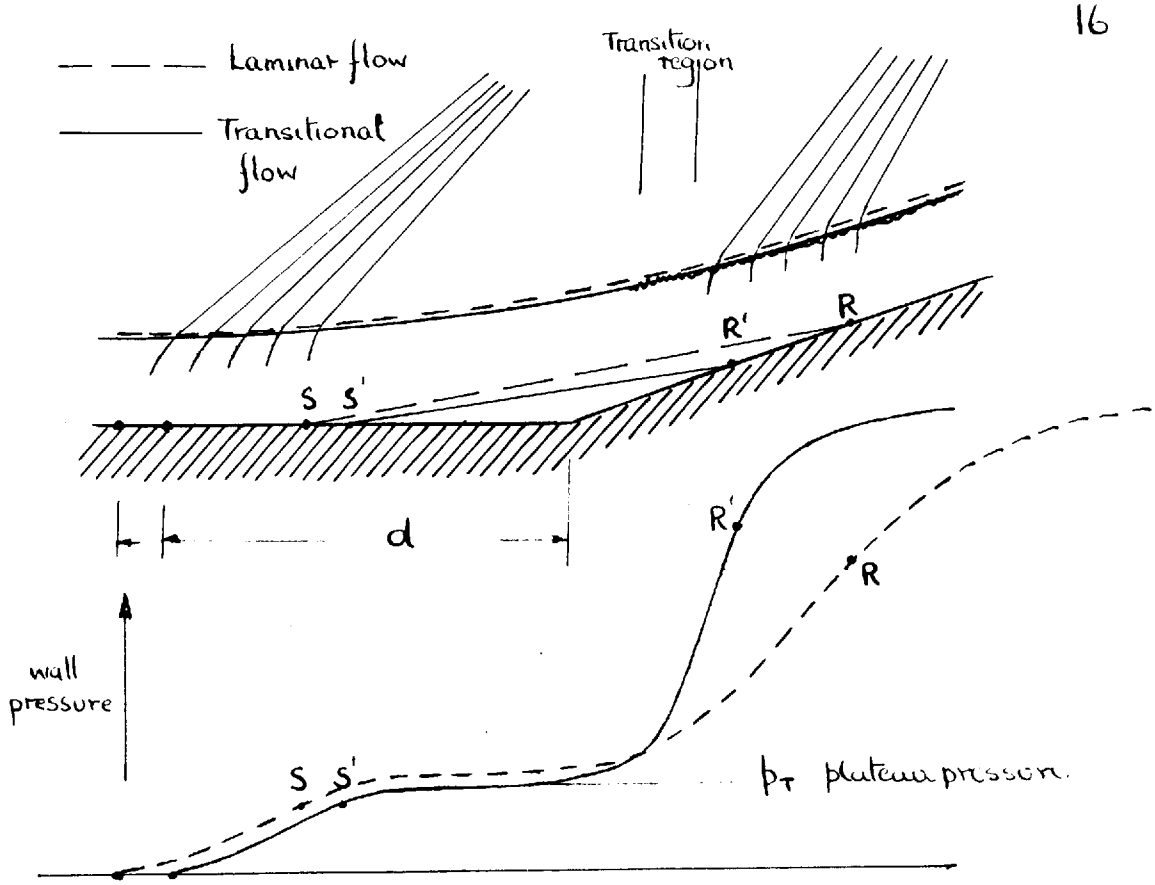

Fig 4. Separation of a boundary layer with and without transition

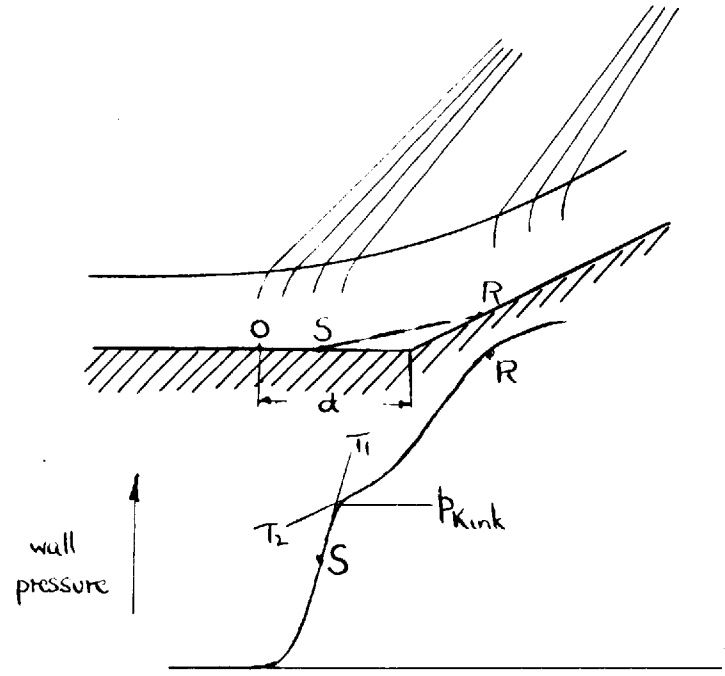

Fig 5 Separation of a turbulent boundary layer.

fluid reversed for a given pressure rise is reduced, the wall pressure falls more rapidly upstream of the re-attachment point as the removal of reversed fluid from the narrow viscous region and retardation of the high velocity regions of the separated layer is facilitated by turbulence.

As the mass of the reversed stream has been reduced due to transition, the equilibrium between that reversed at reattachment and that removed at separation moves so that the pressure rise at reattachment is increased and that downstream of separation reduced, causing deflection of the flow to be decreased at separation and increased at reattachment.

When the boundary layer is turbulent the pressure profile shown in fig. 5 is obtained. The pressure rise required to cause separation is greater than that for a laminar layer as the low velocity regions of the turbulent layer have greater energy. The length of the region of interaction decreases and the pressure gradients at the wall increase, due to the increased rate of energy transfer[13]. The wall pressure does not show a constant region in many turbulent interactions[8,9,10] as the reversed flow region is thin and the fluid at the

wall energized by the rapid interchange of energy with the separated layer promoted by turbulence. However when separation takes place over wedges of large angle at low Mach number a large region of reversed flow and a region of constant pressure have been observed[16].

The present study is concerned with boundary layer separation in a nozzle. The associated flow patterns and the conditions under which they occur will now be discussed.

In a supersonic nozzle gas is expanded from a high pressure reservoir reaching sonic velocity at the throat or section of minimum area, and finally accelerating to supersonic velocities in the divergent or expansion section. As the gas accelerates the wall pressure falls, and at any given point in the nozzle is a function of the nozzle profile and the reservoir pressure. Therefore the exit pressure of the jet is determined by the flow in the nozzle and the jet will have to expand or be compressed depending on whether the ambient pressure is greater or less than the exit pressure. If the exit pressure is less than the ambient pressure, on entering the atmosphere the jet and boundary layer are compressed. Fluid at atmospheric pressure flows (see fig 6b) into,

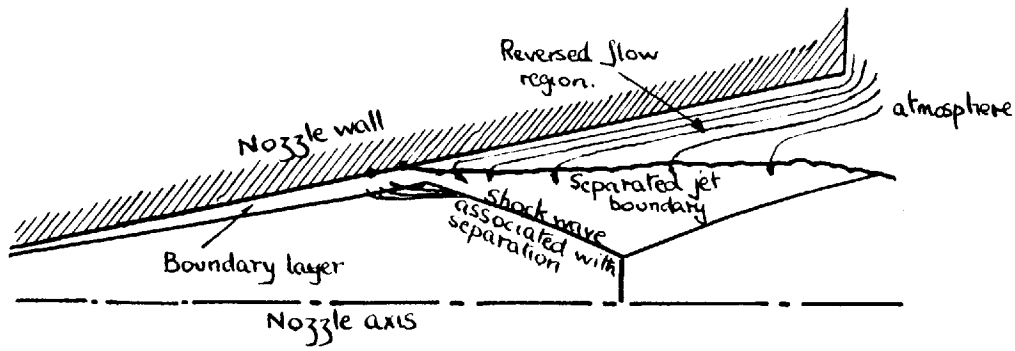

(a)

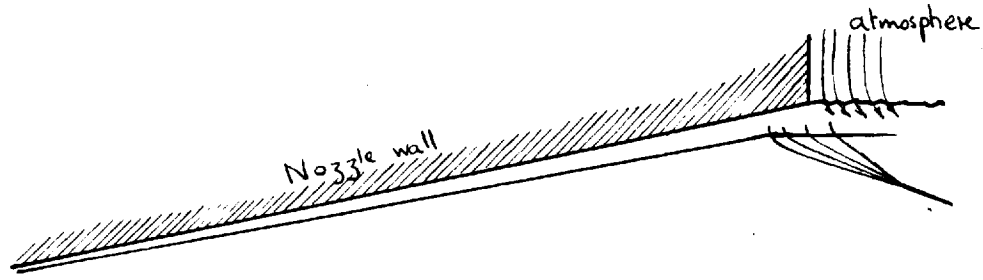

(b)

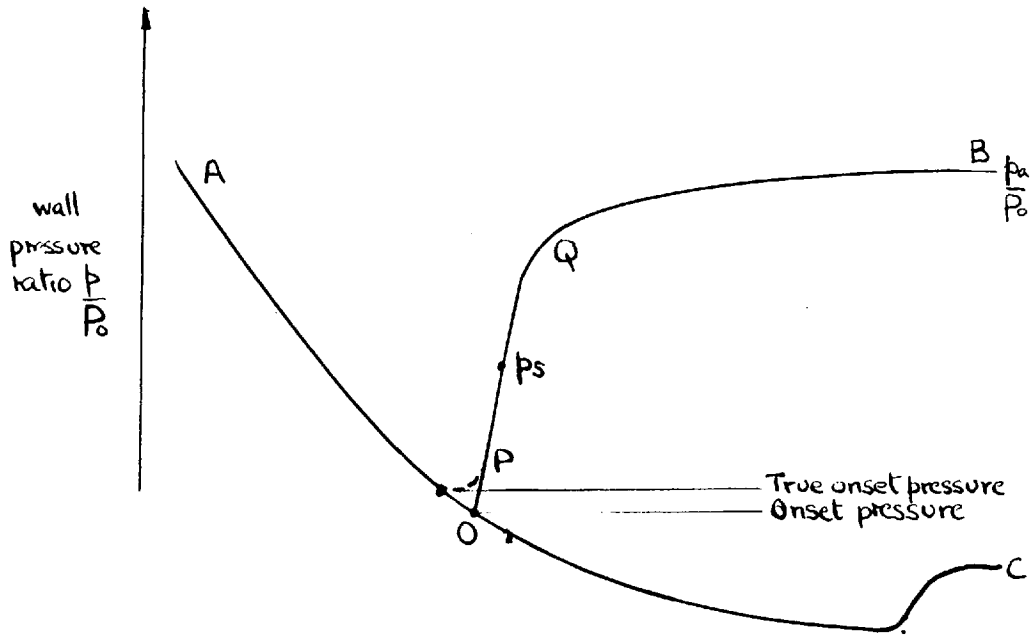

AOPQB Wall pressure profile for separating jet in (a)
AOC Wall pressure profile for separating jet in (b)

Fig 6 Flow separation in an overexpanded nozzle

and mixes with the low velocity regions of the jet boundary at the orifice, raising their pressure, causing them to thicken, deflecting and compressing the supersonic regions. The pressure rise is propagated upstream in the subsonic regions of the boundary layer in the same way as that upstream of separation. The compression fan associated with this compression coalesces and forms an oblique shock wave in the main body of the jet. If the atmospheric pressure is increased, a stage is reached when the low velocity regions of the boundary layer can no longer surmount the pressure barrier and the flow separates. As the separation position moves upstream (see fig 6a) the pressure rise causing it decreases, because the wall pressure increases in the wetted flow region of the nozzle. Therefore the energy causing separation supplied by the reversed stream to the separated layer would decrease compared with that of the fluid in the slow moving regions of the boundary layer. When the energy required to separate the boundary layer and that supplied by the reversed stream are equal, equilibrium is reached and no further separation takes place upstream.

For long regions of reversed flow, the pressure head

loss in overcoming friction can be significant and must be taken into account when determining the pressure rise causing separation.

From the foregoing discussion, the separation process in a nozzle would be expected to be the same as that over wedges and steps etc, with the same differences between laminar and turbulent flow provided, the pressure and velocity gradients in the mainstream of the jet do not alter the separation process, and that correction is made for the pressure head loss in the reversed flow region due to friction.

SECTION 3. Literature Survey.

It was shown in the last section that the position of transition was important when studying boundary layer separation phenomena. It is convenient, therefore, to divide this survey on the work in wind tunnels into three categories, dependent on the position of transition relative to separation. Separation and the effect of transition in over expanded nozzles will be dealt with separately.

3.1. Laminar Boundary Layers.

Results for boundary layers laminar over the whole region of interaction.

A characteristic of the separation of a laminar boundary layer over a step or wedge is the region of nearly constant pressure termed the plateau pressure p_T, in the wall pressure profile (see fig. 3 & 7)[8,10]. The separation pressure p_s and the plateau pressure are of the order of 15% to 30% greater than the onset pressure p_o at the beginning of interaction. Laminar separations are steady, no oscillations are present in the flow[6,17]. Gadd et al[10] defined upstream influence (distance d

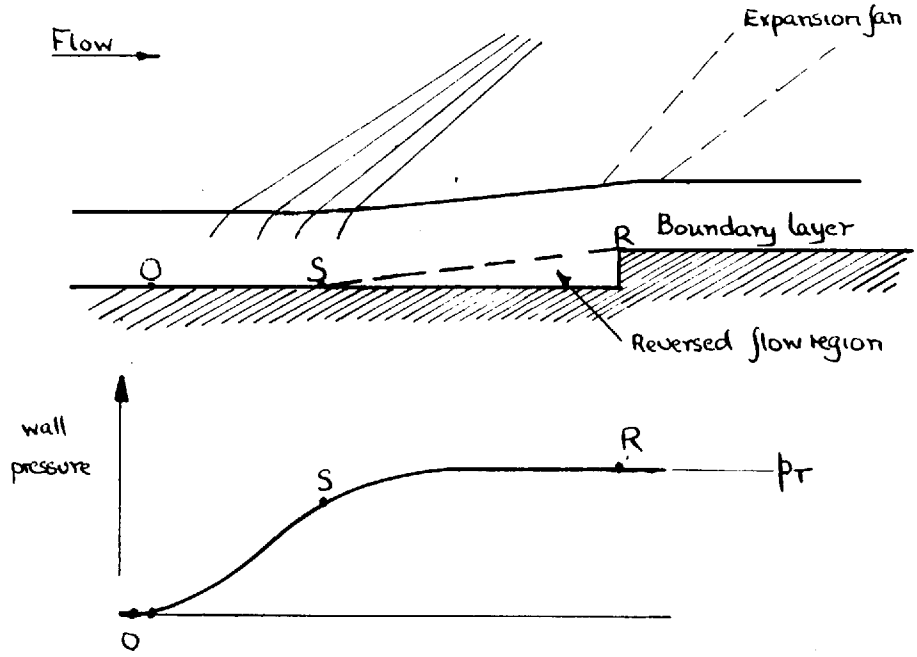

Fig 7 The separation of a laminar boundary layer over a step.

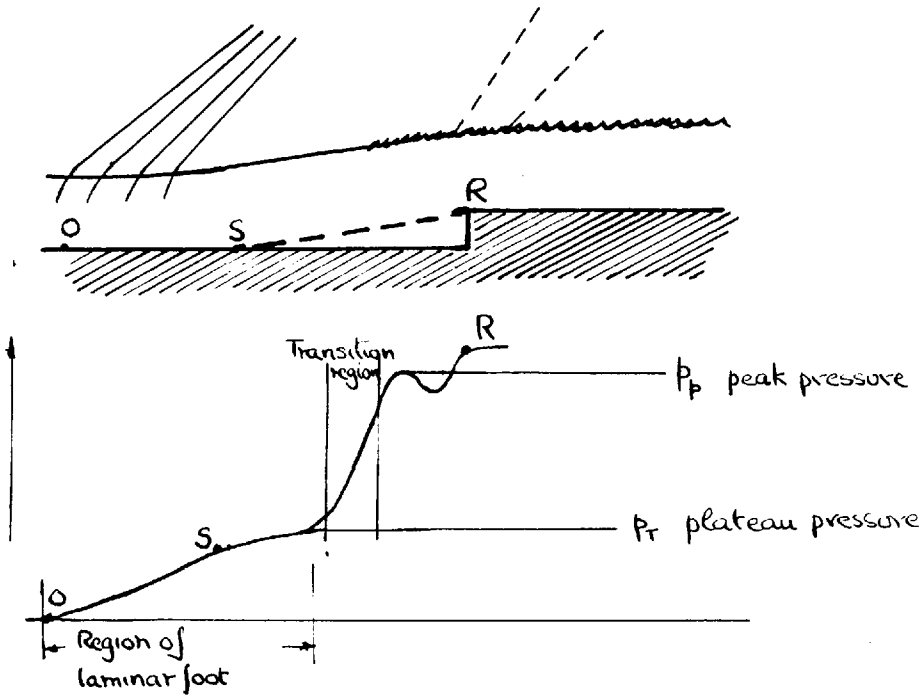

Fig 8 The separation of an initially laminar layer over a step with transition taking place before reattachment

in fig 3) in terms of the boundary layer displacement thickness δ_o^+ at the onset point. They found that the value of $\frac{d}{\delta_o^+}\left(\frac{10^4}{Ro}\right)^{\frac{3}{4}}$ was independent of Reynolds number Ro, and increased as the shock strength increased and free stream Mach number decreased. The same parameter was found to be greater for separation caused by an oblique shock wave generated by a wedge in the mainstream striking the boundary layer, than for a wedge placed on the flat plate producing the same overall pressure rise at the wall.

Other workers[8] have shown that the pressure distribution upto the plateau region is independent of the agency causing separation. The rise in pressure to separation and to the plateau region defined as $\frac{ps - po}{po}$ and $\frac{pT - po}{po}$ respectively were found to decrease with increasing Reynolds number and increase with increasing Mach number.

The flow velocities of the fluid in the reversed flow region under the separated layer were too small to be measured[18].

The separation of laminar boundary layers will be discussed further in the next section on transitional separation.

3.2. Transitional Boundary Layers.

Results for boundary layers laminar at separation but turbulent before reattachment.

When a boundary layer is laminar at separation but becomes turbulent before reattachment, the flow patterns observed are represented in figs. 4 & 8 [8 9 10 12]. The pressure distribution upstream of the transition region is characteristic of a laminar separation, but when transition occurs the wall pressure increases rapidly. The type of pressure distribution shown in fig. 4 is observed when separation is caused by a wedge or strong incident shock wave[10], but when the reversed flow region is large as in the separation over a step, there is a peak in the pressure distribution just upstream of the step face (see fig. 8). The peak has been attributed to a stagnation point being formed in the reversed stream flowing down the step face[8]. A considerable variation in the pressure over the face of the step has been observed[8 19], when transition takes place before re-attachment. When transition did not take place the step face pressure was equal to that in the reversed flow region and did not vary. Lange[19] attributed the

variation in step face pressure to sizeable subsonic velocities in the reversed flow region.

Where there is an extensive region of laminar flow downstream of separation, the plateau pressure is defined as the constant pressure at the top of the laminar foot (see fig 4). When transition takes place close to separation and the region of laminar flow is limited, the plateau pressure is defined as the pressure at the first point of inflexion in the wall pressure curve, (see fig 8). The plateau and separation pressures are not affected[8.9] by the position of transition, provided there is a region of laminar flow downstream of the separation position.

Gadd and Holder[9] used the experimental results from a number of sources to show that for laminar separations the pressure coefficient C_{pT} decreases with increasing Mach and Reynolds number; the latter variation was between $Ro^{-\frac{1}{4}}$ and $Ro^{-\frac{1}{2}}$. Inconsistencies between the different experimental data were attributed to differences in the free stream turbulence levels in different tunnels. As the level increases there is a tendency for transition to occur at lower Reynolds numbers, shortening the laminar foot. The reduction

in length of the foot is equivalent to an increase in the Reynolds number at the onset point, which causes a reduction in plateau pressure and so, in tunnels with high turbulence levels, values of C_{pT} are low.

Chapman et al[8] found that $\frac{pT - po}{po}$ and $\frac{ps - po}{po}$ were proportional to $Ro^{-\frac{1}{4}}$, provided the position of transition was not close to the separation position, showing that there is a relationship between separation and plateau pressure. If transition occurred near separation the flow became unstable.

The position of separation is difficult to measure experimentally. A Stanton[10] or surface tube has been used which measures the total pressure of the fluid near the wall. The total pressure is greater than the local wall pressure when the boundary layer is attached, when separation takes place it is equal to, or, where there is reverse flow taking place, less than, the local wall pressure. Therefore comparison of the surface tube and wall pressures reveals the positions of separation and reattachment. The results obtained in this way for $\frac{ps}{po}$ were 1.14, 1.14 and 1.33 at Mach numbers of 2, 3 & 4 respectively. The Reynolds number was varied

between 2 x 10^5 and 4 x 10^5 and appeared to have no effect on the ratio.

Chapman et al[8] used an oil film technique to find the position of separation. The oil collects along the line of separation as the attached stream and reversed stream move it downstream and upstream respectively. The technique was claimed to be very accurate. $\frac{ps - po}{po}$ was found to vary with Reynolds number as $Ro^{-\frac{1}{4}}$. At Mach = 2 and Ro = 2.5 x 10^5 $\frac{ps}{po}$ = 1.10 which is lower than the value 1.14 obtained by Gadd and Holder. When transition was close to the separation position the variation of $\frac{ps - po}{po}$ with Reynolds number reversed and approached the corresponding values of $\frac{pT - po}{po}$.

With regard to the various theories for laminar separation Gadd[20], Ritter and Kno[21] predict that the pressure increase at separation should vary as $Ro^{-\frac{1}{4}}$, Donaldson and Lange[22] suggest that ps - po should vary as $Ro^{-\frac{1}{2}}$. For the value $\frac{ps}{po}$ Gadd predicted 1.10, 1.18 and 1.27 respectively for M = 2, 3 & 4 with Ro = 2.5 x 10^5. Comparison of the theoretical and experimental results show that there is reasonable agreement between them. Using a modification of the Crocco-Lees method[13] Gadd

and Holder[23] obtained theoretical curves for the pressure distribution through a region of laminar separation; these have the same overall shape as the experimental curves. However the theoretical curves exhibit negative pressure gradients downstream of separation and upstream of the corner producing separation while the experimental ones do not.

In a study of separation over steps of different heights, Beastall and Eggink[24] observed the characteristic pressure distribution shown in fig. 8 for the transitional regime. The peak pressure increased with step height for a given Mach number. As the results are not complete in the region of the laminar foot, no comparison is possible with the results of Gadd[25] and Chapman[8]. However the pressure rise to separation was found to take place over a greater number of boundary layer thicknesses for laminar than for turbulent layers confirming Lighthills[26] observations on Mair's[17] work.

The effect of surface curvature on separation is two fold. Firstly, the pressure gradients associated with the curvature alter the velocity profile in the boundary layer upstream of the separated region; secondly, there is the effect of the wall curving away from beneath the

separated layer. Gadd[27] investigated the effect of convex curvature on separation, using an externally generated oblique shock wave as the disturbing agency and two different plates, one with a curved region at the downstream end and the other flat for comparison. With laminar boundary layers the pressure distribution had a characteristic laminar foot irrespective of where separation took place, but the ratio $\frac{p_T}{p_0}$ was lower when the pressure rise upto separation took place entirely on the curved region of the plate. Beastall & Eggink[24] also demonstrated the existence of a laminar foot for the flow up a convex step.

Transitional separation is not steady. High speed motion picture studies[8] have shown the flow to be unsteady between transition and reattachment. When transition takes place at the separation point large fluctuations in the flow are observed. Mair[17] found that under certain conditions the separation point oscillated with frequencies upto 6000c/s. Wilkie[28] observed large fluctuations in the flow in nozzles, when the conditions are such that transition could reasonably be expected to be taking place at the separation point.

In supersonic flow it is difficult to make a clear

distinction between laminar and turbulent boundary layers in terms of Reynolds number, as the transition point depends on the free stream turbulence level of the tunnel being used. There also seems to be a Mach number effect, as it has been found[8 16 29] that, when the boundary layer is made turbulent artificially by means of trips, the transition point moves downstream as the free stream Mach number is increased; the Reynolds number at transition increases with Mach number. It also appears[30] that transition from a turbulent to a laminar boundary layer can take place. A turbulent boundary layer at the inlet of a supersonic jet changing to a laminar one at the outlet.

3.3. Turbulent Boundary Layers.

Results for boundary layers turbulent over the whole region of interaction.

When separation of a turbulent boundary layer takes place the flow patterns shown in figs. 5 & 9[8,10,11,12,16] are observed. The region of interaction is considerably shorter than that of a laminar boundary layer of the same initial thickness. Compression takes place rapidly and the pressure gradients measured at the wall are high. When separation is caused by a wedge or strong incident shock wave, there is a characteristic kink in the pressure distribution. The kink pressure is defined as that given by the intersection of the maximum and minimum slope tangents T_1 and T_2 in fig. 5.

The pressure rise to separation is approximately 5 times[8,9,10,11] larger than that associated with laminar layers. The pressure distribution is independent of the agency causing separation upto the kink position only. It is unusual to find a region of constant pressure[8,16] in the reversed flow region, similar to the plateau pressure of laminar separation, which is independent of the model causing separation. The eddying motion of

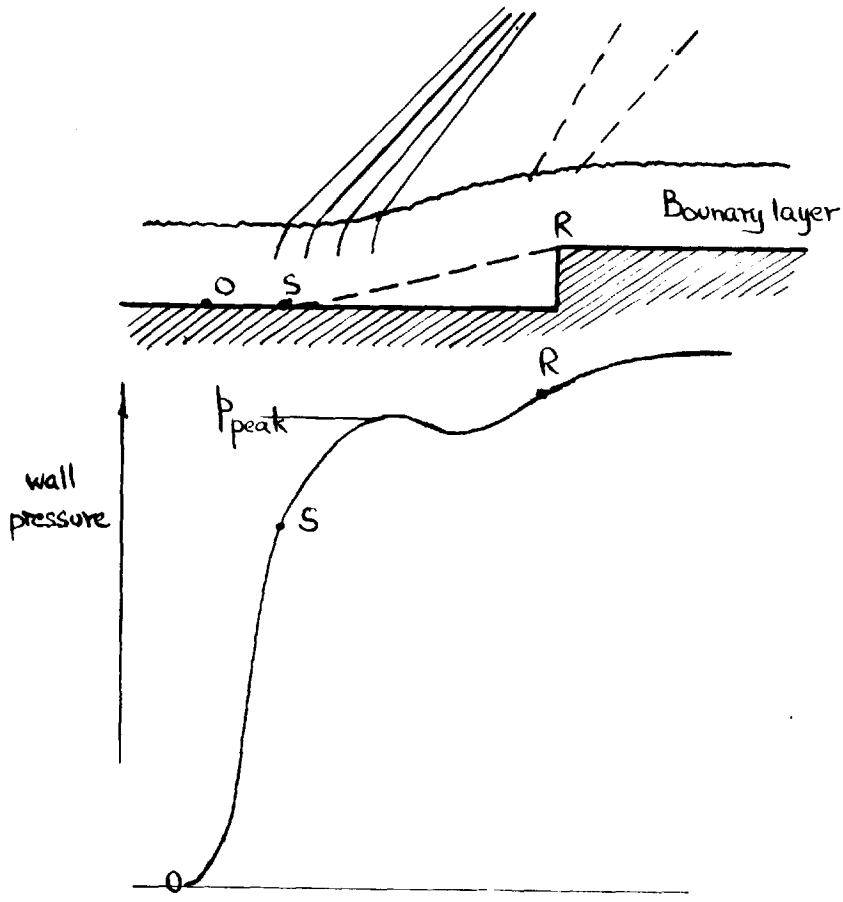

Fig 9 The separation of a turbulent boundary layer over a step.

the turbulent layer energises the fluid in the reversed stream; Mach numbers of 0.4[10] and 0.3[11] have been measured in the reversed stream for separations at free stream Mach = 3.

Using a wedge on a flat plate similar to one used by Chapman[8], Kuehn[16] obtained a region of constant or plateau pressure in the wall pressure distribution, when the free stream Mach numbers were low, and the reversed flow region large. As the Mach number increased the region of constant pressure disappeared, followed by the kink in the pressure distribution at a point where Chapman's results indicate separation was still taking place.

When separation takes place over a step it is difficult to define a kink pressure[8 9]. However when the step is greater than a critical height[11] there is a well defined maximum in the pressure distribution. For a given free stream Mach number the peak pressure (see fig. 9) increases as the step height is increased[11 24] until a critical value is reached. Bogdonoff[11] showed that the peak pressure is only dependent on the step height, upto a height of approximately two boundary layer thicknesses. When the step height was less than one boundary layer thickness, the mechanism of separation for the small

region of interaction was different from that observed for the larger regions associated with higher steps. It appears that in the small regions the step interferes with the viscous thickening of the boundary layer and modifies the flow patterns.

Gadd and Holder[10 18] found that the upstream effect d, defined in fig. 5, measured in terms of the boundary layer displacement thickness δ^{+}_{o}, was independent of Reynolds number over the range covered (Rt upto 10^7). The quantity $\frac{d}{\delta^{+}_{o}}$ appeared to be a function of shock strength and Mach number only, increasing as the shock strength increased and the Mach number decreased. As with laminar separations the upstream effect was greater for an external shock, than for a wedge producing the same overall pressure rise. Gadd and Holder[23] have pointed out an apparent anomaly between their results for upstream influence and those obtained by Bogdonoff[11] and Kuehn[16] at Princeton. The results of the latter show a smaller upstream influence than those of the former. As the Reynolds numbers were different in the two tunnels, Gadd and Holder suggested that the divergence might be due to Reynolds number effects.

An analysis carried out by Gadd and Holder[9], of the kink and separation pressure results of a number of workers showed that there is a tendency for C_{pk} and C_{ps}, the kink and separation pressure coefficients respectively, to decrease with increasing Reynolds number, but as the results were few and scattered the magnitude of the decrease could not be reliably estimated. For flow over a step the variation of C_{pp}, the peak pressure coefficient, was small.

Chapman et al[8] have shown, that for steps there is a small but persistent trend for peak pressure to decrease with increasing Reynolds number. $\frac{p_p - po}{po}$ being proportional to $\sqrt{cf}$, a coefficient dependent on Reynolds number only. The quantity $\frac{ps - po}{po}$ also decreased with increasing Reynolds number (cf ref 9) in approximately the same way as peak pressure i.e. $\frac{ps - po}{po} \propto \sqrt{cf}$. Over the range of Reynolds numbers investigated $\sqrt{cf}$ was approximately proportional to $Ro^{-\frac{1}{10}}$.

The effect of curvature on turbulent boundary layer separation is small. Gadd[27] points out that as compression upstream of separation takes place over a length equivalent to 10 and 2^{11} [26] boundary thicknesses for

laminar and turbulent separations respectively, it would be reasonable to surpose that the effect of wall curvature on a tubulent boundary layer is less than that for a laminar one. His results confirmed this. He concluded that for turbulent boundary layers, data obtained from separations on a flat surface were applicable to curved surfaces, provided the radius of curvature of the wall under the separating layer was larger than three times the distance from the leading edge to the region of interaction.

Turbulent separations are steady[8 17] but not to the extent of laminar ones. Thomann[15] and Kuehn[16] found that the flow patterns associated with turbulent boundary layer separation were steady, until the region of reversed flow reached a critical size, whereupon they became progressively more unstable as the size increased.

SECTION 3.4. Separation in Overexpanded Nozzles.

When separation takes place in an overexpanded convergent divergent nozzle the flow pattern and pressure distribution shown in fig. 6 has been observed[28 31]. The pressure given by the intersection of the pressure curve for the expanding gas with that for the pressure rise in the separation region is referred to by numerous authors[28 31 32 33] as the separation pressure. It is apparent, by comparison of the flow pattern shown in fig. 6 with those for turbulent separations over steps, that the pressure defined above approximates to the onset pressure and it will henceforth be referred to as such. The true value of onset pressure will be greater than that given by the intersection of the two pressure curves, as the wall pressure cannot undergo a discontinuous rise, but will rise gradually as shown by the dashed curve in fig. 6. It has not been possible to measure the true onset pressure as the experiments have been carried out on small nozzles where the pressure rise at separation takes place over very small distances. As a result, it has been physically impossible to obtain enough pressure points to make a detailed plot of the first part of the

pressure rise at separation. Usually only two or three points have been obtained on the first part of the pressure distribution, PQ in fig. 6.

Separation of the flow in conical nozzles discharging to atmosphere has been investigated by a number of workers. Using axisymmetric conical nozzles of 5° to 30° divergence half angle, Fraser[34] found that separation took place when the exit pressure of the jet was about half that of atmospheric. This value was apparently independent of divergence half angle.

Summerfield, Foster and Swan[32] and Foster and Cowles[33], using axisymmetric conical nozzles of 10° to 20° divergence half angle, concluded that the flow was one dimensional and isotropic upto separation. The onset pressure ratio $\frac{p_o}{p_a}$ varied between 0.27 and 0.41 and appeared to be independent of reservoir pressure, divergence half angle, and specific heat of the gas used.

McKenny[31], studying the flow of nitrogen through a straight sided two dimensional nozzle of 15° half angle, found that the onset pressure ratio varied between 0.38 and 0.41. The separation position was assumed to coincide with the intersection of the separation shock produced and the nozzle wall. This position was obtained from

shadow photographs, and was on average about 0.2 units of area ratio downstream of the initial pressure rise. The values obtained for $\frac{p_s}{p_o}$ in this way were all approximately equal to 1.9. As separation took place between area ratios of 4 and 5.6, the Mach numbers at separation were approximately equal to 3. For separations over steps[8 11] $\frac{p_s}{p_o} \sim 2$ for M = 3. McKenny's value appears therefore to be a little low. If flow photographs[8] for turbulent separations over steps in the neighbourhood of M = 3 are studied, the separation position measured by means of oil films, occurs either at or slightly downstream of the intersection of the separation shock produced and the wall. If separation occurs downstream of the intersection it would account for McKennys low result.

Using axisymmetric conical nozzles of 5° to 33° divergence half angle, Scheller and Bierlein[35], found that the onset pressure ratio $\frac{p_o}{p_a}$ varied between 0.20 and 0.82 for different angles of divergence and reservoir pressures.

In an attempt to define the onset pressure more accurately, Green[36] tried to correlate the results of a number of workers for axisymmetric nozzles of 15°

divergence half angle. He found no fundamental basis for the correlation and the results of nozzles other than 15^{o} are still at variance.

Summarising the work of the Californian Institute of Technology, Summerfield[37] states that the onset pressure is 0.4 of the ambient pressure without the effect of the latter being investigated. Sutton[38] made a similar assumption.

Wilkie[28] investigated three types of nozzle, axisymmetric curved, two dimensional curved and axisymmetric conical nozzles 10^{o} to 20^{o} divergence half angle. For axisymmetric conical nozzles discharging to atmosphere, the onset pressure ratio $\frac{p_o}{p_a}$ was between 0.33 and 0.43. Mean values of $\frac{p_o}{p_p}$ obtained for each nozzle were between 0.37 and 0.40, however the definition of the peak pressure p_p is not precise. In the curved nozzles the onset pressure was not proportional to the ambient pressure.

By attaching extensions to the nozzles and making the separated flow reattach, a reversed flow region was formed, and Wilkie measured a pressure in this region and assumed that the results obtained were the same as those for a jet separating into an atmosphere of the same pressure. Wilkie states that his results show that the onset pressure is determined only by the ambient pressure. However the onset pressure results tabulated for axisymmetric conical nozzles discharging to atmosphere show a distinct trend to increase as the reservoir pressure decreases, indicating that $\frac{p_a}{p_o}$ increases as the Mach number at separation increases. The same trend is apparent from the results of Ashwood et al[39] and McKenny[31].

Arens and Spiegler[40] studying separation in two dimensional and conical nozzles of 7^o to 22^o divergence half angle found that the pressure ratio $\frac{p_a}{p_o}$ was equal to the peak pressure ratio $\frac{p_p}{p_o}$ obtained by Chapman for turbulent separations over steps, and showed a similar dependence on free stream Mach number.

Tucker[41] investigating the flow of air at low pressure and high Mach number in a nozzle with an adjustable divergence half angle found that the flow

separated without a characteristic rise in the pressure distribution. Schlieren photographs of the flow show that separation took place in the absence of a shock wave, and continued to expand after separation. By roughening the nozzle walls at the throat the Mach number at separation was increased from 3.9 to 5.7. On the other hand roughening the surface of a nozzle discharging to atmosphere has been found to have no effect on separation[42]. It appears therefore that there is a fundamental difference between the separation process in nozzles at high speeds and low pressure, and those discharging to normal atmosphere. The effect observed by Tucker is similar to that observed by Green and Nall[43] in a nozzle discharging to atmosphere. They found that, by cooling the nozzle wall by injection of nitrogen, the pressure rise at separation could be reduced considerably.

SECTION 4. Theory of Shock Wave Boundary Layer Interaction with Flow Separation.

It can be seen from the review presented in the previous section that flow separation in over-expanded nozzles takes place predominantly in regions where the boundary layer is turbulent. As the theory of shock wave boundary layer interaction with flow separation has been presented to enable a comparison of experimental results and those predicted by theory to be made, theories dealing with turbulent boundary layer separation only are considered.

Although a considerable amount of work has been carried out on shock wave boundary layer interaction in the experimental field, little progress has been made in determining the precise flow pattern in the region of interaction. Detailed analysis has been attempted[10 11] on a limited scale. The results show that the flow pattern in a region of shock wave boundary layer interaction is extremely complicated, and that the usual simplifying assumptions of boundary layer theory, negligible pressure and velocity gradients normal to the wall, are not valid.

Because of the large pressure gradients and the small scale of the phenomenon, a detailed analysis of

the flow pattern would involve almost insurmountable experimental difficulties. Therefore theoretical treatments have been carried out by postulating a model of the interaction, making simplifying assumptions and then testing the results against experiment.

One model[14] which was used had the boundary layer divided into two parts; an outer layer in which viscous effects are neglected and compressibility effects are taken into account, and an inner low speed layer in which compressibility is neglected and viscous forces are taken into consideration. The solution is obtained by studying the growth of the inner viscous layer, using the boundary conditions determined by the flow conditions at the inner edge of the outer inviscid layer. The results for pressure distribution in the region of interaction are only in good agreement with experiment upto the separation position; further downstream the theory and experiment are at variance. It appears therefore, at first sight, that the theory gives the correct result for upstream influence. However the experimental results obtained at the N.P.L[10] with which the theory was compared, appear to depend on the agency causing separation, also they do not agree with those obtained at Princeton[11 16]

under apparently similar conditions.

Although the theory discussed above attempts a semi detailed analysis of the flow pattern and gives a result for the pressure distribution throughout the region of interaction, it is of limited use from an engineering standpoint as it does not predict when separation will take place or the extent of the ultimate pressure rise.

Greater success has been achieved by assuming that the pressure rise at separation is discontinuous. When turbulent boundary layer interaction takes place the pressure rises very rapidly over a small distance, therefore a justifiable simplifing assumption is that the pressure rise takes place at a shock wave in the mainstream. The regions of the mainstream adjacent to the boundary layer can then be assumed to be compressed at the point where the shock wave emerges from the layer. By applying the laws of conservation of momentum and energy across the discontinuity, results for the ultimate pressure rise can be determined, which are in good agreement with experiment. A theory of this type will be discussed below.

4.1. Theoretical Analysis of Turbulent Boundary Layer Separation by Crocco and Probstein[44].

In this treatment the boundary layer flow is defined in terms of mean parameters chosen so that the relationship between them can be obtained from the transformation of the equivalent incompressible boundary layer solution. The flow in the boundary layer is then treated as if it were one dimensional, and the variation in the velocity distribution in the region of interaction taken into account by means of the relationship between the mean parameters. The pressure is assumed to rise discontinuously at a shock wave which extends to the top edge of the boundary layer.

The following assumptions are made[13]:-

(1) The static pressure is constant across the boundary layer and equal to the local static pressure pex.

(11) Heat transfer between the fluid and solid surface is zero, and that the stagnation enthalpy is constant across the boundary layer and equal to that at $y = \delta$ (where δ is the boundary layer thickness) in the external flow.

The mass flux of the flow in the boundary layer is given by

$$m = \int_0^{\delta} \rho u \, dy \qquad (1)$$

and the momentum flux by

$$I = \int_0^{\delta} \rho u^2 dy \qquad (2)$$

The mean flow velocity in the boundary layer is defined by:-

$$\bar{u} = I/_m \qquad (3)$$

and a mean density and temperature by the mass flow relationship $m = \bar{\rho}\bar{u}\delta = \frac{p\bar{u}\delta}{R\bar{T}}$ (4)

By defining a reduced mass flow rate $\bar{m} = mao$ equation 4 becomes $\bar{m} = \frac{p\bar{u}\delta a_o}{R\bar{T}}$ (5)

where ao is the stagnation speed of sound.

If δ^+ and δ^{++} are the displacement and momentum thicknesses of the boundary layer respectively at $y = \delta$ then

$$\delta^+ = \int_0^{\delta} \left(1 - \frac{\rho u}{\rho_{ex} u_{ex}}\right) dy = \delta - \int_0^{\delta} \frac{\rho u}{\rho_{ex} u_{ex}} dy \qquad (6)$$

and

$$\delta^{++} = \int_0^{\delta} \frac{\rho u}{\rho_{ex} u_{ex}} \left(1 - \frac{u}{u_{ex}}\right) dy = \delta - \delta^+ - \int_0^{\delta} \frac{\rho u^2}{\rho_{ex} u_{ex}^2} dy \qquad (7)$$

where subscript ex refers to quantities at the mainstream edge of the boundary layer.

If $K = \frac{I}{m u_{ex}}$ then by utilizing equations 1, 2, 6 & 7 it can be shown that $\frac{\bar{u}}{u_{ex}} = K = \frac{\delta - \delta^+ - \delta^{++}}{\delta - \delta^+}$ (8)

and also that

$$\frac{T_o}{\bar{T}} = \frac{T_o}{T_{ex}} \frac{(\delta - \delta^+)^2}{\delta(\delta - \delta^+ - \delta^{++})} \qquad (9)$$

by using equations 1, 4, 6 & 8,

where To refers to the stagnation temperature of the mainstream flow.

However Stewartson[45] has shown for laminar layers, with Prandtl number equal to unity, viscosity μ proportional to temperature T and zero heat transfer, that any compressible boundary layer flow with prescribed variation of the external flow velocity can be reduced to an equivalent incompressible boundary layer flow with a transformed external velocity distribution. That is, from a given incompressible flow a family of compressible flows can be generated whose solutions are related in a simple way to the incompressible solution.

Crocco used this transformation to express equations 8 and 9 in terms of the equivalent incompressible boundary layer quantities i.e.:-

$$\frac{\bar{u}}{u_{ex}} = K = \frac{\delta_i - \delta_i^+ - \delta_i^{++}}{\delta_i - \delta_i^+} \qquad (10)$$

$$\frac{\bar{T}}{T_o} = \int - \frac{\gamma - 1}{2} K^2 M_{ex}^{+2} \quad \text{or} \quad \frac{\bar{T}}{T_o} = \int - \frac{\gamma - 1}{2} \bar{M}^{+2} \qquad (11)$$

where $$f = \frac{(\delta_i - \delta_i^{+} - \delta_i^{++})\delta_i}{(\delta_i - \delta_i^{+})^2}$$

and $$M_o^{+} = \frac{u}{a_o}$$

Crocco[13] observed that for every incompressible boundary layer flow there is a relationship between f and K, and also for certain low speed laminar boundary layers, that a single f - K curve could be used to represent the boundary layer flow through regions of acceleration and retardation. The one parameter description can then be extended by means of the Stewardson transformation to the corresponding compressible flows. By defining a value for δ_i and using the conventionally defined values of δ_i^{+} and δ_i^{++}, Crocco obtained a f - K relationship, from incompressible laminar boundary layer solutions for accelerated and retarded flow. The f - K curve obtained showed that K decreased and f increased steadily as the boundary layer was retarded until at separation K remained constant as f increased. Hence Crocco reduced the boundary layer equations to a simple form involving mean temperature and velocity and found a simple relationship between the mean parameters which held for the pressure distribution in the region of interaction.

While in the case of laminar boundary layers Crocco found it possible to describe the flow involving separating and reattaching regions as a particular curve in the $\int f$ - K plane from theoretical considerations. He found that nothing of the kind could be done in the turbulent case, as the effect of compressibility on turbulent boundary layers is not known. But by making the assumption that every turbulent dissipative flow involving separated and separating regions can be described as a particular curve in the $\int f$ - K plane, a curve was obtained from the very limited low speed data available. The curve started from K = 1.0 f = 1.0, passed through the zero pressure gradient flat plate point, K = 0.89, $\int f$ = 1.022 and rose steadily to the separation value of K = 0.72 $\int f$ = 1.295 after which it continued as the line K = 0.72. This curve was then used to compute the peak pressure rise for a separating turbulent boundary layer.

The model adopted is shown in Fig. 10. The mainstream is deflected sharply at the point at which the shock wave emerges from the boundary layer. The boundary layer is considered at stations 1 and 2 which are at positions such that the pressure across the boundary layer can be assumed constant. Separation is assumed to take

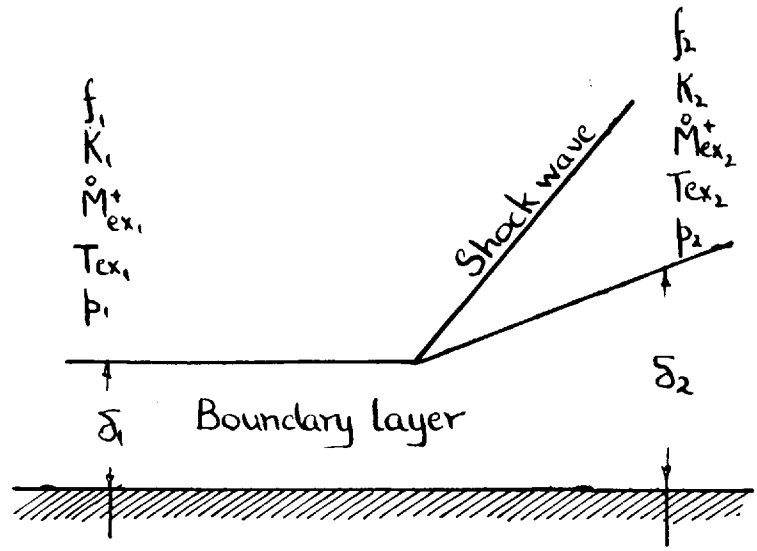

Fig.10. Crocco's model of an oblique shock wave emerging from a turbulent boundary layer on a plane surface

place between the two stations. The model is independent of the agency causing separation provided the peak pressure is reached before other effects interfere with the separation process.

It can be shown from equations 5 10 and 11 that

$$\bar{m} = \frac{p\delta \overset{\circ}{M}^{+}_{ex}\,\gamma}{\sqrt{f/K - \frac{\gamma-1}{2} K \overset{\circ}{M}^{+2}_{ex}}} \qquad (12)$$

The further assumption is made that the interaction takes place over a sufficiently small distance, so that the effects of skin friction, pressure gradient and mixing between the boundary layer and mainstream can be neglected. Since the pressure rises to the peak pressure over 3 - 5 boundary layer thicknesses the assumption is justified.

It follows that $\bar{m}_1 = \bar{m}_2$ (13)

for the boundary layer between stations 1 and 2.

Taking a momentum balance

$$\bar{m}_1 \overset{\circ}{M}^{+}_{1} - \bar{m}_2 \overset{\circ}{M}^{+}_{2} = \delta_1 (p_2 - p_1) \qquad (14)$$

and from the Hugioniot relationships across a shock wave

$$\frac{T_{ex_2}}{T_{ex_1}} = \frac{\frac{\gamma+1}{\gamma-1} + \frac{p_2}{p_1}}{\frac{\gamma+1}{\gamma-1} + \frac{p_1}{p_2}} \qquad (15)$$

also $$\frac{T_{ex}}{T_o} = 1 - \frac{\gamma-1}{2} \overset{\circ}{M}{}_{ex}^{+2} \qquad (16)$$

and $$M^2 = \frac{\overset{\circ}{M}{}_{ex}^{+2}}{1 - \frac{\gamma-1}{2} \overset{\circ}{M}{}_{ex}^{+2}} \qquad (17)$$

If it is assumed that all quantities at station 1 are known, then there are seven unknowns T_{ex_2}, $\overset{\circ}{M}{}_{ex_2}^{+}$, p_2, $\bar{m}_2$, K_2, f_2 and δ_2, and only six equations 12, 13, 14, 15, 16 and the graphical f - K path. But when separation takes place $K_2 = K_{sep}$ = constant and the problem is reduced to six unknowns and five equations apparently leaving the boundary layer thickness ratio as a parameter of the problem. However by using equation 12 in the form $\bar{m}_1 = \dfrac{p_1 \delta_1 \overset{\circ}{M}{}_{ex_1}^{+} \gamma}{f_1/K - \frac{\gamma-1}{2} K_1 \overset{\circ}{M}{}_{ex_1}^{+}}$ and making the appropriate alegebraic combinations of equations 12, 13, 14, 15, 16 and 17 it can be shown that

$$\frac{p_2 - p_1}{\gamma p_1}\left\{\frac{f_1}{K_1^2}\left(\frac{1}{M_1^2}\right) + \frac{\gamma-1}{2}\left(\frac{f_1}{K_1} - 1\right)\right\} =$$

$$1 - \frac{1}{M_1}\cdot\frac{K_2}{K_1}\left(\frac{2}{\gamma-1}\right)^{\frac{1}{2}}\left\{1 + \frac{\gamma-1}{2} M_1^2 - \left(\frac{\frac{\gamma+1}{\gamma-1} + \frac{p_2}{p_1}}{\frac{\gamma+1}{\gamma-1} + \frac{p_1}{p_2}}\right)\right\}^{\frac{1}{2}} \qquad (18)$$

which can be solved as a quadratic in M_1^2

If equation 12 had been used in the form

$$m_2 = \frac{f_2 \delta_2 M_{ex_2}^{+} \gamma}{f_2/K_2 - \frac{\gamma-1}{2} K_2 M_{ex_2}^{+}}$$

an analogous expression to equation 18 would be obtained involving the ratio $\frac{\delta_1}{\delta_2}$ and f_2. Hence by moving the assumption that K_2 is constant in equation 18 implies that for separated flow the variation in f_2 is equal and opposite to that of $\frac{\delta_1}{\delta_2}$.

Crocco found from the limited data available that the original estimate of Ksep = 0.72 was too low when comparing experimental and theoretical results. However by choosing another value Ksep = 0.76 and using the flat plate point $f_1 = 1.022$ $K_1 = 0.89$, good agreement with experimental results was obtained. The peak pressure values tabulated below are therefore based on Ksep = 0.76.

TABLE I.

$\frac{p_2}{p_1}$	M_1	
1.7	1.422	Change in the pressure rise across a separating turbulent boundary layer with Mach number, calculated from Crocco's theory.
1.8	1.587	
2.0	1.911	
2.2	2.242	
2.4	2.583	
2.6	2.952	
2.8	3.324	
3.0	3.795	

SECTION 5 The calculation of the flow properties in the nozzle.

The calculation is conveniently divided into two parts; calculation of the flow pattern in the divergence and in the throat region.

5.1. Calculation of the flow pattern in the nozzle by the method of characteristics

These calculations relate specifically to the nozzle described in section 7.2, which is a two dimensional nozzle with a designed convergence radius of one inch, tangential to a straight divergence of 10° half angle.

During preliminary experiments with this nozzle interferograms of the type shown in fig 11 were obtained. Each fringe in the wetted flow region corresponds to a line of constant Mach number. It can be seen that the flow is two dimensional as the Mach profiles are curved. The measured wall pressure ratios corresponding to the flow in fig 11 were higher than values calculated from one dimensional isotropic flow theory (see fig 12). Other workers[28,35,42] have found the same effect. It has been shown[46] Chap 8 that the wall pressure ratio obtained when

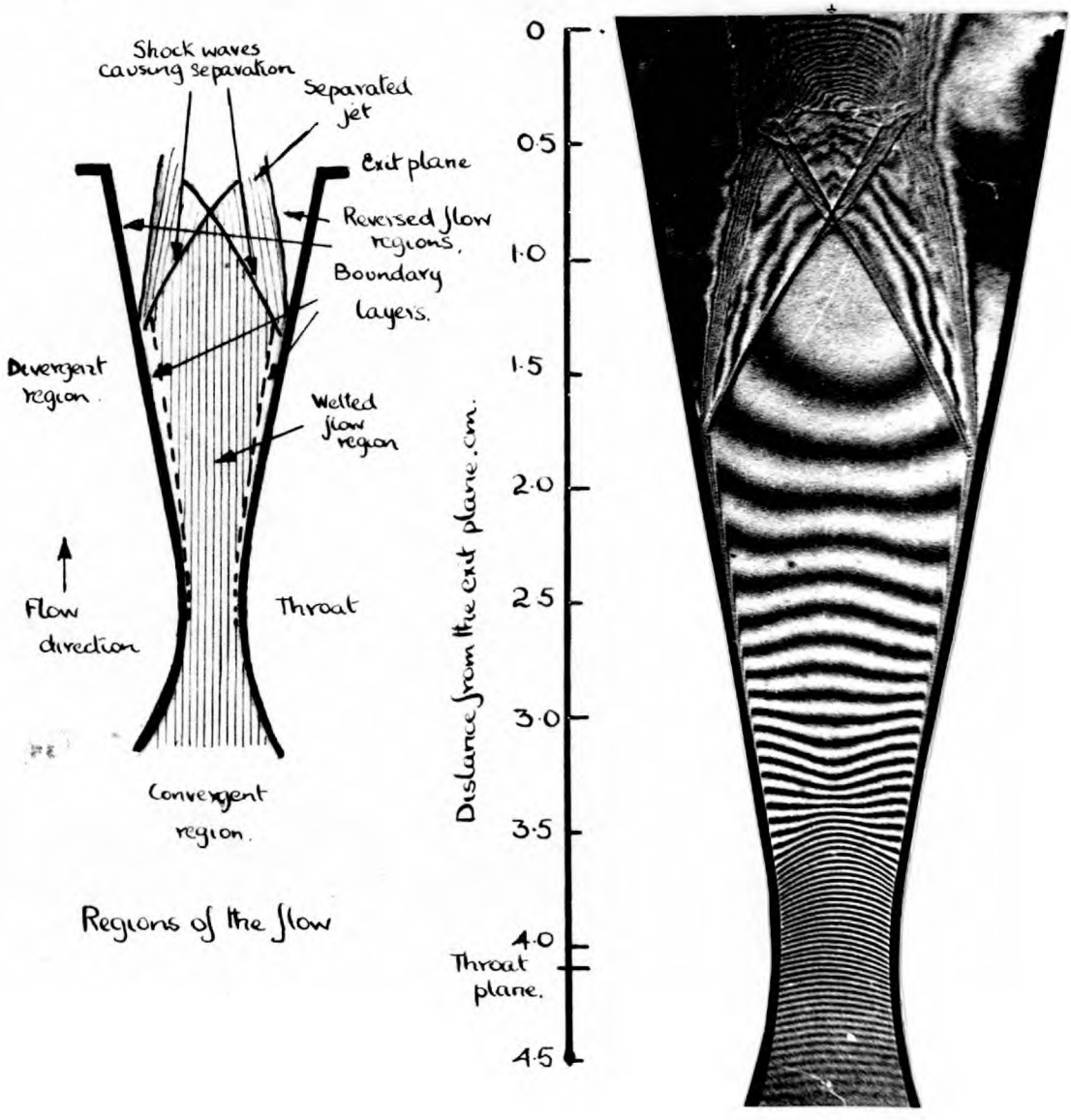

Fig 11 Fringe pattern in the nozzle obtained using the infinite fringe method.

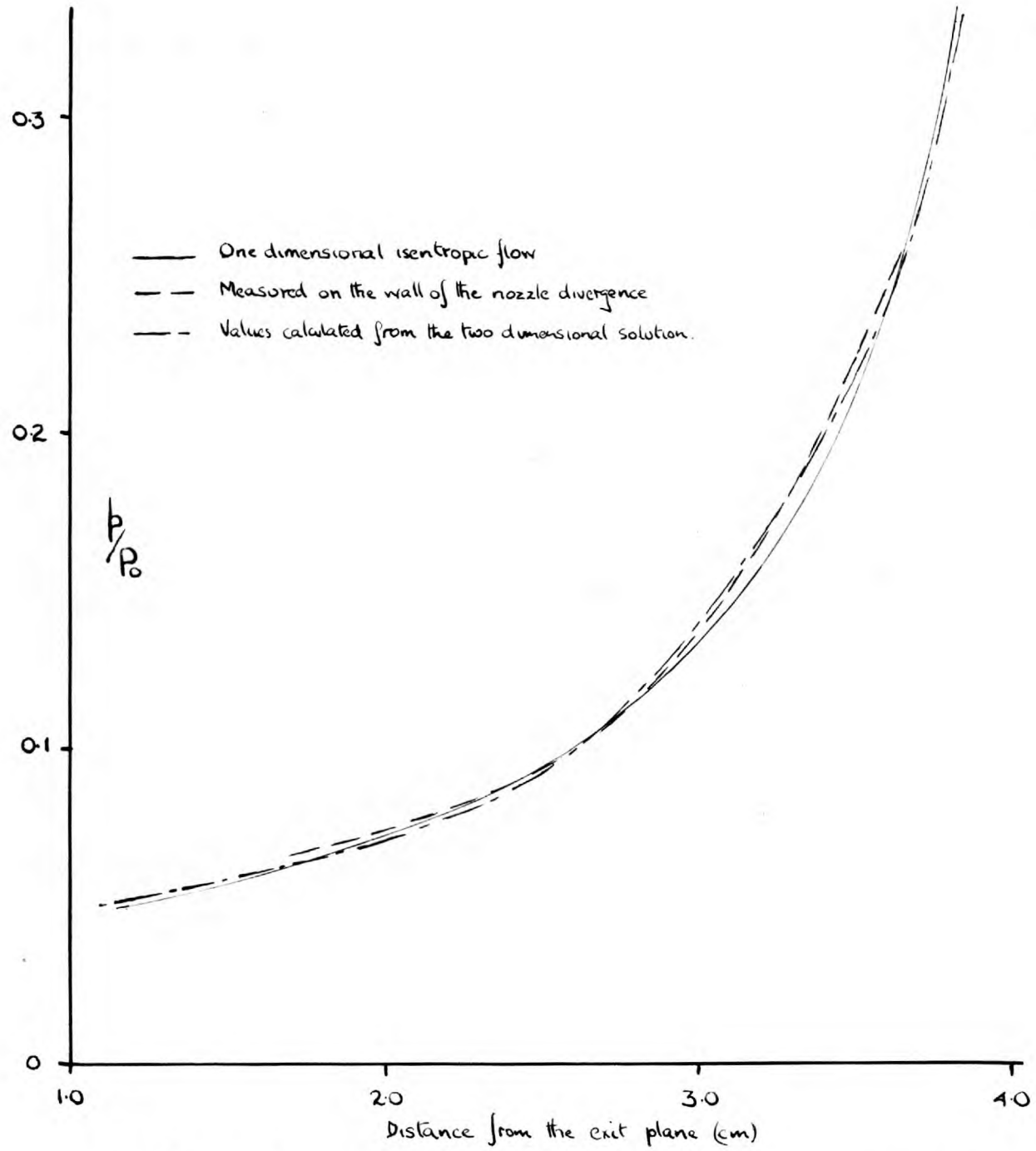

Fig. 12. Comparison of the measured static pressure ratios with the one and two dimensional isentropic values.

friction and drag are taken into consideration is greater than the corresponding isentropic value. Therefore the divergence between the one dimensional and the measured wall pressures can be attributed to friction and two dimensional effects.

As it was not possible to estimate the error in the pressure ratio, determined on the assumption of one dimensional flow, by qualitative means the flow pattern in the nozzle had to be calculated. This was done by using the method of characteristics (see appendix 2).

5.1.1. Boundary conditions for the characteristic net.

It was decided for simplicity to assume that at the throat plane, the fluid in the nozzle was moving uniformly at Mach number 1, that is a straight sonic profile was assumed. The more exact Mach number 1 profile obtained by solving the two dimensional flow equation in the limited throat region (see part 2 of this section) has been used by Erdmann[47] and Harrop[48.49.] as the boundary condition for a characteristic net. The resulting net while more exact is considerably more complicated than that obtained by using a straight sonic profile. However the extra complication was not warranted here, since the flow in the

nozzle was not isentropic. The solution therefore which is based on the assumption of isentropic flow was only required for qualitative comparison with the experimental flow pattern.

The dimensions of the actual nozzle were measured and used in the construction of the characteristic net. The method of measurement and the dimensions are presented in appendix 1.

The characteristic net was constructed by assuming that the flow in the nozzle was symmetrical. Therefore the theoretical flow pattern was obtained by considering the flow between the axis of the nozzle and the bottom wall only. For the purpose of calculation the curved region of the nozzle wall downstream of the throat was assumed to be made up of a number of incremental deflections of 0.5^{o}. The coordinates of the deflection points were calculated by assuming that the actual wall was circular.

The equation to the wall at the throat was assumed to be $(x-a)^2+(y-b)^2 = R^2$, where a is the distance from the throat plane to the exit plane of the nozzle, b the distance from the origin to the line $y = o$, and R the profile radius. The agreement between the calculated and measured points was satisfactory (see table 2)

TABLE 2.

Comparison of the measured coordinates, x and y with those calculated for the bottom wall of the throat.

x cms	3.7	3.8	3.9	4.0	4.1	4.2	4.3	4.4	4.5	4.6
y calc	4.112	4.129	4.142	4.150	4.154	4.153	4.148	4.138	4.124	4.106
y mean measured	4.112	4.129	4.142	4.150	4.155	4.155	4.149	4.138	4.125	4.107

TABLE 3.

Coordinates of the deflection points used in the construction of the characteristic net.

Deflection°	x cms	y cms	Deflection point No.
0	4.134	4.154	0
0.5	4.114	4.154	1
1.0	4.094	4.153	2
1.5	4.074	4.153	3
2.0	4.054	4.153	4
2.5	4.034	4.152	5
3.0	4.014	4.150	6
3.5	3.994	4.149	7
4.0	3.974	4.148	8
4.5	3.954	4.147	9
5.0	3.934	4.145	10
5.5	3.915	4.144	11
6.0	3.895	4.142	12
6.5	3.875	4.139	13
7.5	3.835	4.134	15
8.0	3.815	4.132	16
8.5	3.796	4.129	17
9.5	3.756	4.122	19
10.0	3.736	4.119	20

when R = 2.29cms.

b = 1.864cms.

a = 4.134cms.

The coordinates of the deflection points calculated from the equation given above are tabulated in table 3.

5.1.2. Graphical Construction of the Characteristic net.

The outline of the bottom wall of the nozzle was drawn twenty times full size using the measured coordinates presented in appendix 1, except in the throat region where the deflection points were used.

The net was constructed (fig. 13) using the method of points described in appendix 2. The angle of each individual characteristic line to the datum was found by using the scheme presented in fig. 11a appendix 2. The calculation of the first few points represented in fig 14 is presented in detail in table 4. The mach angles corresponding to the mean Pressure numbers were obtained from reference 50.

5.1.3. The Mach number profiles:

The Mach number profiles are shown in fig 13 in

Fig 13 Flow pattern in the nozzle calculated by the method of characteristics

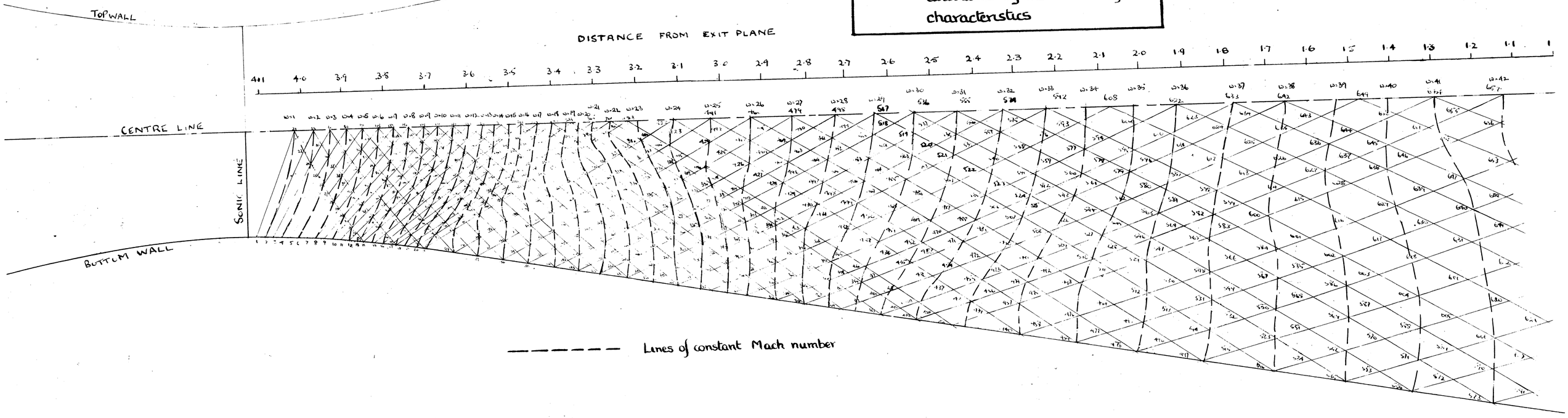

TABLE 4.

Method of calculating initial points in characteristic net, see fig 14 for angles A.B.C.etc.

Point	Method	A	B	C	D	Mean P	P Mean	Mean D	Angle to datum
1	Bot wall exp.of 0.5°fm. initial conditions	499.5	500	999.5	-0.5	999.25	$\overset{+}{6}9.58$	-0.25	$\hat{A} = \overset{+}{6}9.33$
21	Top wall exp.of 0.5°fm. 1.	499.5	499.5	999.0	0				
2	Bot wall exp.of 0.5°fm. 1.	499.0	500	999.0	-1.0	998.75	$\bar{6}5.90$	-0.25	$\hat{B} = \bar{6}6.15$
22	Top wall exp.of 0.5°fm. 2.	499.0	499.5	998.5	-0.5	998.75	$\overset{+}{6}5.90$	-0.75	$\hat{C} = \overset{+}{6}5.15$
3	Bot wall exp.of 0.5°fm. 2.	498.5	500	998.5	-1.5	998.25	$\bar{6}3.16$	-0.75	$\hat{D} = \bar{6}3.91$
23	Top wall exp.of 0.5°fm. 3	498.5	499.5	998.0	-1.0	998.25	$\overset{+}{6}3.16$	-1.25	$\hat{E} = \overset{+}{6}1.91$

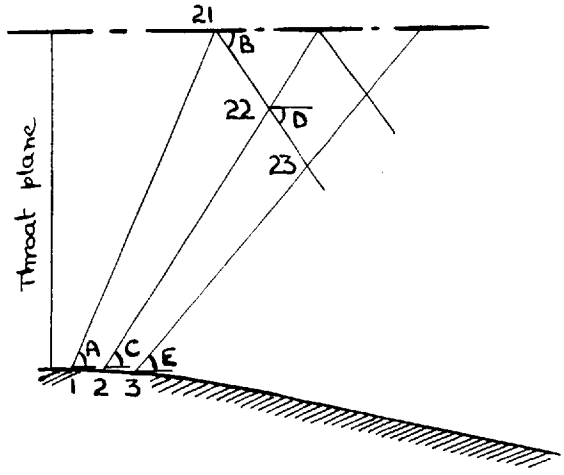

Fig. 14. Representation of angles used in table 4.

TABLE 5

Mach numbers and pressure ratios corresponding to the deflection angles in Fig 13 (From reference 52)

Deflection angle θ^{o}	Mach number M	p/p_o	Deflection angle θ^{o}	Mach number M	p/p_o
0	1.000	0.5283	22.0	1.844	0.1626
1.0	1.082	0.4790	23.0	1.879	0.1541
2.0	1.133	0.4496	24.0	1.915	0.1459
3.0	1.177	0.4249	25.0	1.950	0.1381
4.0	1.218	0.4029	26.0	1.986	0.1306
5.0	1.257	0.3827	27.0	2.023	0.1234
6.0	1.294	0.3640	28.0	2.059	0.1165
7.0	1.330	0.3464	29.0	2.096	0.1100
8.0	1.366	0.3298	30.0	2.134	0.1037
9.0	1.400	0.3140	31.0	2.172	0.0977
10.0	1.435	0.2991	32.0	2.210	0.0920
11.0	1.469	0.2848	33.0	2.249	0.0866
12.0	1.503	0.2711	34.0	2.289	0.0814
13.0	1.537	0.2581	35.0	2.329	0.0765
14.0	1.571	0.2456	36.0	2.369	0.0718
15.0	1.605	0.2336	37.0	2.411	0.0673
16.0	1.639	0.2222	38.0	2.452	0.0630
17.0	1.673	0.2112	39.0	2.495	0.0590
18.0	1.707	0.2006	40.0	2.538	0.0552
19.0	1.741	0.1905	41.0	2.582	0.0516
20.0	1.775	0.1808	42.0	2.626	0.0481
21.0	1.810	0.1715			

increments of 1^{o} turning angle, the corresponding Mach numbers and pressure ratios are tabulated in table 5.

The pressure ratios obtained from the intersection of the Mach number profiles with the bottom wall of the nozzle are tabulated in table 6 together with the values, calculated from the measured area ratios (see appendix 1) using the one dimensional isentropic theory, and measured during the test in which the interferiogram in fig 11 was taken.

It can be seen from fig 12, that the wall pressure ratios calculated by the method of characteristics are in better agreement with the experimental results than those obtained from one dimensional theory. Comparison of the theoretical and experimental flow fields will be carried out in more detail in section 10.

TABLE 6

Comparison of the theoretical and measured pressure ratios in the nozzle.

Dist from Exit plane cm.	p/P_o from characteristic solution fig 13	p/P_o from Measurement of $\frac{A}{A_t}$ Appendix 1	p/P_o from test shown in fig 11
1.1	0.0505		
1.2	0.0528	0.0499	
1.3	0.0547		
1.4	0.0568		
1.5	0.0589		
1.6	0.0605	0.0589	
1.7	0.0633		
1.8	0.0659		0.0687
1.9	0.0683		0.0711
2.0	0.0713	0.0713	0.0738
2.1	0.0746		0.0765
2.2	0.0780		0.0800
2.3	0.0820		0.0835
2.4	0.0865		0.0878
2.5	0.0920		0.0929
2.6	0.0990		0.0990
2.7	0.1073		0.1065
2.8	0.1168	0.1151	0.1150
2.9	0.1275		0.1255
3.0	0.1397	0.1342	0.1375
3.1	0.1532		0.1506
3.2	0.1687	0.1581	0.1655
3.3	0.1838		0.1825
3.4	0.2005	0.1928	0.2002
3.5	0.2183		0.2218
3.6	0.2390	0.2434	
3.7	0.2685		
3.8	0.3145	0.3232	
3.9	0.3685	0.3746	
4.0	0.4230	0.4287	

5.2. Calculation of the Sonic Profile at the throat.

When a nozzle is designed by the method of characteristics it is customary to use either a straight sonic profile[28 51] or one obtained[47.49.52] by a series solution of the two dimensional flow equation as the boundary condition at the throat. As the actual sonic profile at the throat can be obtained from the interferograms of the flow, the theoretical profile was calculated from the two dimensional flow equation to ascertain whether it was a better approximation to the actual conditions than a straight sonic profile.

Consider the nozzle throat shown in fig 15. Let the coordinates of the centre be 0.0, then the profile is symmetrical about the axes x and y. The fluid flowing in the convergent section will accelerate upto the throat and if sonic velocity is not reached will decelerate on entering the divergent section and the pressure will rise. The flow will then be symmetrical about both axes. But as soon as sonic velocity is reached in the throat, the fluid can either decelerate or accelerate on moving downstream depending on whether the exit pressure is greater or less than the pressure in the throat. If the latter

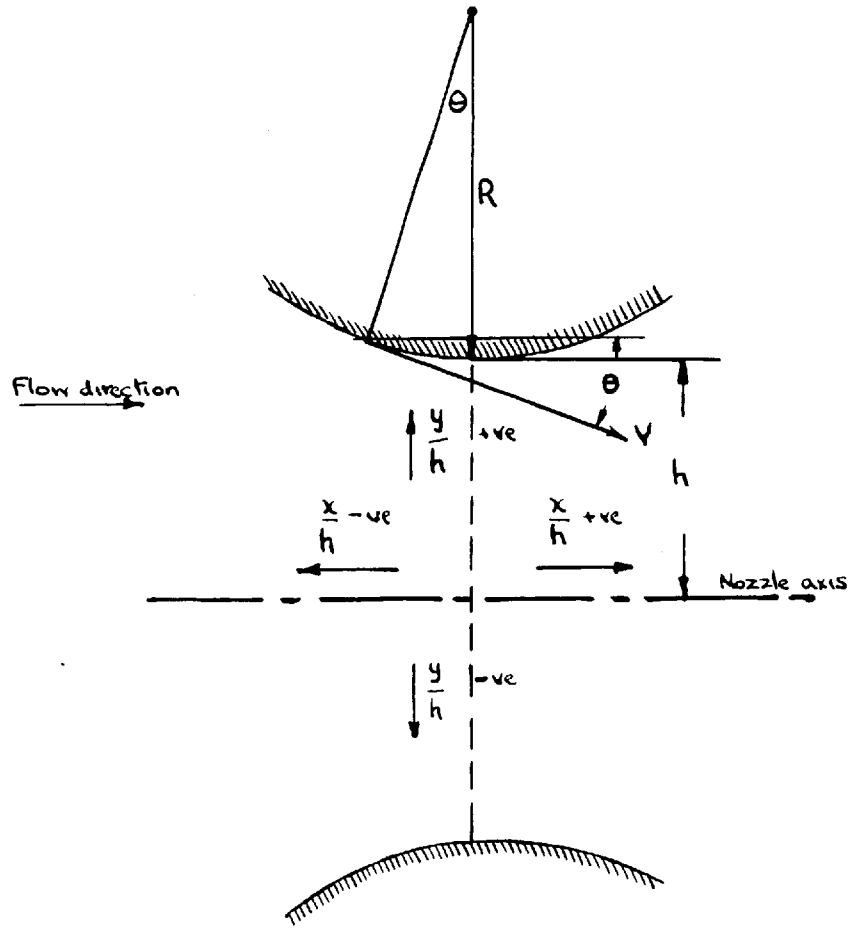

Fig.15. Coordinates used in the solution of the two dimensional flow equation in the throat

condition pertains the flow will become supersonic and be asymmetrical about the y axis.

Taylor[53] used the properties of nozzle flow described above to obtain a solution to the potential flow equation in the throat region. He described the velocity potential in terms of a polynomial in x and y and determined the unknown coefficients by applying the equation of motion and the boundary conditions.

For asymmetrical flow about the y axis the expression for u or $\frac{\partial \phi}{\partial x}$ must contain all powers of x and only even powers of y. The further condition that v or $\frac{\partial \phi}{\partial y}$ contains odd powers of y must also be fulfilled as the flow is symmetrical about the x axis. The general form of the solution satisfying the above requirements is given by:-

$$\phi = a_1x+a_2x^2+a_3x^3+a_4x^4+c_2y^2+c_3xy^2+c_4x^2y^2+1_5y^4 \qquad (1)$$

For potential irrotational flow in two dimensions it can be shown that:-

$$\left(1-\frac{\phi_x^2}{a^2}\right)\phi_{xx}+\left(1-\frac{\phi_y^2}{a^2}\right)\phi_{yy}-\frac{2\phi_x\phi_y\phi_{xy}}{a^2}=0 \qquad (2)$$

But $$M^2=\frac{\phi_x^2+\phi_y^2}{a_t^2}$$

and equation 2 becomes

$$\phi_{xx}+\phi_{yy}=\frac{a_t^2}{2a^2}\left(\phi_x\frac{\partial M^2}{\partial x}+\phi_y\frac{\partial M^2}{\partial y}\right) \qquad (3)$$

By integration of Eulers equation $\int \frac{dp}{p} + \frac{V^2}{2} = 0$ for isentropic flow where $p/p_t = (\rho/\rho_t)^{\gamma}$ the subscript t refering to the throat conditions, it can be shown that:-

$$\frac{T}{T_t} = \frac{a^2}{a_t^2} = 1 - \tfrac{1}{2}(\gamma-1)(M^{+2}-1) \qquad (4)$$

Therefore equation 3 can be written

$$\phi_{xx} + \phi_{yy} = \frac{1}{1-\frac{1}{2}(\gamma-1)(M^{+2}-1)} \left\{ \phi_x \frac{\partial M^{+2}}{\partial x} + \phi_y \frac{\partial M^{+2}}{\partial y} \right\} \qquad (5)$$

The flow at the walls must be tangential, then with reference to fig 15

$$\frac{\phi_y}{\phi_x} = \tan\theta = \frac{x}{(R^2-x^2)^{\frac{1}{2}}} = \frac{x}{R}\left(1-\frac{x^2}{R^2}\right)^{-\frac{1}{2}}$$

expanding for $-1 < x < 1$

$$\frac{\phi_y}{\phi_x} = \frac{x}{R} + \frac{1}{2}\frac{x^3}{R^3}$$ neglecting terms x^5 and above

By substitution of ϕ (eqn. 1) in the equation of motion (eqn 5) and in the boundary condition (eqn 6), two identities are obtained in x and y. Eight equations can then be obtained in the unknown coefficients by equating the coefficients of x and y upto the second power. This has been done in appendix 3 and equations for M^+ obtained for a value of $\frac{h}{R} = 0.1111$, where h is the half width of the throat. The value of $\frac{h}{R}$ chosen corresponded to the actual nozzle used for the calculation of the characteristic net in the first part of this section.

When $\frac{h}{R} = 0.1111$ ie. $2h = 0.5090$ cms and $R = 2.29$ cms.

$$M^{+2} = 0.9650 - 0.4471 \frac{x}{h} + 0.1654 \frac{x^2}{h^2} - 1.584 \frac{x^3}{h^3} + 0.1144 \frac{y^2}{h^2} - 0.08471 \frac{xy^2}{h3} \qquad (7)$$

When sonic conditions are reached $M^{+2} = 1$ and equation 7 can be solved for $\frac{y}{h}$ by choosing a value of $\frac{x}{h}$. This has been done and the results tabulated in Table 29 section 10, together with the variation of the Mach number M^+ along the axis $\frac{x}{h} = 0$. Comparison of the experimental and theoretical sonic profiles will be carried out in section 10.

SECTION 6. The Mach Zehnder Interferometer.

Optical techniques possess several distinct advantages for the investigation of high speed gas flows. They are free from inertia lags, do not require the introduction of mechanical probes into the field, and record conditions throughout an extended flow field rather than the conditions at one point. The principal techniques are the interferometric, schlieren and shadow graphic; these all detect changes in refractive index associated with changes in speed of a compressible fluid stream.

Consider a stream of compressible fluid confined by glass windows, through which a parallel beam of light passes, and eventually falls onto a screen. Then if the stream is supersonic or near supersonic, the density changes and associated changes in refractive index corresponding to changes in speed of the fluid will be large and can be easily detected. The changes in refractive index retard the light beam and deflect it. The retardation is measured by the interferometric technique, the deflection by the schlieren, and changes in deflection between two adjacent points by the shadowographic.

In the interferometric technique, the density in the

test section is obtained by measuring the change in time of arrival of the beam in relation to a second beam which does not pass through the test section. In the schlieren method the flow pattern is obtained by observing the deflection caused by density gradients normal to the light beam, and in the shadowographic technique by the variation in deflection caused by changes in the density gradient.

Of the three methods the interferometric technique is the only one capable of yielding accurate quantitative results, the others are extensively used to show the position and type of density disturbance in the stream under investigation.

The type of interferometer commonly used for the study of gas dynamics is the Mach Zehnder, originated in 1890 by Mach[54] and Zehnder[55] working independently. The basic arrangement is shown in fig 16. Light from a source is collimated by a lens system L_1, the collimated beam is split into two beams of equal irtensity by a semi reflecting plate S_1 (fig 16). The reflected beam passes through the test section and is recombined with the transmitted beam at the second semi reflecting plate S_2. The recombined beam passes through the camera lens system and falls onto a screen or photographic plate at P. This

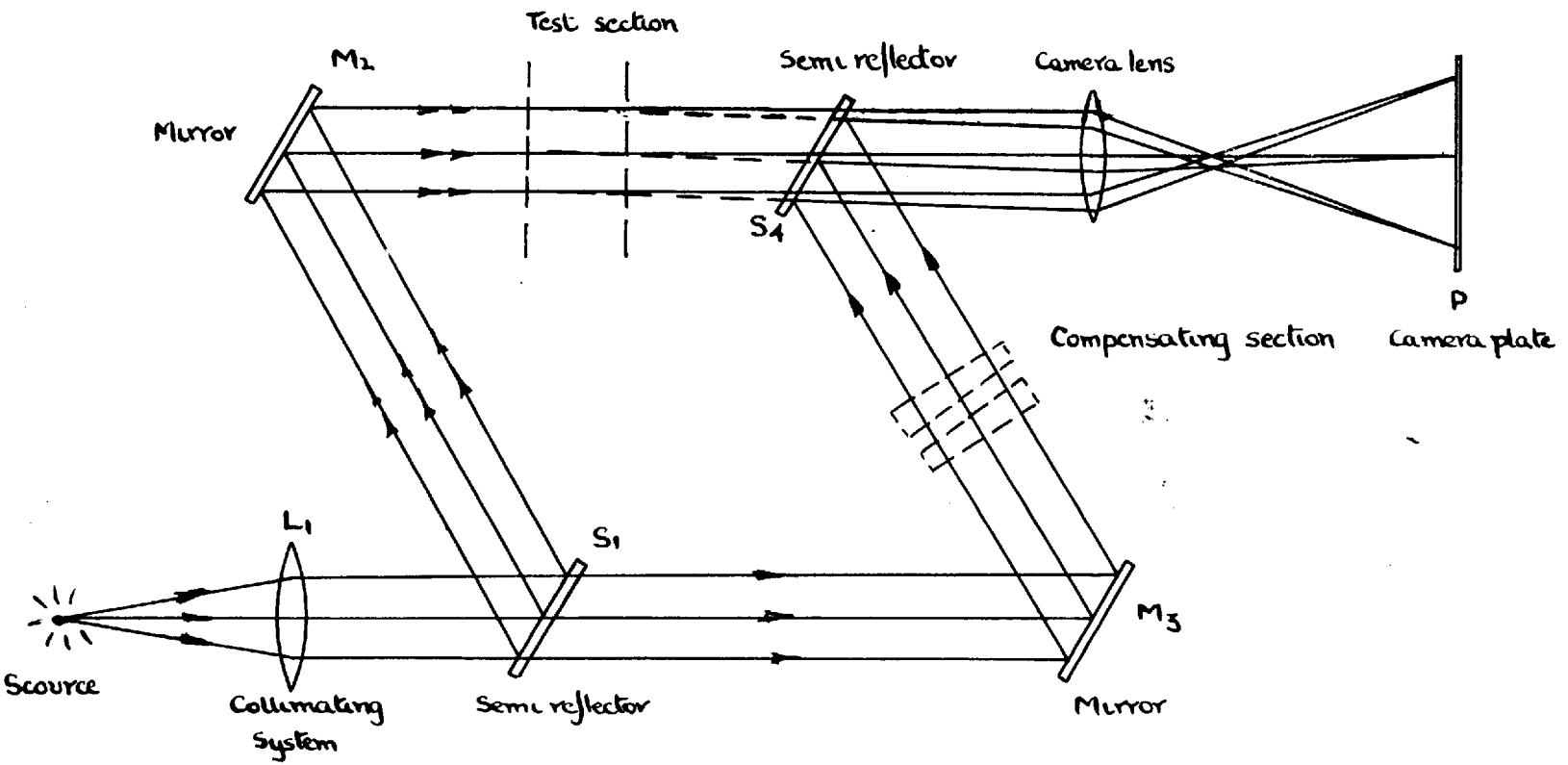

Fig 16. The basic arrangement of the Mach Zehnder interferometer

arrangement fulfils the necessary condition for interference, namely that the two interfering light beams originate at the same source..

The theory of the instrument is complex and incomplete in most treatments. Fairly complete surveys have been carried out by Winkler[56], Kinder[57] and Tanner[58], the latter includes a review of the methods of setting up two beam interferometers. Ladenburg and Bersharder[59] gave a brief account of the theory adequate for a working knowledge. Details of the sensitivity application and evaluation of interferograms are also given. Weyl[60], Winkler[61] and Schardin[62] describe methods by which interferograms of two dimensional and three dimensional phenomena can be carried out.

Various applications of the Mach Zehnder interferometer to the study of three dimensional high speed gas flow have been discussed by Winkler[61.63] and Ladenburg[59.64.65]. Bershader[51] investigated the flow in two dimensional nozzles to determine whether it was feasible to apply interferometry to wind tunnel studies. The results showed that accurate density determinations could be made by this technique. In later work by Bershader[66], a method of calculating the refraction error due to density gradients

in the flow was given. One result of the calculation was that if the focal plane of the camera is $\frac{D}{3}$ from the exit window, where D is the breadth of the test section, then the error due to refraction is negligible.

6.1. Description of the interferometer employed.

The Mach Zehnder interferometer (see fig 17) used in this work was designed and constructed by the German firm of Lutz for the study of the flow through wind tunnels.

The Y shaped base was constructed of heavy gauge steel tube 6" diameter. This in turn was supported on three springs to eliminate vibrational coupling between the nozzle and the instrument. The springs were designed for a 10" depression giving a calculated natural frequency for the whole assembly of 1 c.p.s.[67]. These springs completely eliminated all vibration from the concrete floor on which the nozzle stand and interferometer were mounted.

The 6" diameter optical elements of the interferometer were mounted on the corners of a 60° parallelogram in a 12" diameter steel tube, matt black finished on the inside. The assembly containing the optical elements was mounted on an axis between two pillars fixed to the 'Y' shaped base,

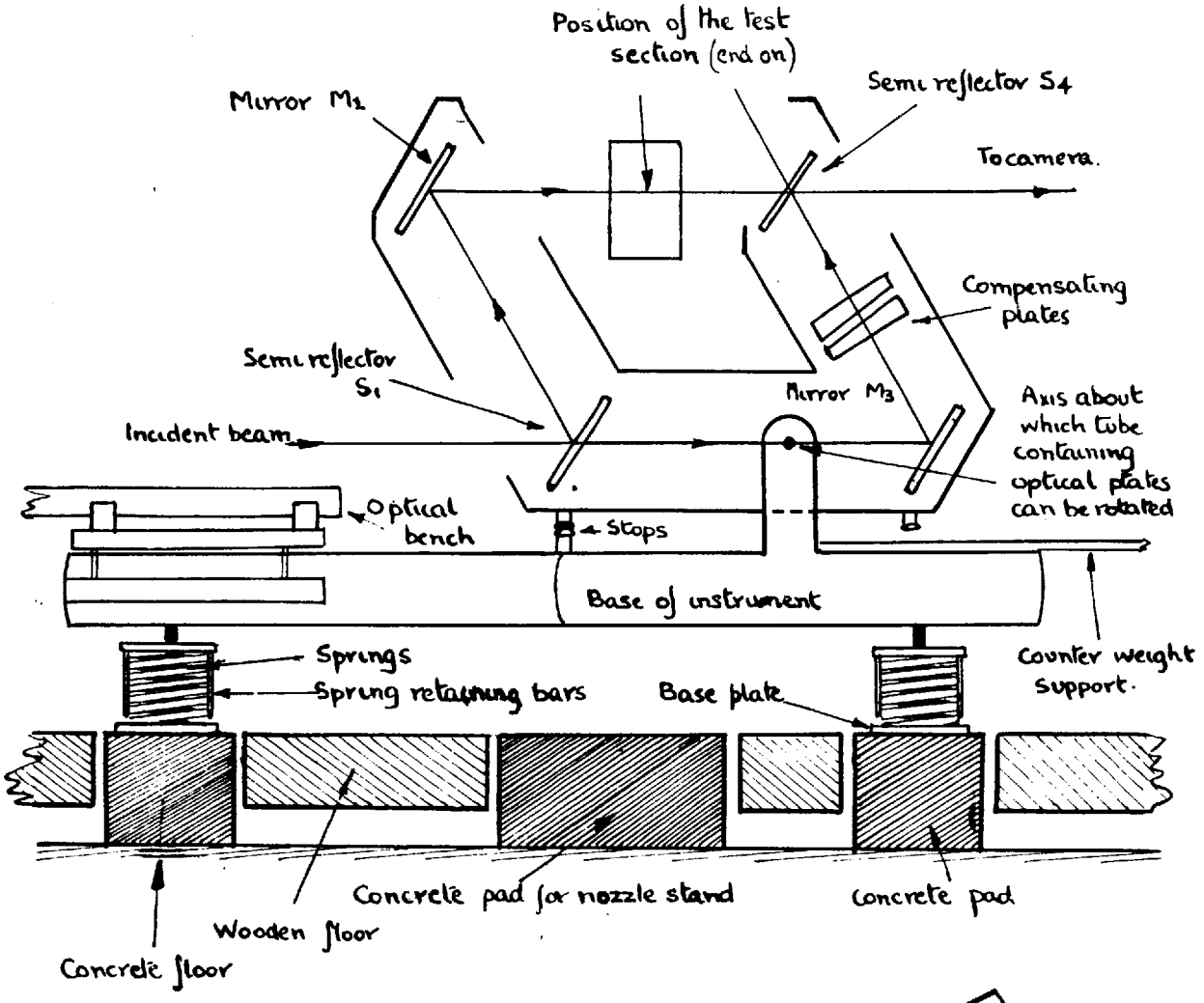

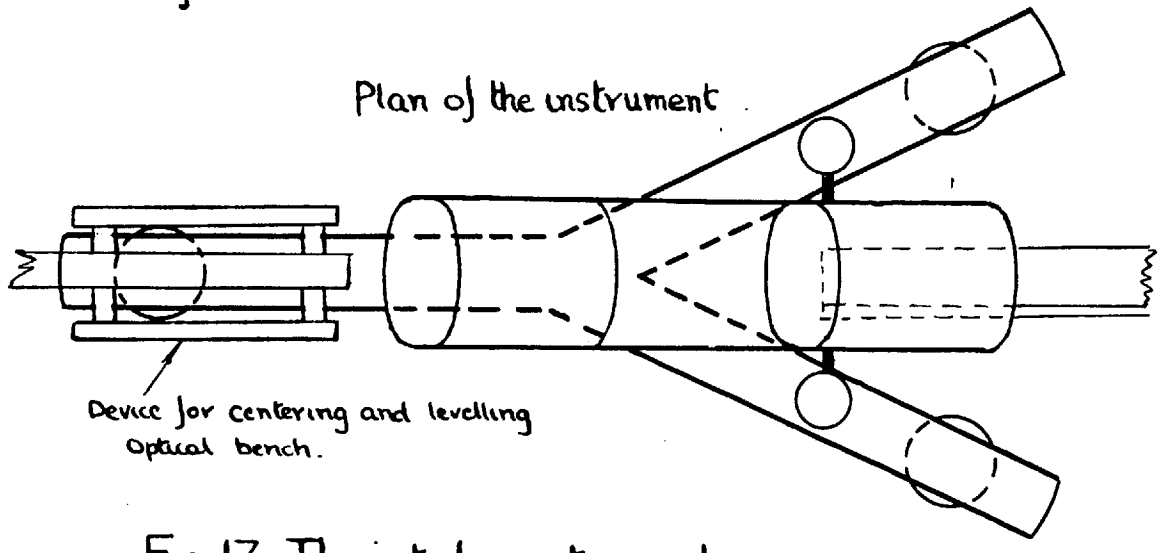

Fig 17 The interferometer used.

so that it could be turned through 60° bringing the optical plates into the horizontal plane. The compensating plates were slightly wedge shaped, the angle being approximately 3°.

The optical plates were mounted in gimbals, permitting rotation about an axis in the optical surface of the plate. Rotation to very fine limits could be carried out by means of micrometer screws acting through lever reduction gears. The screws were connected to a control panel by means of flexible drives, so that very fine adjustments could be carried out while observing the fringes in the emergent beam.

6.2. The Light Scource.

The light from the scource should be as monochromatic as possible as the number of observable fringes decreases as the band width increases. The number of observable fringes obtained with a source of half band width λ' and peak wavelength λ_p varies between $\frac{1}{3}\frac{\lambda_p}{\lambda'}$ to $\frac{\lambda_p}{\lambda'}$ depending on the amount of stray light, the photographic process and the acceptable minimum contrast between fringes. The brightness of the source should be as high as possible to get maximum intensity from minimum size. If the source is too large the light entering the interferometer will not be in phase and the number of observable fringes will be

63 58 68

reduced.

Critera for the angular opening of the source has been given as $w = \sqrt{\frac{2\lambda p}{f_2}}$ [68] or $w < 10^{-2}$ [69], where f_2 is the focal length of the collimating lens.

The speed of the source must be high, to prevent any blurring of the fringes due to standing vibrations in the jet[51 66].

The most satisfactory source for filling the above requirements has been found to be a condenser discharge[61 65 68 69 70 71] between metal electrodes in air, a monochromator or filter being used to make the light monochromatic.

The condenser size and voltage varies widely with different observers, as it is not possible to give a rating to a condenser in terms of light output, as the intensity and duration of the spark are functions of the energy stored in the condenser, its inductance and the circuit construction. The light required also depends on the optics of the interferometer and the photographic technique used. Therefore a satisfactory light source was obtained by selecting the smallest condenser which gave a spark of sufficient luminous energy and speed when discharged through a low inductance circuit[71 72].

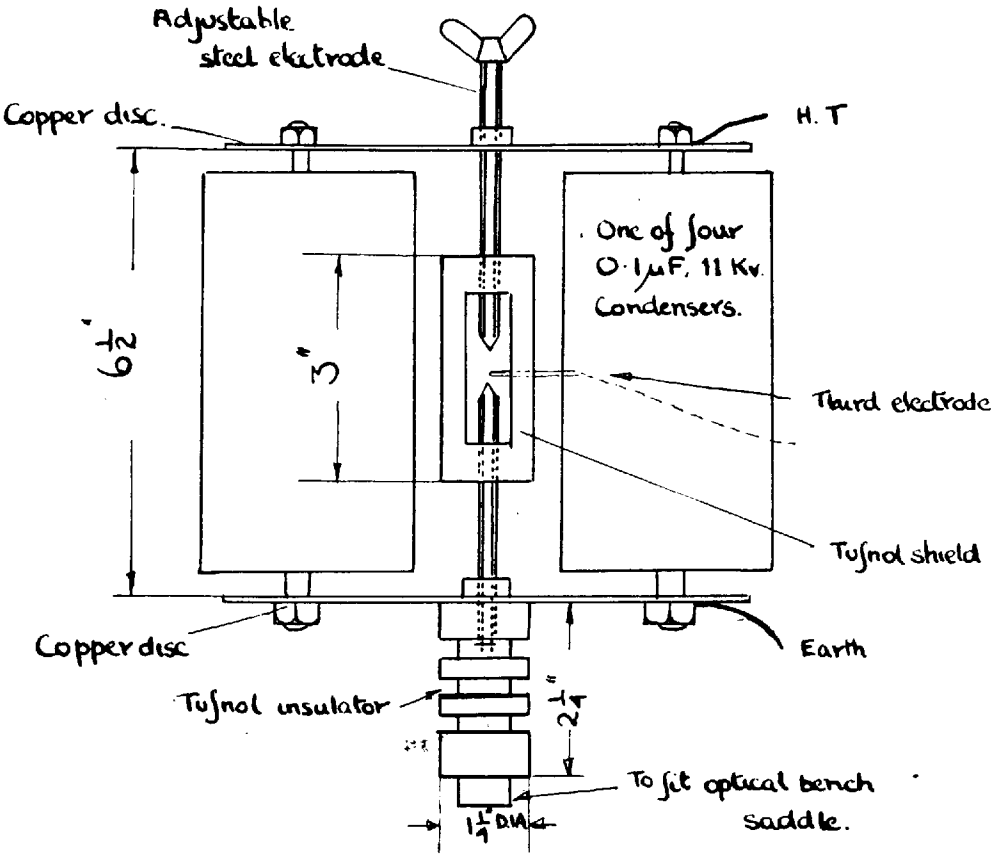

Fig 18. The light source

After several attempts with different condensers the arrangement shown in fig. 18 was found to be satisfactory. The source consisted of two steel electrodes held in a Tufnol shield. A third electrode was placed approximately $\frac{1}{8}$ in. above the earthed electrode. The four low inductance condensers, 0.1 μF. 11 Kv. working, were packed between two circular copper plates, which carried the steel electrodes through their centres. The spark was fired by discharging a spark between the third and earthed electrodes.

6.3. The Ancillary Optical Equipment.

The arrangement of the ancillary optical equipment is shown schematically in fig. 19. The light from the spark source was condensed onto a slit, by means of a f.2.5, 7 in. lens of good optical quality. Monochromatic light was obtained by means of a dielectric filter placed after the slit. The filter had a peak transmission of 18.6% at . ^{o}A, and a half band width of 100^{o}A. The green light was collimated by a f.6.3, 19.5 in. lens.

The light source, slit and filter, etc. were mounted on an optical bench fixed to the base of the interferometer

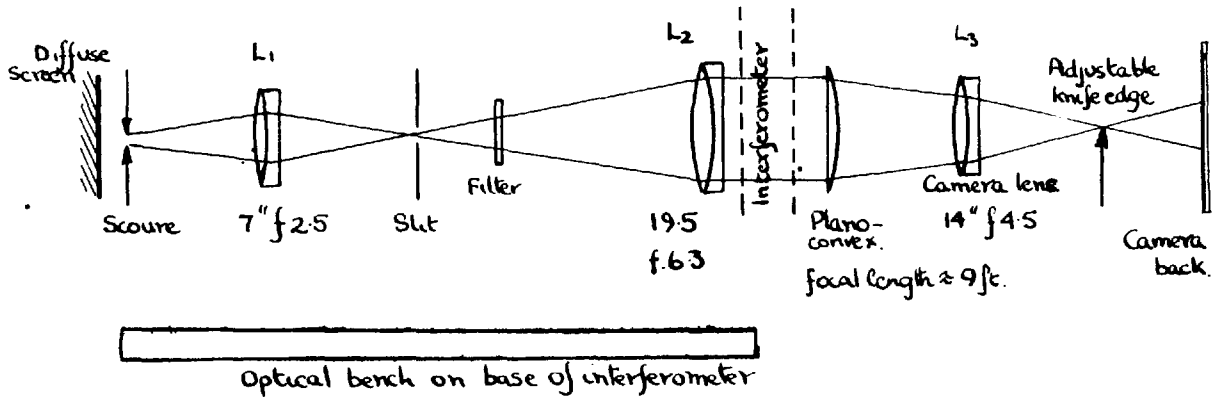

Fig 19. The ancillary optical equipment.

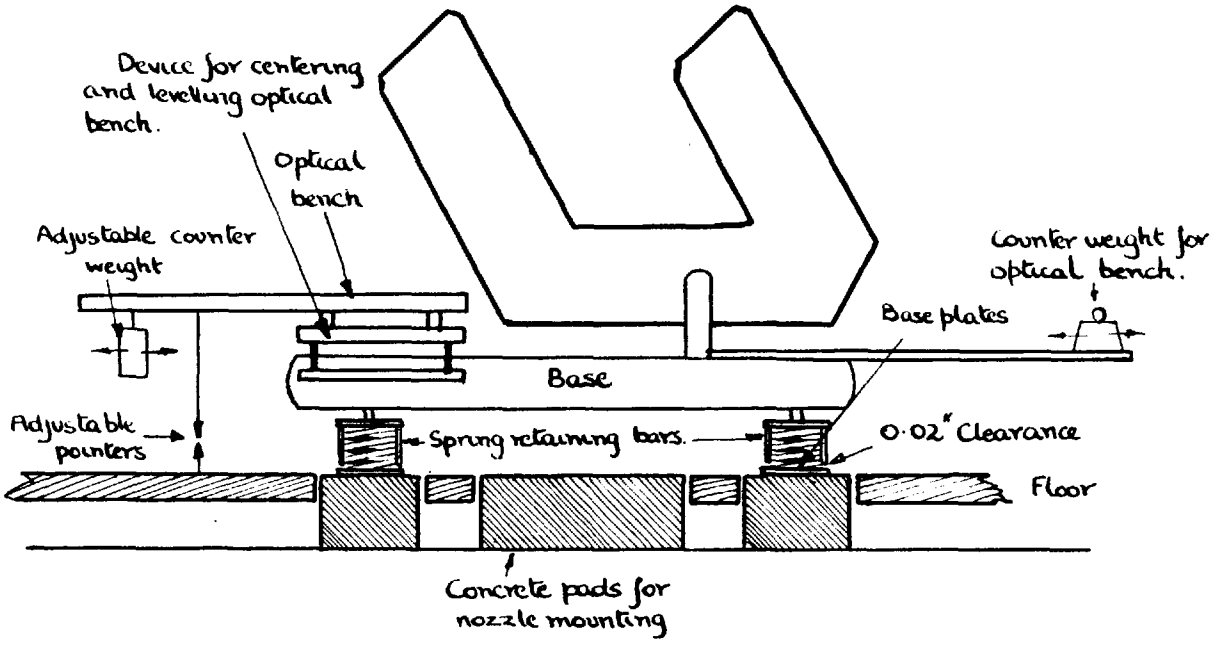

Fig 20. Apparatus for levelling the interferometer.

(see fig 17). The bench could be adjusted in the horizontal and vertical planes to align the optical axes of the source and interferometer. The emergent beam of the interferometer was condensed onto a f.4.5, 14 in. camera lens by a plano-convex lens of good optical quality.

6.4. Method of Maintaining the Orientation of the Interferometer Relative to the Test Section.

In a two dimensional nozzle the flow properties vary in the x and y directions and are constant in the z direction. Therefore to obtain an interferogram from which changes in property along the x and y coordinates can be calculated, the light beam must be parallel to the z axis; that is perpendicular to the test section windows.

The depression of the antivibration springs was found to change slightly with time, altering the position of the interferometer so that the light beam was no longer perpendicular to the test section windows. Therefore a method was devised for checking the position of the interferometer before each run.

When the interferometer had been set up, the lengths of the spring retaining bars (see fig. 20) were adjusted until there was 0.02 in. clearance with the base plates.

The pointer on the optical bench was centred on the corresponding one on the floor with 0.02 in. clearance. Immediately before each test the clearances were checked and any lateral swing detected by the non coincidence of the pointers.

The counterweights shown in fig 20 were found to be necessary to distribute the load on the springs evenly and also to make adjustments possible.

6.5. Density Determination and Fringe Orientation.

Atmosphere density prevails in the test section before the flow takes place. While gas is flowing through the nozzle a density distribution exists which is in general different from atmosphere. Therefore the optical path of a light ray passing across the channel will change when flow takes place. The object of the interferometry is to provide a means whereby the change in optical path length can be measured. Two methods have been used to do this; the infinite fringe and fringe shift methods.

In the infinite fringe method the optical plates are parallel and the fringe width infinite, ideally one fringe covering the whole field of view. When flow takes place

fringes appear which represent lines of constant density. Then if ρ_c is the density on one fringe and ρ_b that on the next, $\rho_c = \rho_b + \frac{\lambda_p}{KD}$, where K is the Gladstone-Dale constant. The method was only used, as in fig 11, to obtain a pictorial representation of the flow. It was not used for density determination, because it suffers from the disadvantage in that corrections cannot be made for optical defects in the interferometer plates and for refraction and boundary layer effects within the test section. In the fringe shift technique, the change in optical path caused by the flow causes a shift of the interference fringes. Then as the index of refraction and hence the density at any point in the channel depends on x and y only, the fringe shift $s(x,y)$ can be easily converted to the density $\rho(x,y)$ by the relationship

$$\rho(x,y) = \rho_a + \frac{s(x,y)}{KD} \lambda_p \quad [59,60]$$

where ρ_a is the atmosphere density.

The fringe shift at a point in the flow field, measured in units of no flow fringe spacing, is independent of the spacing and orientation of the fringes in the no flow condition[59,60,65]. However the fringe spacing should be as small as possible[61] and in studies involving boundary layers[51,73] it is convenient to orientate the fringes

perpendicular to the axis of symmetry as it is then possible to follow a fringe through a boundary layer.

6.6. Reference Regions.

The methods of linking density change with fringe position have been discussed, but to be of any practical use it must be possible to measure fringe position and changes in it. In the relationship $\rho_{xy} = \rho_a + \frac{S_{xy}}{KD}\lambda_p$ the calculation of the density ρ_{xy} depends on a knowledge of the no flow density ρ_a and S_{xy} the fringe shift.

The atmospheric density ρ_a can be easily obtained. To calculate the fringe shift the fringes in the flow and no flow interferograms must be correspondingly numbered. To do this a region must exist in which the fringes remain in the same position before and during the test; this is called the reference region. The reference regions used in this study were in the stagnant air at the end of the nozzle blocks (see fig 25).

It must also be possible to follow a given fringe through a discontinuity like a shock wave. In many interferometric studies[59 66 71] the five or six fringes given by a white light source have been used to follow

fringes across shock waves. This could not be done in this research as it was not possible to obtain white light fringes. With white light 60 fringes were obtained of very low contrast. Tanner[58] has shown that any difference in the thickness of glass in the two beams of the interferometer reduces fringe contrast and increases their number due to dispersion. He gives as the limit for the difference in glass thickness as:-

$$w = \frac{z^2}{6200} \text{ cms}$$ where z is the number of fringes in the absence of dispersion. With white light the maximum difference in glass thickness is therefore approximately 4.0×10^{-3}cm. The value for the instrument used was approximately 5×10^{-2}cm. which exceeds the limit and hence white light fringes could not be obtained.

6.7. The Method of Increasing the Density Range Covered by the Available Fringes.

If the maximum positive and negative fringe shifts produced by the flow in the nozzle are -N and + M, the number of fringes required is N + M, and when there are No fringes in the no flow field the number of fringes required will in general be increased by No. In a high speed wind tunnel of breadth D and stagnation density ρ_o, the range of

densities encountered in the flow will usually be a large fraction of ρ_o. The corresponding fringe shift $K\rho_o D/\lambda p$ together with the No fringes in the no flow field represents the approximate minimum number of fringes required.

Using the interferometric system already described 70 distinct fringes could be obtained. Therefore the maximum pressure that could be used was approximately 50 p.s.i.g. As this pressure is considerably below the pressures used in this work a method of utilizing the available fringes more effectively was developed.

By using the compensating plates to set up the fringes as described in appendix 5 fringe shifts upto 90 could be obtained by making the fringe sequence reverse. In fig 21 the usual type of flow and no flow interograms obtained using the fringe shift technique are shown, with corresponding fringes numbered. In fig 22 the range of fringe shifts has been increased by causing the fringe sequence to reverse in the flow interferogram, increasing the range of density measured.

No flow

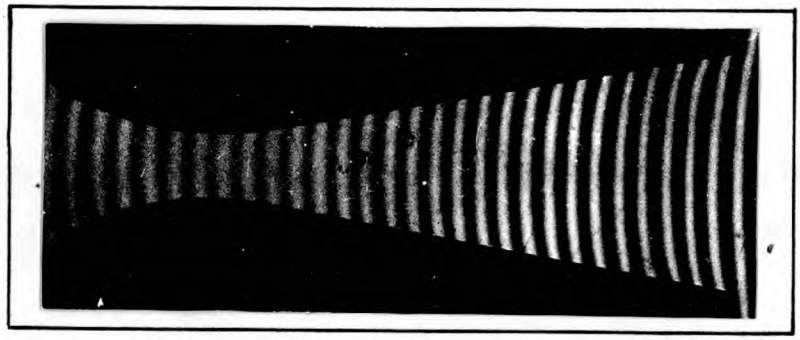

Flow

(a)

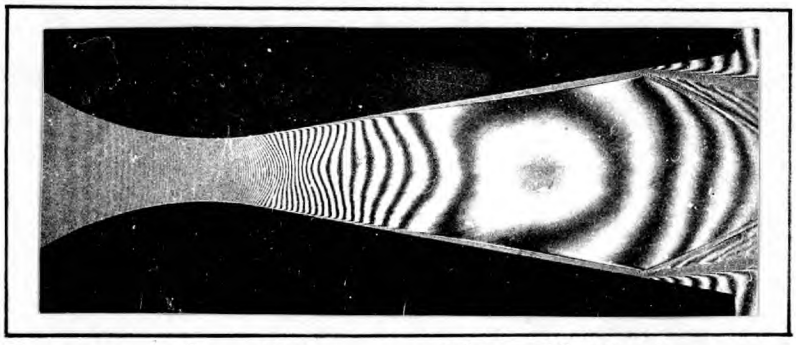

Fig 21 Flow and no flow interferograms taken with the beams BB + CC interfering (Appendix 5) so that the fringe sequence reverses.

No flow

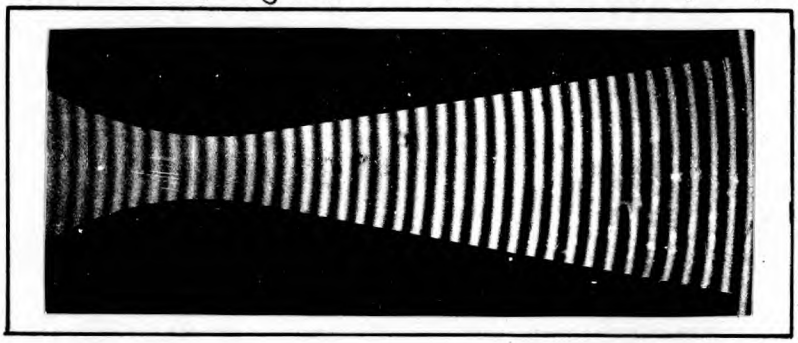

Flow

(b)

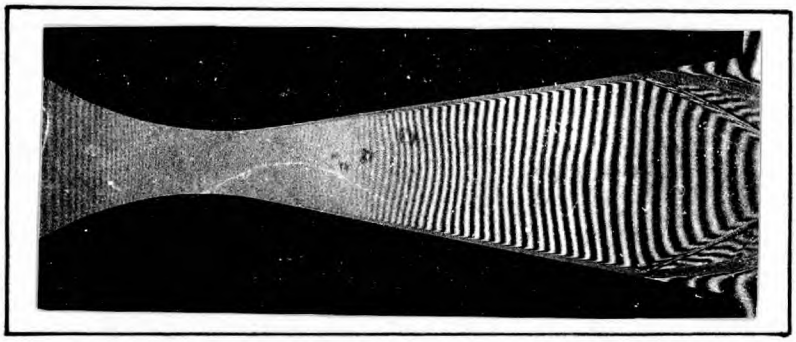

Fig 22. Flow and no flow interferograms taken with the beams AA + CC interfering (Appendix 5) so that the fringe sequence does not reverse

Fig 21+22. Interferograms demonstrating the different fringe patterns that could be obtained by manipulation of the compensator plates.

SECTION 7. DESCRIPTION OF APPARATUS.

The interferometer and its associated optical equipment were described in the last section. The nozzle with its associated equipment and the method by which it was mounted will now be described.

7.1. The Compressed Air System.

The air supply system is shown schematically in fig 23. The oil and water were removed from the air obtained from the compressor B in four separators CDEF, at a pressure of 130 atm, maintained by the needle valve G. The dried air passed into the storage bottles HH having a total capacity of 135 cu.ft. at a maximum pressure of 120 atm.

The water content of the stored air, approximately 1.4×10^{-4} lb water[74]/lb of dry air was below the maximum[75] that could be tolerated if condensation shocks were to be avoided in the nozzle.

The air in the storage bottles passed by way of stop valve I and 100 ft of $1\frac{1}{2}$ in. bore pipe to a quick opening valve J.[76] The pressure immediately upstream of the nozzle was maintained by two diaphram reducing valves L and K.

When the stagnation pressure in the nozzle was small

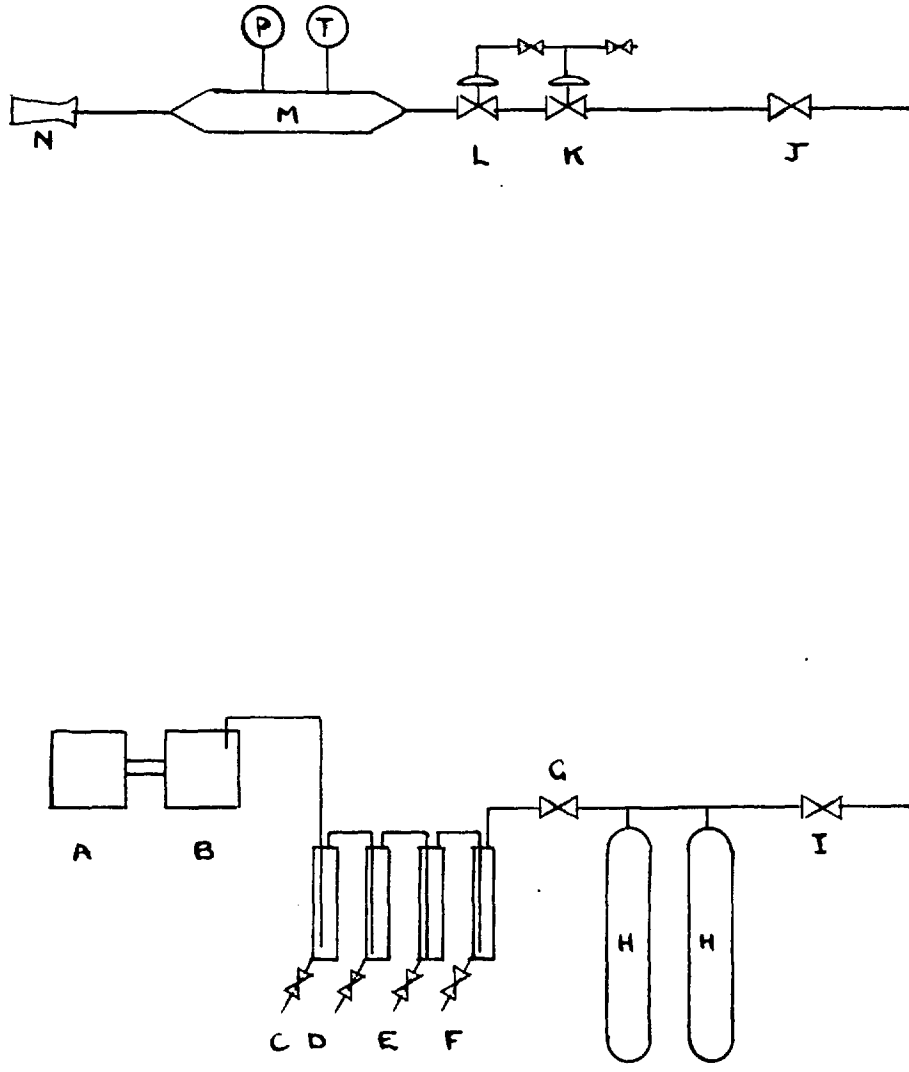

A. Diesel engine
B. 3 stage Air compressor
C Air cooled separator
D Water " "
E " " "
F Separator packed with activated carbon.
G Regulating valve.
J. Quick opening valve
H 135 cu. ft air bottles.
I Stop valve
K High pressure regulating valve
L Low " " "
M Settling chamber in which temperature and pressure were measured.
N Nozzle.

Fig 23 The air supply system.

compared with the storage pressure, and only one reducing valve used, it was found that the valve seat chattered causing the downstream pressure to fluctuate rapidly. The problem was overcome by reducing the pressure drop across the valve by incorporating a second valve.

The second valve was connected to the settling chamber M, where the pressure and temperature of the air were measured immediately before it expanded in the nozzle.

7.2. Design of the Nozzle.

A nozzle was required in which the Mach number at separation could be varied by changing the stagnation pressure. It was also important that the flow should be as close to one dimensional flow as possible, as then the assumption of constant pressure across the boundary layer could be made, and hence pressure gradients other than those in the stream direction would have no effect on the separation process.

It has been shown theoretically by Taylor[53] and Sauer[52], and practically by Fraser and Rowe[76] that the flow in the throat of a nozzle approaches one dimensional flow as the ratio of convergent section radius to throat width

approaches infinity. Hence for uniform flow at the entry to the divergent section, the convergent section radius should be as large as possible. However the extent to which the radius could be increased was limited by the length of the nozzle that could be accommodated in the holder available.

Uniform flow can only be achieved in a divergent section of zero half angle, but as the flow in such a nozzle becomes choked, the divergence angle should be as small as possible consistent with achieving a reasonable degree of acceleration. Since the constricting effect of the boundary layer in the throat of the nozzle increases as the throat width is decreased, the width should be as large as possible. As the width is increased, however, the flow rate through the nozzle increases and therefore a limitation is imposed by the air supply system.

It is apparent from section 6.5. that the sensitivity of the interferometric method increased as the breadth of the nozzle increased, and so for high sensitivity it should be as large as possible. However the breadth was limited by the number of fringes available, because the density range covered by a given number of fringes decreases as the breadth is increased.

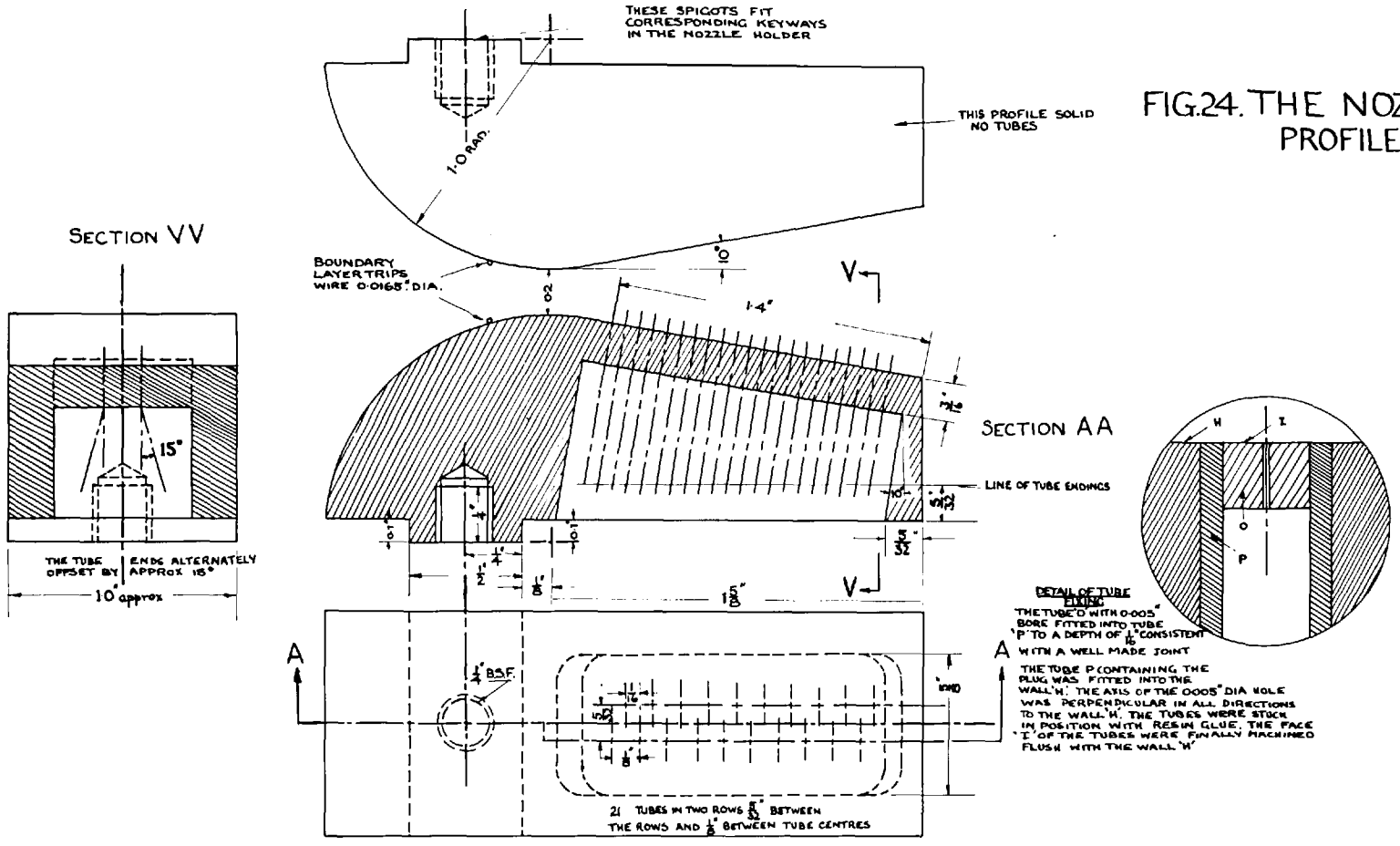

FIG.24. THE NOZZLE PROFILES

The nozzle shown in fig 24, chosen as the reasonable balance between the conflicting requirements, was one of 10^{o} divergence half angle, one inch convergence radius, a throat width of 0.2" and a breadth of one inch.

To obtain symmetrical flow about the axial plane of a small two dimensional nozzle the machining tolerances required are too small to be obtainable practically, therefore all the static pressure holes were placed on one wall of the divergence, and separation on this wall only studied.

In a small nozzle the pressure gardients in the stream direction are large; for example in a two dimensional nozzle of 0.2" throat width and a divergence half angle of 15^{o}, the variation in pressure across a hole of 0.018" dia, (as used by Wilkie[28]) amounts to $\mp$ 2.6% of the static pressure ratio at the axis of the hole. To reduce this error holes of 0.005 in diameter were used, these being the smallest that could be conveniently accommodated consistent with a reasonable response time. Twentyone pressure holes were used, their position and manner of construction are shown in fig 24.

The nozzle holder which has been described previously[77] was modified slightly so that two reference regions (see section 6.6.) could be accommodated. The nozzle holder

with the nozzle blocks mounted is shown in fig 25.

The dimensions of the nozzle and the positions of the pressure holes were obtained by the method given in appendix 1.

Air leaks between the glass windows and the sides of the nozzle were eliminated bypaper gaskets impregnated with soft rubber, cut so that there were no projections into the flow field.

7.2.1. Boundary Layer Trips.

The cause of the assymmetric separation pattern at low stagnation pressures observed in this work (see section 9.2.2.) and by Wilkie[28] was attributed to transition taking place in the boundary layer at the point of separation, as the results were similar to those of Chapman et al[8]. If the supposition were correct, the assymmetric separation would be eliminated by promoting a turbulent boundary layer artificially. Therefore wires were stuck onto the convergent section walls upstream of the throat (see fig 24).

The Reynolds number based on the wire diameter, 0.0165 in, and free stream flow conditions was 1.9×10^5, which was greater than the critical value[29] required to promote turbulence.

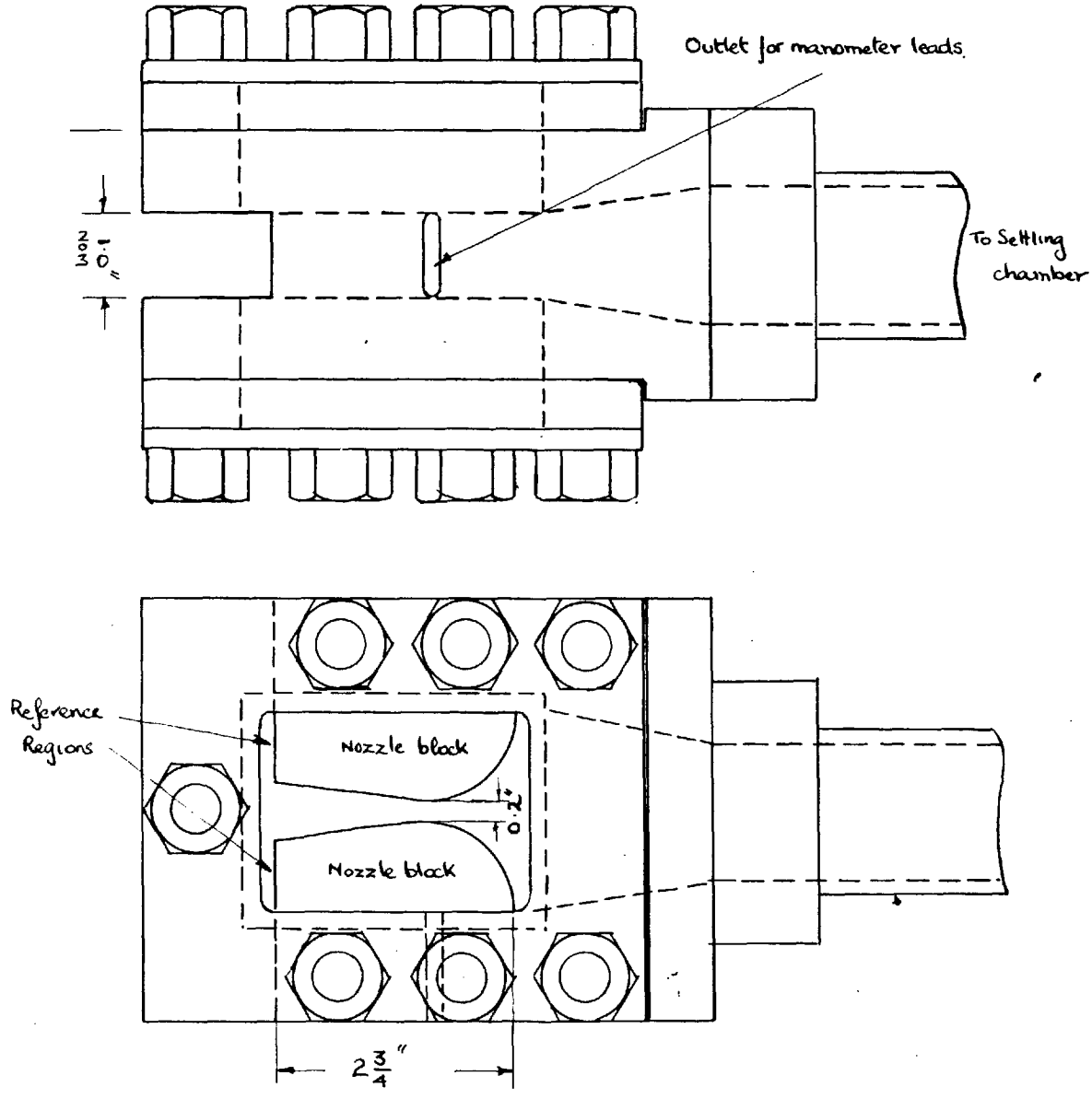

Fig. 25 The nozzle holder.

7.3. Mounting the Nozzle.

The nozzle was connected to the settling chamber by a short length of steel 1½ in. bore tubing. The whole rigid assembly was mounted on a stand so that the nozzle was in the beam of the interferometer. The position of the nozzle assembly on the stand was adjustable in the horizontal and vertical planes.

The stand consisted of one inch bore pipe, cross braced and fixed to concrete pads on the main floor of the buildings, ensuring a rigid structure.

The air from the nozzle was discharged to atmosphere down a 6 in diameter pipe.

7.4. Measurement of Stagnation Pressure.

The pressure of the air in the settling chamber fig 26 was measured by a Bourdon test gauge. The pressure gauge was mounted so that the spark source illuminated it, enabling photographic recording of the reading. Frequent calibration of the gauges were carried out by a dead weight tester.

As the velocity of the air in the settling chamber was small ($\approx$ 14 ft/sec) the difference between the static and

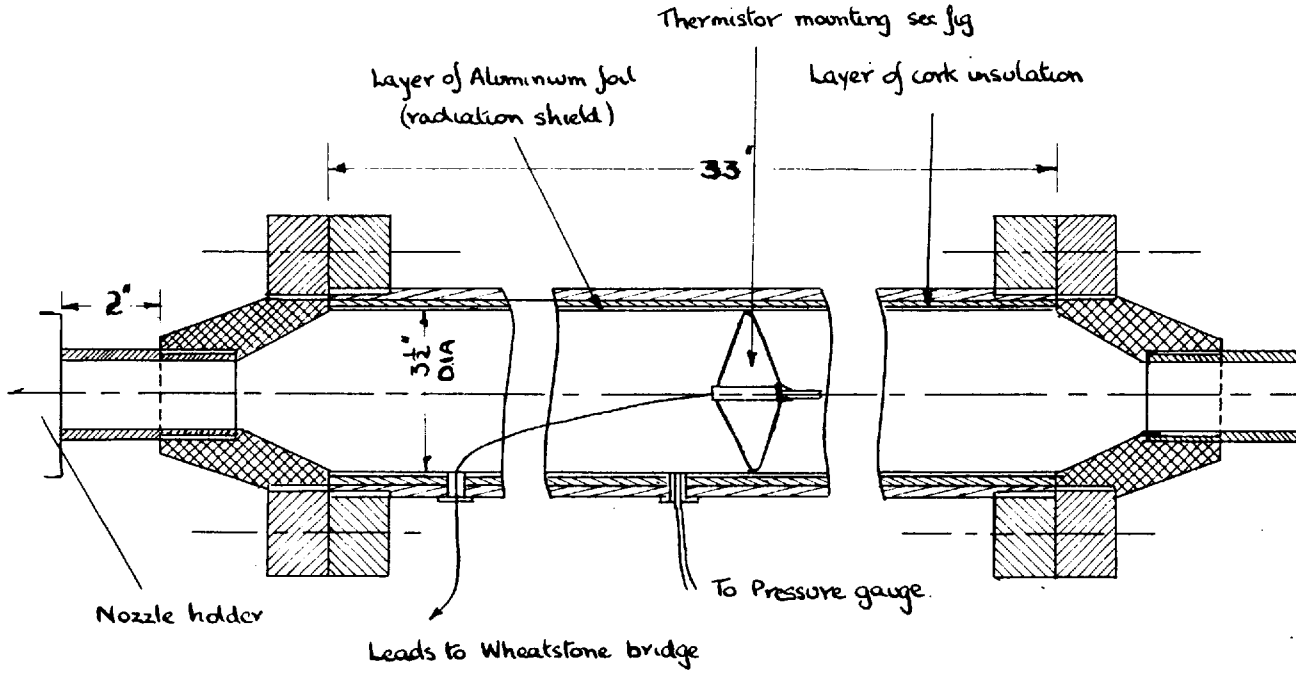

Fig 26 The settling chamber with thermistor mounted

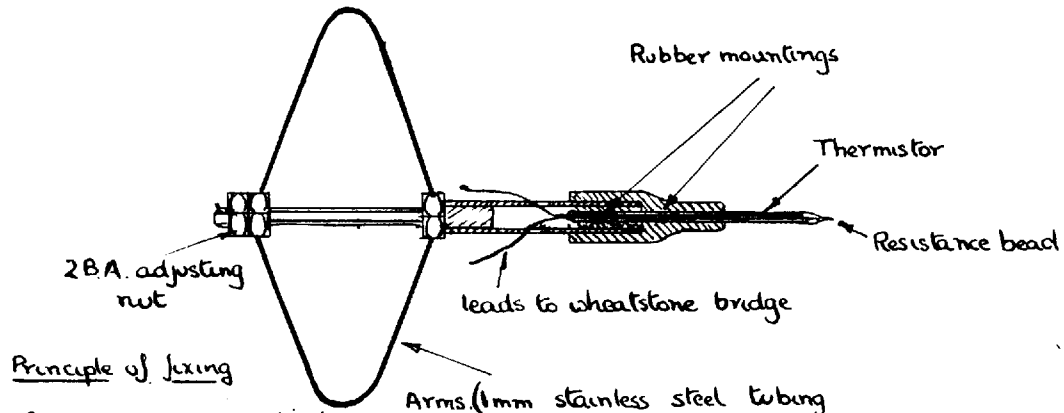

Principle of fixing

By screwing up the adjusting nut the radius of the arms increases jamming the mount inside the settling chamber.

Fig 27. The thermistor mounting.

stagnation pressures was negligible, and therefore the gauge reading was taken as the stagnation pressure of the air in the settling chamber.

7.5. Measurement of the Stagnation Temperature.

The stagnation temperature was measured in the settling chamber by a Stantel F.22 thermistor. The resistance element, 0.02 in dia, was incorporated in the sealed tip of a glass tube mounted on the axis of the settling chamber. The detail of the mounting is shown in fig 27. To avoid the necessity of making a radiation correction to the indicated temperature, the inside of the settling chamber was lined with aluminium foil insulated from the main casing The resistance of the thermistor was measured with a Wheatstone bridge and by using a mirror galvanometer it was possible to detect changes in temperature corresponding to $0.01^{\circ}c$.

Calibration was carried out in a small air bath immersed in a water bath at different constant temperature levels, which were recorded by means of a standard mercury thermometer. As the measurement of resistance necessitates passing a current through the thermistor, electrical power is dissipated in the bead, heating it. The degree of

heating depends on the rate of heat loss from the resistance element.

As the thermistor was calibrated in stagnant air and subsequently used to measure the temperature of a moving air stream, where the rate of heat dissipation from the resistance element was different, the effect of internal heating on the indicated reading was determined. The calibration curves presented in fig 28 were obtained by maintaining two different potentials across the resistance element, such that the power dissipated at 3000 ohms for curves I and II were 1.69 and 0.19 milliwatts respectively. The curve for zero power dissipation in the bead obtained by linear extrapolation is also given.

In all temperature measurements in the settling chamber, the bridge circuit used was identical to that used to obtain curve II. All the results were extrapolated to zero power, as it was assumed that the moving air stream effectively removed the small quantity of heat generated.

The effect of pressure on the thermistor was determined by calibrating at two different pressures 0 and 300 p.s.i. no detectable change of indicated temperature was observed.

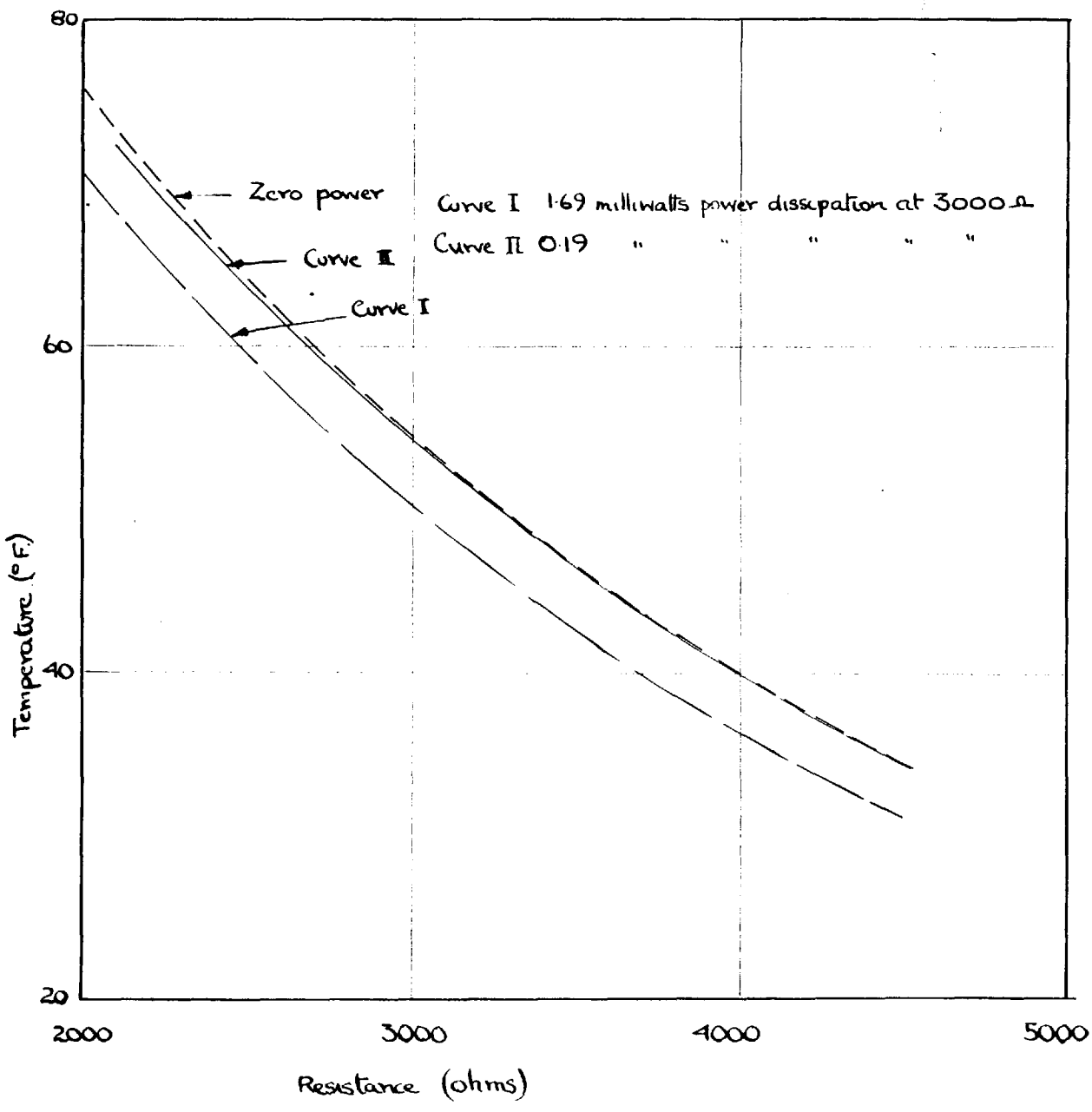

Fig 28 Calibration curves of the thermistor

7.6. Measurement of Static wall pressure in the Nozzle.

The pressures were measured on a bank of 22 mercury manometers connected to the pressure tappings by means of 1.mm. bore tubing via a stop valve. The valve consisted of a roller pivoted off centre and a steel plate. Rotation of the roller clamped the tubes between it and the steel plate, so that the manometer pressures could be recorded at a later stage.

Each manometer tube was 10 ft long so that pressures up to 60 psia could be recorded if necessary.

SECTION 8: Experimental Procedures

The object of this research was to obtain data on the separation of boundary layers in an overexpanded nozzle, so that a comparison of the results with those obtained on steps and wedges in wind tunnels could be made.

The data required were obtained using the nozzle described in section 7.2. and included the wall pressure variation, the density (by interferometory) and the Mach angles (by shadowgraphs and schlieren photographs). Prior to each test the reservoir pressure was adjusted so that separation would take place from the walls of the divergence of the nozzle.

Tests were carried out at a series of intermediate points in the stagnation pressure range of 45 - 165 p.s.ia., corresponding to a range of boundary layer separation positions just downstream of the throat and at the end of the divergence respectively.

Interferograms, focussed and direct shadowgraphs (see section 8.1.2.) and schlieren photographs with simultaneous wall pressure measurements were taken at each intermediate pressure.

A series of tests were carried out over the complete

pressure range with the boundary layer trips fitted in the convergence of the nozzle, in which focussed shadowographs and wall pressure measurements were obtained.

8.1. Optical Methods

8.1.1. Interferometry.

The position of the test section or nozzle with respect to the interferometer is shown in fig 17. The nozzle holder (see fig 25) was arranged on the nozzle stand so that the axis of the nozzle was horizontal and normal to the light beam passing through it. The camera was focussed on an object plane in the nozzle at a distance equal to one third of the nozzle breadth from the window nearest the camera (see section 8.3.1.) and fringes of the desired spacing and oriontation brought into focus by manipulation of the compensating plates (see Appendix 5).

Before each test the orientation of the interferometer relative to the test section was checked (see section 6.4.) and the barometric pressure, temperature and the wet and dry bulb temperatures obtained.

As soon as the no flow interferogram had been taken, air of predetermined pressure was discharged through the

nozzle. When the resistance of the thermister and the levels in wall pressure manometer had reached steady values, the manometer valve was closed and the stagnation pressure recorded simultaneously.

After approximately one hour the air in the test section was assumed to be at room temperature once again and a further no flow interferogram was taken. If this did not match the previous one, or if the room temperatures before and after the test differed by more than one degree centigrade, the test was rejected as far as interferometric results were concerned.

All the interferograms were photographed using Ilford 5G91 recording film developed in 1D.33 for five minutes at 70°F.

8.1.2. Schieren and Shadowgraphic Methods.

The main use of the schlieren and shadowgraphic methods are the direct visualization of the flow so that the positions and shapes of regions of density variation such as those that occur in shock waves expansion waves and boundary layer can be determined. Both methods were used to find the point of transition from laminar to turbulent flow in the boundary layers.

a) Schlieren Method.

This method has been used[51] to determine whether a boundary layer is turbulent or laminar, the turbulence in the layer showing up as a small flocculent detail.

Schlieren photographs of the flow (see fig 29) were obtained by blocking off the second beam of the interferometer at the compensating plates and by placing a knife edge at the focal point of the camera lens which was focussed on the same image plane as used for the interferograms. The height of the knife edge was adjusted until the illumination of the screen was reduced approximately by half. White light was used and a slit size 0.4 mm square. No other alterations were made to the spark source or the collimating optics shown in fig 19. The film used was identical to that used to photograph interferograms.

b) Direct shadowgraphic Method.

Direct shadowgraphs (see fig 29) were obtained by blocking off one beam of the interferometer at the compensating plates and placing photographic plates parallel to and directly behind the test section windows. For sharp shadowgraphs the source should be small[59 60]; a slit 0.2mm square was used with the filter removed and with no other alterations to the collimating optics.

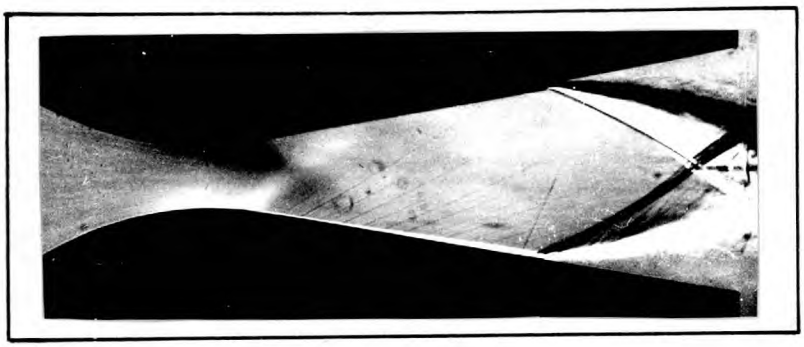

Schlieren photograph

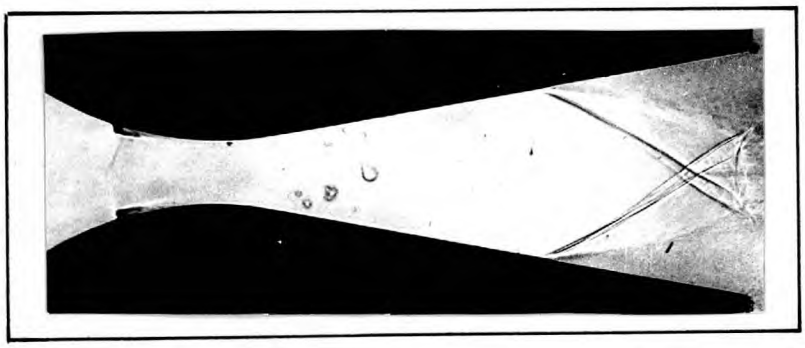

Focussed shadowgraph

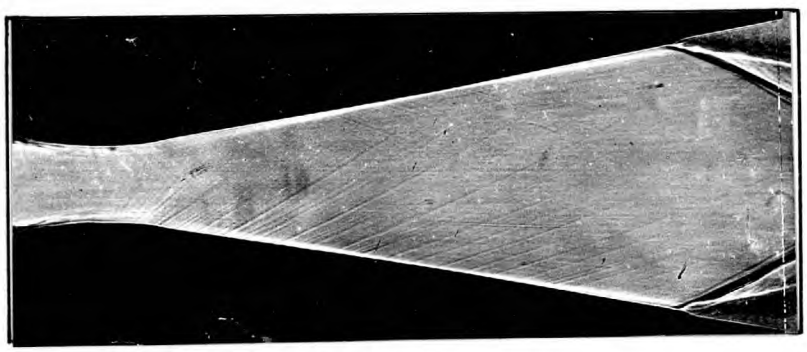

Direct shadowgraph

Fig 29 Schlieren and shadowgraphs of the flow in the nozzle.

c) Focussed Shadowgraphs.

This method differed from the other shadowgraphic technique in that the camera was used. The system used was identical to that for schlieren studies except that the knife edge was removed. As the camera lens had a finite depth of focus, the image illumination did not correspond to that in a plane as in the direct shadowgraphs, but was the integrated result along the light beam for a distance corresponding to the depth of focus of the camera lens. The final image was identical to that formed by the direct shadowgraphic method in that the positions of shock waves and Mach lines were the same, but the boundary layers were different in appearance and the focussed shadowgraphs were usually less sharp in detail (see fig 29).

The focussed and direct shadowographs were obtained using 5G91 film and Ilford H.P.S. plates respectively.

8.2. Measurement and Evaluation of Interferograms.

It can be seen from section 6.5. that the density at any point in the nozzle can be calculated from the fringe shift. Therefore to calculate the fringe shifts, the positions of the no flow and flow fringes must be measured.

The positions of the fringes were measured with a comparator, which consisted of a microscope and cross wires which could be traversed by two micrometer screws at right angles to each other. The same instrument was used to measure the nozzle profile (see appendix 1).

Measurement of the fringe position with a densitometer was not practical as it was found that the effects due to the grain of the film could not be eradicated.

The fringes of the no flow and flow interferograms were measured on a number of traverses parallel to the axis of the nozzle. They were usually one millimetre apart so that the fringes could be represented graphically twenty times full size. The outline of the nozzle on the interferograms was also obtained so that the magnification of the image could be determined by the method given in appendix 6.

The no flow fringe width was obtained by taking the average of the values obtained on the traverses across the nozzle. The variation between the mean and the measured values was between $\mp$ 10% of the mean or $\mp$ 0.1 fringes.

Referring to fig 30, it can be seen that the fringes in the wetted flow region curved sharply on passing into the boundary layer. The width of the boundary layer was

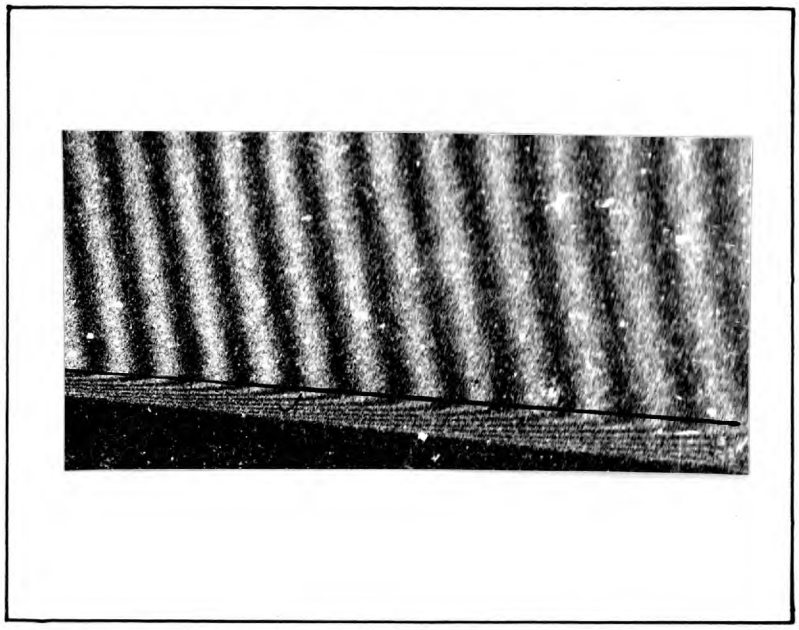

Fig 30. The edge of the boundary layer.

assumed to be the difference between the position of the nozzle wall and the point where the fringes first started to bend.

The position of the bend was measured on each fringe in the walled flow region and plotted together with the nozzle profile so that the boundary layer width could be obtained at any point.

Corresponding fringes in the no flow and flow interferograms were numbered by plotting the measured points for the fringes in the reference regions (see fig 31). Then as there was a slight increase in density in these regions due to slight leakages of high pressure air underneath the nozzle blocks, the fringes moved in a direction corresponding to a density increase. Hence it was possible to number a pair of corresponding fringes (see fig 32) followed by the fringes in the regions of reversed flow.

It was not possible to use white light fringes (see section 6.6) to follow the fringes across the shock waves associated with separation. However the fringes could be traced through the boundary layers underneath the shock waves into the wetted flow region (see fig 33). Therefore the fringes could be numbered throughout the flow field (see fig 31).

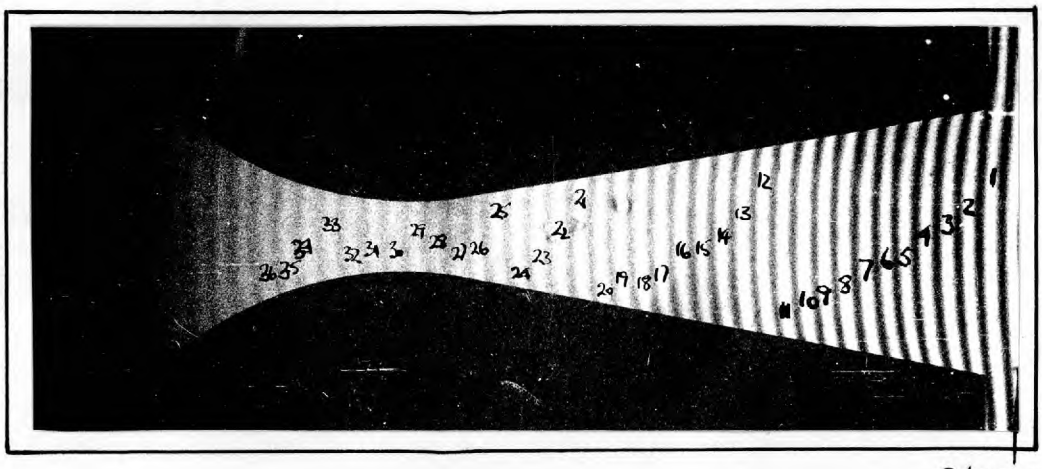

No flow

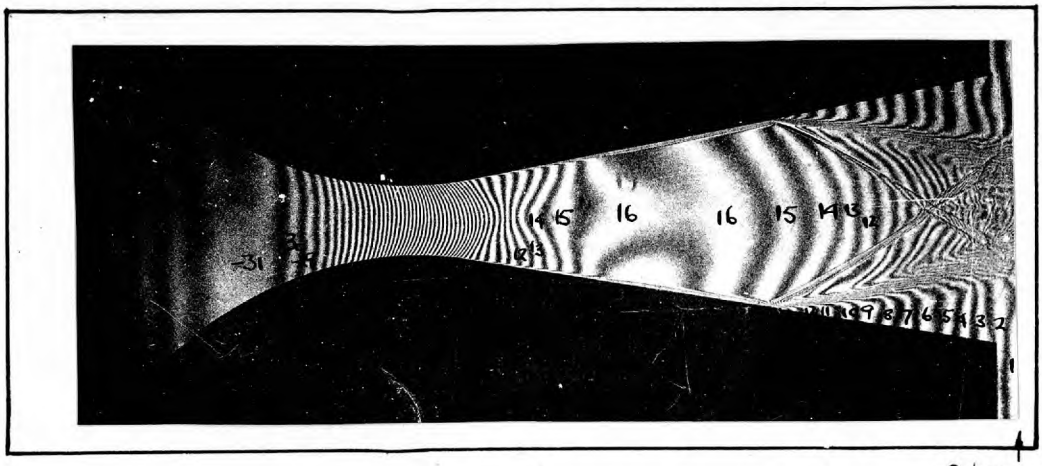

Flow

Fig 31. The flow and no flow interferograms for test 143 P_0 = 99.2 p.s.i.a. with fringes numbered correspondingly

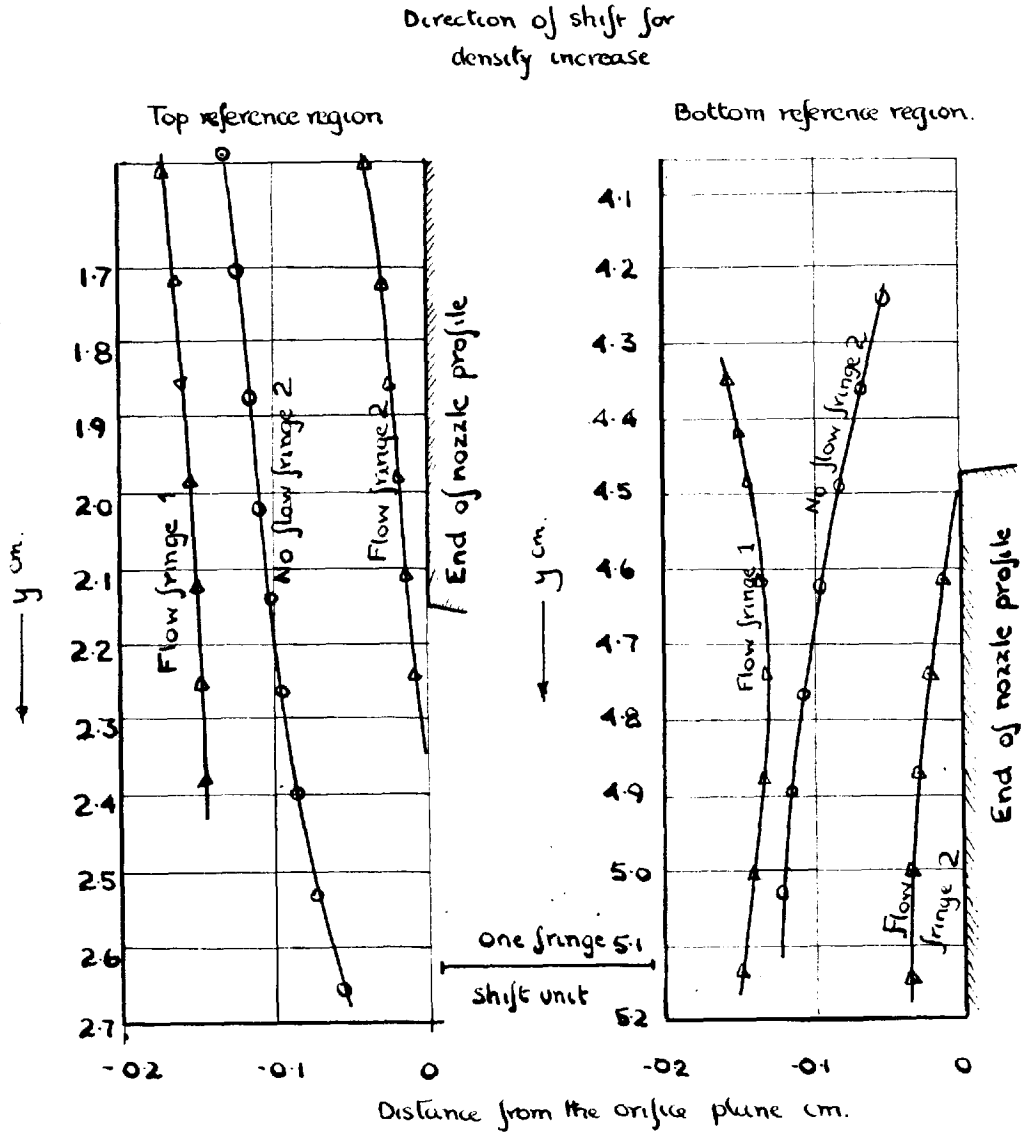

Fig 32 Flow and no flow fringes in the reference regions.

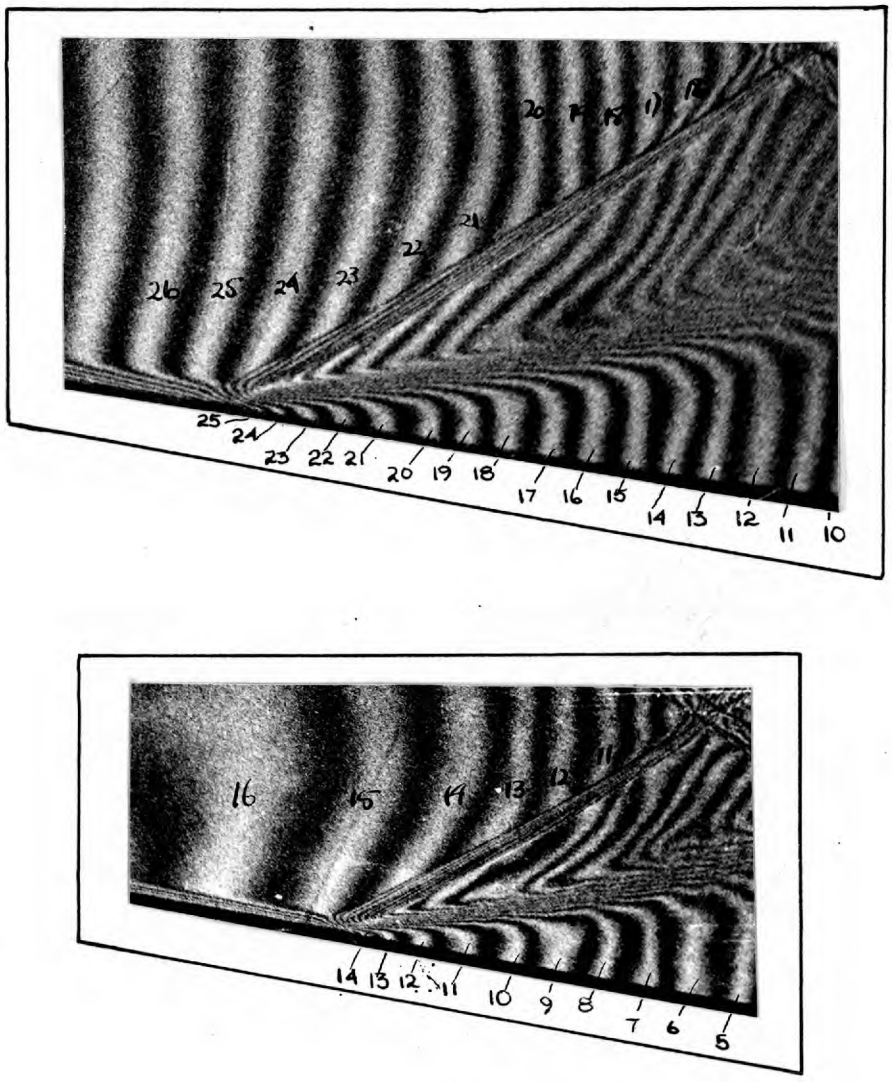

Fig 33 Fringe numbering through the boundary layer underneath the shock waves causing separation.

If the optical elements had been ideal, the fringes in the no flow interferogram would have been straight and parallel. But it can be seen from the curved no flow fringes of the interferogram in fig 31 that the optics were not perfect.

It was therefore necessary to make corrections to the fringe shifts for the imperfections in the optics. This was done by plotting the no flow fringes twenty times full size, together with straight ideal fringes separated by the mean fringe width. Then the correction to the fringe shift for optical imperfections, represented by the distance between the actual no flow fringe and the corresponding idealized fringe could be mapped throughout the flow field. The density was then calculated from the corrected fringe shift using the relation,

$$\rho = \rho_a + \frac{s.\lambda_p}{KD}$$

with the Gladstone Dale constant $K = 0.2269^{63} \frac{cm^3}{gm}$, the peak wavelength of the filter used $\lambda_p = 5461^{o}A$ and the breadth of the nozzle D = 0.9594 in. The reference density ρ_a was calculated from the measurements of atmosphere pressure and temperature with a correction for the water vapour present.

8.3. Errors.

8.3.1. Errors due to refraction of light in the nozzle.

In regions of rapidly changing density such as those that exist in the boundary layers on the walls of the nozzle, there are refractive index gradients normal to the light beam. These gradients cause the beam to be refracted and hence the density calculated on the assumption of unrefracted light may be in error.

Wachtell[66] assumed that the path of a light ray through a boundary layer could be represented by a series. Then by assigning a density distribution to the boundary layer, he showed that for both turbulent and laminar boundary layers evaluation of an interferogram focussed one third of the nozzle breadth from the exit window gave the true density distribution. In accordance with this result all interferograms obtained in this research were taken with the camera focussed on a plane one third of the nozzle width from the exit window.

A more detailed analysis of the same type as Wachtell's has been carried out by Howes and Buchele[78 79]. However this suffers from the same disadvantages as the previous analysis in that it is laborious to apply and is only

suitable for specialized cases of one dimensional flow where only small flow areas are to be interpreted.

Tanner[58] gives a criterion for the upper limit to the refractive index gradient which can be measured with little error as $\alpha = \sqrt{2\lambda p/D}$ where $\alpha = \frac{\lambda p}{s'}$ where s' is the fringe spacing. This was established by considering the equality of the linear deviation of the light in passing through the tunnel and the fringe spacing at the point of interest. In this research the refractive index gradients present in the flow field were all below the upper limit given by Tanner's criterion.

8.3.2. Errors due to intersecting boundary layers in the corners of the nozzle.

The boundary layers on the glass and profile walls of the nozzle coalesce at the corners, with the result that the density distribution in the boundary layers on the metal walls is not uniform in the direction of the light beam. Also as the boundary layer surface is probably rounded off in the corners, the position of the top edge of the boundary layer is uncertain.

Calculations[51 66 78] carried out by assuming a flow pattern in the corner suggest that the error caused by the

coalescence of the boundary layers is negligible. As no experimental data is available to check the flow patterns, it has been assumed that the errors are in fact negligible.

8.3.3. Correction for the boundary layers on the glass walls of the nozzle.

Because the density in the boundary layers on the glass walls is not equal to that in the mainstream, the density across the breadth of the nozzle is not constant. Thus the density measured by interferometry is the average of the densities in the boundary layer and mainstream, and to obtain the latter a correction for the boundary layers must be made to the measured values.

It can be shown that the thickness of a layer at density ρ mainstream which has the same optical retardation as the boundary layer is $\delta - t$ where

$$t = \int_0^{\delta} \frac{\rho_{mainstream} - \rho(z)}{\rho_{mainstream}} dz ,$$

δ is the boundary layer thickness and $\left[\rho(z)\right]_0^{\delta}$ is the density variation in the boundary layer.

Hence correction for the boundary layers on the glass walls can be carried out by reducing the nozzle breadth by $2t$, then

$$\rho_{mainstream} = \rho_{measured} \frac{D}{(D-2t)} \quad \text{or}$$

$$\rho_{mainstream} = \frac{D}{D-2t}\left(\frac{s\Delta P}{KD} + \rho_a\right)$$

As the magnitude of the correction never exceeds 2% in this research, the thickness t can be calculated with little error by replacing $\rho_{mainstream}$ by $\rho_{measured}$. Furthermore the density variation in the boundary layer on the glass walls has been assumed to be the same as that on the profile walls. This assumption was justified as Bersharder[51] using a Laval nozzle showed that the density variation in the boundary layer on the profile walls just below the orifice was in good agreement with that on the glass walls just above the orifice.

The correction curve shown in fig 34 was obtained from boundary layer measurements on interferograms taken at different pressures, and was used to correct the densities tabulated in section 9 unless otherwise stated.

8.3.4. Errors due to oscillations in the jet.

Various observers[51 61 64] have found that the flow pattern in a supersonic jet oscillates rapidly about a mean position, as high speed drum camera studies have shown that the fringes can oscillate with an amplitude of upto 2 fringe shift units[64]. The period of oscillation varying between

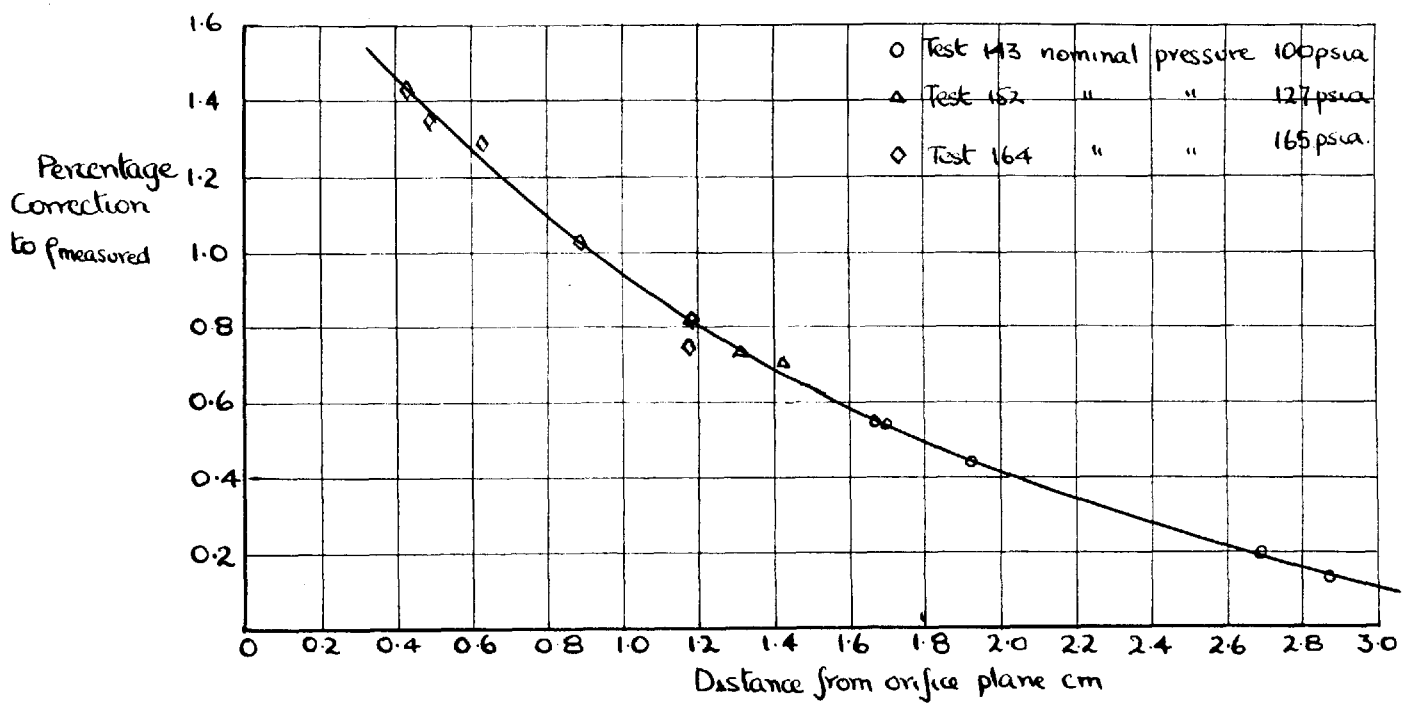

Fig 34 Correction curve for the boundary layers on the glass walls of the nozzle.

5000[51] and 8000[65] c/sec.

In the case of the nozzle used in this research, the flow pattern oscillated as the fringes became slightly blurred when the nozzle was running. In the absence of high speed drum camera records, the error caused was estimated from the results obtained with a divergent nozzle by Bersharder[51], who found that the fringes oscillated with an amplitude of 0.4 fringe shift units at a reservoir pressure of 4 atmospheres. An oscillation of the same amplitude in the nozzle used in this research causes an error which never exceeds ∓ 2%.

8.4. Interpretation of Wall Pressure Measurements.

Owing to the small scale of the separation phenomenon, the pressure holes in the nozzle were not close enough together to obtain an accurate estimate of the onset pressure po (see section 3.4.). Therefore at each intermediate pressure point a series of tests were carried out at slightly different reservoir pressures. The wall pressure ratios obtained for each such series of tests were plotted and the pressure profiles corresponding to the pressure rise to separation (PQ fig 6) were drawn parallel

to each other. The assumption made was that the pressure gradients at separation were the same for each test in the series (see fig 56).

It can be seen from the results in section 9, that when the region of reversed flow was long, the pressure head loss in overcoming friction was significant and must be taken into account when determining the pressure rise causing separation. This was done by expressing the wall pressures in the region of reversed flow as ratios of atmospheric pressure. The ratios were then plotted against distance from the onset point. The points obtained for one series of tests are plotted in fig 35 and it can be seen that they lie on a common curve. The same property was exhibited by all those series of tests in which symmetrical separation took place fig 36. The gradient of the curves decreased continuously at first on moving downstream from the onset point, finally reaching a constant value at a distance of 0.6 cms from the onset point. It was assumed that the entire pressure rise due to the shock had taken place when the pressure gradient became constant and accordingly the peak pressure p_p was somewhat arbitarly defined as the pressure 0.6 cms from the onset point.

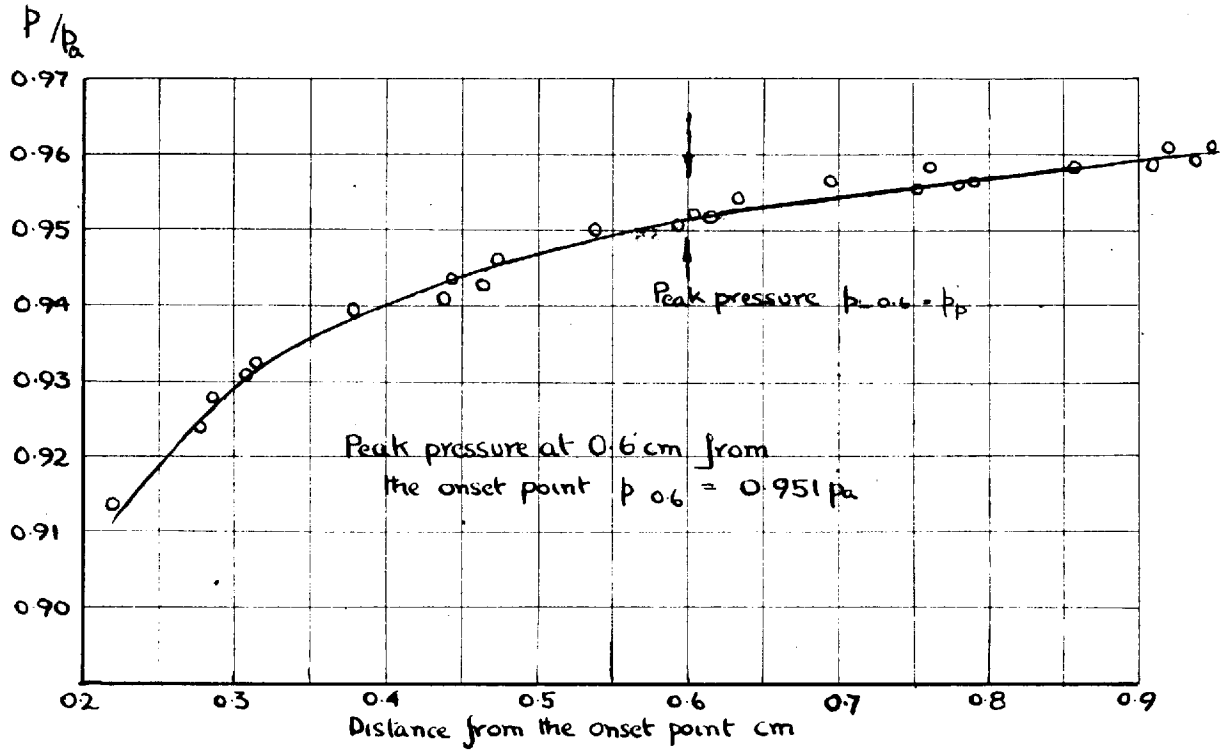

Fig. 35. Pressure profile in the region of reversed flow for tests at nominal pressure of 115 psia.

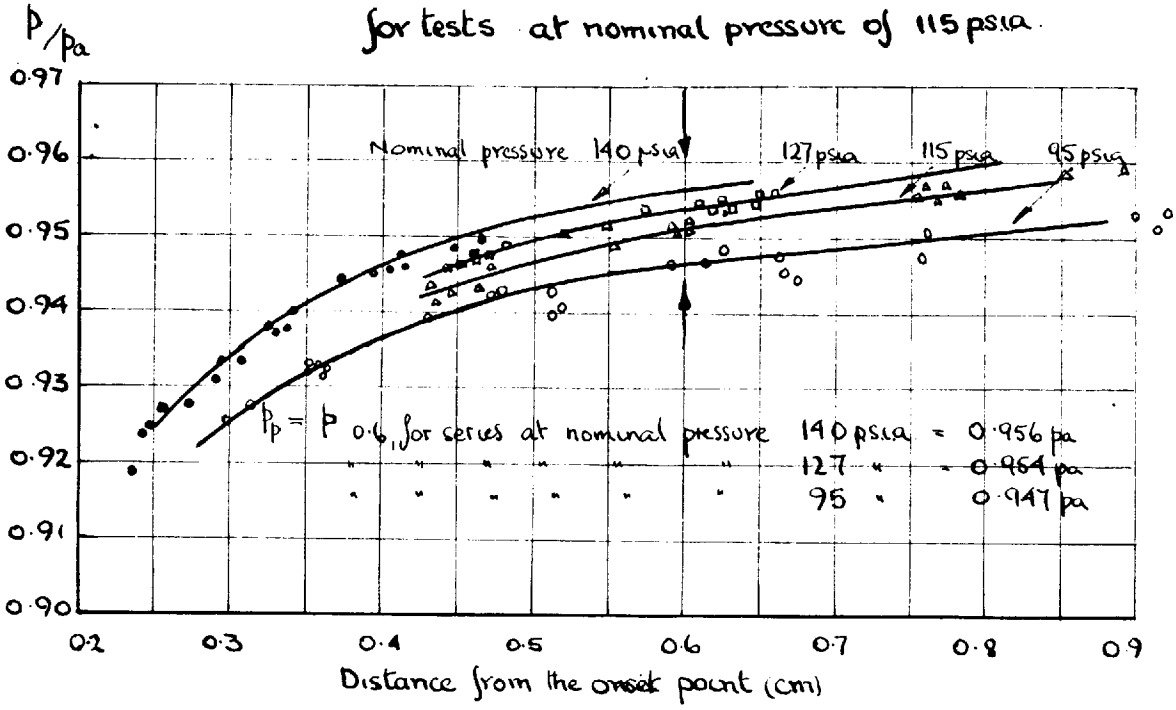

Fig 36. Pressure profiles in the region of reversed flow for those series of tests in which symmetrical separation took place.

SECTION 9. Experimental Results.

For convenience in presentation the results have been divided into three sections, potential flow in the nozzle, flow separation and the boundary layer.

9.1. Flow in the wetted region of the nozzle.

The flow region considered in this section is the region of wetted flow bounded by the reservoir, the edges of the boundary layers on the nozzle walls and the shock waves associated with boundary layer separation, (see fig 11). The wetted flow regions of the interferograms for tests 163, 152, 146, 143 at stagnation pressures of 168.2, 128.2, 100.2 and 99.2 p.s.i.a. respectively, were evaluated. The interferograms are shown in fig 37 and the atmospheric conditions etc. under which the tests were carried out are presented in table 7.

The fringe sequence was made to reverse and repeat in tests 143 and 152 by using the method described in appendix 5. In this way it was possible to determine the density in the convergent, throat and divergent regions for test 143 and in the throat and divergent regions for test 152.

No flow

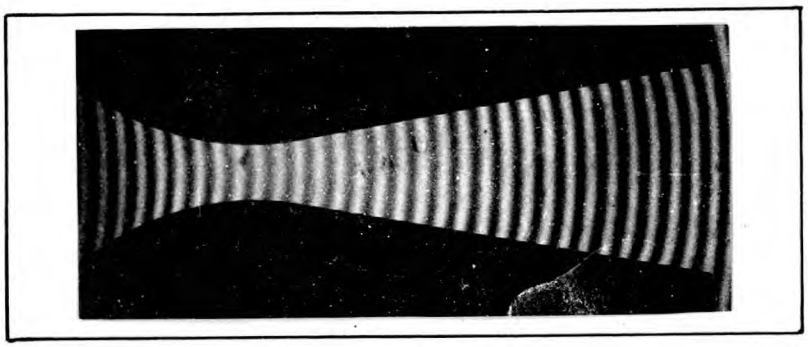

Flow

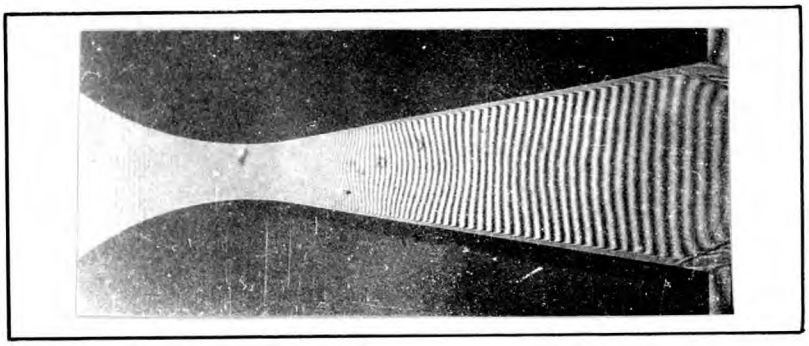

Test 163. Stagnation pressure 168·2 p.s.i.a.

No flow

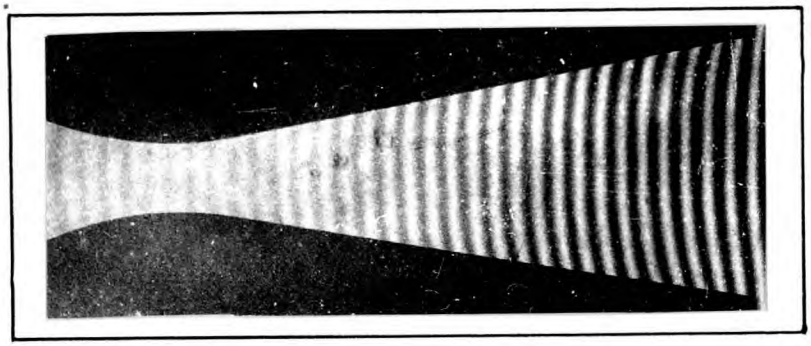

Flow

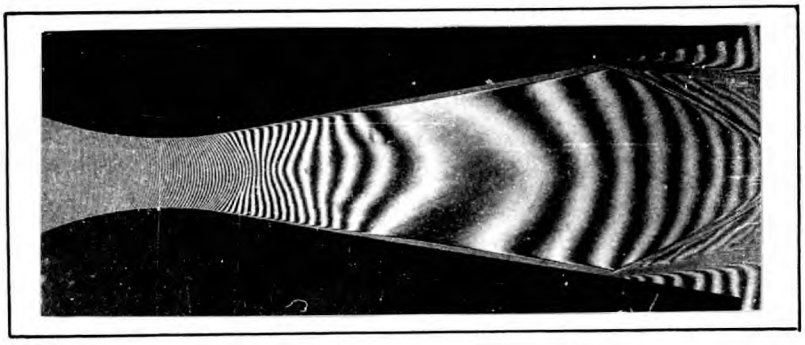

Test 152. Stagnation pressure 128·2 p.s.i.a.

Fig 37 Interferograms of the flow which were evaluated

No flow

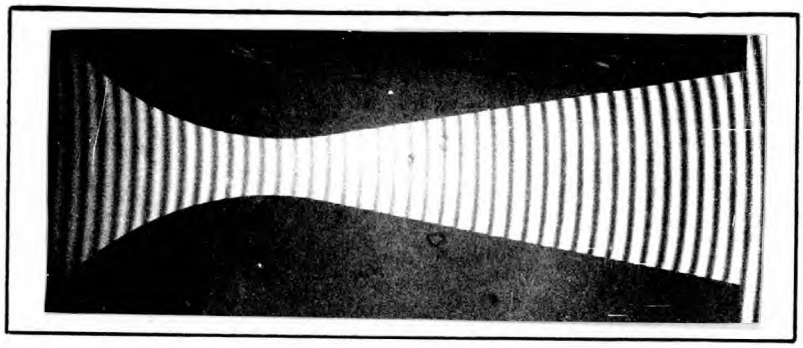

Flow

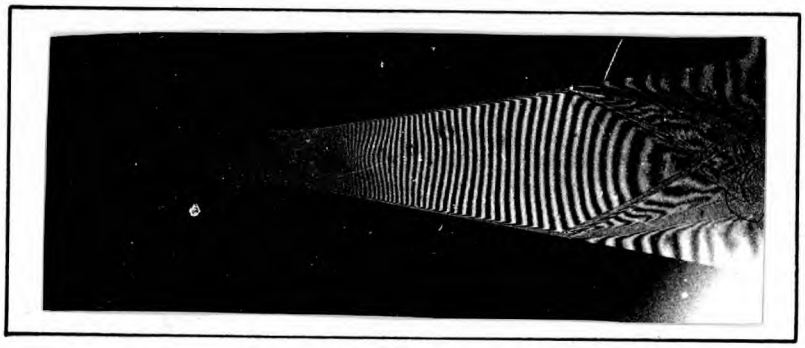

Test 146. Stagnation pressure 100·2 p.s.i.a.

No flow

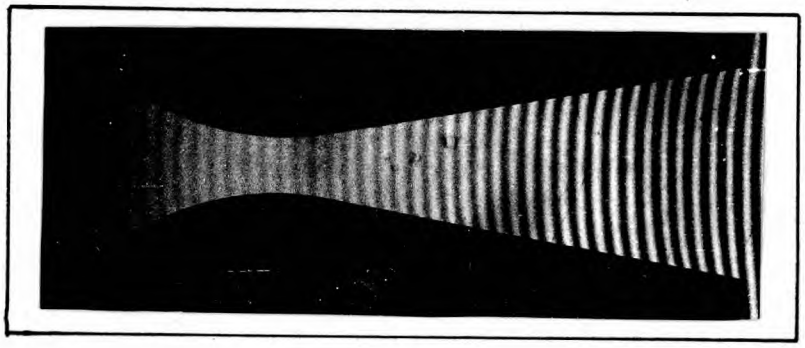

Flow

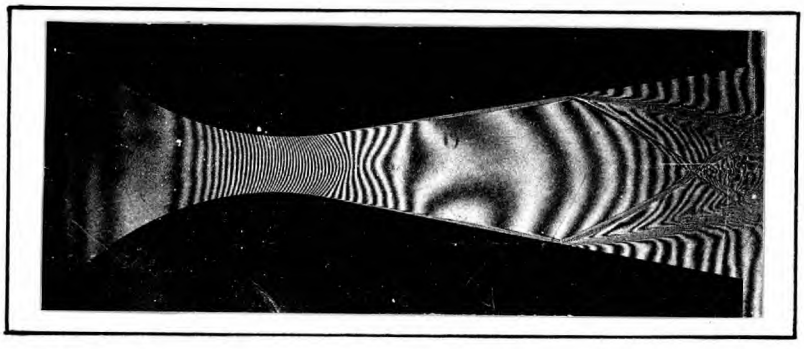

Test 143 Stagnation pressure 99·2 p.s.i.a.

Fig 37 continued.

TABLE 7.

Experimental Constants.

Test	163	152	146	143
Stagnation pressure, P_o, p.s.i.a.	168.2	128.2	100.2	99.2
Stagnation density, ρ_o, gm/litre	13.64	10.77	8.751	8.560
Stagnation temperature, T_o, ^oK	296.3	286.7	275.9	289.0
Atmospheric density, ρ_a, gm/litre	1.160	1.183	1.278	1.212
Atmospheric pressure, pa, p.s.i.a.	14.76	14.64	14.61	14.54
Atmospheric temperature $T_a{}^oK$	305.0	297.0	286.7	279.2
Mean no flow fringe width cm.	0.1915	0.1540	0.1573	0.1456
Relative Humidity	49%	53%	64%	61%
Peak wavelength of filter. cms.	5461×10^{-8}	5461×10^{-8}	5461×10^{-8}	5461×10^{-8}
Gladstone-Dale Constant $^{63}\frac{cm^3}{gm}$	0.2269	0.2269	0.2269	0.2269

9.1.1. Flow variables in the wetted flow region determined by the interferometric method and by wall pressure measurements.

The density ratios measured on the edges of the top and bottom boundary layers and on the centreline and corrected for the boundary layers on the glass walls are tabulated in tables 9 - 12 for tests 143, 146, 152 and 163, together with the pressure ratios measured on the bottom wall of the nozzle. The pressure and density ratios calculated from the measured density ratios on the edge of the bottom boundary layer, and measured pressure ratios respectively, assuming isentropic flow, have also been presented in tables 9 - 12.

In the regions 2.0 - 3.5 cms and 1.6 - 2.7 cms from the exit plane of the nozzle in tests 143 and 152 respectively the widely spaced fringes associated with reversal of the fringe sequence did not permit accurate measurement of the density and therefore the density ratios in these regions have been omitted.

The measured value of the density ratio in the convergent region in test 143, 6.4 cms from the exit plane was 1.0005 compared with the value of 0.998 calculated by assuming one dimensional isentropic flow. As the velocity in this region was low, approximately 50 ft/sec. the good agreement between the one dimensional and measured density ratios indicated

(Continued on page 132.)

TABLE 8.

The measured pressure and density ratios for test 85, stagnation pressure 96.2 p.s.i.a.

Dist. from the exit plane cm.	Measured density ratio Bot. b.l.	℄	Top b.l.	Dist. from the exit plane cm.	Measured p/p_o
4.1	0.5695	0.6018	0.5683	1.8	0.0684
4.15	0.6008	0.6270	0.6008	1.9	0.0704
4.2	0.6310	0.6538	0.6310	2.0	0.0731
4.3	0.6846	0.7023	0.6846	2.1	0.0761
4.4	0.7286	0.7472	0.7286	2.2	0.0795
4.5	0.7710	0.7858	0.7710	2.3	0.0834
4.6	0.8095	0.8205	0.8095	2.4	0.0875
4.7	0.8427	0.8520	0.8427	2.5	0.0926
4.8		0.8780		2.6	0.0987
4.9		0.8998		2.7	0.1059
5.0		0.9190		2.8	0.1144
5.2		0.9465		2.9	0.1247
5.4		0.9642		3.0	0.1365
5.6		0.9758		3.1	0.1496
5.8		0.9839		3.2	0.1642
6.0		0.9910		3.3	0.1818
6.2		0.9948		3.4	0.2014
6.4		0.9979		3.5	0.2208
6.6		1.0006			

TABLE 9.

The density and pressure ratios for test 143, stagnation pressure Po = 99.2 p.s.i.a. together with the values calculated from them by assuming isentropic flow.

Dist. from the exit plane cm.	Measured density ratio Bot.b.l.	℄	Top.b.l.	p/p_o bot.b.l. calc. from ρ/ρ_o	T/T_o bot.b.l. calc. from ρ/ρ_o
0.7		0.1104			
0.8		0.1085			
0.9		0.1073			
1.0		0.1069			
1.1		0.1073			
1.2		0.1084			
1.3		0.1106			
1.4		0.1140			
1.5		0.1181			
1.6		0.1226			
1.7		0.1276			
3.1	0.2502		0.2537	0.1436	0.5744
3.2	0.2692	0.2576	0.2701	0.1593	0.5905
3.3	0.2898	0.2739	0.2890	0.1766	0.6093
3.4	0.3113	0.2953	0.3083	0.1952	0.6270
3.5	0.3335	0.3250	0.3280	0.2149	0.6445
3.6	0.3563	0.3665	0.3473	0.2358	0.6618
3.7	0.3822	0.4116	0.3667	0.2601	0.6806
3.8	0.4123	0.4575	0.4003	0.2893	0.7017
3.9	0.4675	0.5000	0.4530	0.3447	0.7376
4.0	0.5213	0.5527	0.5125	0.4016	0.7706

Dist from the exit plane cm.	p/p_o measured bot.b.l.	ρ/ρ_o calc from p/p_o bot. b.l.	$\frac{T}{T_o}$ calc. from p/p_o bot.b.l.
1.8	0.0679		
1.9	0.0701		
2.0	0.0729		
2.1	0.0761		
2.2	0.0795		
2.3	0.0830		
2.4	0.0872		
2.5	0.0926		
2.6	0.0990		
2.7	0.1060		
2.8	0.1150		
2.9	0.1251		
3.0	0.1365		
3.1	0.1495	0.2572	0.5811
3.2	0.1632	0.2769	0.5958
3.3	0.1800	0.2939	0.6127
3.4	0.1990	0.3156	0.6305
3.5	0.2196	0.3386	0.6485
3.6	0.2446	0.3658	0.6688

4.1	0.5673	0.6010	0.5741	0.4522	0.7971
4.15	0.5890	0.6258	0.6058	0.4766	0.8091
4.2	0.6115	0.6518	0.6348	0.5023	0.8215
4.3	0.6519	0.6990	0.6837	0.5494	0.8428
4.4	0.7245	0.7446	0.7285	0.6369	0.8790
4.5	0.7695	0.7847	0.7698	0.6867	0.8987
4.6	0.8063	0.8192	0.8083	0.7399	0.9042
4.7	0.8416	0.8497	0.8420	0.7859	0.9335
4.8	0.8706	0.8758	0.8716	0.8236	0.9460
4.9	0.8937	0.8978	0.8952	0.8544	0.9561
5.0	0.9130	0.9172	0.9160	0.8804	0.9643
5.2		0.9427			
5.4		0.9633			
5.6		0.9767			
5.8		0.9865			
6.0		0.9929			
6.2		0.9973			
6.4		0.10005			

TABLE 10.

The density and pressure ratios for test 146, stagnation pressure Po = 100.2 p.s.i.a. together with the values calculated from them by assuming isentropic flow.

Dist from the exit plane cm	Measured density ratio Bot.b.l.	℄	Top b.l.	p/p_o bot.b.l. calc. from ρ/ρ_o	T/T_o bot.b.l. calc. from ρ/ρ_o	P/P_o measured bot.b.l.	ρ/ρ_o calc. from p/P_o bot. b.l.	$\frac{T}{To}$ calc from p/Po bot.b.l.
0.8		0.1084						
0.9		0.1061						
1.0		0.1046						
1.1		0.1048						
1.2		0.1066						
1.3		0.1094						
1.4		0.1133						
1.5		0.1176						
1.6		0.1221						
1.7	0.1366	0.1270	0.1375	0.0616	0.4510	0.0657	0.1430	0.4594
1.8	0.1403	0.1323	0.1418	0.0640	0.4558	0.0679	0.1464	0.4637
1.9	0.1442	0.1379	0.1464	0.0665	0.4609	0.0702	0.1499	0.4681
2.0	0.1484	0.1441	0.1508	0.0692	0.4662	0.0731	0.1544	0.4736
2.1	0.1534	0.1508	0.1554	0.0725	0.4724	0.0764	0.1593	0.4796
2.2	0.1584	0.1578	0.1605	0.0758	0.4785	0.0798	0.1644	0.4856
2.3	0.1636	0.1655	0.1660	0.0793	0.4848	0.0833	0.1694	0.4916
2.4	0.1695	0.1737	0.1722	0.0834	0.4917	0.0875	0.1755	0.4980
2.5	0.1767	0.1822	0.1789	0.0883	0.4999	0.0928	0.1830	0.5070
2.6	0.1846	0.1912	0.1864	0.0939	0.5088	0.0988	0.1912	0.5162
2.7	0.1943	0.2008	0.1949	0.1003	0.5193	0.1056	0.2007	0.5261

2.8	0.2058	0.2110	0.2042	0.1093	0.5314	0.1148	0.2130	0.5388
2.9	0.2192	0.2215	0.2164	0.1194	0.5449	0.1252	0.2267	0.5525
3.0	0.2342	0.2329	0.2345	0.1310	0.5595	0.1363	0.2408	0.5658
3.1	0.2514	0.2444	0.2529	0.1447	0.5757	0.1487	0.2563	0.5801
3.2	0.2697	0.2568	0.2695	0.1597	0.5921	0.1646	0.2756	0.5971
3.3	0.2888	0.2734	0.2896	0.1759	0.6084	0.1825	0.2967	0.6152
3.4	0.3113	0.2960	0.3097	0.1952	0.6270	0.2009	0.3178	0.6323

TABLE 11.

The density and pressure ratios for test 152, stagnation pressure Po = 128.2 p.s.i.a. together with the values calculated from them by assuming isentropic flow.

Dist. from the exit plane, cm.	Measured density ratio			p/p_o bot.b.l. calc. from ρ/ρ_o	T/T_o bot b.l. calc. from ρ/ρ_o	p/p_o measured bot.b.l.	ρ/ρ_o calc from p/p_o bot. b.l.	$\frac{T}{To}$ calc from p/Po bot.b.l.
	Bot.b.l.	℄	Top.b.l.					
-0.2		0.0932						
-0.1		0.0906						
0		0.0880						
0.1		0.0863						
0.2		0.0856						
0.3		0.0847						
0.4		0.0864						
0.5		0.0881						
0.6		0.0901						
0.7		0.0924						
0.8		0.0946						
0.9		0.0971	0.1073					
1.0		0.0995	0.1099					
1.05	0.1079			0.0443	0.4104	0.0512	0.1197	0.6563
1.1	0.1095	0.1025	0.1130	0.0452	0.4129	0.0525	0.1217	0.6485
1.2	0.1126	0.1055	0.1161	0.0470	0.4175	0.0545	0.1251	0.6308
1.3	0.1164	0.1089	0.1194	0.0493	0.4231	0.0566	0.1285	0.6139
1.4	0.1201	0.1130	0.1227	0.0514	0.4284	0.0587	0.1319	0.5968
1.5	0.1242	0.1178	0.1262	0.0539	0.4341	0.0607	0.1352	0.5809
1.6	0.1290		0.1297	0.0569	0.4408	0.0627	0.1383	0.5662
1.65	0.1311			0.0582	0.4436	0.0639	0.1403	0.5521
2.7		0.2011	0.1942					

2.75	0.1962			0.1023	0.5213	0.1097	0.2063	0.5380
2.8	0.2025	0.2112	0.2050	0.1067	0.5279	0.1142	0.2122	0.5319
2.9	0.2161	0.2215	0.2173	0.1171	0.5419	0.1250	0.2264	0.4557
3.0	0.2317	0.2331	0.2331	0.1291	0.5572	0.1366	0.2413	0.4533
3.1	0.2500	0.2451	0.2516	0.1435	0.5744	0.1494	0.2572	0.4491
3.2	0.2678	0.2580	0.2709	0.1581	0.5903	0.1642	0.2752	0.4448
3.3	0.2874	0.2742	0.2892	0.1746	0.6073	0.1812	0.2952	0.4402
3.4	0.3084	0.2969	0.3074	0.1922	0.6247	0.1994	0.3161	0.4355
3.5	0.3313	0.3300	0.3270	0.2129	0.6428	0.2196	0.3386	0.4334
3.6	0.3549	0.3712	0.3476	0.2240	0.6521	0.2290	0.3489	0.4278
3.7	0.3788	0.4146	0.3693					
3.8	0.4148	0.4596	0.4052					
3.9	0.4736	0.5053	0.4588					
4.0	0.5279	0.5537	0.5202					
4.1	0.5721	0.6049	0.5813					
4.15	0.5940	0.6294	0.6095					
4.2	0.6190	0.6540	0.6378					
4.25	0.6470	0.6782	0.6635					

TABLE 12.

The density and pressure ratios for test 163, stagnation pressure Po = 168.2 p.s.i.a. together with the values calculated from them by assuming isentropic flow.

Dist from the exit plane. cm.	Measured density ratio Bot.b.l.	℄	Top.b.l.	p/p_o bot b.l. calc. from ρ/ρ_o	$\frac{T}{T_o}$ bot b.l. calc. from ρ/ρ_o	p/p_o measured bot. b.l.	ρ/ρ_o calc. from p/p_o bot. b.l.	$\frac{T}{T_o}$ calc. from p/Po bot.b.l.
0.2	0.0812	0.0757	0.0837	0.0298				
0.3	0.0835	0.0786	0.0853	0.0310				
0.4	0.0855	0.0804	0.0870	0.0320		0.0404	0.1010	0.3998
0.5	0.0878	0.0823	0.0891	0.0332	0.3779	0.0415	0.1037	0.4039
0.6	0.0902	0.0846	0.0917	0.0345	0.3820	0.0429	0.1056	0.4068
0.7	0.0928	0.0867	0.0946	0.0359	0.3863	0.0443	0.1079	0.4104
0.8	0.0955	0.0892	0.0976	0.0373	0.3908	0.0459	0.1107	0.4146
0.9	0.0984	0.0918	0.1005	0.0389	0.3954	0.0476	0.1137	0.4191
1.0	0.1014	0.0947	0.1035	0.0406	0.4004	0.0494	0.1166	0.4233
1.1	0.1047	0.0977	0.1066	0.0418	0.4038	0.0513	0.1204	0.4280
1.2	0.1079	0.1012	0.1101	0.0444	0.4104	0.0533	0.1232	0.4328
1.3	0.1114	0.1048	0.1137	0.0462	0.4158	0.0555	0.1268	0.4377
1.4	0.1153	0.1087	0.1180	0.0486	0.4214	0.0577	0.1304	0.4427
1.5	0.1193	0.1132	0.1222	0.0510	0.4274	0.0599	0.1338	0.4473
1.6	0.1237	0.1179	0.1266	0.0536	0.4335	0.0622	0.1375	0.4522
1.7	0.1279	0.1231	0.1305	0.0562	0.4393	0.0646	0.1413	0.4571
1.8	0.1322	0.1287	0.1356	0.0588	0.4451	0.0671	0.1453	0.4622
1.9	0.1362	0.1349	0.1404	0.0613	0.4504	0.0696	0.1490	0.4670
2.0	0.1404	0.1415	0.1455	0.0640	0.4560	0.0723	0.1531	0.4721
2.1	0.1453	0.1485	0.1508	0.0671	0.4622	0.0755	0.1580	0.4780
2.2	0.1503	0.1560	0.1561	0.0704	0.4686	0.0789	0.1630	0.4840
2.3	0.1567	0.1641	0.1620	0.0747	0.4765	0.0828	0.1687	0.4908

2.4	0.1629	0.1724	0.1681	0.0788	0.4838	0.0871	0.1749	0.4979
2.5	0.1696	0.1813	0.1747	0.0834	0.4918	0.0921	0.1820	0.5059
2.6	0.1776	0.1906	0.1822	0.0890	0.5009	0.0981	0.1905	0.5221
2.7	0.1879	0.2003	0.1913	0.0963	0.5124	0.1050	0.1999	0.5252
2.8	0.2003	0.2108	0.2015	0.1053	0.5256	0.1135	0.2114	0.5370
2.9	0.2139	0.2215	0.2142	0.1154	0.5396	0.1247	0.2261	0.5517
3.0	0.2290	0.2318	0.2310	0.1270	0.5545	0.1356	0.2400	0.5650
3.1	0.2462	0.2431	0.2503	0.1405	0.5708	0.1452	0.2547	0.5787
3.2	0.2661	0.2560	0.2686	0.1567	0.5889	0.1629	0.2731	0.5963
3.25		0.2649						

TABLE 13.

The Mach number, pressure, density and temperature ratios for isentropic one dimensional flow in the nozzle.

Dist from the exit plane. cm.	Mach number	p/p_o	ρ/ρ_o	T/T_o	A/A_t
0.0	2.874	0.0329	0.0873	0.3770	3.756
0.2	2.830	0.0352	0.0916	0.3844	3.601
0.4	2.782	0.0379	0.0966	0.3925	3.462
0.6	2.745	0.0401	0.1005	0.3988	3.323
0.8	2.700	0.0430	0.1056	0.4068	3.183
1.0	2.653	0.0462	0.1112	0.4154	3.044
1.2	2.602	0.0499	0.1176	0.4248	2.902
1.4	2.551	0.0541	0.1245	0.4346	2.765
1.6	2.496	0.0589	0.1322	0.4452	2.627
1.8	2.435	0.0647	0.1415	0.4574	2.484
2.0	2.373	0.0713	0.1519	0.4703	2.345
2.2	2.305	0.0807	0.1656	0.4871	2.264
2.4	2.233	0.0889	0.1775	0.5008	2.064
2.6	2.152	0.1008	0.1942	0.5192	1.922
2.8	2.067	0.1151	0.2135	0.5391	1.786
3.0	1.968	0.1342	0.2383	0.5634	1.644
3.2	1.863	0.1581	0.2678	0.5904	1.511
3.4	1.733	0.1928	0.3086	0.6249	1.369
3.6	1.517	0.2434	0.3644	0.6678	1.232
3.8	1.380	0.3232	0.4463	0.7242	1.104
3.9	1.273	0.3746	0.4911	0.7526	1.055
4.0	1.170	0.4287	0.5461	0.7851	1.022
4.1	1.000	0.5283	0.6339	0.8333	1.000
4.2	0.950	0.5595	0.6604	0.8471	1.002
4.3	0.833	0.6343	0.7224	0.8780	1.026
4.4	0.745	0.6918	0.7686	0.9001	1.065
4.5	0.683	0.7322	0.8014	0.9148	1.108
4.6	0.601	0.7834	0.8400	0.9326	1.187
4.7	0.495	0.8457	0.8872	0.9533	1.371
4.8	0.389	0.9007	0.9280	0.9705	1.625

that the air did not undergo a significant temperature change due to friction and heat imput from the surroundings on passing from the settling chamber, where the stagnation conditions were recorded, into the nozzle.

The small difference, 0.05%, between the density measured in the settling chamber and that in the beginning of the convergent section indicated that there was no significant error in the method of correcting the indicated thermistor temperature for the power dissipated in the resistance element given in section 7.5. This result was substantiated by the density ratios measured in the convergent section for test 85 at stagnation pressure 96.2 p.s.i.a., which are tabulated in table 8.

Although the flow was one dimensional in test 143 in the convergent section upto 5.1 cms from the exit plane, as shown by figs. 38 and 43, the density variation was not the same as that for one dimensional isentropic flow. The difference between the two values was confirmed by the results tabulated in table 8 for test 85, and was equal to 3.7% at 5.1 cms from the exit plane in test 143.

It can be seen from the curvature of the density ratio profiles in figs. 38 - 42 that the flow was not one dimensional. It is also apparent from figs. 43 - 46 that

(continued on page 135)

Fig 38 Density ratio profiles in the throat and convergent regions for test 143. P_0 = 99·2 p.s.i.a.

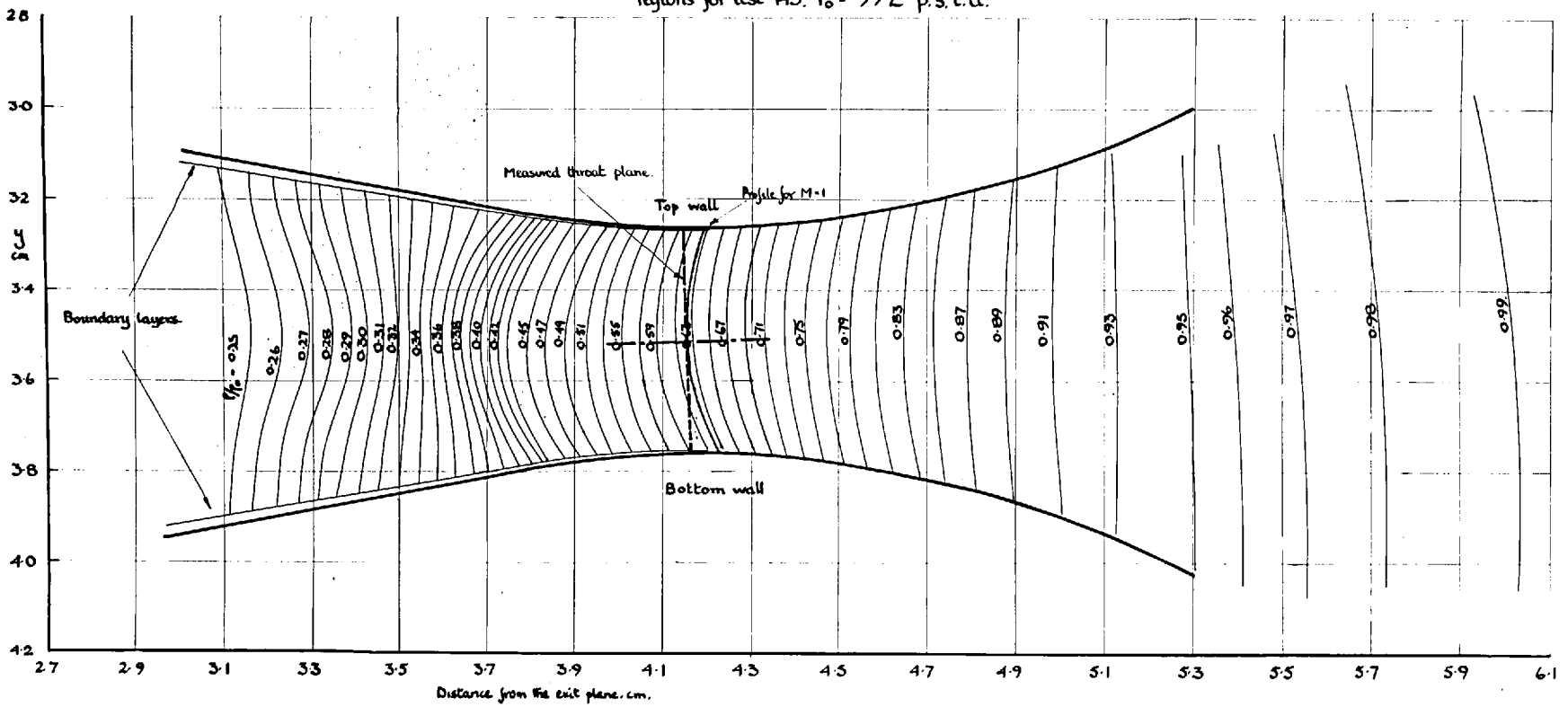

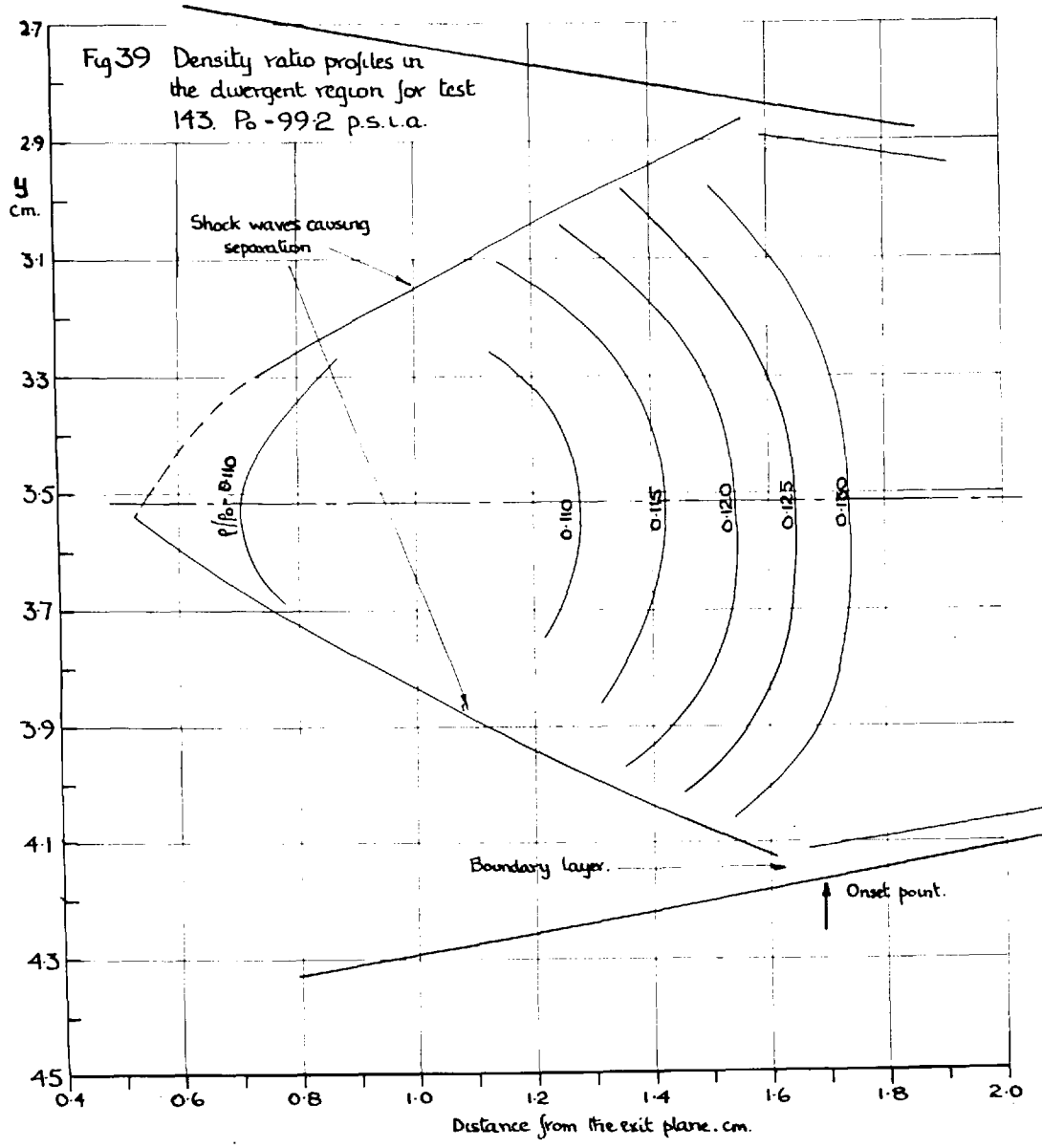
Fig 39 Density ratio profiles in the divergent region for test 143. P₀ - 99·2 p.s.i.a.
y cm.
2·7
2·9
3·1
3·3
3·5
3·7
3·9
4·1
4·3
4·5
Shock waves causing separation
ρ/ρ₀ 0·110
0·110
0·115
0·120
0·125
0·130
Boundary layer.
Onset point.
0·4
0·6
0·8
1·0
1·2
1·4
1·6
1·8
2·0
Distance from the exit plane. cm.

Fig. 10. Density ratio profiles in the divergent region for test 146. P_o = 100·2 p.s.i.a.

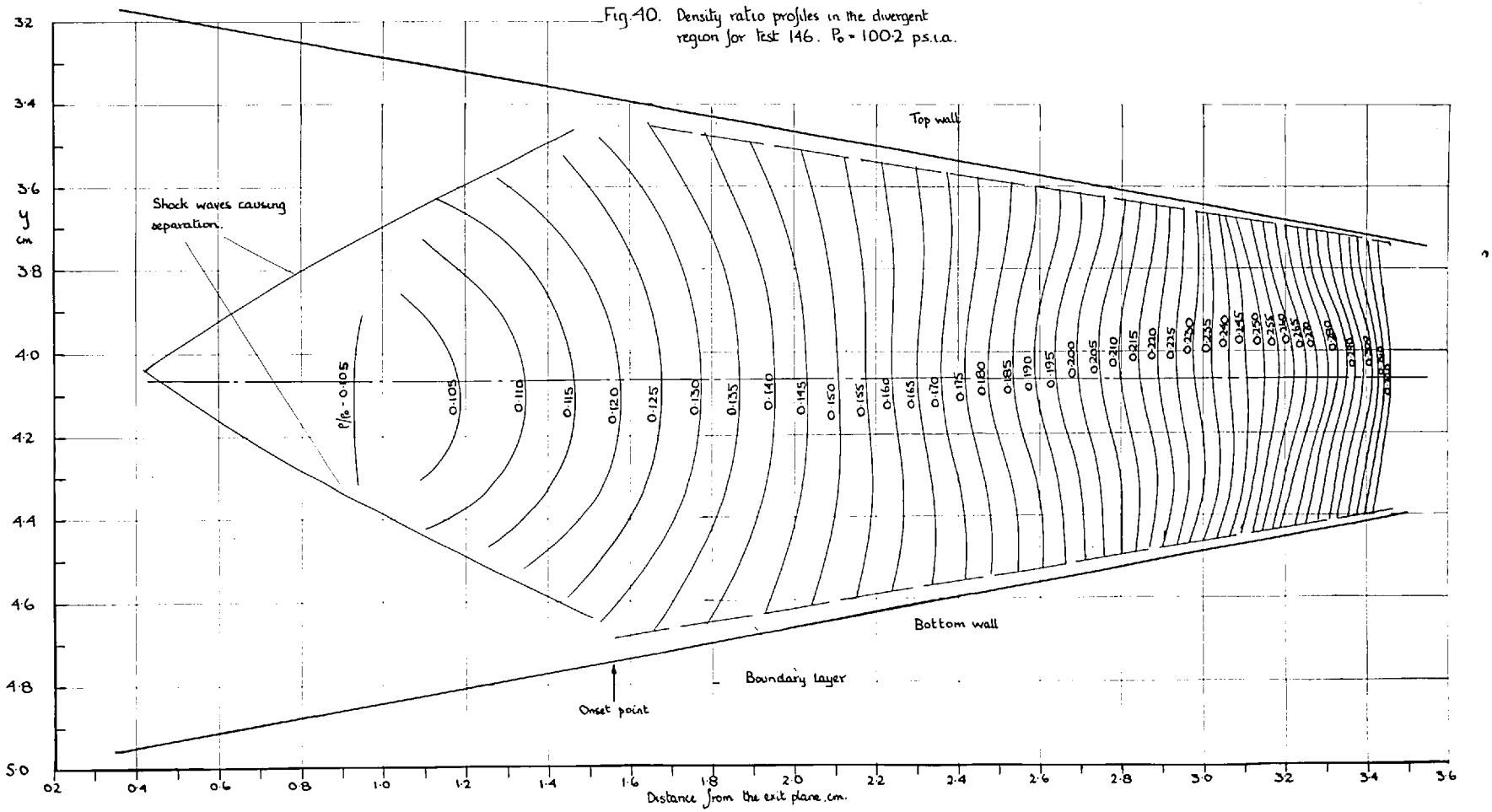

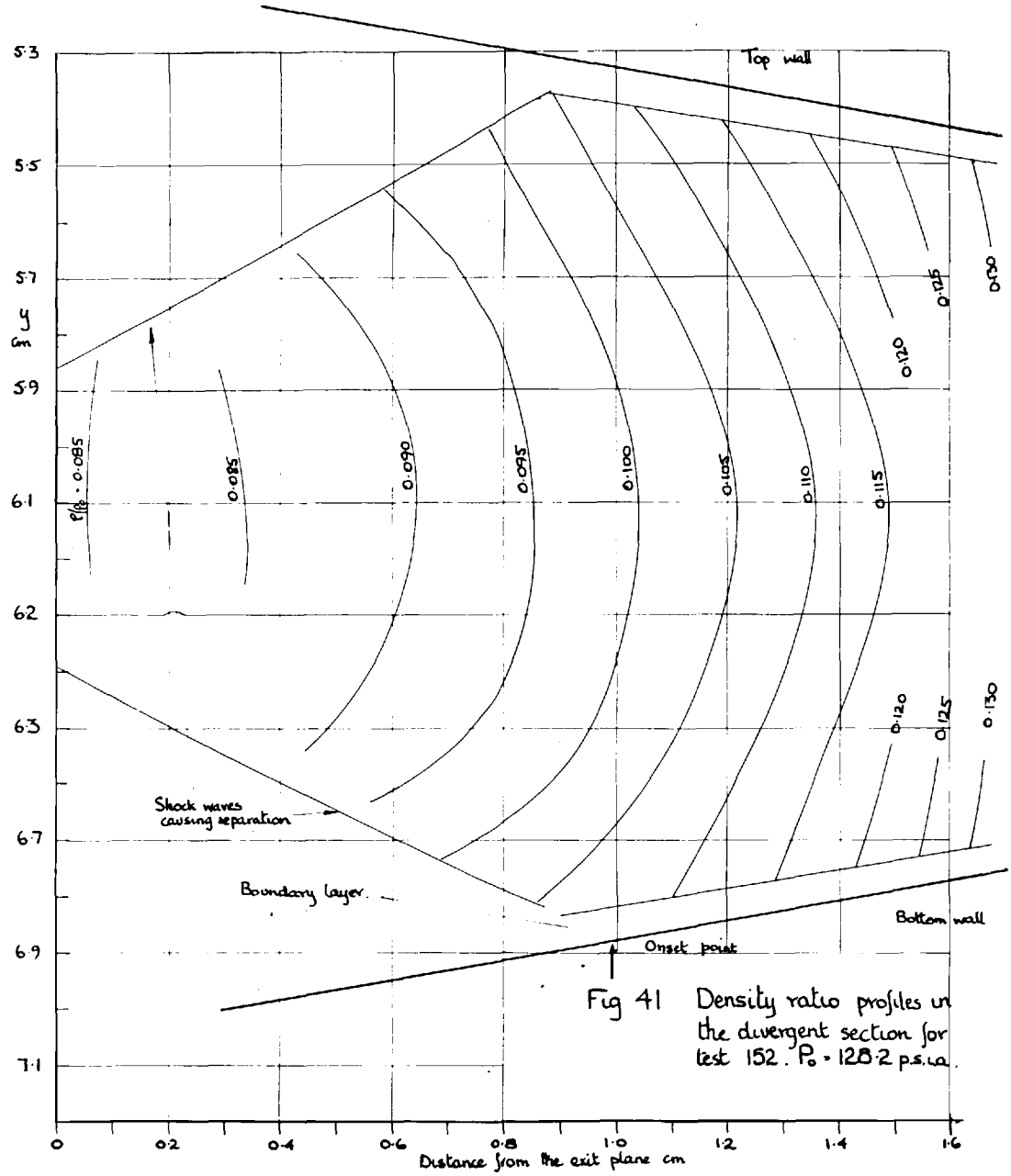

Fig 41 Density ratio profiles in the divergent section for test 152. P_o = 128·2 p.s.i.a.

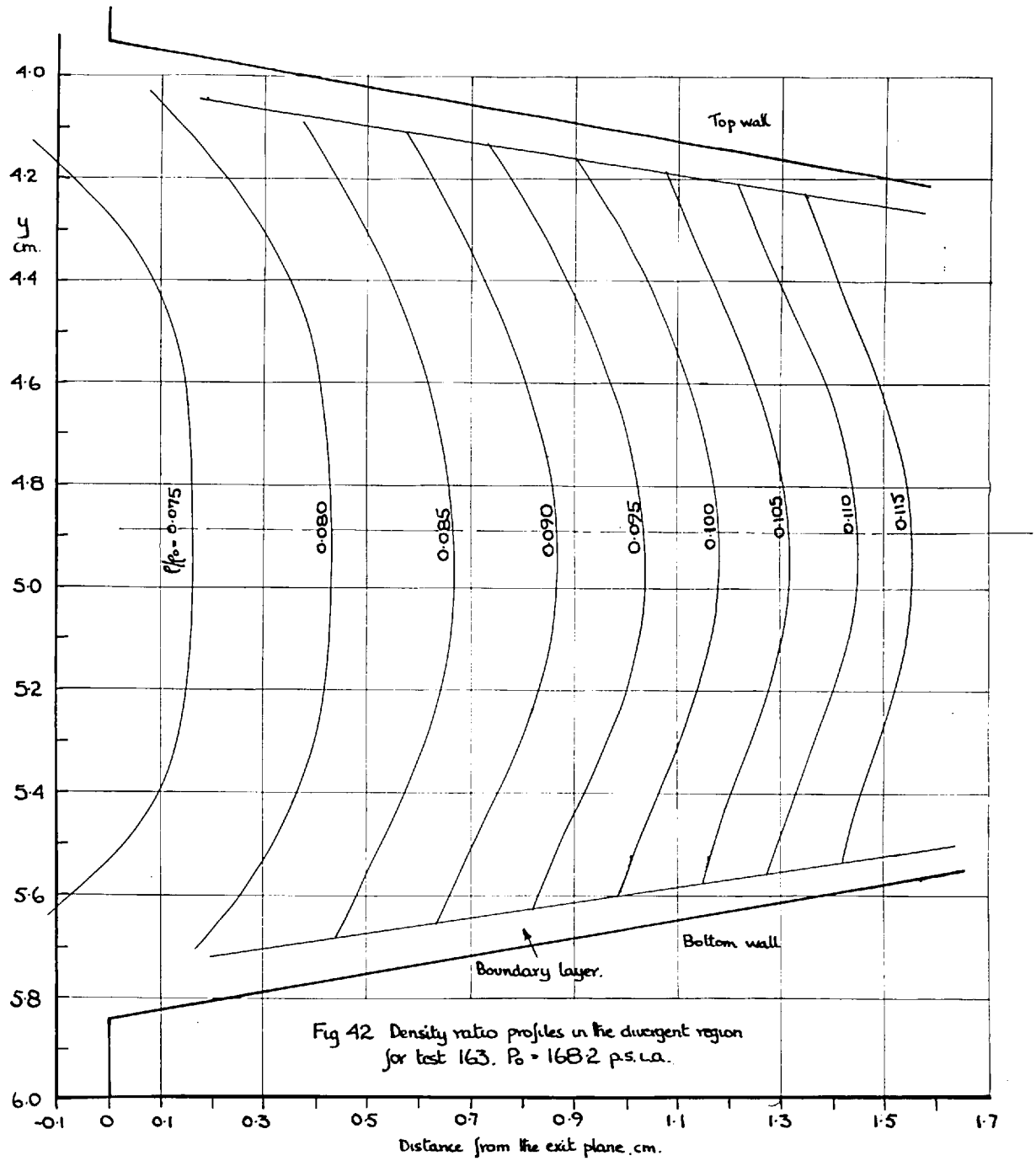

Fig 42 Density ratio profiles in the divergent region for test 163. P_0 = 168·2 p.s.i.a.

the flow was not symmetrical as the density ratios on the edges of the top and bottom boundary layers at corresponding distances from the exit plane were not equal. The density ratio profiles have been plotted in the throat for tests 143 and 152 in figs 38 and 47 respectively, and the throat plane represented as the line joining the maximum and minimum in the nozzle profile at the throat obtained in appendix 1. The density profiles were almost symmetrical about an axis drawn perpendicular to the throat plane, indicating that slight skew of the throat was the cause of the assymmetries in the flow pattern.

The flow pattern in the nozzle did not exhibit the same degree of assymmetry in every test since the differences between the density ratios on the top and bottom and those on the centreline, presented in table 14 overleaf, were not constant.

Table 14.

Assymmetry of the flow pattern.

Distance from the exit plane cm.	Test	Stagnation pressure p.s.i.a.	Difference between the density ratio measured on the edge of the bottom boundary layer and that on the centre-line	Difference between the density ratio measured on the edge of the top boundary layer and that on the centreline
2.6	146	100.2	-3.5%	-2.5%
	163	168.2	-6.8	-4.9
3.2	143	99.2	4.5	4.8
	146	100.2	5.5	5.5
	152	128.2	4.0	5.0
	163	168.2	3.8	4.9
3.8	143	99.2	-10.9	-13.8
	143	100.2	-9.8	-12.5
	152	128.2	-9.8	-12.0

As the variations in the quantities given above at a given point in the flow were not large and did not show any systematic variation with reservoir pressure, they were probably due to oscillations in the flow pattern of the type discussed in section 8.3.4.

With reference to figs 39 - 41 it can be seen that the density ratio profiles curved downstream of the onset point towards the shock waves associated with separation. As the point of intersection of the shock waves was approached, the

curvature increased. Comparison of the profiles in the neighbourhood of the shock waves in tests 143 and 146, with the corresponding ones in test 152, showed that the curvature was associated with the presence of the shock waves. For instance, the profile for a density ratio of 0.115 intersected the centreline at 1.425, 1.465 and 1.490 cms from the exit plane for tests 143, 146 and 152 respectively. But in the former two tests the curvature of the profile was much greater above and below the centreline than in the latter test, where the shock waves were further downstream. The same result was apparent from a comparison of the flow patterns in tests 152 and 163, shown in figs 41 and 42 respectively.

It can be seen from figs 43, 44 and 45 that the density on the centreline passed through a minimum downstream of the onset point. The positions of the minima in the density relative to the onset point are given below in table 15.

Table 15.

Position of the minimum in the density on the centreline in the vicinity of the onset point.

Test	Position of the onset point (cm. from the exit plane)	Position of the minimum in the density on the centreline (cm. from the exit plane)	Distance between the position of the minimum and the onset point (cm)	Percentage difference between the density on the centreline at the minimum and the corresponding one dimensional value.
143	1.684	1.0	0.7	-4.0
146	1.666	1.05	0.6	-5.7
152	0.995	0.2	0.8	-9.5
163	could not be determined	-	-	-

As the minimum in the density only appeared in the vicinity of the shock waves and was approximately the same distance from the onset point for tests at different pressures, it was associated with the flow between the two shock waves associated with separation.

The agreement between tests 143 and 146 was excellent over the coincident parts of the measured regions. In the region 3.1 to 3.4 cms from the exit plane the greatest difference between corresponding values of the density ratio was -0.45% or +0.18% relative to the values for test 143. Comparison of the density ratios on the centreline between

1.1 and 1.7 cms from the orifice showed that those for test 143 at stagnation pressure 99.2 p.s.i.a. were slightly higher than those for test at 100.2 p.s.i.a.

In test 152 the density ratios in the throat region were 0.5 to 1.0% above the corresponding values in test 143, while in the region 3.2 cms from the exit plane they were equal: on moving further downstream the values in test 152 began to fall below those in test 143, the difference reaching a maximum of 3% in the region where comparisons could be made.

The density ratios in test 163 were generally below those measured in test 152. In the region 3.1 to 3.2 cms from the exit plane they were between 0.6 and 1.6% below the values in test 143, the difference increasing to 3.5 - 4.5% in the region 1.4 to 1.7 cms from the exit plane.

It is apparent from the foregoing discussion that the density ratio at a given point in the flow decreased as the reservoir pressure increased. It can also be seen from figs 44, 45 and 46 and table 15 that the departure from isentropic flow increased as the reservoir pressure increased.

The pressure ratios measured in the four tests, tabulated in tables 9 - 12, showed a slight tendency to decrease as the reservoir pressure was increased. The

(Continued on page 145)

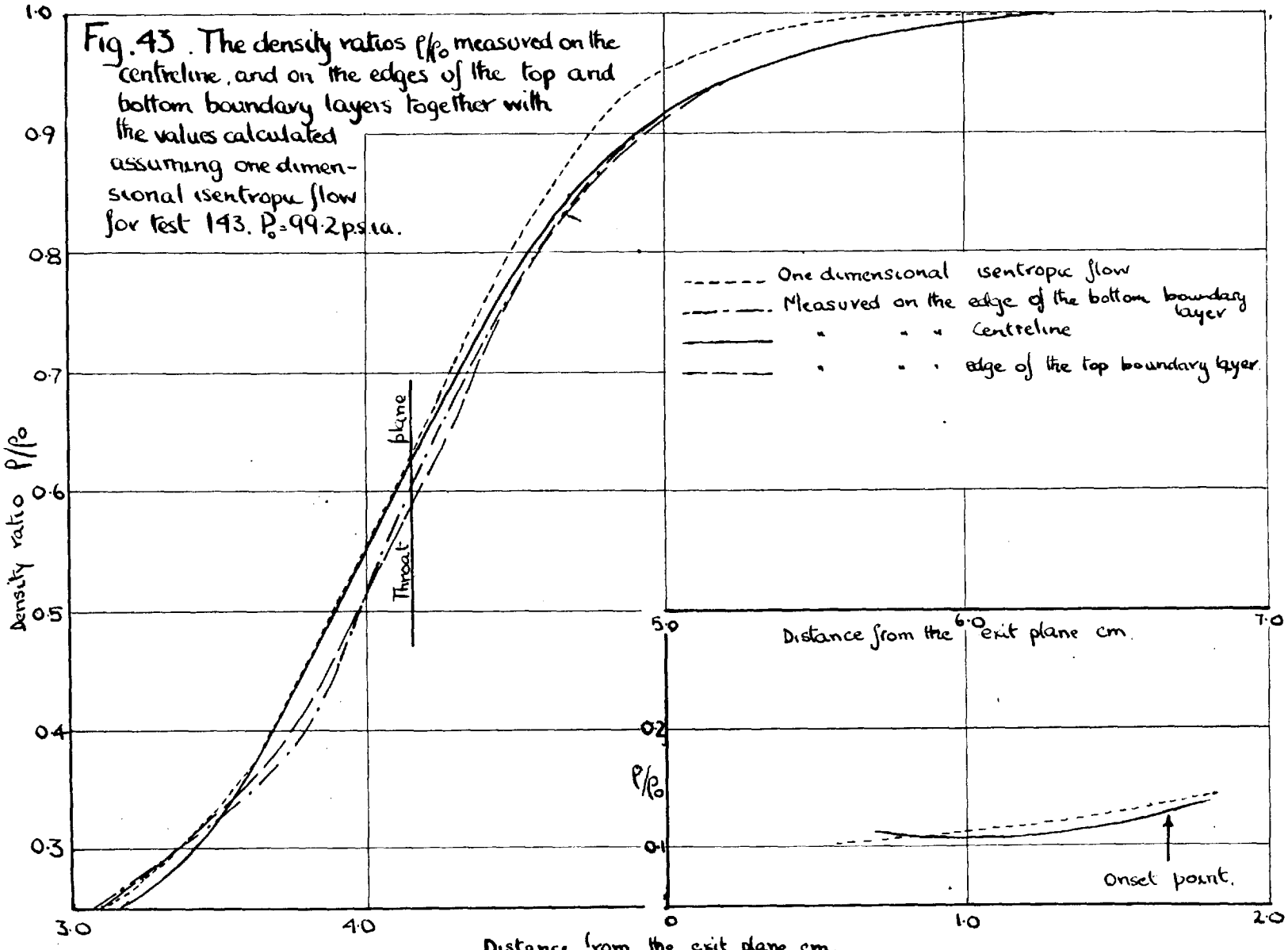
Fig. 43. The density ratios P/P₀ measured on the centreline, and on the edges of the top and bottom boundary layers together with the values calculated assuming one dimensional isentropic flow for test 193. P₀=99·2 p.s.i.a.
One dimensional isentropic flow
Measured on the edge of the bottom boundary layer
Centreline
edge of the top boundary layer
Density ratio P/P₀
1·0
0·9
0·8
0·7
0·6
0·5
0·4
0·3
Throat plane
3·0
4·0
5·0
6·0
7·0
Distance from the exit plane cm.
0·2
0·1
P/P₀
0
1·0
2·0
Onset point.

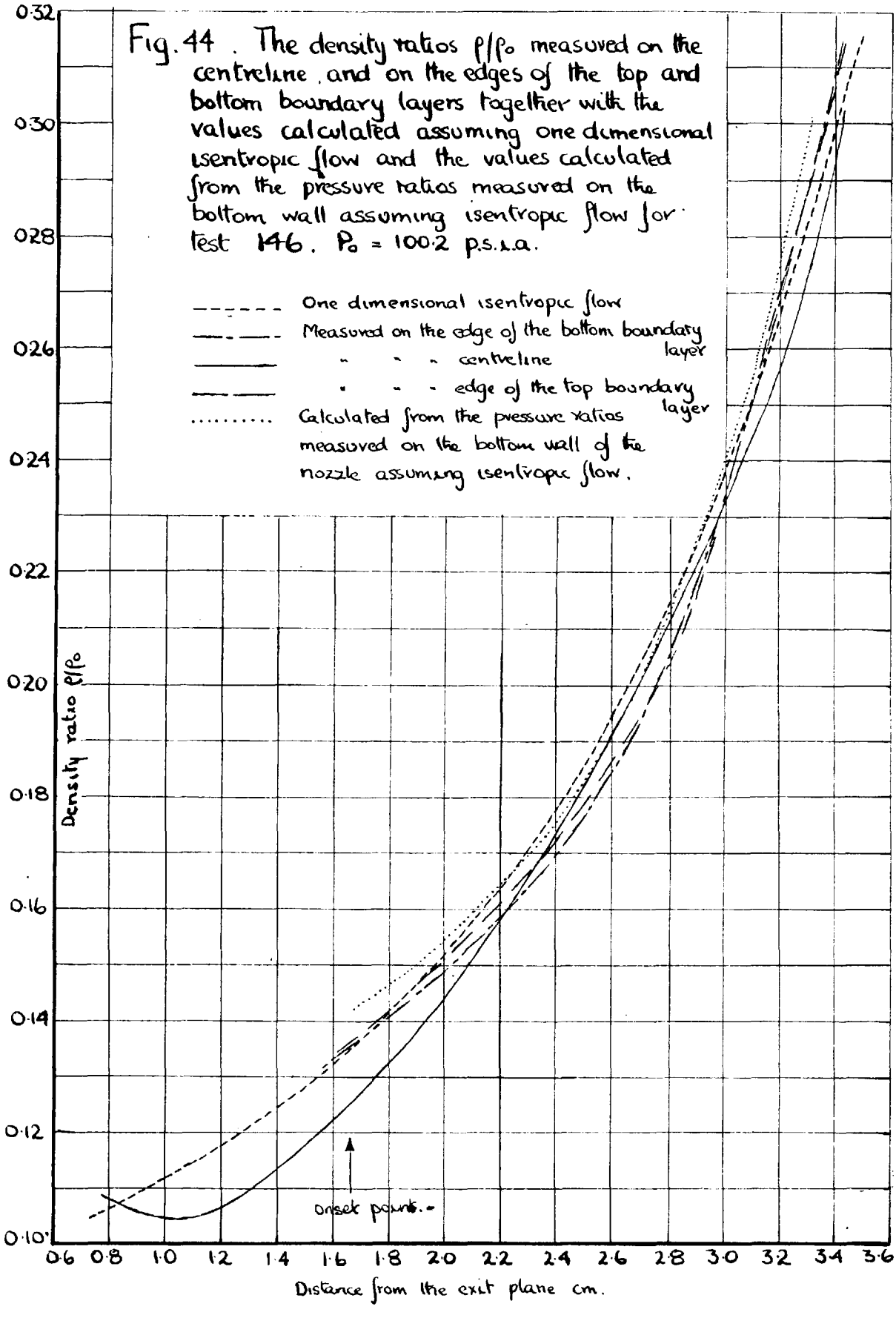
Fig. 44. The density ratios ρ/ρ₀ measured on the centreline and on the edges of the top and bottom boundary layers together with the values calculated assuming one dimensional isentropic flow and the values calculated from the pressure ratios measured on the bottom wall assuming isentropic flow for test 146. P₀ = 100·2 p.s.i.a.
One dimensional isentropic flow
Measured on the edge of the bottom boundary layer
centreline
edge of the top boundary layer
Calculated from the pressure ratios measured on the bottom wall of the nozzle assuming isentropic flow.
Density ratio ρ/ρ₀
0·32
0·30
0·28
0·26
0·24
0·22
0·20
0·18
0·16
0·14
0·12
0·10
Onset points.
0·6 0·8 1·0 1·2 1·4 1·6 1·8 2·0 2·2 2·4 2·6 2·8 3·0 3·2 3·4 3·6
Distance from the exit plane cm.

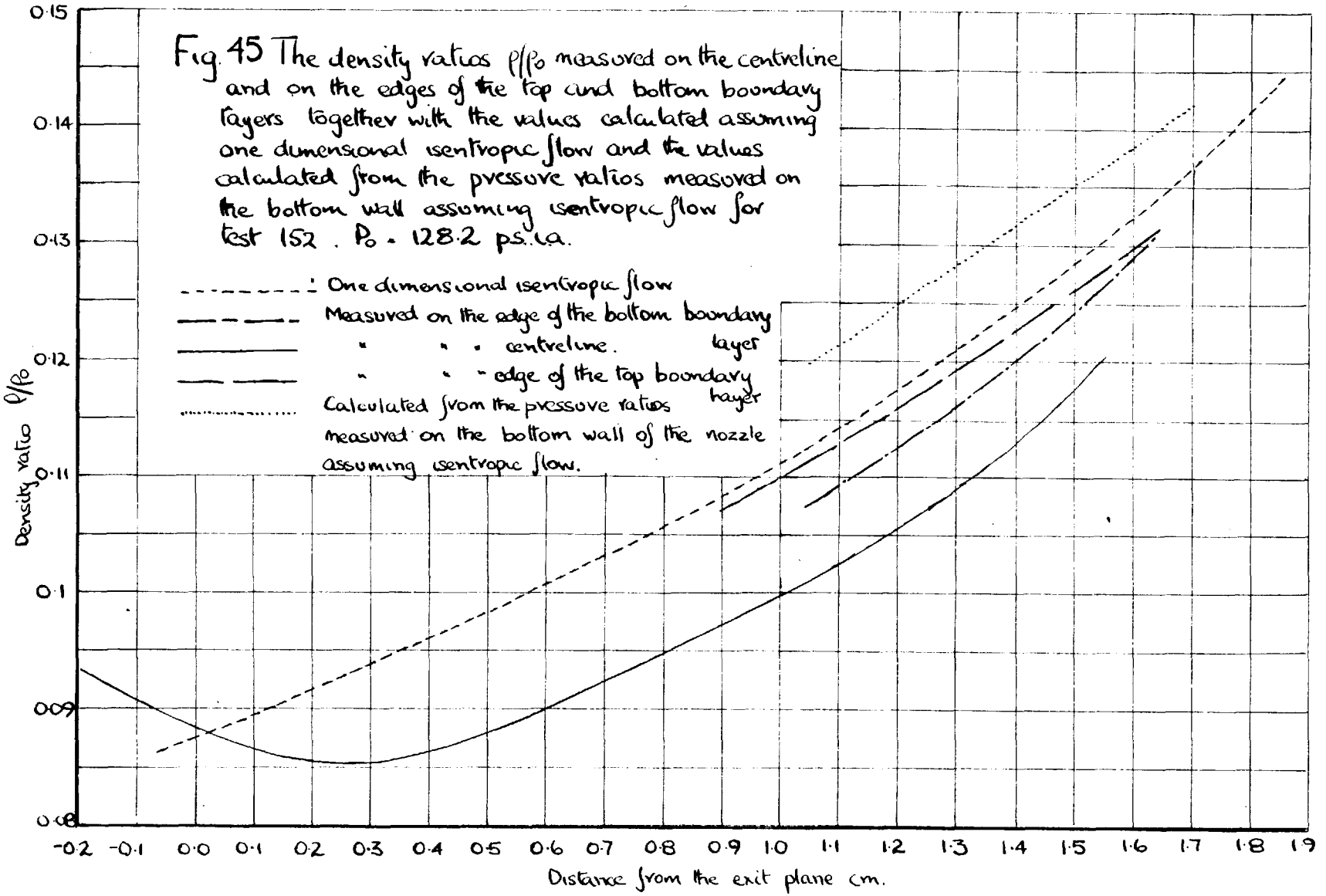

Fig. 45 The density ratios ρ/ρ_0 measured on the centreline and on the edges of the top and bottom boundary layers together with the values calculated assuming one dimensional isentropic flow and the values calculated from the pressure ratios measured on the bottom wall assuming isentropic flow for test 152. $P_0 = 128.2$ p.s.i.a.

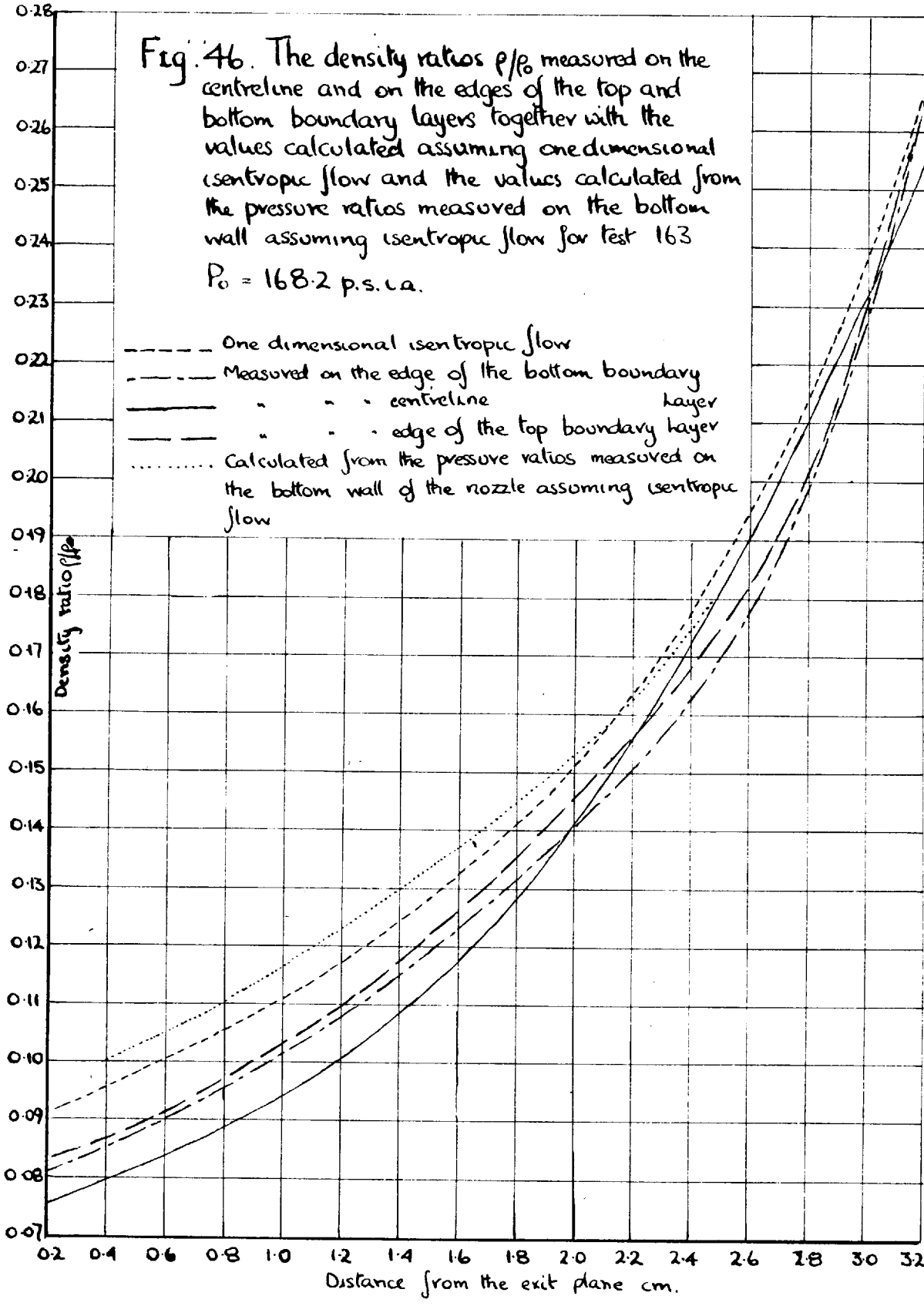
Fig. 46. The density ratios ρ/ρ₀ measured on the centreline and on the edges of the top and bottom boundary layers together with the values calculated assuming one dimensional isentropic flow and the values calculated from the pressure ratios measured on the bottom wall assuming isentropic flow for test 163
P₀ = 168.2 p.s.i.a.
One dimensional isentropic flow
Measured on the edge of the bottom boundary layer
" " centreline
" " edge of the top boundary layer
Calculated from the pressure ratios measured on the bottom wall of the nozzle assuming isentropic flow
Density ratio ρ/ρ₀
0·28
0·27
0·26
0·25
0·24
0·23
0·22
0·21
0·20
0·19
0·18
0·17
0·16
0·15
0·14
0·13
0·12
0·11
0·10
0·09
0·08
0·07
0·2
0·4
0·6
0·8
1·0
1·2
1·4
1·6
1·8
2·0
2·2
2·4
2·6
2·8
3·0
3·2
Distance from the exit plane cm.

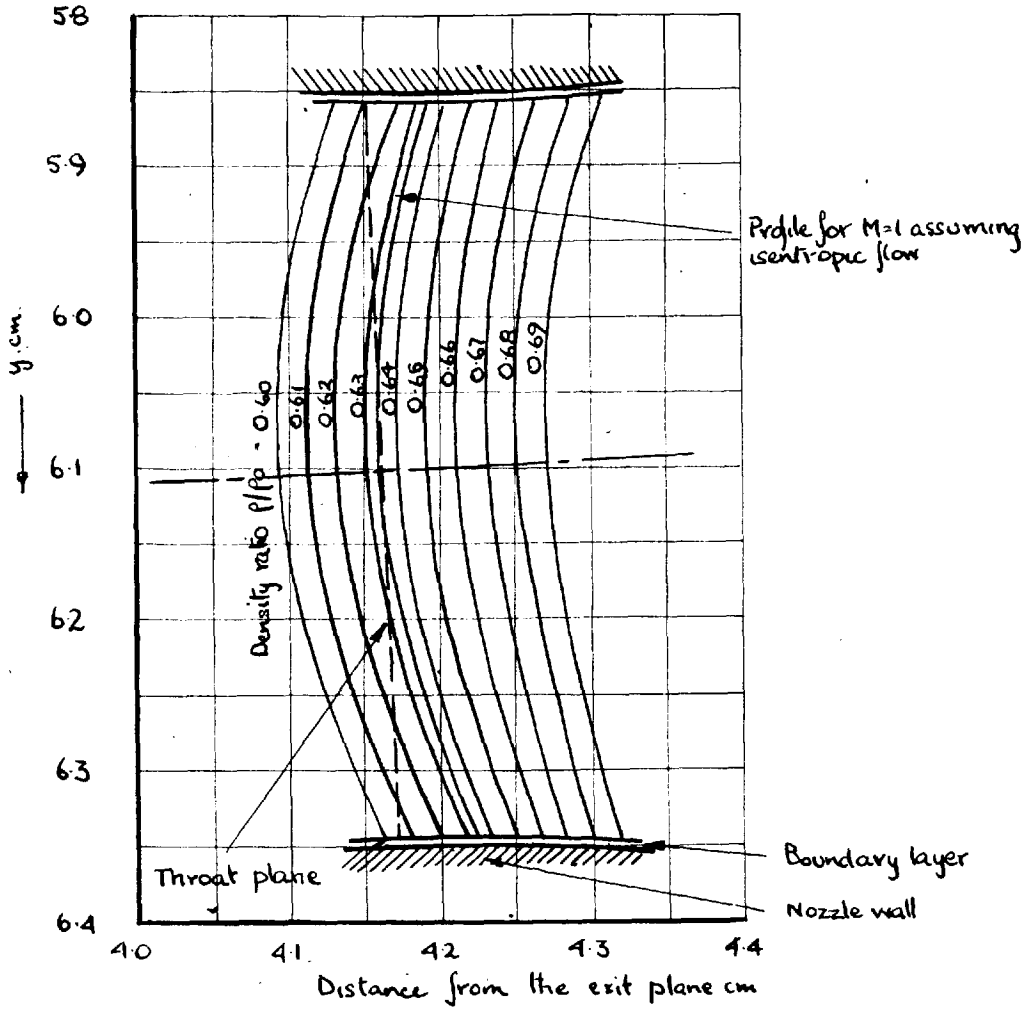

Fig. 47. Test 152. P_o = 1282 p.s.i.a. Flow pattern in the throat region.

pressure ratios calculated from the density ratios measured on the edge of the bottom boundary layer have been plotted in figs 48 - 51 with the measured pressure ratios. The measured values were above the calculated ones and at the onset points in tests 146 and 152 they were 7% and 15% above respectively. In test 163 where it was not possible to determine the onset point, the measured pressure ratio at 0.4 cms from the exit plane was 26% above the value calculated from the density ratio.

Conversely the density ratios calculated from the measured pressure ratios assuming isentropic flow, plotted in figs 44 - 46, 48 and 50, were above the measured values, the difference at a given point increasing as the reservoir pressure was raised, and on moving down the divergence in any test.

The results discussed above show that the divergences between the measured flow properties and those calculated assuming isentropic flow were large and increased as the reservoir pressure increased. Therefore the Mach number at any point could not be calculated from either the density or the pressure ratio by making the assumption of isentropic flow.

Accordingly it was assumed that the expansion in the

(Continued on page 150.)

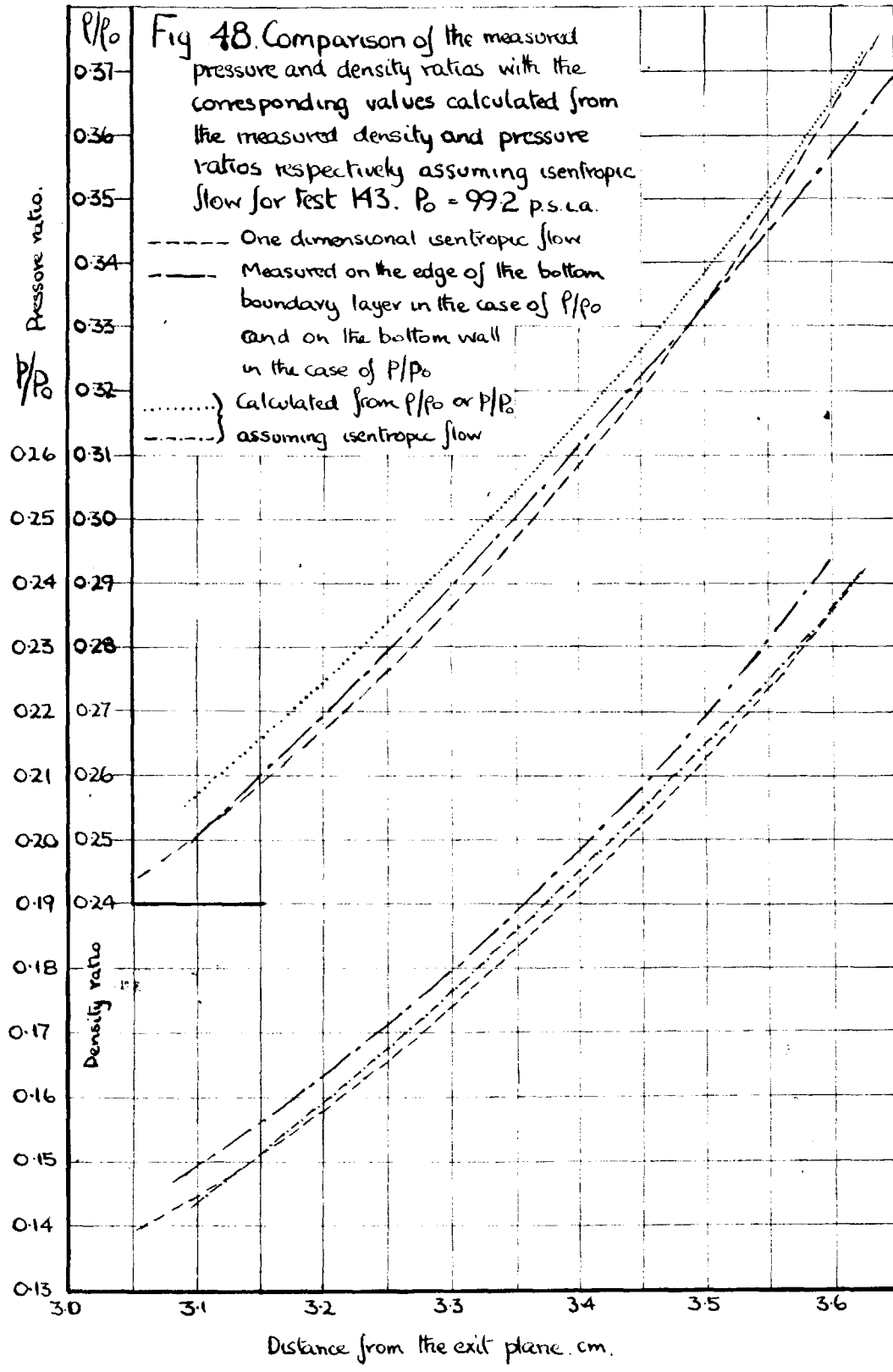

Fig 48. Comparison of the measured pressure and density ratios with the corresponding values calculated from the measured density and pressure ratios respectively assuming isentropic flow for Test 143. P_o = 992 p.s.i.a.

- – – – – One dimensional isentropic flow
- ——— Measured on the edge of the bottom boundary layer in the case of P/Po and on the bottom wall in the case of P/Po
- ..... } Calculated from P/Po or P/Po
- -.-.-. } assuming isentropic flow

Fig. 49. Comparison of the pressure ratios measured on the bottom wall of the nozzle, with the values calculated from the density ratios measured on the edge of the bottom boundary layer assuming isentropic flow, for test 196. P_o 100·2 p.s.i.a.

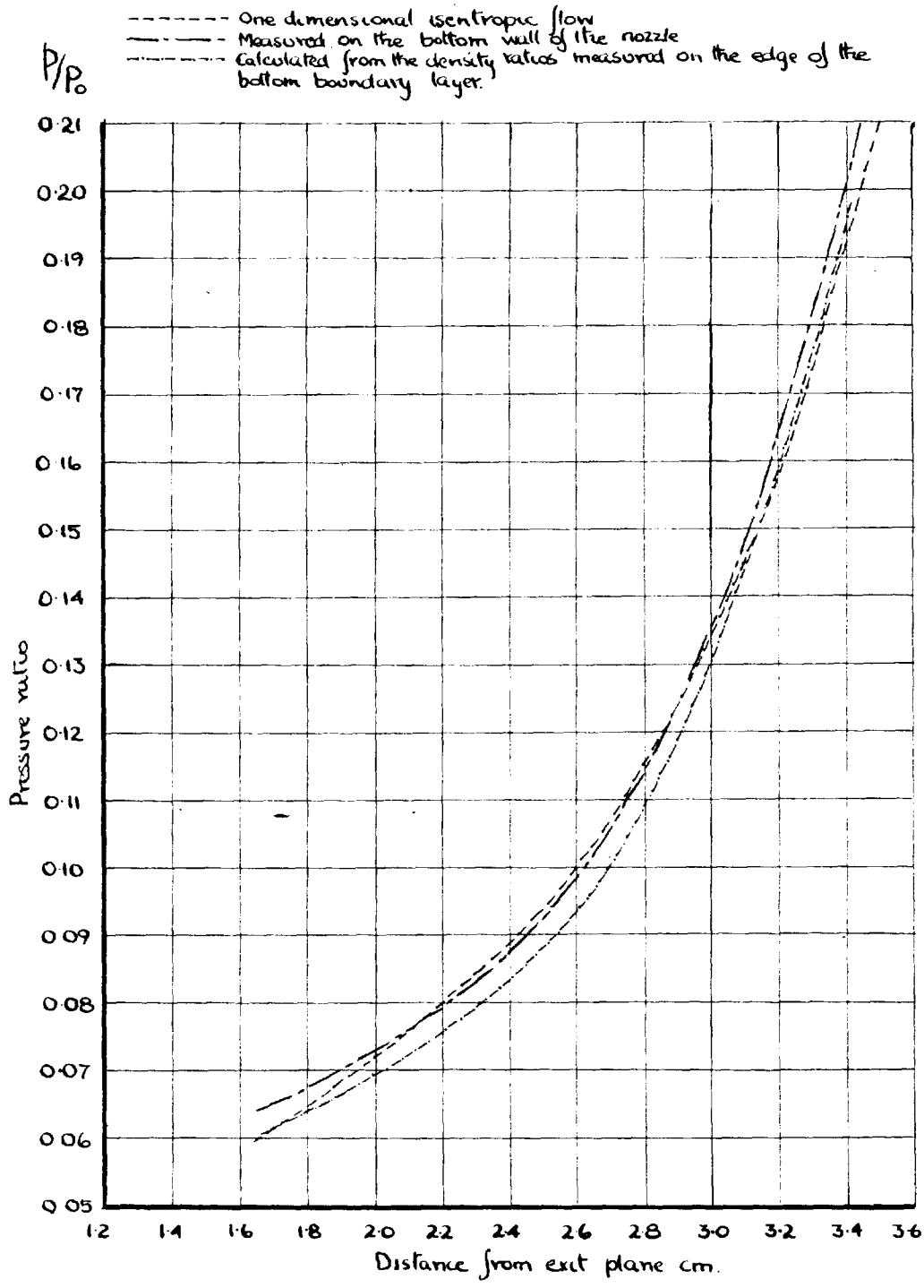

Fig. 50. Comparison of the measured pressure (p/p_o) and density (ρ/ρ_o) ratios with the corresponding values calculated from the measured density and pressure ratios respectively, assuming isentropic flow, for test 152. P_o = 128·2 p.s.i.a.

----- One dimensional isentropic flow

····· Calculated from p/p_o

-·-·- " " ρ/ρ_o

— — — Measured on the edge of the bottom boundary layer in the case of ρ/ρ_o and on the bottom wall in the case of p/p_o

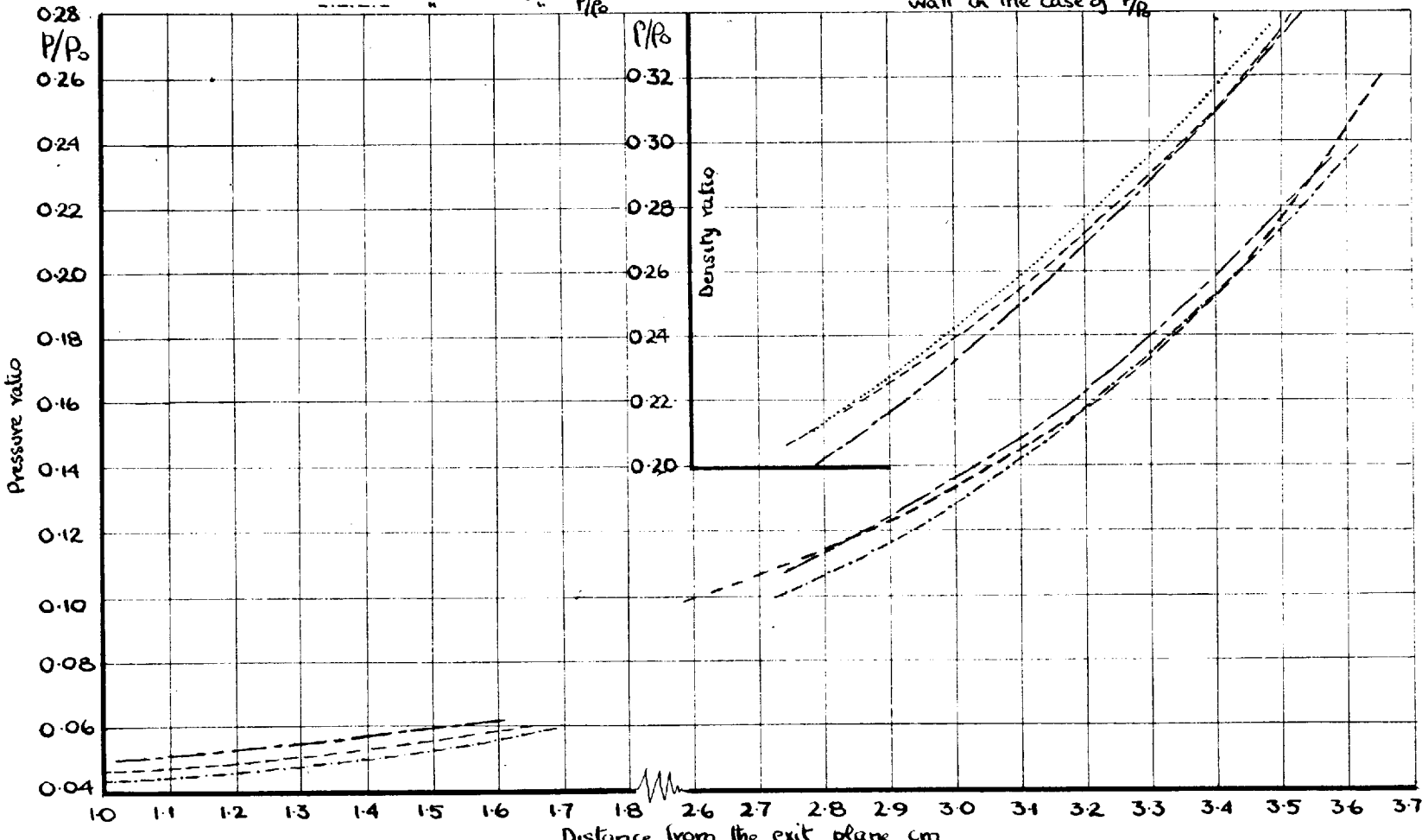

Fig. 51. Comparison of the pressure ratios measured on the bottom wall of the nozzle with the values calculated from the density ratios measured on the edge of the bottom boundary layer assuming isentropic flow, for test 163. P_o = 168·2 p.s.i.a.

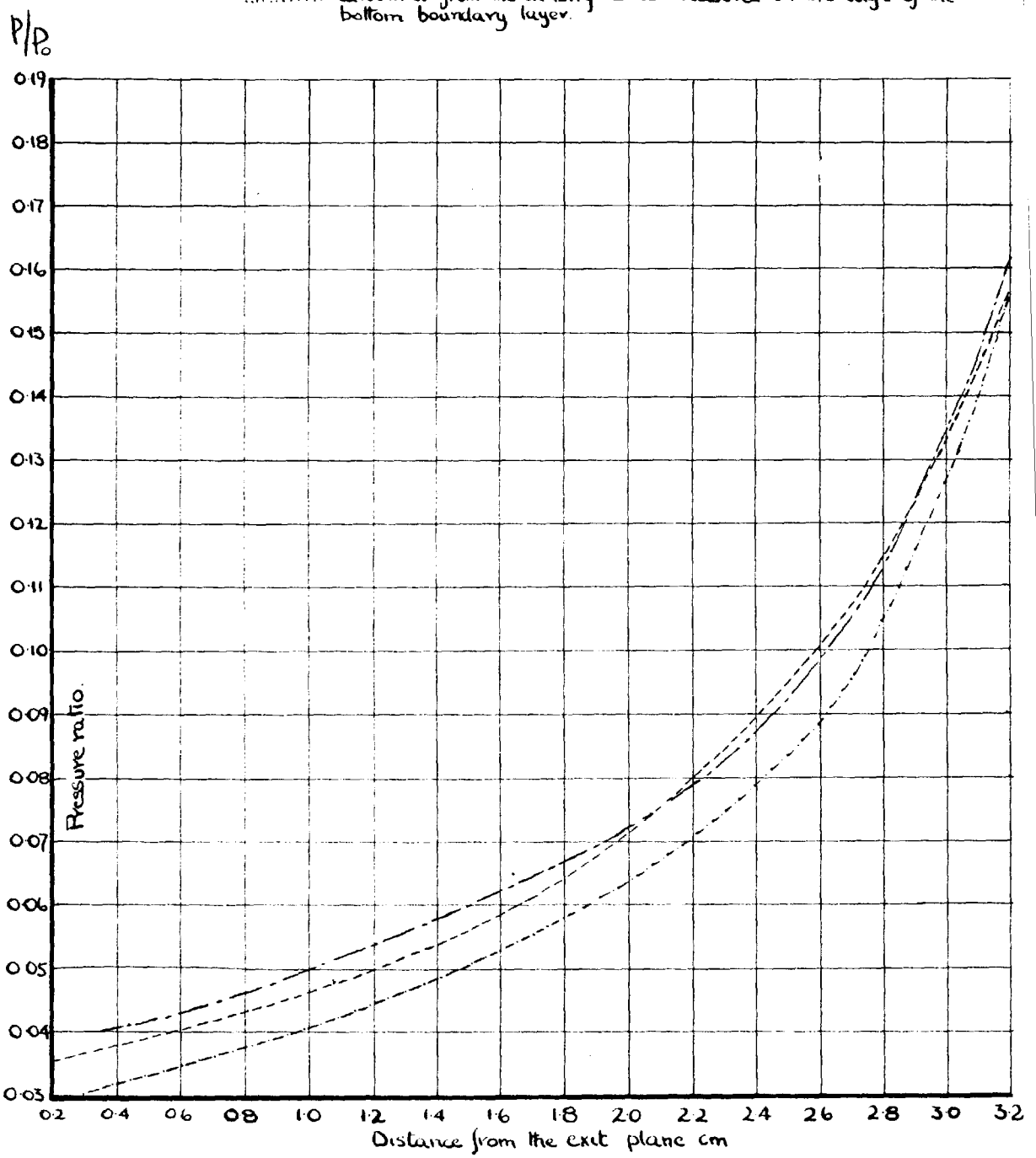

nozzle could be represented by the irreversible adiabatic expansion of a perfect gas. Then it can be shown that the relationship,

$$V^2 = 2Cp(To - T) \quad \text{or} \quad M^2 = \frac{2}{\gamma - 1}\left(\frac{To}{T} - 1\right)$$

is valid. The temperature ratio, derived from corresponding values of the density and pressure ratios on the edge of the bottom boundary layer and the bottom wall respectively, was used to calculate the Mach number. The Mach number corresponding to a given density ratio could only be calculated in this way in the regions where pressure measurements could be obtained. To estimate the Mach number corresponding to a density ratio in the nozzle outside these regions, a method of extrapolating to the reservoir had to be found.

The most convenient method of representing the temperature ratio results so that the extrapolation could be carried out conveniently, was on a temperature-entropy diagram. Therefore the entropy change was calculated at the same time as the Mach number and plotted against temperature ratio. Then as the entropy must continuously increase from zero at the reservoir, extrapolation to the regions where temperature and entropy results were obtained could be carried out, as shown in fig 52.

The entropy change ΔS in expanding from $Po, \rho o,$ to $p, \rho,$

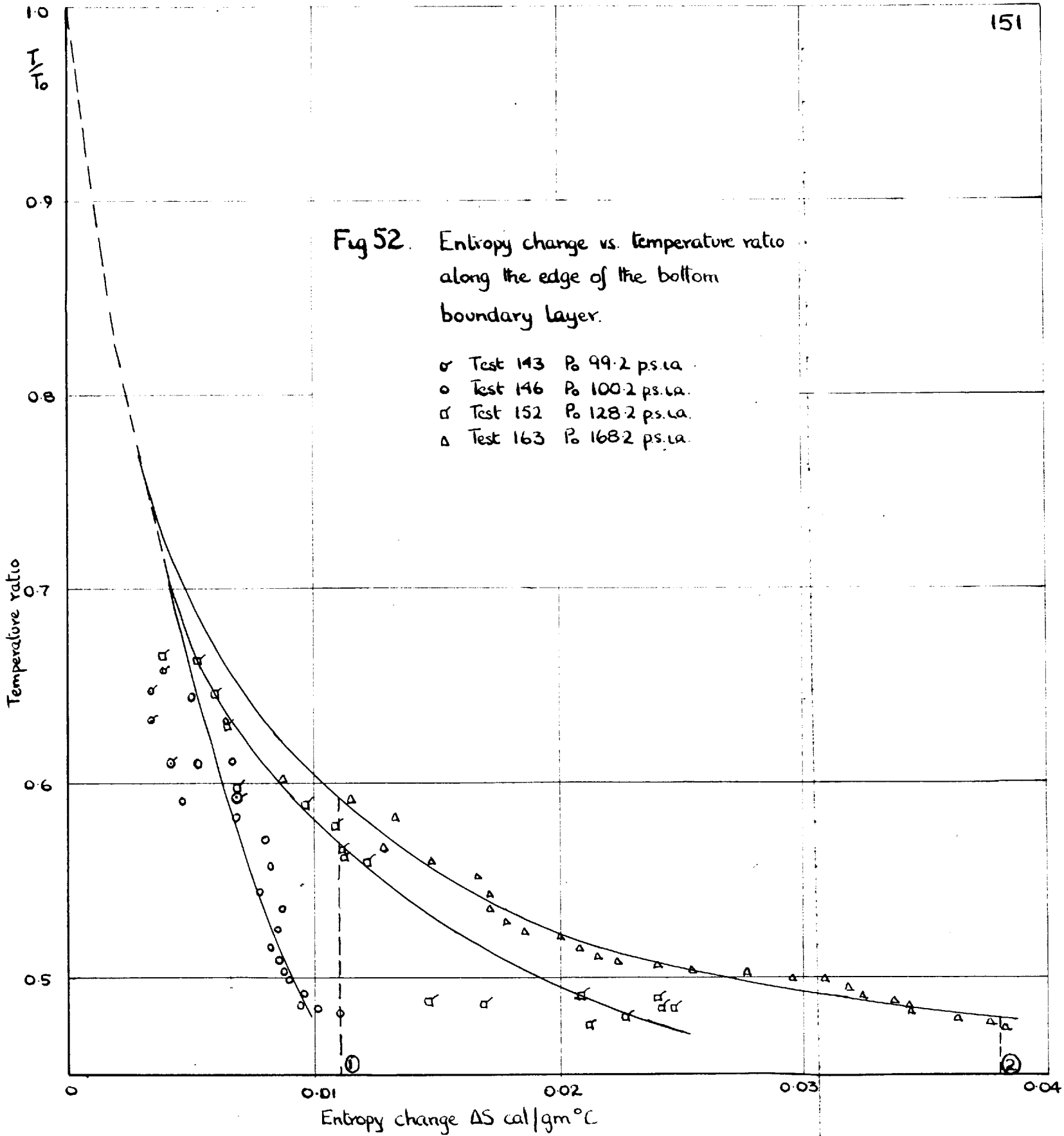

Fig 52. Entropy change vs. temperature ratio along the edge of the bottom boundary layer.

- ◦ Test 143 P_0 99·2 p.s.i.a.
- o Test 146 P_0 100·2 p.s.i.a.
- □ Test 152 P_0 128·2 p.s.i.a.
- △ Test 163 P_0 168·2 p.s.i.a.

is given by:-

$$\Delta S = C_p \ln \left(\frac{p}{p_o}\right)^{\frac{1}{\gamma}} \frac{\rho_o}{\rho}$$

$$\text{or } \Delta S = 0.5513 \log_{10} \left(\frac{p}{p_o}\right)^{\frac{1}{\gamma}} \frac{\rho_o}{\rho} \quad \frac{\text{cal}}{\text{gm}^{\circ}\text{C}}$$

where $\gamma = 1.4$ and $C_p = 0.2394$ cal/gm$^{\circ}$C.

The entropy change ΔS, the temperature ratios and the Mach numbers, calculated from the density and pressure ratios in tests 143, 146, 152 and 163 have been tabulated in table 16. The Mach numbers are represented graphically in fig 53 together with those calculated in the next section from Mach angle measurements.

It can be seen from fig 52 that for any given temperature ratio the entropy change increases with reservoir pressure, and from fig 53 that the Mach number at any given position in the divergence decreases.

9.1.2. The Mach number determined by the measurement of Mach angle.

The slight irregularities in the surface of the bottom wall of the nozzle caused by the pressure holes produced Mach lines in the flow, which were photographed using the direct shadowographic technique. These Mach lines can be seen clearly in the three shadowographs taken at stagnation pressures

TABLE 16.

Entropy change, temperature ratio, and Mach number on the edge of the bottom boundary layer.

Dist from the exit plane	TEST 143			TEST 146			TEST 152			TEST 163		
cm	ΔS cals gm°C	T/T_o	M	ΔS cals gm°C	T/T_o	M	ΔS cals gm°C	T/T_o	M	ΔS cals gm°C	T/T_o	M
0.4										0.0402	0.4727	2.362
0.5										0.0382	0.4727	2.362
0.6										0.0376	0.4758	2.347
0.7										0.0362	0.4776	2.339
0.8										0.0343	0.4806	2.325
0.9										0.0343	0.4836	2.311
1.0										0.0337	0.4872	2.295
1.05							0.0211	0.4745	2.353			
1.1							0.0228	0.4795	2.331	0.0324	0.4900	2.282
1.2							0.0241	0.4841	2.310	0.0318	0.4940	2.263
1.3							0.0245	0.4861	2.299	0.0309	0.4952	2.244
1.4							0.0239	0.4888	2.287	0.0295	0.4984	2.243
1.5							0.0208	0.4888	2.287	0.0276	0.5021	2.227
1.6							0.0164	0.4861	2.299	0.0254	0.5028	2.224
1.65							0.0146	0.4874	2.292			
1.7				0.0110	0.4823	2.316				0.0239	0.5051	2.214
1.8				0.0101	0.4839	2.310				0.0224	0.5075	2.202
1.9				0.0094	0.4868	2.296				0.0215	0.5110	2.188
2.0				0.0096	0.4926	2.269				0.0208	0.5150	2.170
2.1				0.0089	0.4981	2.245				0.0200	0.5196	2.151

Dist from the exit plane	TEST 143			TEST 146			TEST 152			TEST 163		
cm	S cals $gm^{o}C$	T/T_o	M	S cals $gm^{o}C$	T/T_o	M	S cals $gm^{o}C$	T/T_o	M	S cals $gm^{o}C$	T/T_o	M
2.2				0.0087	0.5038	2.219				0.0186	0.5232	2.134
2.3				0.0085	0.5091	2.195				0.0178	0.5284	2.113
2.4				0.0082	0.5161	2.166				0.0171	0.5347	2.086
2.5				0.0085	0.5252	2.126				0.0171	0.5430	2.052
2.6				0.0087	0.5353	2.082				0.0166	0.5524	2.013
2.7				0.0078	0.5434	2.049				0.0148	0.5588	1.988
2.75							0.0121	0.5590	1.985			
2.8				0.0082	0.5578	1.991	0.0112	0.5639	1.971	0.0128	0.5667	1.956
2.9				0.0080	0.5712	1.938	0.0108	0.5784	1.908	0.0133	0.5830	1.891
3.0				0.0068	0.5820	1.895	0.0096	0.5895	1.866	0.0115	0.5922	1.856
3.1	0.0068	0.5951	1.844	0.0045	0.5914	1.859	0.0068	0.5976	1.834	0.0087	0.6020	1.181
3.2	0.0041	0.6084	1.792	0.0052	0.6120	1.788	0.0064	0.6131	1.780	0.0066	0.6122	1.779
3.3	0.0033	0.6226	1.739	0.0064	0.6318	1.707	0.0064	0.6304	1.712			
3.4	0.0033	0.6387	1.681	0.0050	0.6453	1.658	0.0059	0.6464	1.654			
3.5	0.0036	0.6566	1.617				0.0052	0.6628	1.595			
3.55		0.6856	1.513				0.0038	0.6668	1.580			

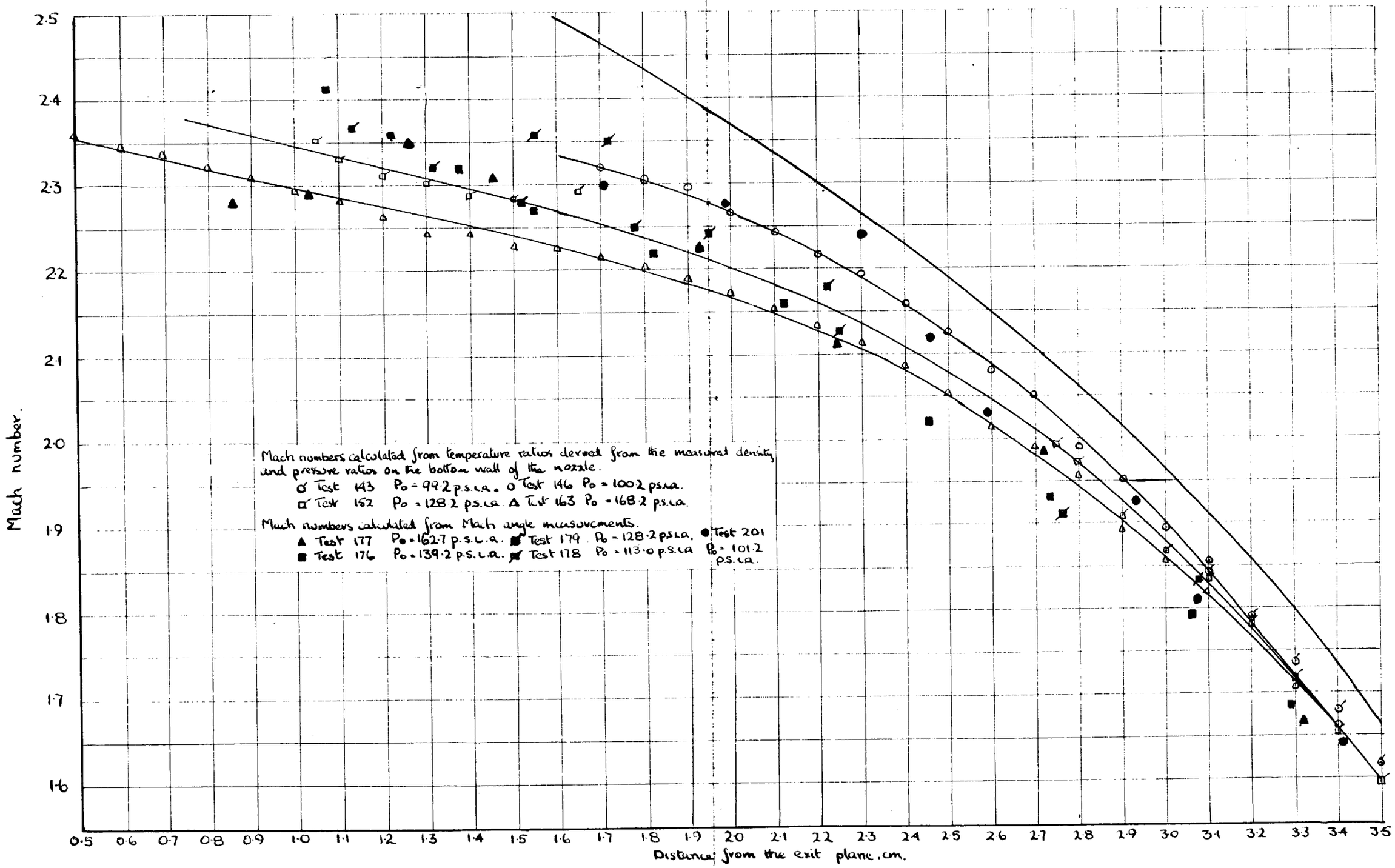

Fig.53. Mach number variation along the edge of the bottom boundary layer.

shown in fig 54.

However due to the refraction of the incident beam of light in the boundary layer, the position of the nozzle walls on the shadowographs did not correspond to that of the actual wall. There was a discontinuity in the wall profile at the point of separation associated with the sudden change from a boundary layer, with its associated high refractive index gradients, to the region of reversed flow, where the gradients were negligible. To determine the position of the apparent wall on the shadowographs relative to the actual wall position, the nozzle profile on the shadowographs was measured and the position of the bottom wall compared with that on a no flow interferogram. This has been done in fig 55 where the shadowograph was taken at a stagnation pressure of 139.2 p.s.i.a. The difference of 0.015 cm between the two results in the region of reversed flow was small, and therefore, the position of the actual wall on the shadowograph was obtained by producing the apparent wall in this region back to the throat (see fig 54).

The Mach angle was assumed to be the angle between the tangent to a Mach line at the edge of the flow region and the actual wall. The angle so measured was further assumed to be that corresponding to a point on the edge of the

(a)

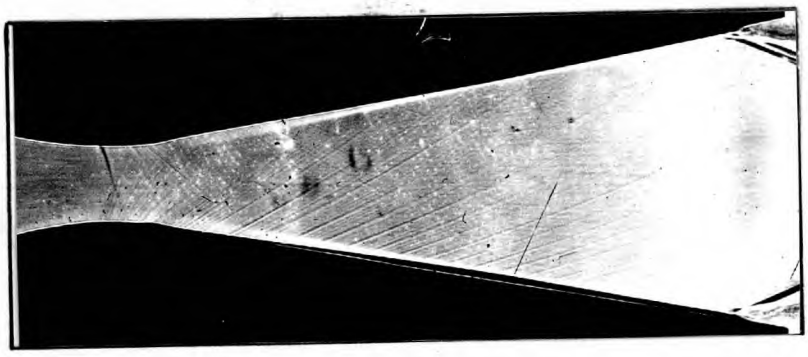

Test 177 P_o = 162·7 p.s.i.a.

(b)

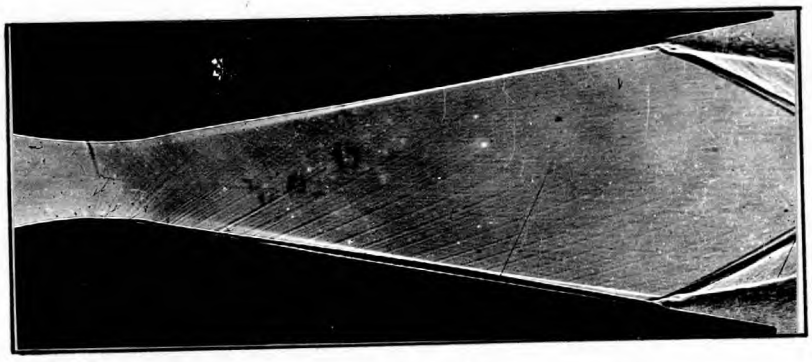

Test 176 P_o = 139·2 p.s.i.a.

(c)

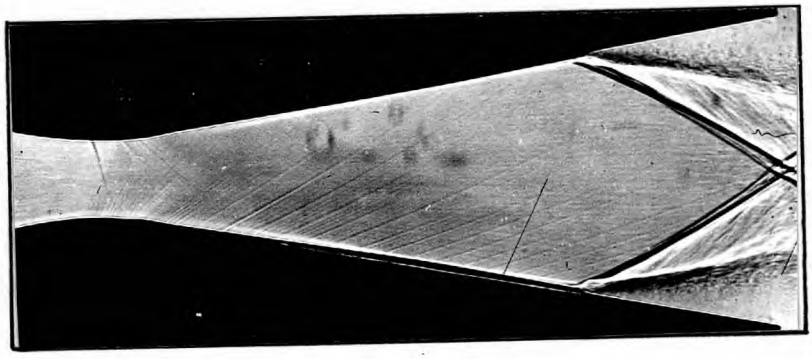

Test 178 P_o = 113·0 p.s.i.a.

Fig 54. Direct shadowgraphs of the flow in the nozzle showing the Mach lines.

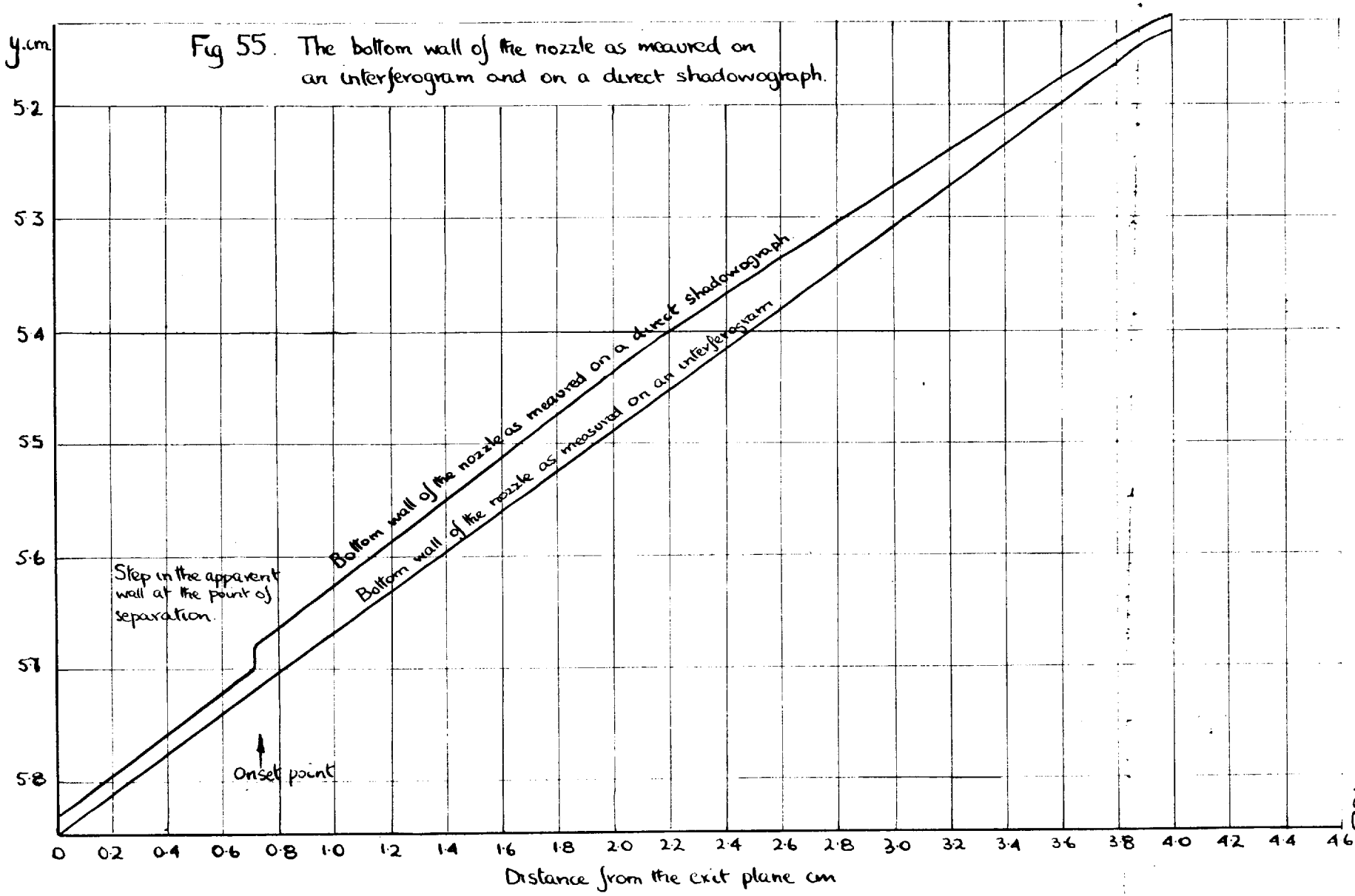
Fig 55. The bottom wall of the nozzle as measured on an interferogram and on a direct shadowograph.
y.cm
5·2
5·3
5·4
5·5
5·6
5·7
5·8
Bottom wall of the nozzle as measured on a direct shadowograph.
Bottom wall of the nozzle as measured on an interferogram
Step in the apparent wall at the point of separation.
Onset point
0
0·2
0·4
0·6
0·8
1·0
1·2
1·4
1·6
1·8
2·0
2·2
2·4
2·6
2·8
3·0
3·2
3·4
3·6
3·8
4·0
4·2
4·4
4·6
Distance from the exit plane cm

TABLE 17.

Mach number determined from Mach angle measurements

Test	Stagnation pressure p.s.i.a.	Distance from the exit plane. cms.	Mach number	Mach number measured interferometrically in test 163 Po = 168.2 p.s.i.a.
177	162.7	3.32	1.66	1.67
		2.72	1.99	1.98
		2.24	2.14	2.12
		1.93	2.25	2.18
		1.46	2.31	2.25
		1.26	2.35	2.27
		1.03	2.29	2.30
		0.86	2.28	2.32
176	139.2	3.29	1.68	
		3.06	1.79	
		2.73	1.93	
		2.45	2.02	
		2.12	2.16	
		1.82	2.22	
		1.55	2.27	
		1.38	2.32	
		1.22	2.36	
		1.07	2.42	
179	128.2	2.22	2.18	
		1.77	2.25	
		1.51	2.28	
		1.31	2.32	
		1.13	2.37	
178	113.0	3.08	1.83	
		2.76	1.91	
		2.25	2.12	
		1.95	2.24	
		1.72	2.35	
		1.55	2.36	
201	101.2	3.41	1.64	
		3.07	1.81	
		2.93	1.93	
		2.59	2.03	
		2.46	2.12	
		2.30	2.24	
		1.99	2.28	
		1.71	2.30	

bottom boundary layer, at the same distance from the exit plane as the intersection of the tangent produced and the actual wall.

The Mach numbers obtained have been tabulated in table 17 and plotted in fig 53 with the interferometric results. The Mach numbers obtained interferometrically in test 163 at stagnation pressure 168.2 p.s.i.a. have been tabulated in table 17 with those obtained from Mach angle measurements in test 177 at stagnation pressure 162.7 p.s.i.a. The maximum difference of 3.5% between the two sets of results was caused by the difficulty in measuring the Mach angles to an accuracy of greater than $\pm 0.5^{\circ}$.

9.2. Flow Separation.

Tests were carried out in which wall pressure measurements were obtained at the same time as shadowographs, interferograms and schlieren photographs over a stagnation pressure range of approximately 45 to 165 p.s.i.a. The flow pattern in the vicinity of the separation point was found to be symmetrical and the pressure gradients at the wall high in the stagnation pressure range 165 - 95 p.s.i.a. However on subsequent reduction of pressure the flow pattern became assymmetrical and the pressure gradients decreased.

Accordingly the flow separation results have been divided into three groups, symmetrical, assymmetrical and those obtained when the boundary layer trips described in section 7.2.1. were fitted.

9.2.1. Results for Symmetrical Separation.

The tests were carried out in groups A, B, C, D, E & F at nominal stagnation pressures of 165, 140, 127, 113, 100 and 95 p.s.i.a., respectively. The pressure within each group was varied over a range of approximately 3 p.s.i.a.

The wall pressure results for one of the groups have been tabulated in table 18 and it can be seen that the maximum error in the wetted region of flow was $\mp$ 0.5%. In the case of the results in table 18, the wetted region extended to pressure tapping 18 as at 19 the pressure ratios diverge considerably signifying that separation had taken place.

With reference to fig 56 where the results in table 18 have been represented graphically, it can be seen that if the results for one of the tests had been plotted separately, it would not have been possible to make an accurate assessment of the onset point position, with the points available. For instance in test 183 the initial pressure rise took place

TABLE 18

Wall pressure ratios for the tests in group B, nominal Stagnation pressure 140 p.s.i.a.

TEST		155	156	159	176	180	183
Stagnation Pressure Po		139.1	139.3	139.8	139.2	138.5	141.8
Pressure tapping	Dist from exit plane. cm.						
1	3.506	0.2170	0.2196	0.2219	0.2201	0.2221	0.2159
2	3.357	0.1913	0.1920	0.1933	0.1921	0.1933	0.1923
3	3.190	0.1613	0.1616	0.1626	0.1615	0.1625	0.1619
4	3.042	0.1411	0.1416	0.1422	0.1415	0.1420	0.1417
5	2.886	0.1231	0.1234	0.1239	0.1234	0.1239	0.1243
6	2.729	0.1071	0.1074	0.1079	0.1073	0.1078	0.1076
7	2.574	0.0969	0.0969	0.0972	0.0968	0.0973	0.0971
8	2.423	0.0882	0.0882	0.0886	0.0882	0.0885	0.0880
9	2.261	0.0818	0.0818	0.0821	0.0817	0.0820	0.0820
10	2.108	0.0767	0.0766	0.0769	0.0765	0.0768	0.0767
11	1.953	0.0715	0.0713	0.0713	0.0712	0.0714	0.0714
12	1.797	0.0677	0.0676	0.0677	0.0676	0.0676	0.0676
13	1.639	0.0631	0.0631	0.0632	0.0629	0.0632	0.0632
14	1.486	0.0610	0.0608	0.0609	0.0607	0.0608	0.0608
15	1.329	0.0569	0.0568	0.0569	0.0566	0.0568	0.0569
16	1.169	0.0533	0.0532	0.0534	0.0531	0.0533	0.0532
17	1.019	0.0505	0.0503	0.0503	0.0501	0.0502	0.0503
18	0.861	0.0475	0.0473	0.0474	0.0472	0.0472	0.0473
19	0.701	0.0813	0.0797	0.0761	0.0735	0.0561	0.0453
20	0.544	0.0985	0.0980	0.0982	0.0974	0.0954	0.0899
21	0.386	0.1007	0.1002	0.1005	0.1002	0.0988	0.0954

Fig 56 The wall pressure ratio p/p_0 vs distance from the exit plane for the tests in Group B, nom. stagnation pressure 140 p.s.i.a.

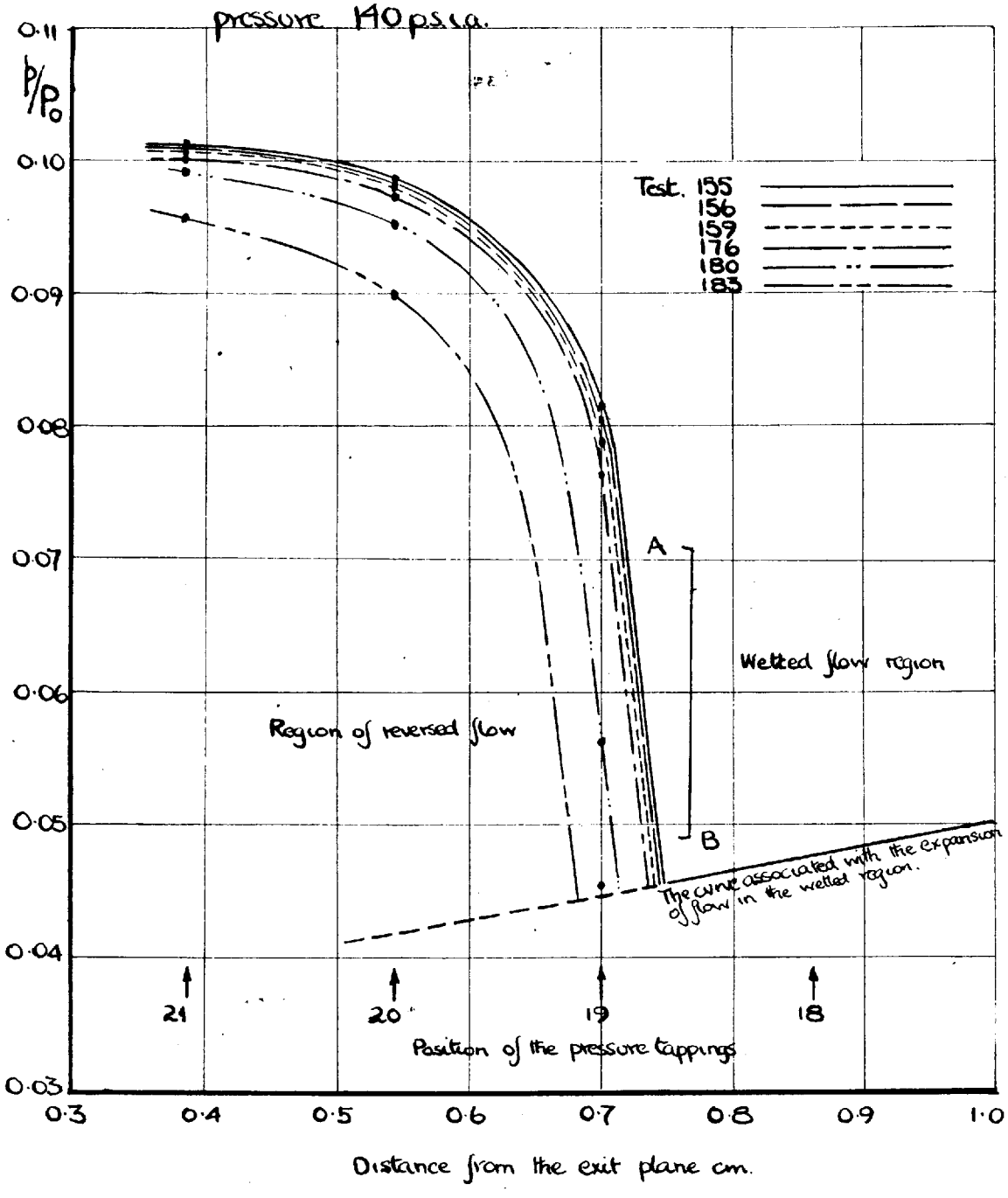

Fig 57. The wall pressure ratio vs distance from the exit plane for the tests in Groups E and F at nominal stagnation pressures 100 and 95 p.s.i.a respectively.

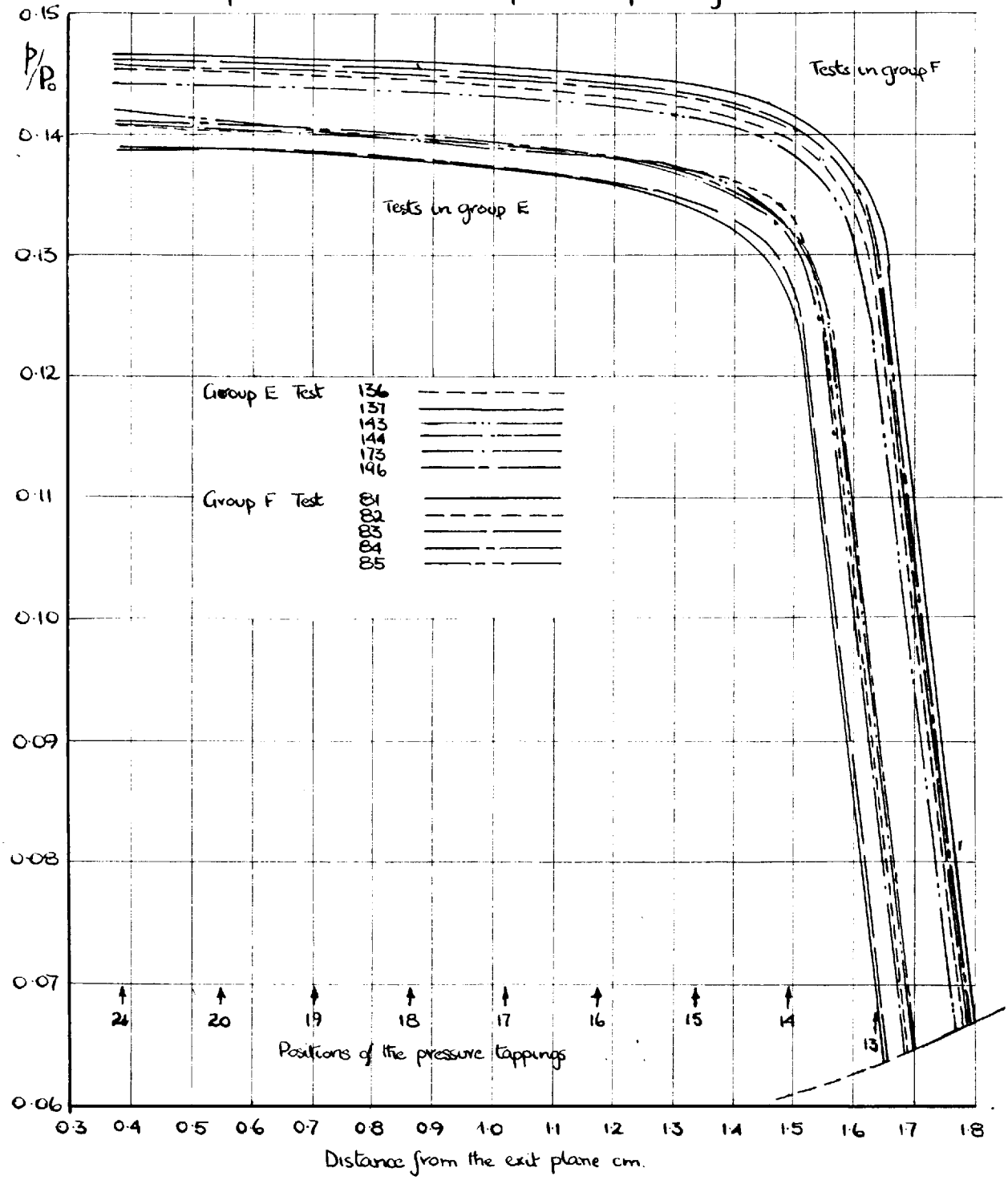

between holes 19 and 20 and no results were obtained on this part of the pressure curve. However by changing the pressures slightly at which the tests were carried out in the group, thereby altering the position of separation, it was possible to determine the onset pressure accurately, by making the assumption that the pressure gradient for the first initial steep pressure rise was the same for all the tests. For example in fig 56 the curves in the region AB representing the initial pressure rise were drawn straight and parallel to each other. The range of positions over which this could be done was very limited, and hence the error in the determination of the onset point for a given test was much less than that obtained by using the results of a single test. The curve associated with the expansion of the flow in the wetted region was extrapolated downstream of the last tapping recording the pressure in this region by using the results obtained in tests at higher pressure. In group B the curve for the expansion in the wetted region was extrapolated downstream of tapping 18 by using the results obtained in group A where separation took place downstream of hole 20.

The results for onset and peak pressure, as defined in sections 3.4 and 8.4 respectively, have been tabulated in

table 19, with the Mach and Reynolds numbers at the onset point.

The Mach numbers were determined from the interferometrically measured values presented in fig 53. When the tests were carried out a stagnation pressures intermediate to those for which interferograms were evaluated, the Mach numbers were obtained by extrapolation between the interferometric results.

Shadowographs of the flow in the pressure range discussed above, presented in fig 58, show that the shock pattern associated with the boundary layer separation from the nozzle walls remained symmetrical as the stagnation pressure was decreased until group E was reached. For instance the shock pattern for test 186, Po = 98.9 p.s.i.a. was not symmetrical (see fig 58d). The position of separation did not oscillate and the flow pattern was reproducible, as in tests 137 and 138 carried out at the same stagnation pressure and discharging to atmospheres of identical pressure, the results for onset pressure and position were in excellent agreement. The curves for the pressure ratio variation in the reversed flow regions in group E were not all the same shape and unlike those for the tests at higher pressure, crossed each other, (see fig 57). This effect was due to

TABLE 19.

The position of, the Mach and Reynolds number, and the pressure at, the onset point for the tests in groups A, B. C. D. E. & F.

Test	Stagnation pressure Po p.s.i.a.	Atm pressure pa. p.s.i.a.	Peak pressure p_p p.s.i.a.	Onset pressure po p.s.i.a.	Position of onset point, cm from exit plane	Pressure ratio at the on onset point p/p_o	p_o/p_a	p_o/p_p	Reynolds No x 10^{-6}	Mach No
Group A Norminal Stagnation pressure 165 p.s.i.a.										
162	166.3	14.83		6.64	(0.343)	0.0399	0.447		2.59	2.38
182	172.5	14.49		6.61	(0.157)	0.0383	0.456			2.39
177	162.7	14.75		6.56	(0.394)	0.0403	0.443		2.56	2.37
Group B Nominal Stagnation pressure 140 p.s.i.a.										
155	139.1	14.77	14.13	6.36	0.747	0.0457	0.430	0.450	2.12	2.365
156	139.3	14.78	14.14	6.35	0.742	0.0456	0.430	0.449	2.15	2.366
159	139.8	14.85	14.20	6.36	0.736	0.0455	0.428	0.448	2.14	2.367
176	139.2	14.75	14.11	6.33	0.731	0.0455	0.429	0.449	2.11	2.368
183	141.8	14.49	13.86	6.25	0.681	0.0441	0.431	0.451	2.30	2.374
180	138.5	14.48	13.85	6.25	0.710	0.0451	0.432	0.451	2.30	2.370
Group C Nominal Stagnation pressure 127 p.s.i.a.										
150	128.0	14.68	14.01	6.44	0.993	0.0503	0.439	0.460	2.09	2.349
151	127.3	14.68	14.01	6.44	1.011	0.0506	0.439	0.460	2.11	2.348
152	128.2	14.68	14.01	6.43	0.995	0.0502	0.438	0.459	2.12	2.349
153	127.2	14.80	14.12	6.47	1.031	0.0509	0.437	0.458	2.09	2.345
154	127.0	14.81	14.13	6.47	1.035	0.0510	0.437	0.458	2.07	2.344
175	125.7	14.80	14.12	6.44	1.045	0.0512	0.435	0.456	2.06	2.342
179	128.2	14.53	13.85	6.36	0.959	0.0496	0.438	0.459	2.28	2.354
184	125.4	14.54	13.87	6.35	1.015	0.0506	0.437	0.458	2.18	2.346

Group D Nominal Stagnation pressure 113 p.s.i.a.

141	117.6	14.62	13.91	6.47	1.239	0.0550	0.443	0.465	1.70	2.342
142	116.4	14.65	13.94	6.53	1.304	0.0561	0.446	0.469	1.94	2.334
148	115.6	14.64	13.93	6.51	1.311	0.0563	0.445	0.467	1.90	2.332
149	116.6	14.64	13.93	6.52	1.293	0.0559	0.445	0.468	1.97	2.335
174	114.5	14.75	14.04	6.50	1.333	0.0568	0.441	0.463	1.78	2.330
178	113.0	14.48	13.78	6.41	1.325	0.0567	0.443	0.465	1.88	2.331
185	114.8	14.49	13.79	6.44	1.296	0.0561	0.444	0.467	1.87	2.335
186	115.0	14.58	13.87	6.47	1.306	0.0562	0.444	0.466	1.81	2.334

Group E Nominal Stagnation pressure 100 p.s.i.a.

136	100.0	14.50	13.71	6.45	1.682	0.0645	0.445	0.470	1.64	2.325
137	101.7	14.68	13.91	6.47	1.644	0.0636	0.441	0.465	1.67	2.331
143	99.2	14.58	13.76	6.41	1.684	0.0646	0.440	0.466	1.65	2.324
144	100.7	14.57	13.79	6.41	1.646	0.0637	0.440	0.465	1.65	2.331
173	100.7	14.77	13.96	6.49	1.680	0.0644	0.439	0.465	1.58	2.326
196	98.9	14.57	13.73	6.41	1.693	0.0648	0.440	0.467	1.59	2.323
138	101.7	14.68	13.91	6.46	1.645	0.0635	0.440	0.465	1.66	2.331

Group F Nominal Stagnation pressure 95.0 p.s.i.a.

81	95.1	14.56	13.79	6.43	1.800	0.0676	0.442	0.466		2.116
82	96.5	14.58	13.81	6.47	1.781	0.0670	0.444	0.469		2.118
83	95.6	14.60	13.83	6.43	1.775	0.0673	0.440	0.465		2.119
84	95.5	14.49	13.74	6.43	1.783	0.0673	0.440	0.468		2.118
85	96.2	14.46	13.69	6.43	1.760	0.0668	0.445	0.470		2.121

(a)

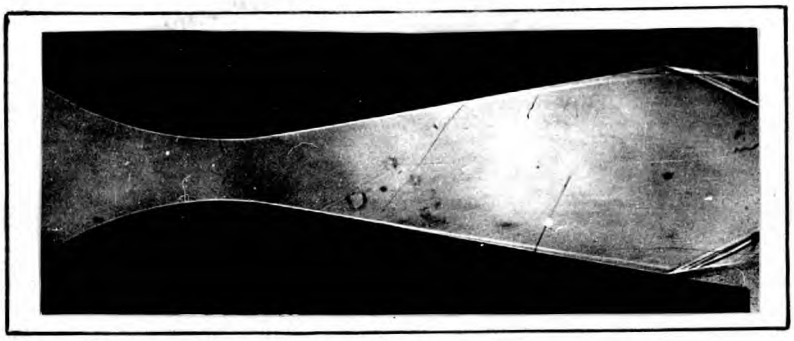

Group B test 183 P_o = 141·8 p.s.i.a.

(b)

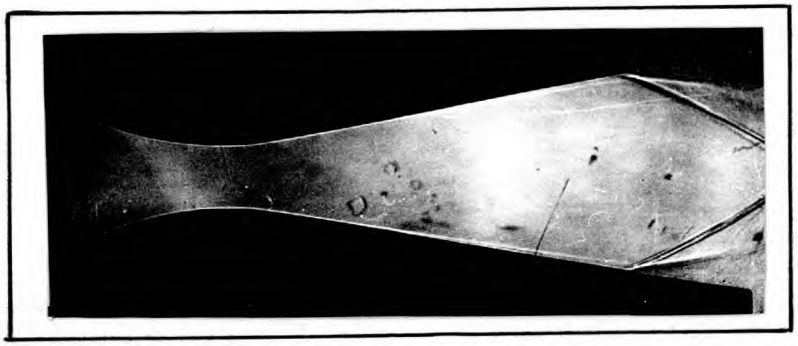

Group C. test 184 P_o = 125·4 p.s.i.a.

(c)

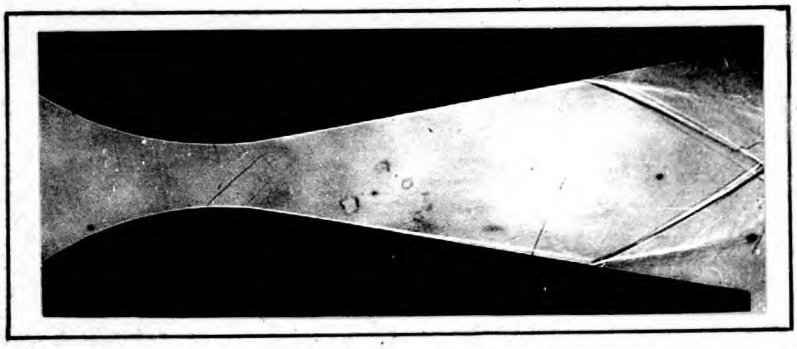

Group D. test 185 P_o = 114·8 p.s.i.a.

(d)

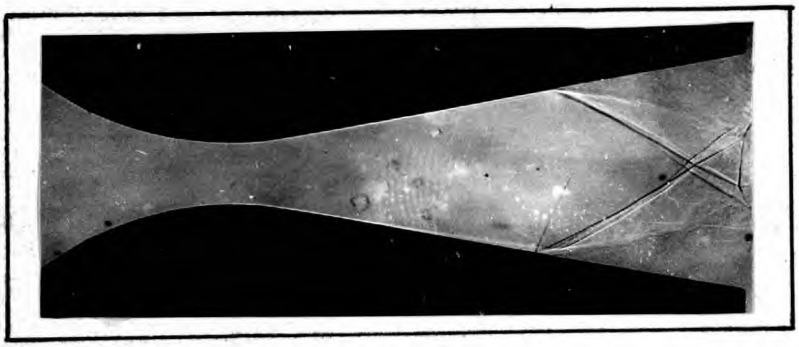

Group E test 196 P_o = 98·9 p.s.i.a.

Fig 58 Shadowgraphs of symmetrical separation (taken with white light).

the alteration in the flow conditions of the reversed stream caused by the changes in the shape of the reversed flow region, associated with the assymmetrical separation.

On further reduction of pressure the character of the separation phenomenon changed and will be discussed in the next section.

The results presented in table 19 include those for tests in group A at the highest stagnation pressure used, in which separation took place close to the exit plane of the nozzle, downstream of the last pressure tapping. As a result, the pressure rise at separation could not be recorded. Therefore an approximation to the onset pressure was obtained by extrapolating the curve in the wetted region to the exit plane, and assuming that the onset point corresponded to the position of the discontinuity at the separation point in the wall profile on the corresponding direct shadowograph, (see fig 54).

The onset pressures measured in group A did not follow the trend shown by those in the previous tests as they were greater than those in group B, with the result that the ratio $\frac{p_o}{p_a}$ was unexpectedly high. These effects were caused by the exit plane being reached before the pressure rise downstream of the separation point could be completed.

The shock wave system associated with separation appeared on interferograms and shadowgraphs to be made up of more than one shock wave; for instance in figs 54c and 58c a weak shock system can be seen clearly inside a much stronger one. This effect and the rise in density ratio between the shock waves described in section 9.1.1., can be explained if it is assumed that the shock waves also cause the boundary layer on the glass walls to separate.

The density ratio across the shock wave on the bottom wall was determined from the interferogram for test 85 Po = 96.2 p.s.i.a. and presented in table 20 below with the corresponding pressure ratios calculated from the appropriate Rankine Hugoniot relationship with $\gamma = 1.4$.

TABLE 20.

Density and pressure ratios across the shock wave causing separation on the bottom wall in test 85 Po = 96.2 p.s.i.a.

y cms	ρ_2/ρ_1	p_2/p_1	p_1/p_2
2.4	1.718	2.173	0.4601
2.45	1.728	2.193	0.4559
2.5	1.729	2.195	0.4555
2.55	1.729	2.195	0.4555
2.6	1.730	2.198	0.4549
2.65	1.737	2.211	0.4523
2.7	1.743	2.222	0.4501
Centreline 2.217			
Onset point 2.875	-	-	-

Subscript 1 refers to conditions upstream of the shock wave and 2 to those downstream.

On moving towards the onset position, the pressure ratio p_1/p_2 approached the peak pressure ratio $p_{p_1}/p_{p_2} = 0.470$ obtained from the wall pressure measurements.

The results for tests 81 - 85 have been presented in table 19 and although the stagnation pressures were lower than those in group E, the shock pattern at separation was symmetrical, and the curves for the pressure variation in the region of reversed flow were all the same shape and did not cross each other, (see fig 57).

All the tests in group F were preliminary, carried out with hard paper gaskets fitted between the nozzle blocks and the glass windows. It was not possible to cut these gaskets so well as those which were used in all the tests subsequent to test 85. The differences between the results in group F and E therefore, demonstrated that changes in the material and fit of the thin gaskets between the glass and nozzle blocks altered the stagnation pressure at which symmetrical separation was obtained.

The shock waves associated with the separations discussed in this section originated well inside the boundary layers (see figs 37&58) and were very similar in appearance to those observed by Chapman et al[8] in turbulent separations over steps and wedges. The pressure variations

downstream of the onset point were also very similar.

The boundary layer Reynolds numbers at the onset point, calculated from the free stream flow conditions and the length along the axis of the nozzle from the throat plane to the onset point have been tabulated in table 19. For Reynolds numbers above 1.6×10^6 (group E) the separation phenomenon showed all the characteristics of the steady separation of a turbulent boundary layer. At lower Reynolds numbers with the exception of group F separation of a different type of boundary layer occurred.

TABLE 21

The Pressure, Mach and Reynolds numbers at the onset points for tests in group G, nominal stagnation pressure 87 p.s.i.a.

Test	Stagnation pressure Po p.s.i.a.	Stagnation temperature T_o° A.	Atm pressure p_a p.s.i.a.	Peak pressure p p.s.i.a.	Onset pressure po p.s.i.a.	Dist of onset point from the exit plane cm.	$\frac{po}{p_p}$	$\frac{po}{p_a}$	Reynolds number x 10^{-6}	Mach number
Turbulent separation on both walls of the nozzle.										
109	86.9	292.5	14.67	13.67	6.29	1.983	0.460	0.429	1.27	2.271
111	87.3	292.5	14.66	13.65	6.29	1.973	0.461	0.429	1.30	2.275
113	86.6	292.5	14.55	13.62	6.32	2.015	0.460	0.435	1.24	2.265
114	86.4	292.7	14.66	13.62	6.26	1.989	0.460	0.427	1.27	2.270
115	84.3	291.3	14.62	13.59	6.31	2.070	0.464	0.432	1.2	2.253
116	83.1	291.0	14.62	13.57	6.34	2.117	0.467	0.434	1.17	2.241
Turbulent separation on one wall transitional on the other.										
164	82.4	292.6	14.79		6.92-7.19	2.261-2.423	0.460-0.476		1.13-1.19	2.203-2.244
165	83.9	293.6	14.79		6.66-6.83	2.261-2.108	0.450-0.462		1.11-1.17	2.203-2.244
166	83.4	293.4	14.73		6.74-6.76	2.108-2.261	0.457-0.459		1.10-1.17	2.203-2.244
168	87.2	290.0	14.81		6.63	2.108	0.447		1.24	≈2.244
193	82.6	289.0	14.51		6.67-7.20	2.108-2.261	0.460-0.496		1.12-1.18	2.203-2.244
202	83.9	288.7	14.78		6.80-7.08	2.108-2.261	0.460-0.476		1.13-1.19	2.203-2.244
Transition very close to separation on both walls of the nozzle.										
112	86.2	292.1	14.66		6.53	2.108	0.445		1.2	2.244
171	84.0	293.1	14.76		6.54	2.108	0.446		1.17	≈2.244

SECTION 9.2.2.

The Results for Assymmetric Separation.

In the previous section the shock system and the flow in the vicinity of separation became assymmetric in some of the tests in group E, at a nominal stagnation pressure of 100 p.s.i.a. when the boundary layer Reynolds number was approximately 1.6×10^6. On further reduction of the pressure the type of separation obtained in the nozzle changed, and will be discussed in this section with reference to the tests in groups G to M at nominal stagnation pressures of 87, 80, 73, 66, 59, 52 and 45 p.s.i.a. respectively.

The results obtained in the tests of group G have been tabulated in table 21 and the different types of separation observed in this group will be discussed with reference to Figs 59 and 63.

Examination of the flow photographs presented in Fig 59 indicates that three different types of separation took place within group G. In tests 113 and 116 the shock waves associated with separation of the boundary layers on both the top and bottom walls of the nozzle were strong and similar to those in fig 58 for the tests at higher pressure. Similarly the wall pressures were found to be steady, the

(Continued on page 181.)

(a)

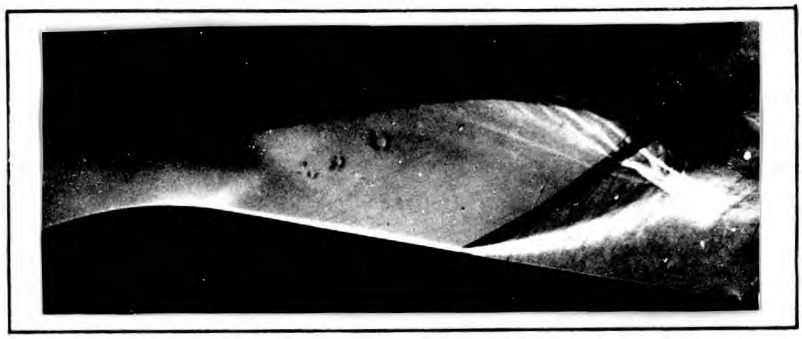

Test 171. $P_o = 84.0$ p.s.i.a. Schlieren photograph

(b)

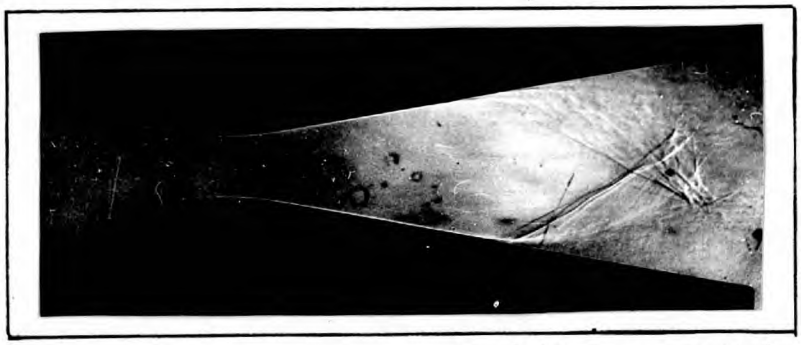

Test 193. $P_o = 82.6$ p.s.i.a. Point of laminar separation Point of transition
Shadowgraph (taken with white light)

(c)

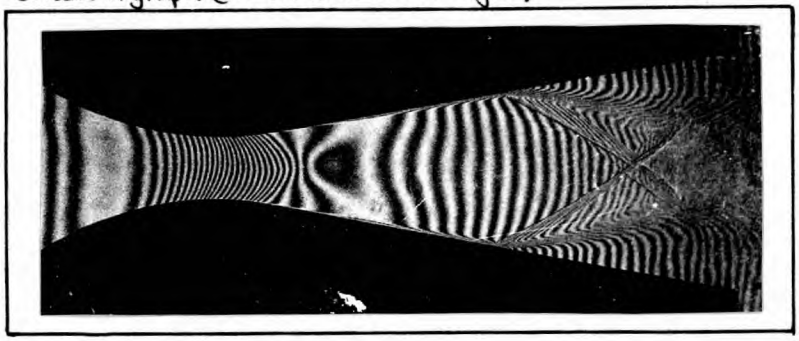

Test. 113 $P_o = 86.1$ p.s.i.a. Interferogram

(d)

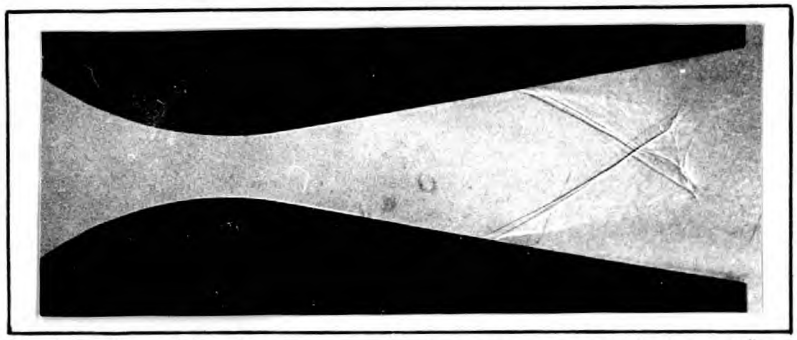

Test 116 $P_o = 83.1$ p.s.i.a. Shadowgraph (taken with green light)

Fig 59. Photographs of the flow in Group G.
nominal stagnation pressure 87.0 p.s.i.a.

(a).

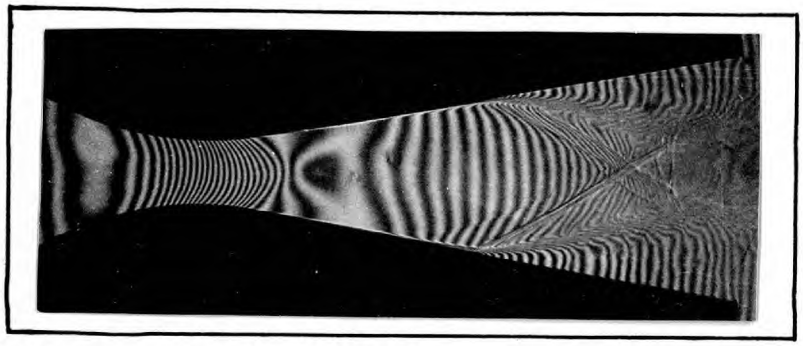

Group H. Test 129 P_o = 81·3 p.s.i.a. Interferogram

(b)

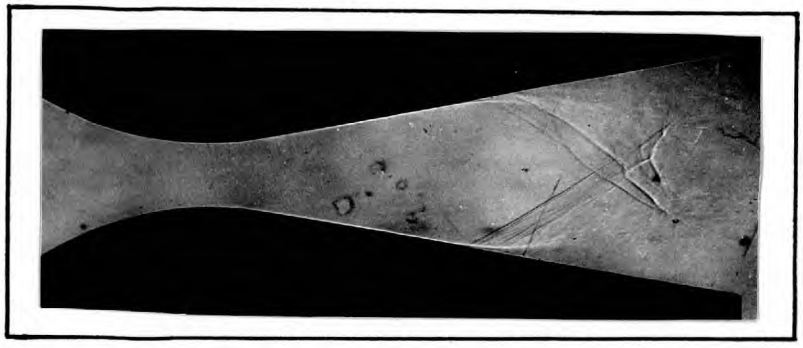

Group H. Test 190 P_o = 80·3 p.s.i.a. Shadowgraph (taken with white light)

(c)

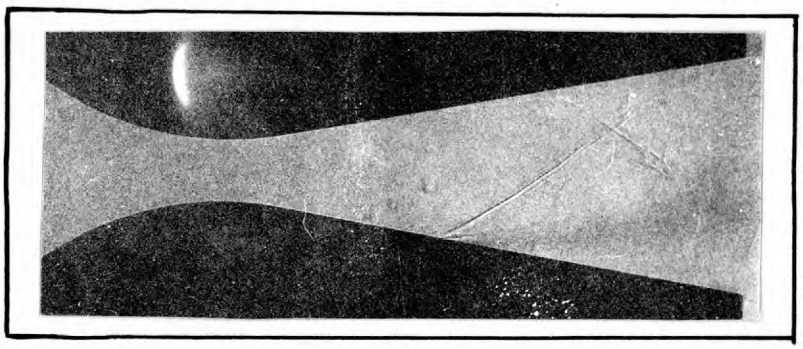

Group I Test 89 P_o = 73·9 p.s.i.a. Shadowgraph (taken with green light)

(d)

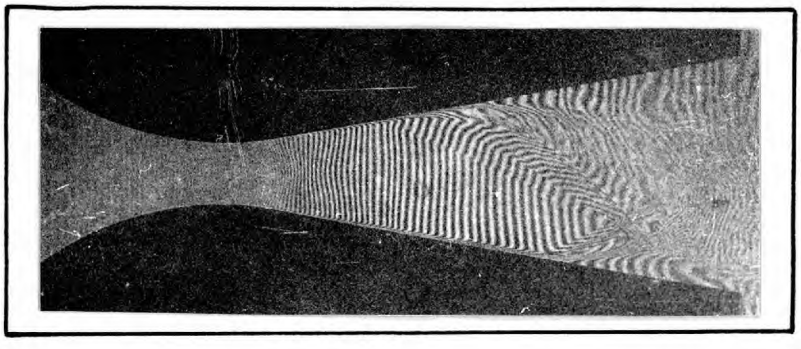

Group I Test 92 P_o = 73·5 p.s.i.a. Interferogram

Fig 60 Photographs of the flow in Groups H and I nominal stagnation pressures 80·0 & 73·0 p.s.i.a. respectively.

(a) Group J
Shadowgraph
(taken with white light)
Test 192
P_o = 65.2 p.s.i.a

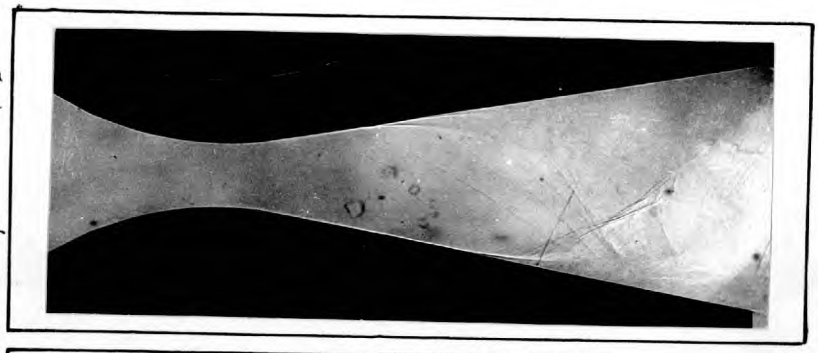

(b) Group J
Shadowgraph
(taken with green light)
Test 118
P_o = 65.2 ps.i.a.

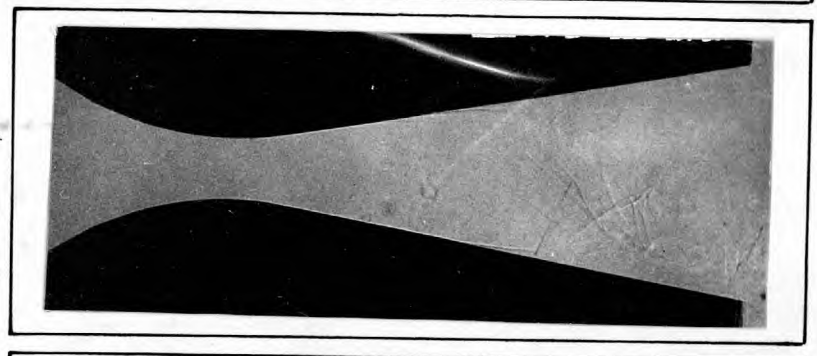

(c) Group K.
Shadowgraph
(taken with green light)
Test 125
P_o = 57.3 p.s.i.a

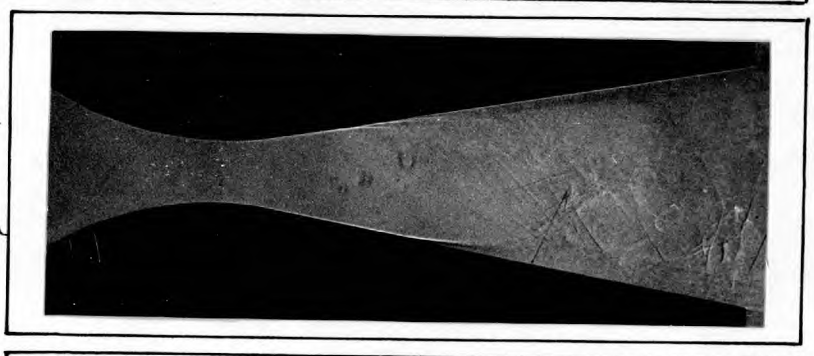

(d) Group K.
Interferogram
Test 124
P_o = 58.1 p.s.i.a

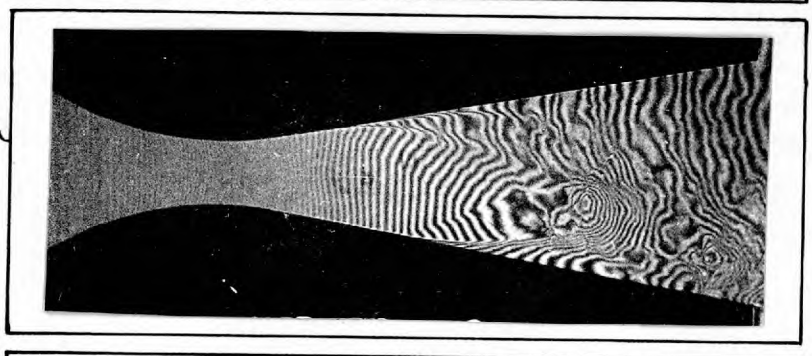

(e) Group K
Shadowgraph
(taken with white light)
Test 191
P_o = 59.5 p.s.i.a

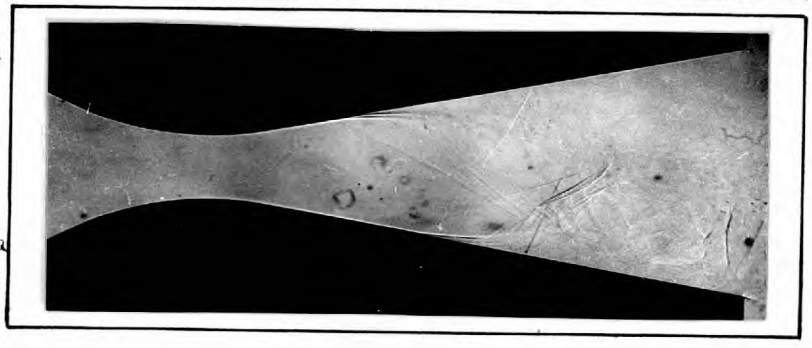

Fig 61. Photographs of the flow in Groups J + K nominal stagnation pressure 66.0 and 59.0 ps.i.a. respectively

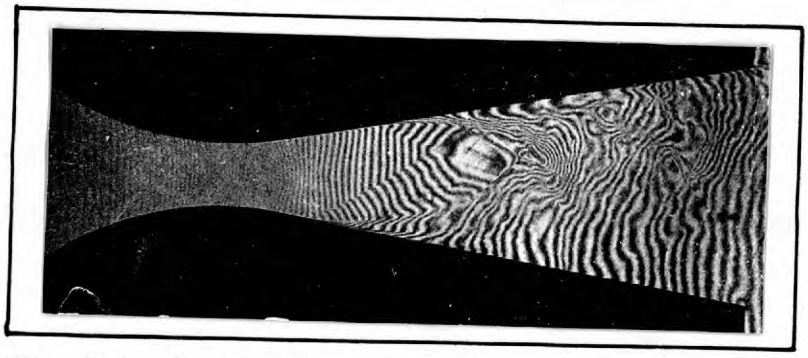

Group L. Test 97. P_o = 53·6 p.s.i.a. Interferogram

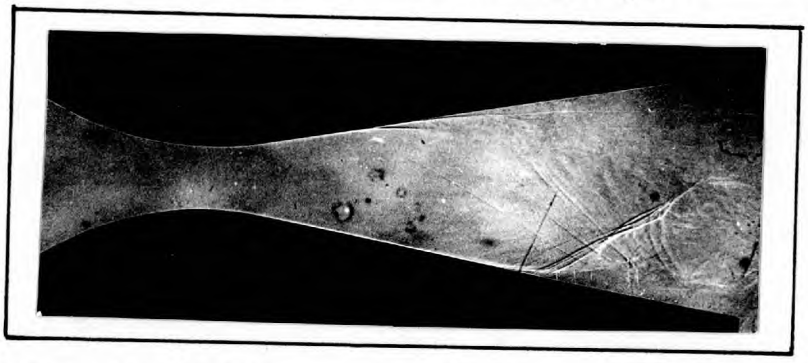

Group L Test 194 P_o = 53·3 p.s.i.a. Shadowgraph (taken with white light)

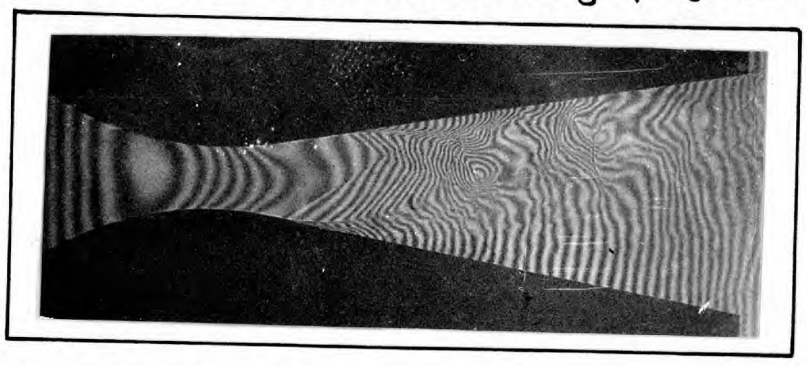

Group M Test 103 P_o = 46·1 p.s.i.a. Interferogram

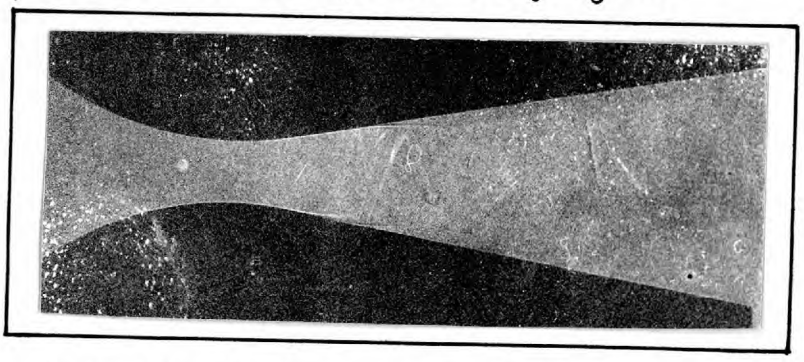

Group M Test 106. P_o = 46·0 p.s.i.a. Shadowgraph (taken with green light)

Fig 62 Photographs of the flow in Groups L and M nominal stagnation pressures 52·0 + 45·0 p.s.i.a. respectively

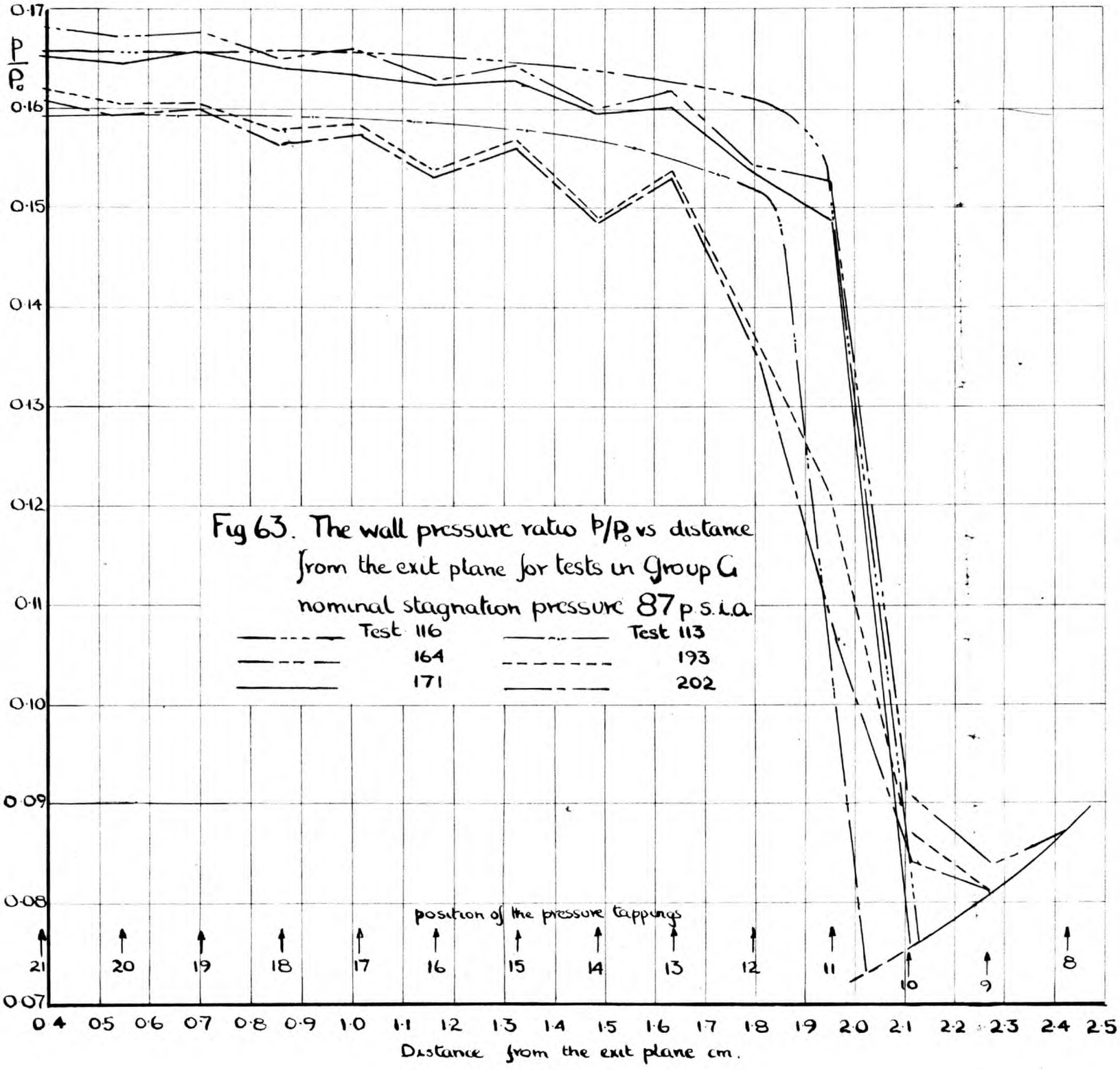

Fig 63. The wall pressure ratio P/P_0 vs distance from the exit plane for tests in Group G nominal stagnation pressure 87 p.s.i.a.

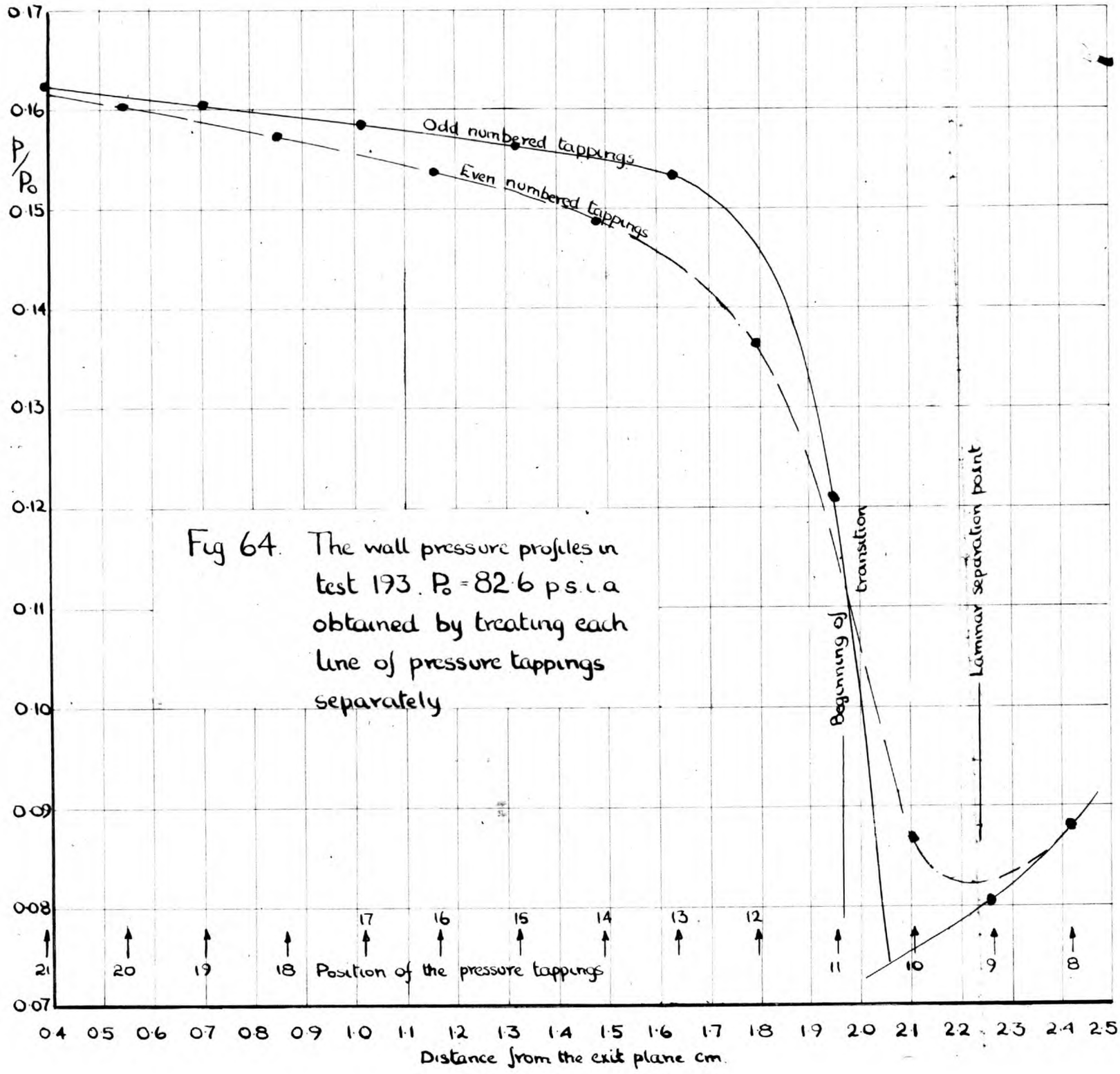

Fig 64. The wall pressure profiles in test 193. P_o = 82·6 p.s.i.a obtained by treating each line of pressure tappings separately

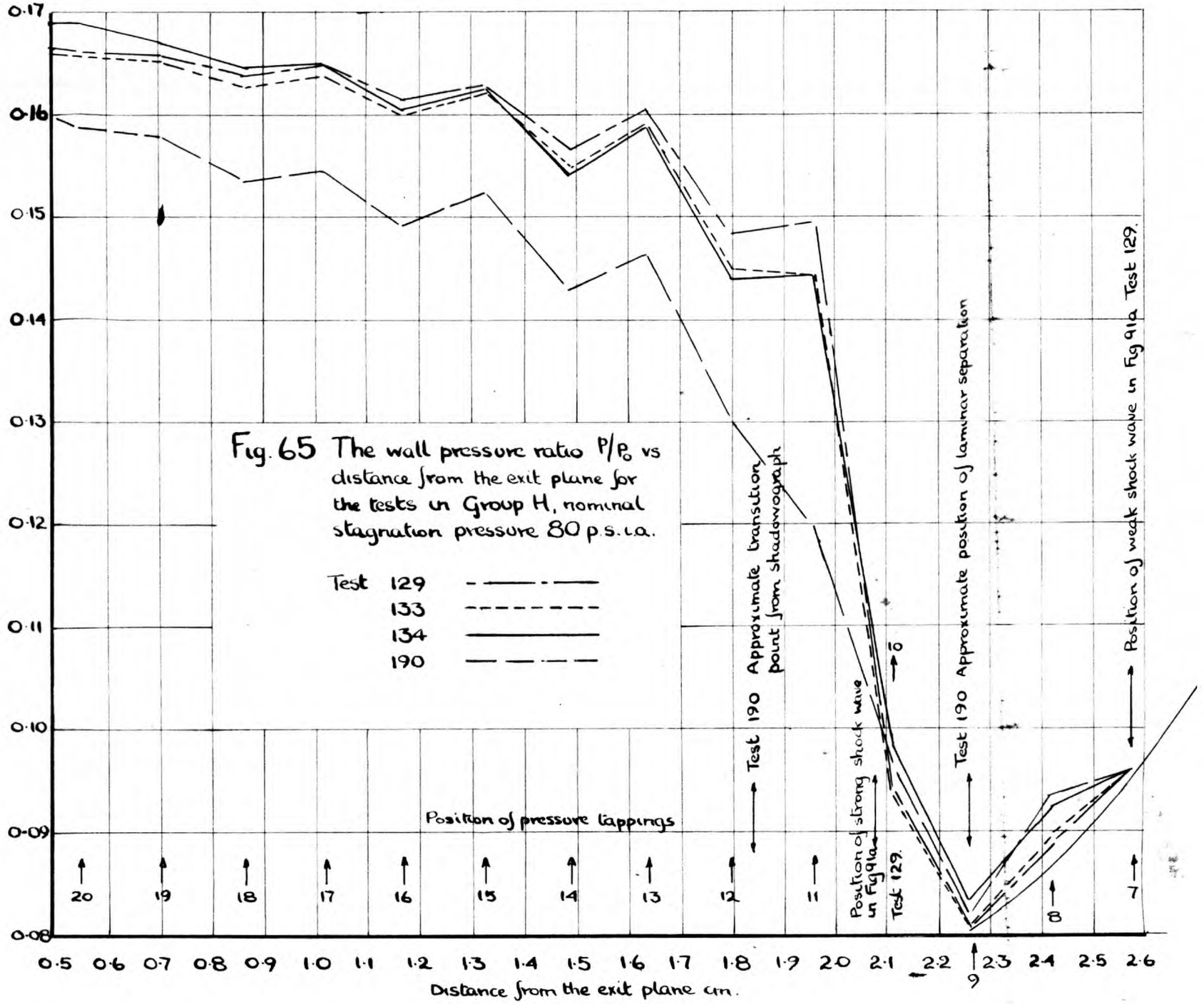

Fig. 65 The wall pressure ratio P/P_0 vs distance from the exit plane for the tests in Group H, nominal stagnation pressure 80 p.s.i.a.

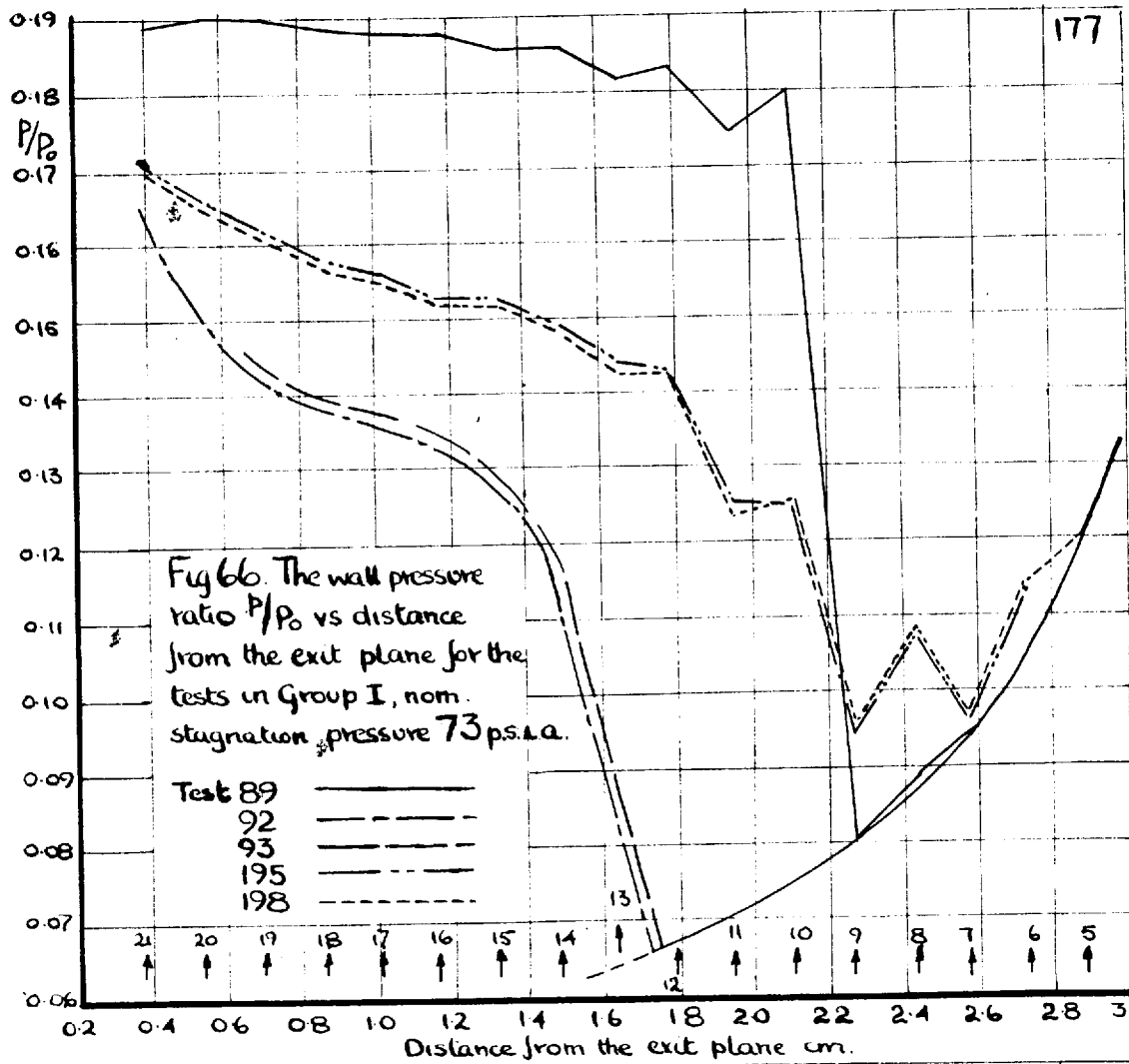

Fig 66. The wall pressure ratio P/P_0 vs distance from the exit plane for the tests in Group I, nom. stagnation pressure 73 p.s.i.a.

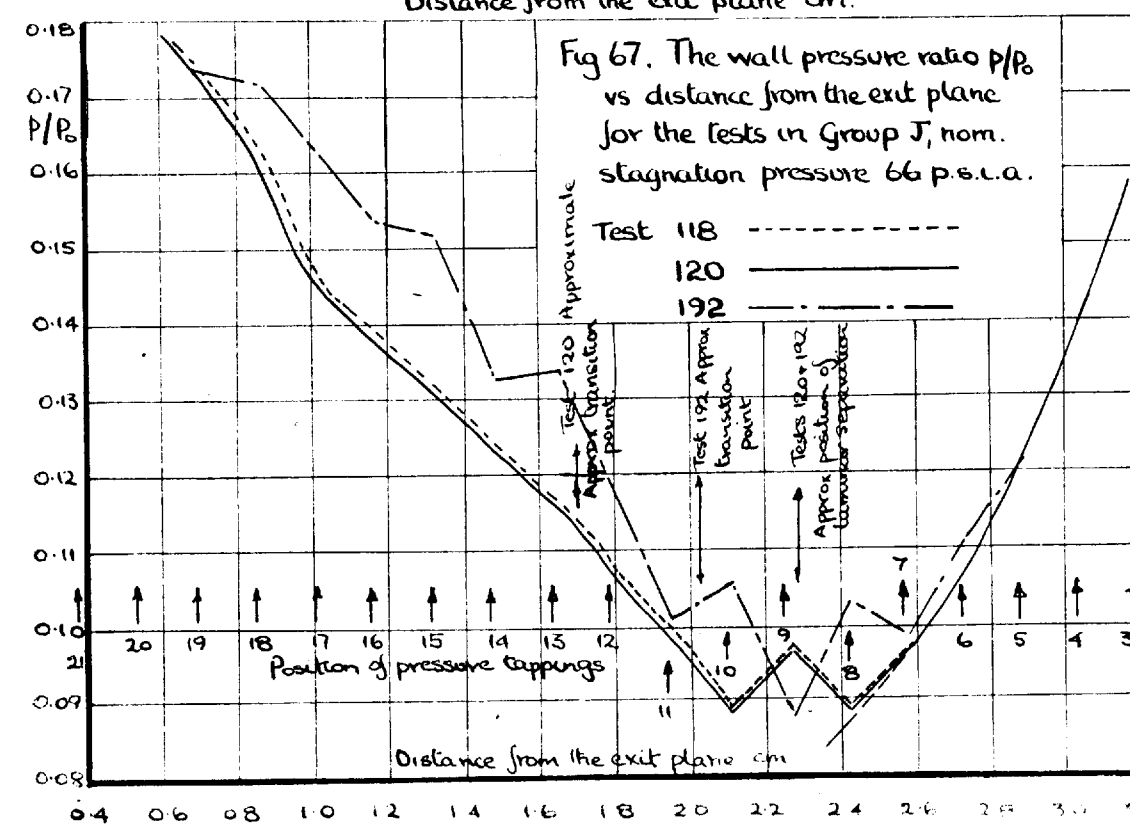

Fig 67. The wall pressure ratio P/P_0 vs distance from the exit plane for the tests in Group J, nom. stagnation pressure 66 p.s.i.a.

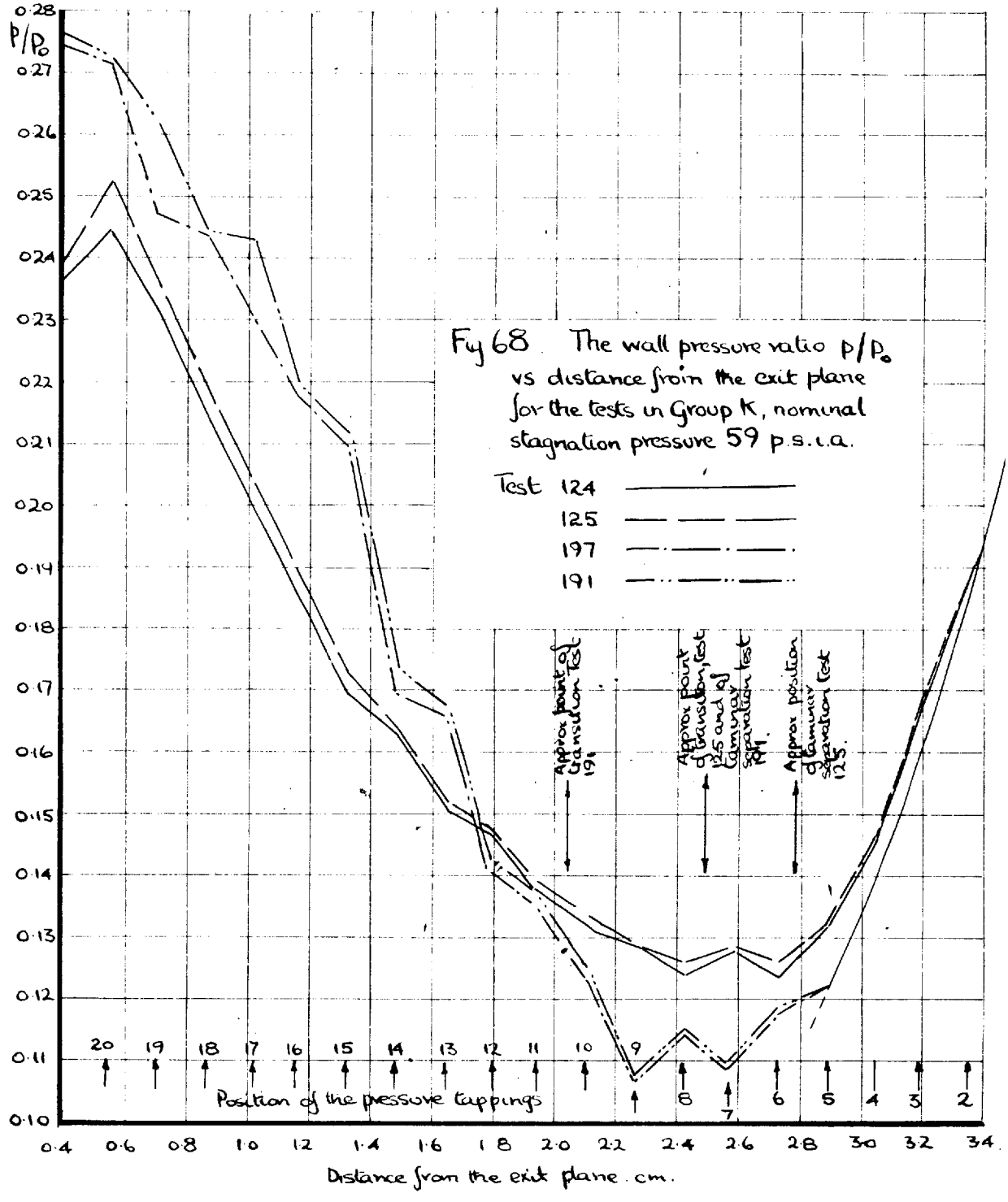

Fig 68 The wall pressure ratio p/p_0 vs distance from the exit plane for the tests in Group K, nominal stagnation pressure 59 p.s.i.a.

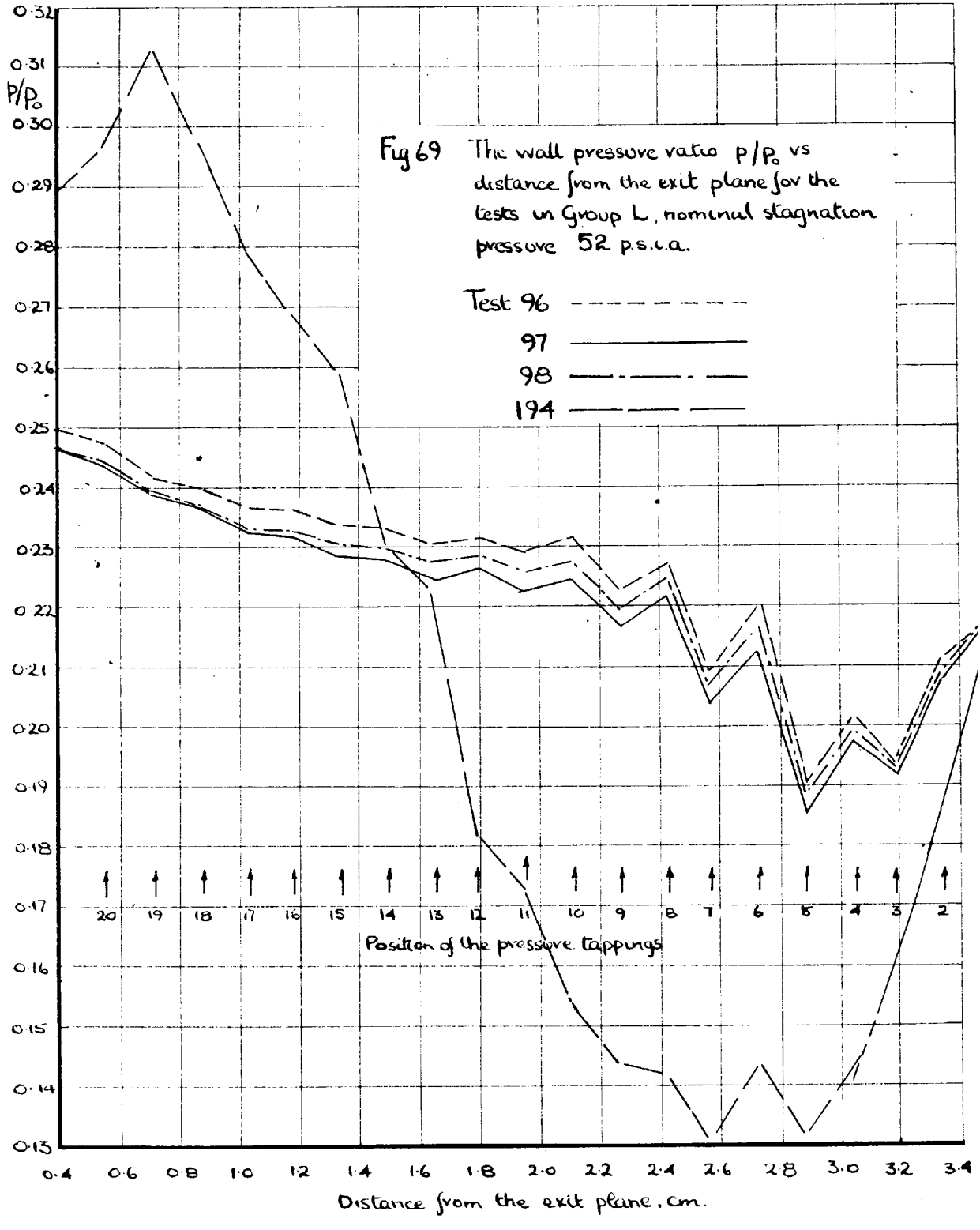

Fig 69 The wall pressure ratio p/p_o vs distance from the exit plane for the tests in Group L, nominal stagnation pressure 52 p.s.i.a.

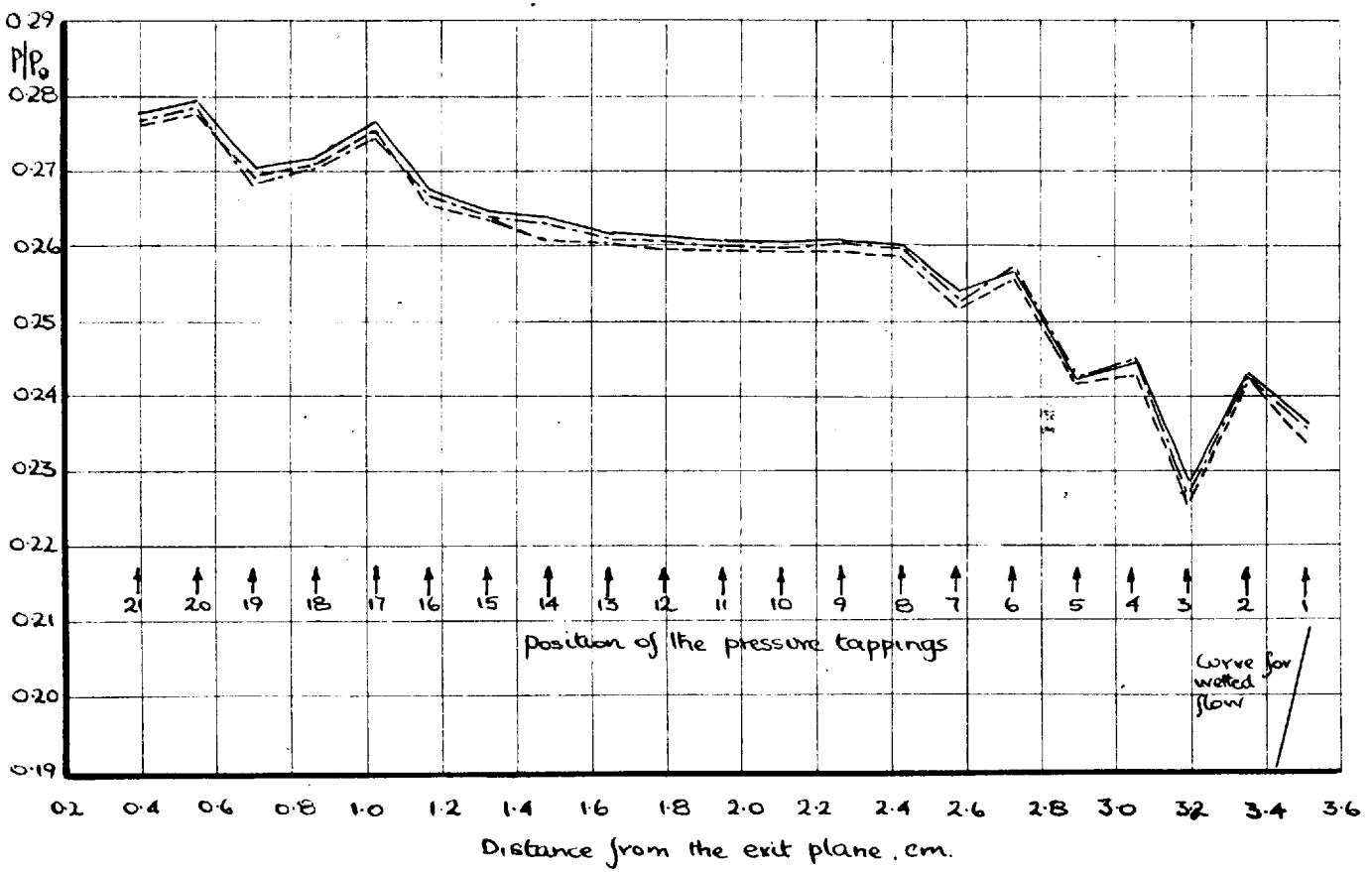

Fig 70 The wall pressure ratio p/P_0 vs distance from the exit plane for the tests in Group M, nominal stagnation pressure 45. p.s.i.a.

Test 103 - - - - - - - - -
105 —·—·—·—·—
106 ———————

compression of the boundary layer on the bottom wall rapid, and the variation of pressure along the bottom wall of the nozzle the same. Hence the boundary layers in tests 113 and 116 on both the top and bottom walls of the nozzle were turbulent before separation.

The onset pressure po and the ratio $\frac{po}{p_p}$ were in general below the values expected from the trend shown by the tests at higher stagnation pressures in the previous section. The reason for the reversal of the trend is not known but is probably due to separation taking place close to transition. As in the previous section the shock waves associated with separation appeared to be complex apparently consisting of more than one shock wave. For instance in fig 59d separation of the boundary layer appeared to take place by means of a compression fan.

Turbulent separations of the type discussed above took place when the Reynolds number of the boundary layer on the bottom wall was in the range $1.17 - 1.30 \times 10^6$. At slightly lower Reynolds numbers, $1.03 \sim 1.19 \times 10^6$, the wall pressure variation changed completely. For example in test 193, Po = 82.6 p.s.i.a., the shock system and the wall pressure variation associated with separation were different to that previously observed.

The wall pressure variations in tests 164 and 202 at stagnation pressures of 82.4 and 83.9 respectively, shown in fig 63 were the same as that in test 193, and it can be seen that the pressures measured at the even numbered pressure tappings were lower than those at the odd. The effect was reproducible and was not affected by changing the pressure lines to the manometer, from the even to the odd numbered tappings and vice versa. The manometer levels during these tests were steady and no hum or vibratory noise usually associated with an oscillating separation position was heard.

It can be seen from fig 24 that the pressure tappings were placed alternately on either side of the nozzle wall centreline, and that the odd numbered were nearest the observer when viewing the flow photographs in figs 59, 60, 61 and 62. Then if the separation position was not at the same distance from the exit plane across the complete breadth of the nozzle, the pressure variation recorded by the odd and even numbered holes would be different. For instance in test 193 two types of separation occur on the bottom wall, as in fig 59b a white line characteristic[80] of laminar separation can be seen moving gradually away from the wall upstream of a shock system characteristic of a turbulent separation which originates in the regions close to the wall.

By treating the corresponding wall pressure results obtained at the two lines of tappings separately in fig 64 two curves were obtained. With the odd numbered tappings the curve was the same as that obtained for turbulent separations at higher stagnation pressures. The curve obtained by using the even numbered holes had an initial gradual compression of the type associated with laminar separation, followed by a pressure rise characteristic of transition taking place in the separated layer. The points of laminar separation and beginning of transition as depicted by the wall pressure variation were in good agreement with the corresponding positions measured on the flow photograph.

The Schlieren photograph in fig 59a and the wall pressure variation in fig 63 for test 171, Po = 84.0 p.s.i.a. were representative of the third type of separation obtained in group G. Although the flow photograph indicated that there was some variation in separation position over the nozzle width, there was no evidence of laminar or transitional separation. The wall pressure rose rapidly initially in the same way as in the turbulent separations, but in the region of reversed flow the wall pressures were not steady. The separated jet however did not flap from one side of the nozzle divergence to the other as observed by Wilkie[28].

In all the tests in which a continuous curve for the wall pressure variation could not be drawn through all the results as in fig 64, approximate Reynolds numbers at the onset point were obtained by assuming that the onset point was between the tapping at which a pressure rise above the value expected for wetted flow was first recorded and the tapping immediately upstream of it. It can be seen from the results tabulated in table 21 that the Reynolds numbers at the onset point for turbulent separations were higher than those where transition took place downstream of separation.

Approximate values of the onset pressure were obtained in the same way as the Reynolds numbers, and have been tabulated in table 21. In general the values of the onset pressure and the ratio $\frac{p_o}{p_a}$ were higher, when part of the boundary layer was laminar at separation, than the corresponding values for turbulent separation.

With reference to fig 59a and 59b, it can be seen that separation of the boundary layer on the top wall of the nozzle was laminar and in both tests took place in two definite positions. As the distance from the throat to the separation position on both the top and bottom walls were approximately equal, the Reynolds numbers were also equal.

Therefore the presence of the pressure tappings on the bottom wall of the nozzle must cause transition from a laminar to a turbulent boundary layer to take place at a lower Reynolds number than on the top wall.

The wall pressure variations measured during the tests in group H have been drawn in fig 65. As in the previous group the pressures measured at the even numbered pressure tappings were lower than those at the odd. However in this group of tests the boundary layer was laminar at separation across the whole breadth of the bottom wall, since the pressure rose gradually initially at both lines of pressure tappings and a white line characteristic of laminar separation was present on the flow photographs, for example in fig 60b. Examination of fig 65 indicates that the wall pressure results in test 190 were below those in tests 129, 133 and 134. The difference arose from a change in the shape of the reversed flow region, as in the latter three tests of which the interferogram in fig 60a was an example, the axis of the separated jet was inclined towards the top wall of the nozzle while the flow photograph in fig 60b showed that it was inclined towardsneither wall in test 190.

A weak shock wave can be seen upstream of the stronger shock system on the interferogram in fig 60a obtained in

test 129. The intersection of the weak shock and the bottom wall has been drawn on fig 65 together with that of the stronger shock system, where it can be seen that the former was close to the onset point and the latter to the steep pressure rise associated with transition. The weak shock wave did not appear when the boundary layer was turbulent before separation. It did not appear in the shadowographs of the flow, as sensitivity of the shadowographic method was not high enough, but it could be detected by the Schlieren method, for instance in fig 59a it can be seen on the top wall as the beginning of a compression fan.

Approximate values of the pressure and Reynolds number at the onset point were determined in the same way as in the previous groups. The results for the tests in group H and those in subsequent groups have been tabulated in table 22. The Reynolds numbers at the onset point in group H were generally below those in the previous groups and the values of the onset pressure po and the ratio $\frac{p_o}{p_a}$ greater.

It can be seen from the wall pressure results illustrated in fig 66 that a series of widely different flow patterns were obtained for the tests in group I at nominal stagnation pressure 73 p.s.i.a. The results for tests 195 and 198 were consistent with the hypothesis of laminar separation

TABLE 22.

The Pressure, Mach & Reynolds numbers at the onset points for the tests in Groups H - M, nominal stagnation pressure 80 - 45 p.s.i.a.

Test	Stagnation pressure Po p.s.i.a.	Stagnation temperature T_o °A.	Position of onset point between holes:- or cm from the exitplane	Onset pressure po p.s.i.a.	Atm pressure pa p.s.i.a.	$\frac{po}{pa}$ or po/p_a	po/p_p	Reynolds number x 10^{-6}	Mach No.	Separated jet flowing in contact with bottom wall
Group H. Nominal stagnation pressure 80 p.s.i.a.										
129	81.3	293.8	7 & 8	7.80-7.23	14.60	0.535-0.495		0.963-1.01	2.11-2.15	No
133	82.0	290.9	7 & 8	7.87-7.31	14.66	0.537-0.499		0.944-0.992	2.11-2.15	No
134	80.4	290.9	7 & 8	7.71-7.43	14.66	0.526-0.507		0.967-1.02	2.11-2.15	No
190	80.3	285.7	7 & 8	7.72-7.51	14.63	0.527-0.513		0.940-0.989	2.11-2.15	No
Group I Nominal Stagnation pressure 73 p.s.i.a.										
89	73.9	274.8	7 & 8	7.26-6.58	14.77	0.492-0.445		0.947-1.00	2.11 2.15	No
92	73.5	283.4	1.707	4.75	14.76	0.322	0.479	1.21	2.32	Yes
93	72.6	281.3	1.716	4.74	14.76	0.321	0.483	1.20	2.32	Yes
195	74.9	283.1	5 & 6	9.15-8.49	14.57	0.628-0.582		0.777-0.853	1.97 2.04	No
198	75.1	281.1	5 & 6	9.16-8.53	14.57	0.629-0.585		0.795-0.865	1.97 2.04	No
Group J Nominal Stagnation pressure 66 p.s.i.a.										
118	65.2	283.8	7 & 8	6.29-5.76	14.62	0.430-0.394		0.809-0.856	2.11 2.15	Yes
120	65.5	284.8	7 & 8	6.34-5.77	14.61	0.434-0.395		0.785-0.848	2.11 2.15	Yes
192	65.4	283.3	5 & 6	7.90-6.93	14.62	0.540-0.474		0.682-0.749	1.97 2.04	Yes

Group K.	Nominal stagnation pressure 59 p.s.i.a.							
124	58.1	287.7	2 & 3	11.06-9.55	14.57	0.759-0.655	0.432-0.506	1.69-1.79	No
125	57.3	286.9	2 & 3	10.90-9.43	14.57	0.748-0.647	0.424-0.500	1.69-1.79	No
191	59.5	285.8	5 & 6	7.28-7.07	14.57	0.500-0.486	0.595-0.651	1.97-2.04	Yes
197	59.5	286.7	5 & 6	7.25-6.99	14.62	0.492-0.487	0.613-0.670	1.97-2.04	Yes
Group L.	Nominal Stagration pressure 52 p.s.i.a.							
96	52.7	286.4	1 & 2	11.56-11.13	14.71	0.786-0.757	0.323-0.391	1.59 1.69	No
97	53.6	291.2	1 & 2	11.72-11.11	14.79	0.793-0.752	0.321-0.388	1.59 1.69	No
98	53.3	291.3	1 & 2	11.61-11.11	14.79	0.786-0.751	0.319-0.389	1.59 1.69	No
194	53.3	283.8	4 & 5	7.60-6.99	14.57	0.522-0.480	0.522-0.557	1.86 1.97	Yes
Group M.	Nominal stagnation pressure 45 p.s.i.a.								
			upstream of						
103	46.1	-	1						
105	46.1	-	1	Separation not in region					
106	46.0	-	1	of pressure holes.					

followed by transition in the separated boundary layer. However in these two tests the wall pressures were higher at the even numbered holes than at the odd, the converse being true in the tests in the previcus groups. The wall pressure results and the flow photograph for test 89 in fig 60c showed no laminar characteristics, they were however similar to those obtained in test 171, group G, but unlike this test the wall pressures in the region of reversed flow were steady. In trying to repeat test 89, the flow separated from the top wall before it did on the bottom (fig 60d) with the result that one edge of the separated jet flowed very close to the bottom wall.

In the case of tests 195 and 198 where the axis of separated jet was not inclined appreciably towards either wall, the results for onset pressure were consistent with the trend shown by the tests in the previous groups. In the other tests the results showed greater similarity to those obtained for turbulent separation.

The wall pressure results obtained in the tests in groups J.K.L and M at nominal stagnation pressures of 66, 59, 52 and 45 p.s.i.a. respectively have been presented in figs 67, 68,69 and 70 and the flow photographs in figs 61 and 62.

In groups J and K separation was laminar with transition

downstream. Separation of the top boundary layer in the tests in group J took place before that on the bottom and consequently the separated jet flowed very close to the bottom wall. In a test 192 the flow along the bottom wall was rapid as indicated by the presence of the white line at the exit. The flow of the reversed stream was therefore restricted and consequently the ratio $\frac{po}{pa}$ was lower than the values obtained in subsequent tests when there was no restriction by the separated jet.

The results obtained, for onset pressure and the ratio po/pa during the tests in group K also depended on whether the separated jet flowed in contact with the bottom wall or not. In test 191 for instance it was, as indicated by the presence of the white line at the end of the wall. As in the tests at higher pressure the onset pressure was lower in those where the separated jet flowed in contact with the bottom wall.

The wall pressure results for the tests in the groups L and M show that separation was completely laminar except in the case of test 194, where the separated jet flowed along the bottom wall. The onset pressure results were consistent with those obtained in the other tests where the separated jet did not restrict the flow of the reversed stream.

Fig 71. The pressure ratio p_o/p_a vs Mach number for the tests in groups H–M, nominal stagnation pressure 80 – 45 p.s.i.a.

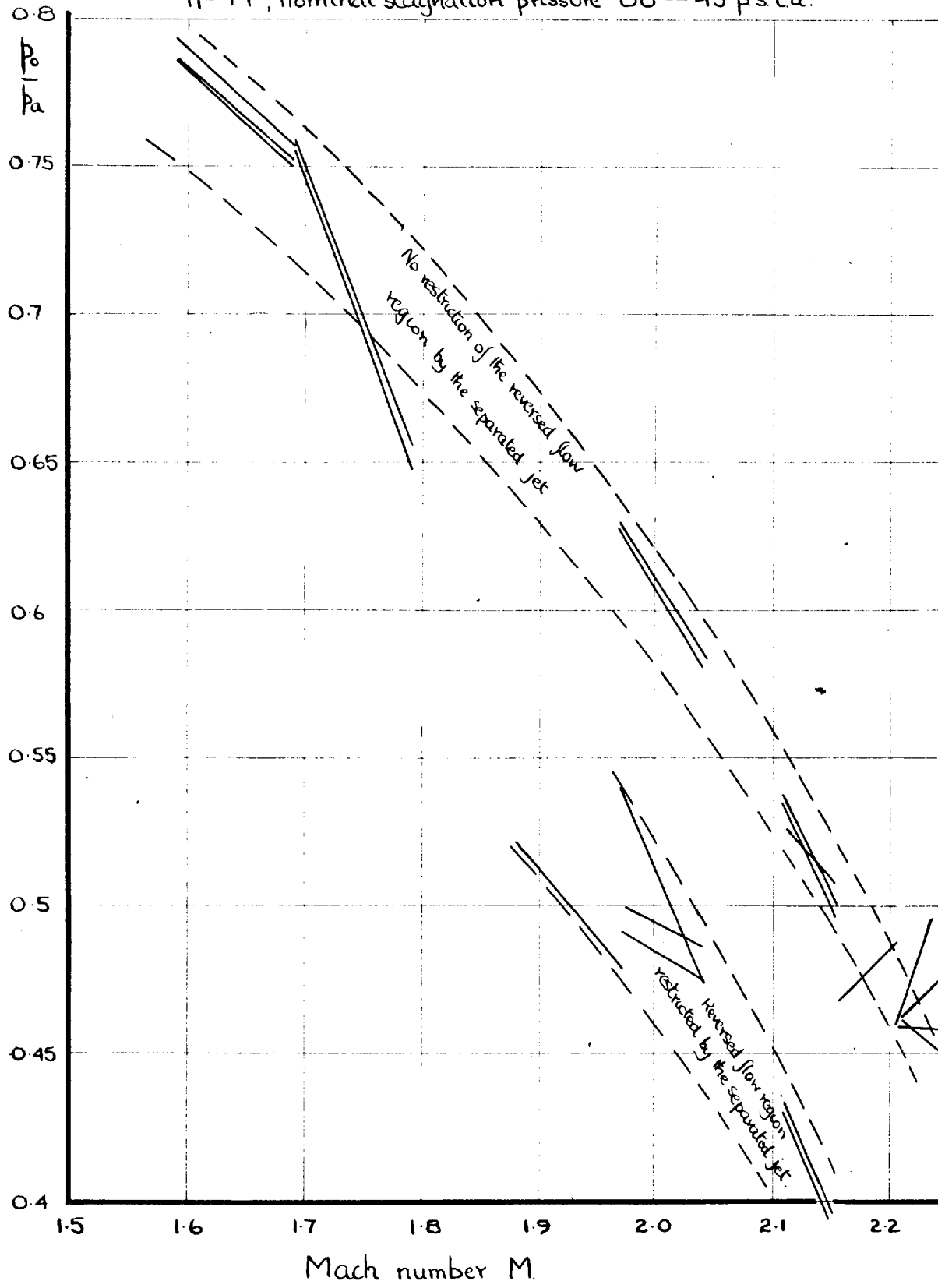

It can also be seen from the flow photographs and wall pressure results, that even when separation was completely laminar, the position of separation varied across the breadth of the nozzle.

The effect of the separated jet in restricting the flow of the reversed stream can be clearly seen in fig 71, where the ratio $\frac{po}{pa}$ has been plotted against Mach number. The ratio $po/_{pa}$ and therefore the onset pressures were lower for those tests where the separated jet flowed close to the bottom wall of the nozzle.

9.2.3. The Effect of the Boundary Layer Trips on the Pressure Rise at Separation.

The tests described in this section were carried out on the nozzle with the boundary layer trips described in section 7.2.1. stuck onto the walls of the convergent section.

The wall pressures were measured and shadowographs obtained over the same stagnation pressure range as used in the previous two sections. As before they were divided into the groups A to M, the nominal pressure for each group being the same as before. The wall pressure results and the shadowographs obtained during this series of tests have been presented in fig 74 and in figs 72 and 73 respectively.

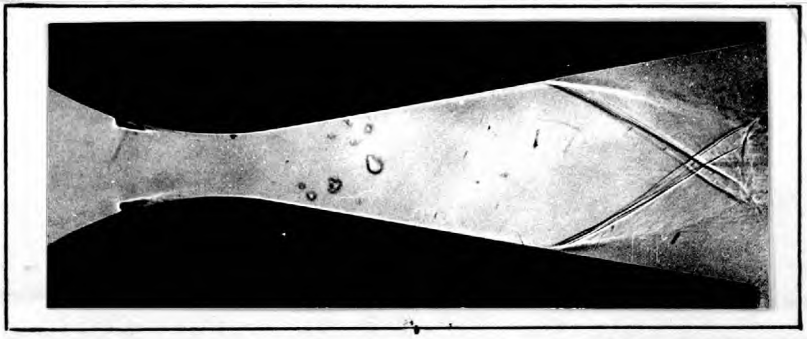

(a) Shadowgraph
Group E
Test 212
P_o = 101·1 p.s.i.a.

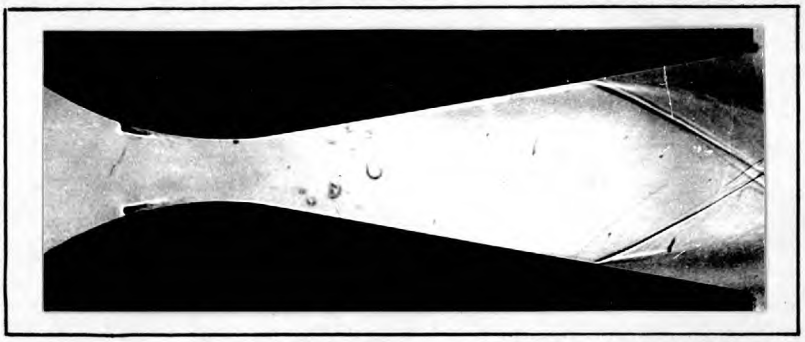

(b) Shadowgraph
Group D
Test 217
P_o = 113·7 p.s.i.a.

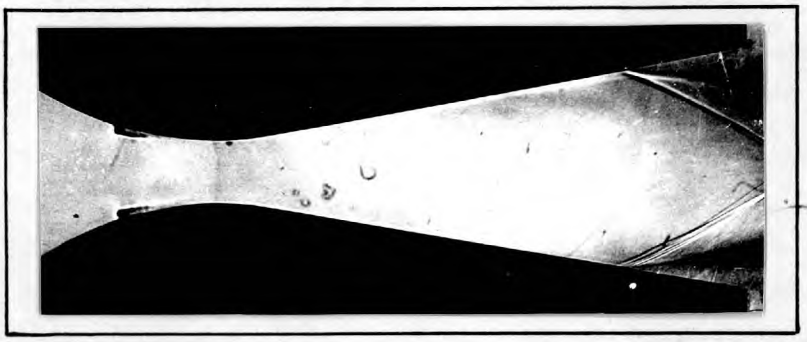

(c) Shadowgraph
Group C
Test 218
P_o = 126·7 p.s.i.a.

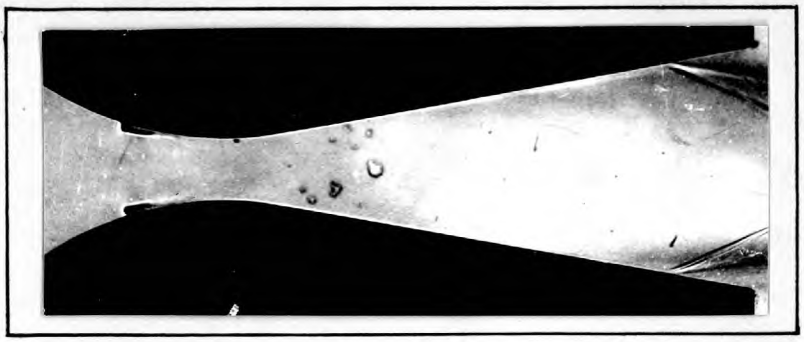

(d) Shadowgraph
Group B
Test 219
P_o = 139·1 p.s.i.a.

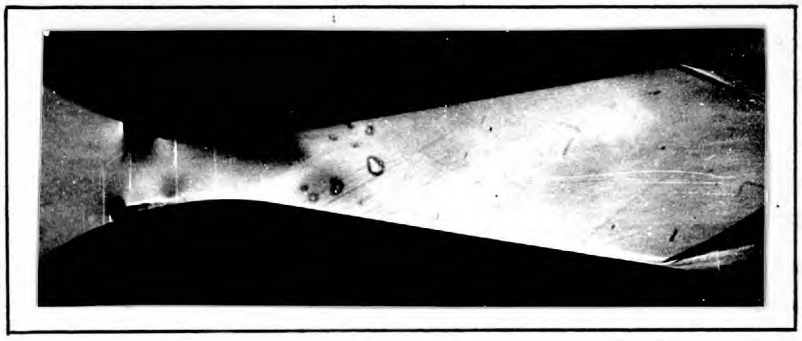

(e) Schlieren photograph
Group B
Test 222
P_o = 139·3 p.s.i.a.

Fig 72 Photographs of the flow for tests in Groups B – E nominal stagnation pressures in the range 140 – 100 p.s.i.a. with boundary layer trips fitted.

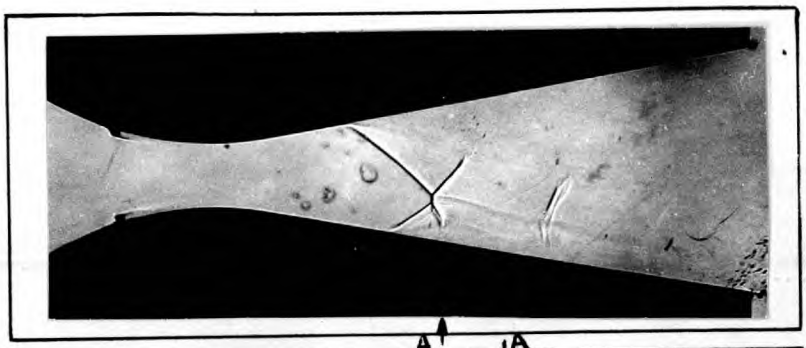

(a.) Shadowgraph
Group M.
Test 207
P_o = 45·8 p.s.i.a.

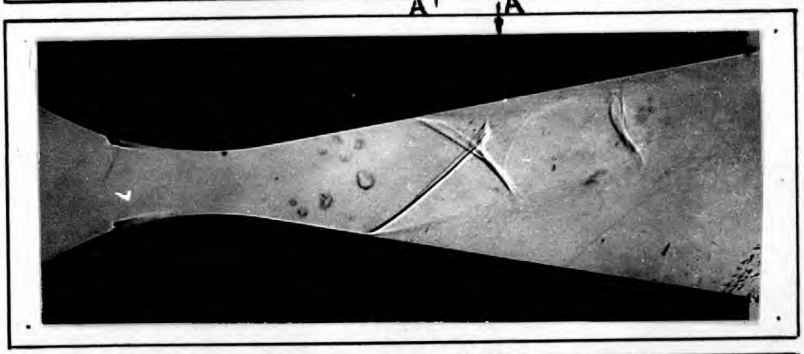

(b) Shadowgraph
Group L
Test 206
P_o = 54·1 p.s.i.a.

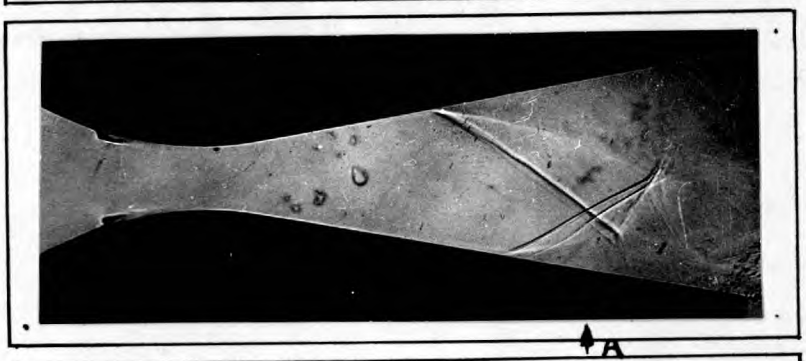

(c) Shadowgraph
Group I
Test 205
P_o = 74·2 p.s.i.a.

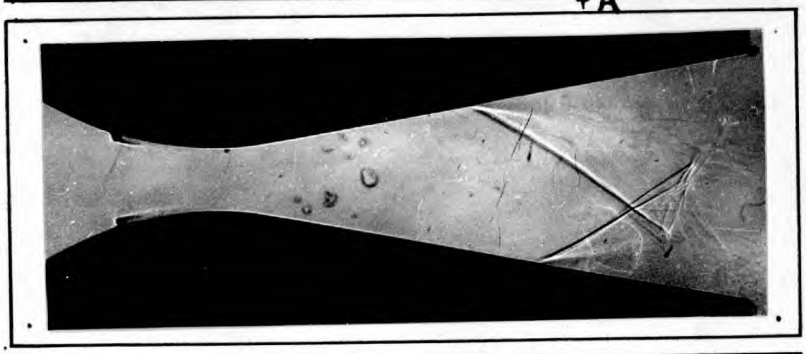

(d) Shadowgraph
Group H
Test 211
P_o = 81·0 p.s.i.a.

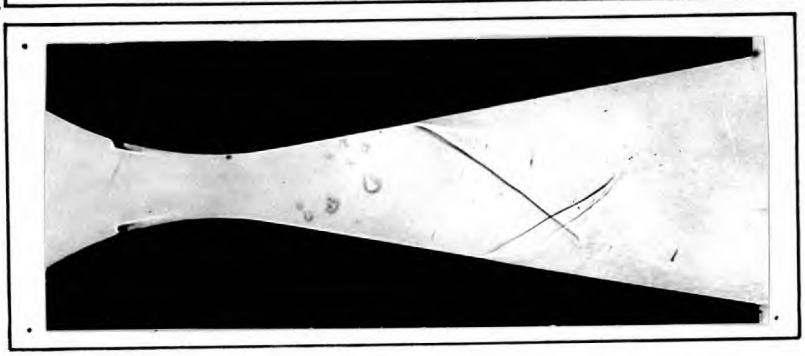

(e) Shadowgraph.
Group G
Test 208
P_o = 83·5 p.s.i.a.

Fig 73 Photographs of the flow for tests in Groups G → M, nominal stagnation pressures in the range 87 – 45 p.s.i.a. with boundary layer trips fitted.

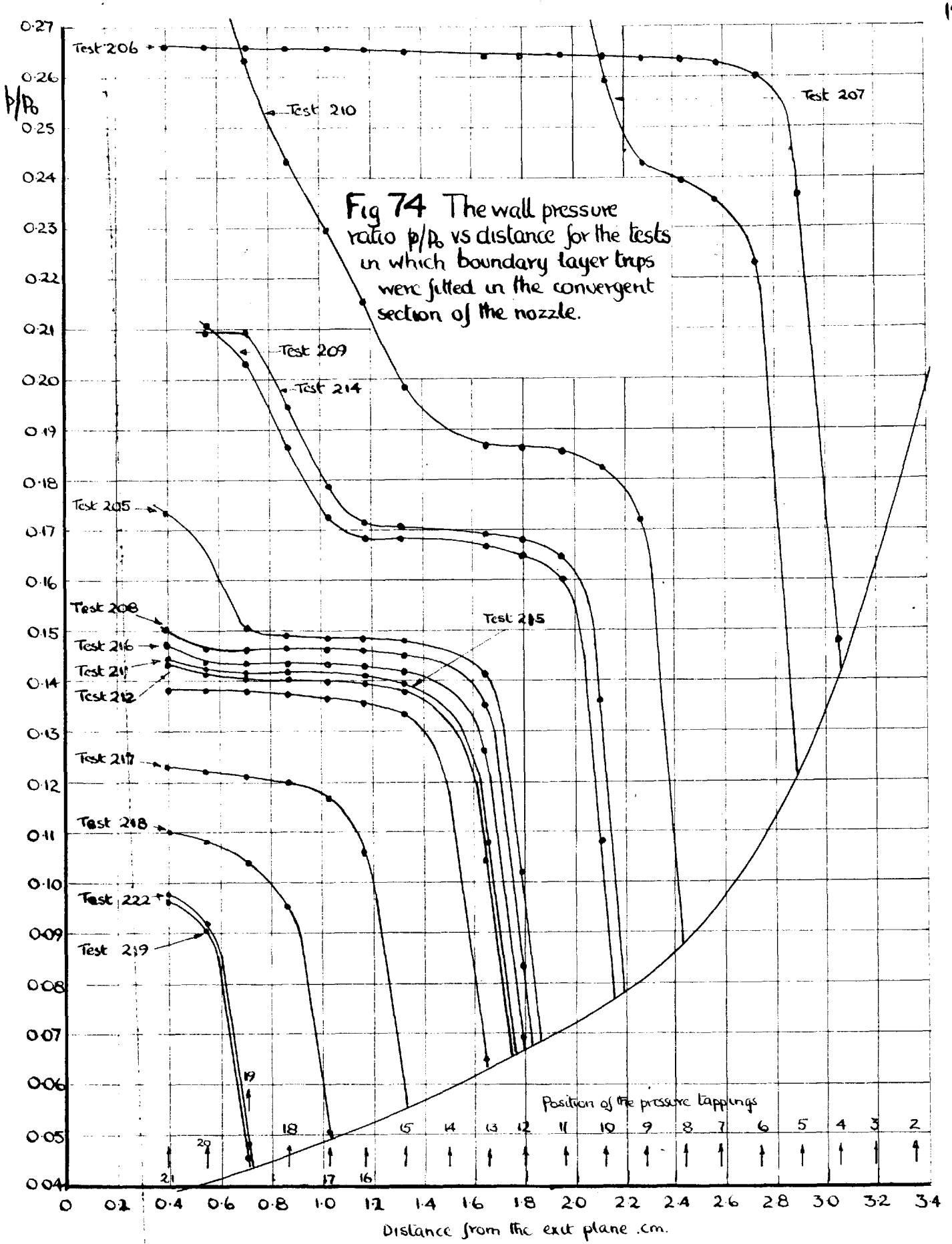

Fig 74 The wall pressure ratio p/p_0 vs distance for the tests in which boundary layer trips were fitted in the convergent section of the nozzle.

The results for onset pressure and position, the peak pressure ratio and the Mach numbers at the onset point have been tabulated in table 23.

Comparison of the shadowographs of the flow obtained during the tests in the groups A to E, show that they were very similar to those illustrated in fig 58 obtained when the trips were not fitted. As before the shock pattern at separation was symmetrical but the appearance of the boundary layers changed. Previously their presence was indicated by white lines separated from the walls, however when the trips were fitted the lines lost definition or disappeared entirely. As before in the tests without trips there was a steep rise in the wall pressure downstream of the onset point characteristic of turbulent separation.

The wall pressure ratios in the wetted region of flow tabulated in table 24, were lower than the corresponding values obtained when the trips were not fitted. The trips therefore caused the flow through the throat of the nozzle to be restricted by thickening the boundary layer on the walls. This had the effect of increasing the area ratio in the divergence of the nozzle.

The Mach number corresponding to the pressure ratio at the onset point was obtained by first determining the

TABLE 23.

Pressure ratios and Mach numbers at the onset point for tests with boundary layer trips fitted.

Test	Stagnation press. P_o p.s.i.a.	Atm. press. pa p.s.i.a.	Peak pressure p_p	Onset pressure po	Dist. of onset point from exit plane cm	p/p_o at onset point	po/pa	$\frac{po}{pp}$	Mach No
group B									
222	139.3	14.71	13.99	6.20	0.701	0.0445	0.421	0.443	2.376
219	139.1	14.72	13.92	6.19	0.699	0.0445	0.421	0.442	2.377
group C									
218	126.7	14.77	13.97	6.27	0.975	0.0495	0.425	0.449	2.356
group D									
217	113.7	14.72	13.84	6.34	1.310	0.0558	0.431	0.458	2.337
group E									
212	101.1	14.78	13.80	6.37	1.640	0.0630	0.431	0.462	2.330
group G									
216	82.0	14.73	11.96	5.57	1.820	0.0677	0.378	0.466	2.306
208	83.5	14.78	11.94	5.59	1.777	0.0669	0.378	0.467	2.314
group H									
215	81.1	14.73	11.47	5.29	1.702	0.0652	0.359	0.461	2.325
211	81.0	14.78	11.42	5.27	1.698	0.0651	0.357	0.462	2.326
group I									
205	74.2	14.80	10.93	5.08	1.850	0.0685	0.343	0.465	2.302

group J									
209	66.4	14.79	11.14	5.11	2.162	0.0770	0.345	0.459	2.240
213	65.4	14.78	11.25	5.11	2.200	0.0782	0.346	0.460	2.232
group K									
210	60.0	14.78	11.96	5.23	2.432	0.0871	0.354	0.467	2.164
group L									
206	54.1	14.81	14.26	7.63	3.057	0.1410	0.515	0.535	1.881
group M									
207	45.8	14.80	11.01	5.42	2.858	0.1184	0.316	0.493	1.987

TABLE 24

Wall Pressure Ratios for tests 220 218 and 212 with Boundary Layer Trips fitted and tests 163 152 & 146 without

Test	220	163	218	152	212	146
Group	A	A	C	C	E	E
Po p.s.i.a.	169.1	168.2	126.7	128.2	101.2	100.2
Pressure hole	p/Po	p/Po	p/Po	p/Po	p/Po	p/Po
1	0.2172	0.2207	0.2161	0.2187	0.2153	0.2220
2	0.1896	0.1922	0.1888	0.1920	0.1884	0.1932
3	0.1602	0.1616	0.1599	0.1618	0.1597	0.1625
4	0.1396	0.1411	0.1396	0.1417	0.1392	0.1411
5	0.1222	0.1231	0.1219	0.1235	-	0.1238
6	0.1064	0.1072	0.1067	0.1078	0.1062	0.1080
7	0.0957	0.0965	0.0959	0.0973	0.0955	0.0974
8	0.0872	0.0879	0.0876	0.0886	0.0868	0.0885
9	0.0812	-	0.0815	0.0821	0.0810	0.0820
10	0.0754	0.0762	0.0757	0.0769	0.0754	0.0767
11	0.0707	0.0709	0.0713	0.0719	0.0708	0.0715
12	0.0664	0.0671	0.0670	0.0680	0.0677	0.0679
13	0.0624	0.0627	0.0628	0.0635		
14	-	0.0604	-	0.0613	Sep.	Sep.
15	0.0556	0.0564	0.0562	0.0572		
16	0.0529	0.0529	0.0529	0.0536		
17	0.0493	0.0499	0.0502	0.0511		
18	0.0465	0.0470	Sep.	Sep.		
19	0.0438	0.0448				
20	0.0416	0.0419				
21	0.0393	0.0403				

distance from the exit plane at which the same pressure ratio occurred in the absence of trips, and then using this distance to obtain the Mach number from the curves presented in fig 53.

The Mach numbers measured at the onset point were higher than those for the tests in the corresponding groups without trips, consequently the onset pressures and the ratios $\frac{p_o}{p_{pa}}$ and $\frac{p_o}{p_{pp}}$ were lower.

The flow patterns and the wall pressure results obtained during the tests in the groups G to M, showed completely different characteristics to those described in section 9.2.2. Separation took place without any of the laminar characteristics shown before. Instead the pressure rose steeply at the onset point, and separation took place at the same distance from the exit plane across the complete breadth of the nozzle as in the tests at higher stagnation pressures with and without boundary layer trips.

Referring to fig 74 it can be seen that the wall pressure in the tests at low stagnation pressures in the region of reversed flow rose after an initial portion of almost constant pressure. The magnitude of the pressure rise decreased as the stagnation pressure increased until it disappeared in test 212.

The second pressure rise occurred in the neighbourhood of the shock system developed at the intersection of the shock waves associated with separation, like that indicated by point A in fig 73. In test 206 the pressure in the reversed flow region was unexpectedly constant, this was caused by the separated jet flowing close to the top wall of the nozzle, with the result that the shock system at the intersection did not affect the pressure on the bottom wall. In test 212 the flow downstream of the intersection did not reach the bottom wall before the exit plane was reached, consequently no pressure rise was recorded in the reversed flow region.

The onset pressure and the ratio p_o/p_p increased with Mach number in the same way as the values obtained at higher pressure and unlike those obtained when the trips were not fitted, were not dependent on whether the separated jet flowed in contact with the top or bottom wall of the nozzle. The value of $\frac{p_o}{p_a}$ however did depend on the position of the separated jet, there was also a sudden change in its magnitude associated with the appearance of the pressure rise in the reversed flow region.

From a comparison of the tests carried out with trips fitted in the nozzle, with those in the previous two sections,

it is apparent that boundary layer trips in the convergent section were able to promote turbulent separation in the divergent section

SECTION 9.3. Flow in the Region Reversed Flow

The density variation in the regions of reversed flow, between the boundary of the separated jet and the nozzle wall, were determined from the interferograms taken during tests 143, 146 and 152 at stagnation pressures of 99.2, 100.2 and 128.2 p.s.i.a. respectively. The interferograms are shown fig 37 and the results obtained in the wetted flow regions have already been described in section 9.1.

The flow patterns are presented in figs 75 - 78 These were obtained by measuring the density on a number traverses through the reversed flow region. The density was expressed as a ratio of the atmospheric density, and a series of points at constant increment obtained along the traverse. This was done for each traverse and then curves of constant density ratio drawn through the points as shown.

It is apparent from the flow patterns that a number of vorticies were present in the reversed flow region. In tests 143 and 146, at approximately the same stagnation pressure, three vorticies were present. The flow patterns were similar in that the centres of corresponding vorticies were in approximately the same position relative to the shock wave causing separation. The density ratios however were higher in test 143 than in 146. The difference

(Continued on page 206.)

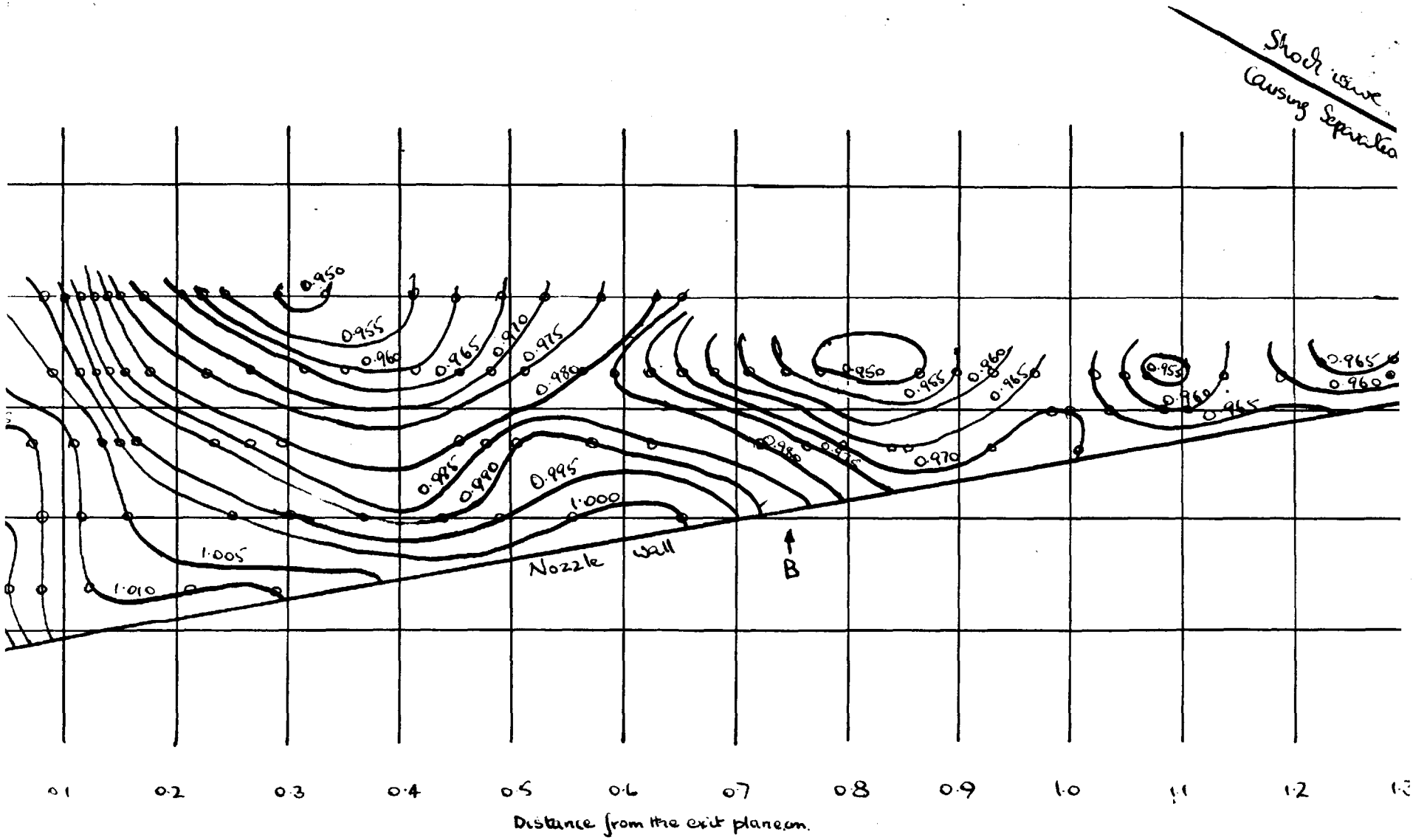

Fig 75. Density ratio profiles ρ/ρ_a for the bottom reverse flow region in test 143, $P_o = 99.2$ p.s.i.a.

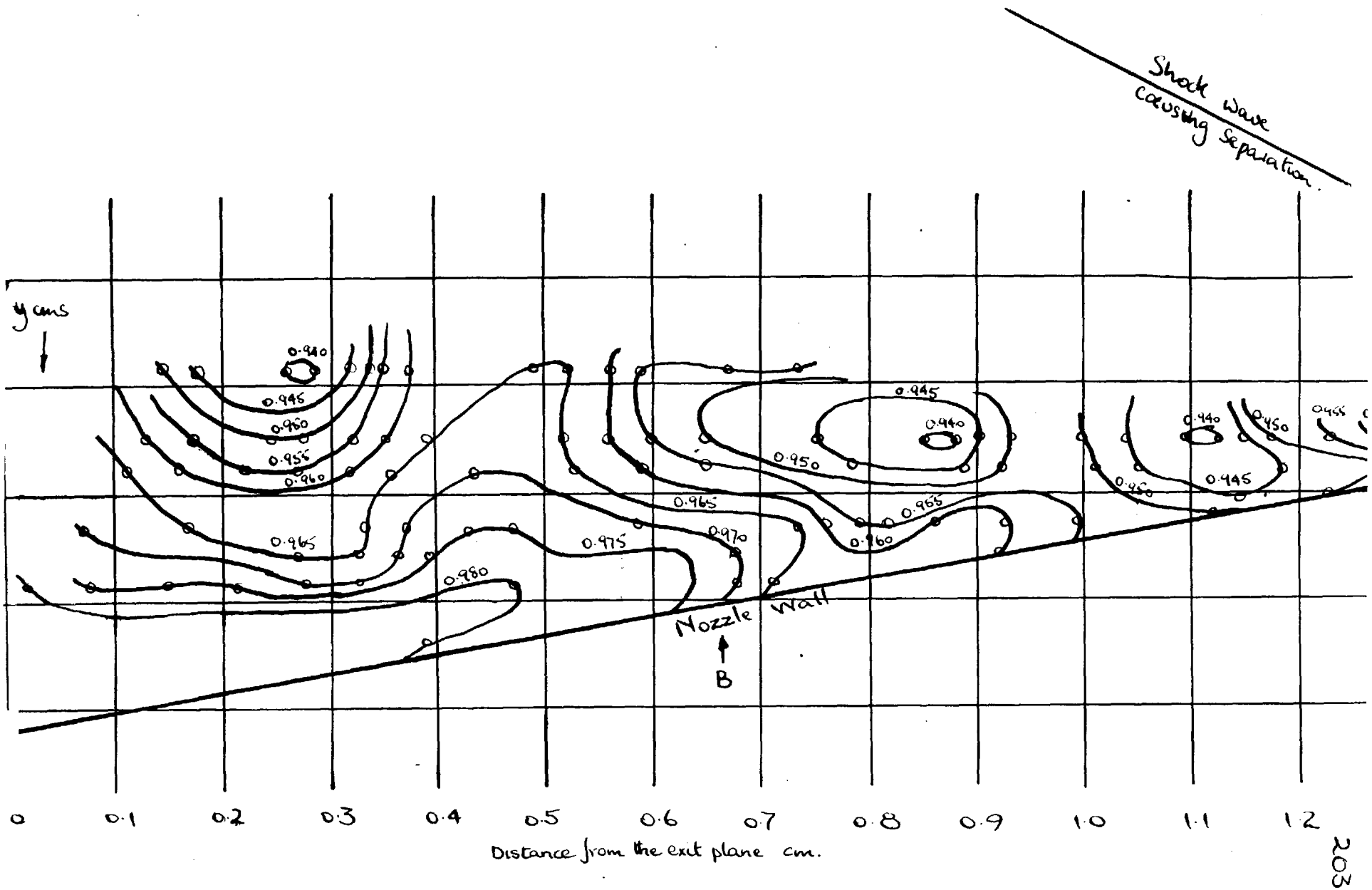

Fig 76 Density ratio profiles ρ/ρ_o for the bottom reverse flow region in test 146 P_o - 100·2 psia

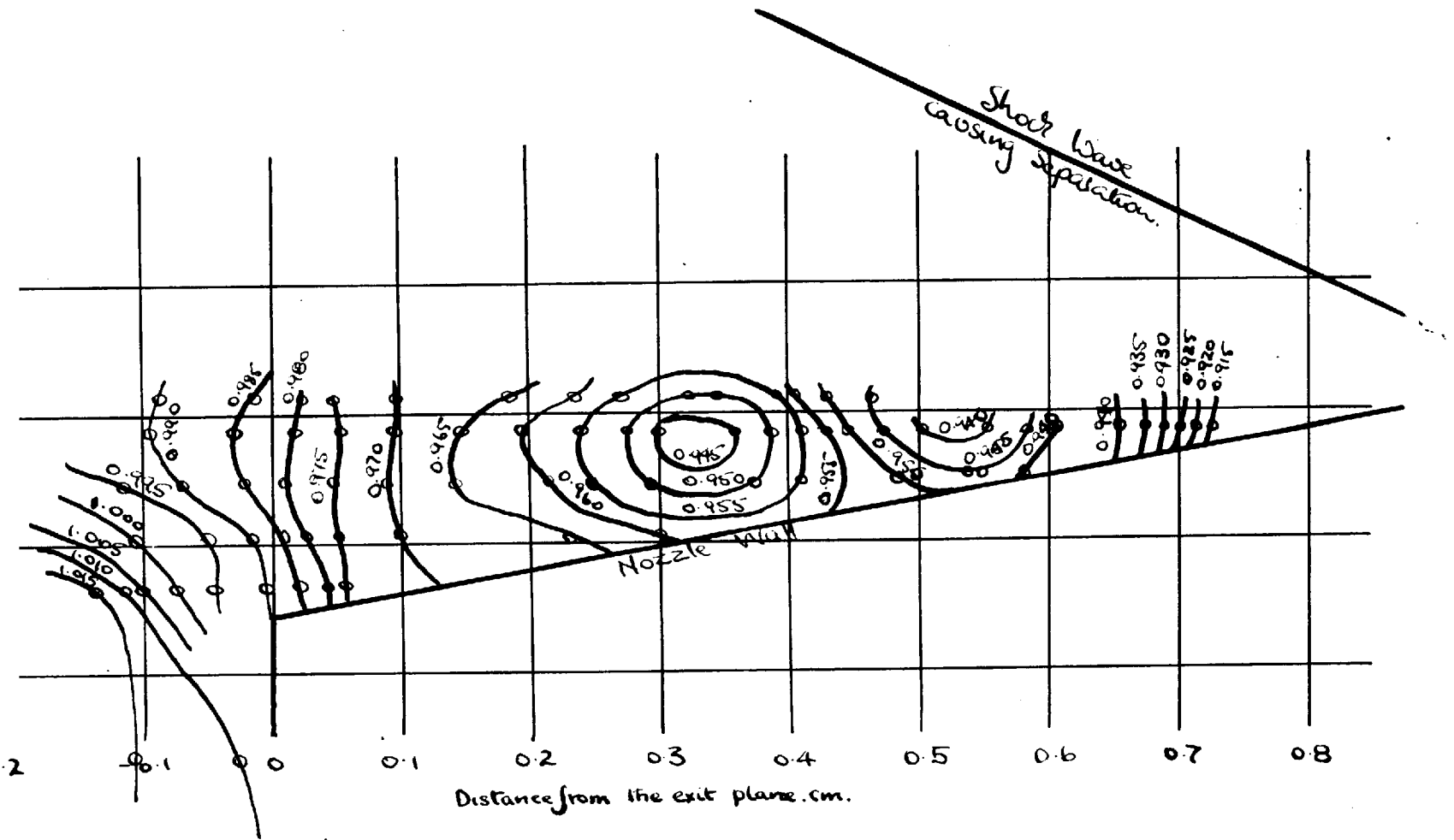

Fig 77. Density ratio profiles ρ/ρ_a for the bottom reverse flow region in test 152. P_0 = 128·2 p.s.i.a.

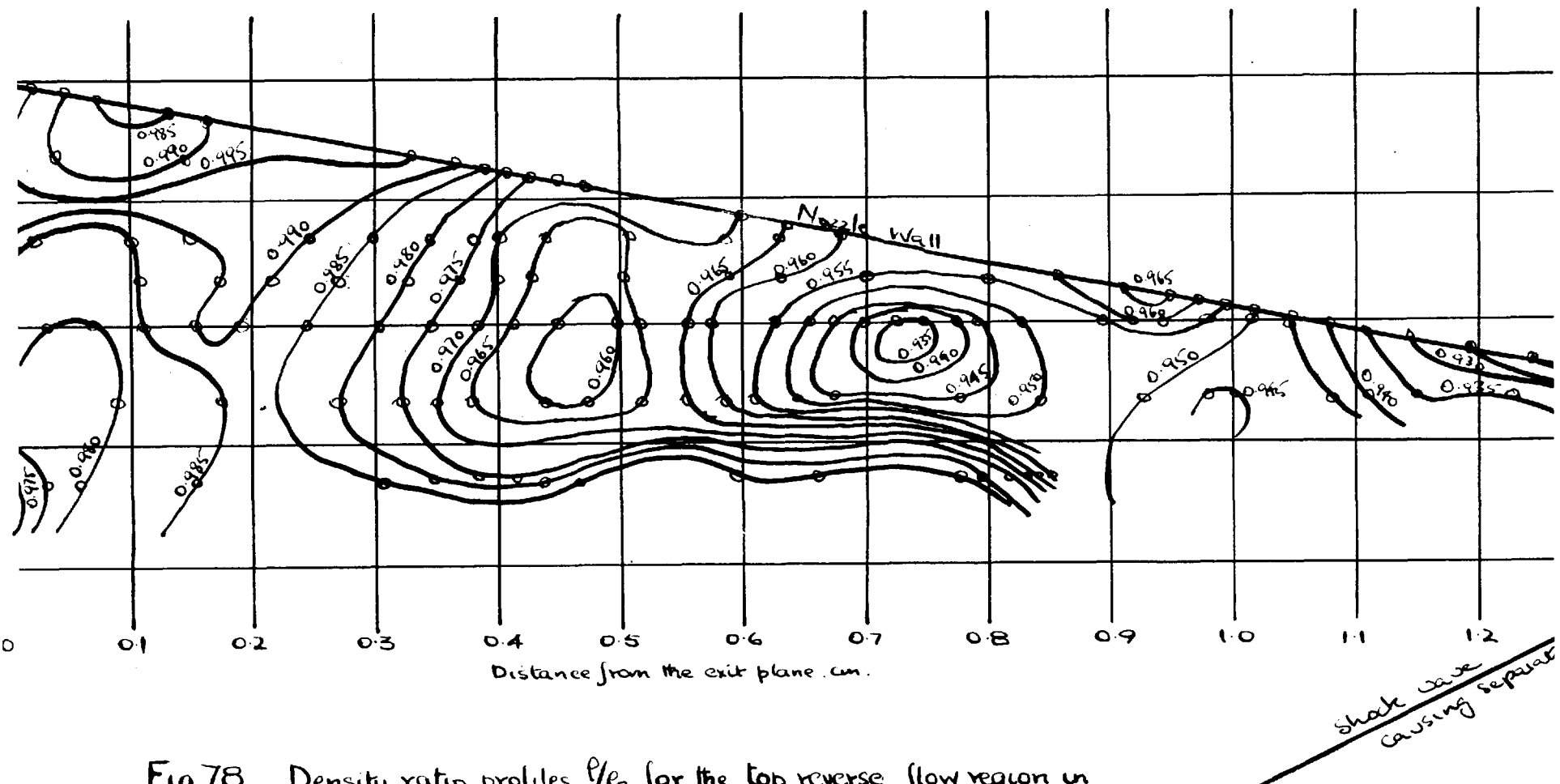

Fig 78 Density ratio profiles ρ/ρ_a for the top reverse flow region in test 143, $P_o = 99.2$ p.s.i.a.

amounted to approximately 0.4 of the no flow fringe width. In terms of the fringe shift unit this error was small, but as the fringe shifts in the reversed flow regions were small, it was large compared with the total shift and was therefore significant.

The maximum fringe shift measured was approximately one fringe shift unit, and an error of ∓ 0.1 units in the position of a fringe caused an error of approximately ∓ 0.75% in the density ratio ρ/ρ_a. The corrections for the non ideality of the interferometer optics (that is, the bending of the no flow fringes) amounted to 50% of the fringe shift in some cases. Accordingly the results are not very accurate, but give a useful qualitative picture of the flow patterns.

In test 152 the stagnation pressure was higher and separation took place nearer the exit plane of the nozzle, and the vortex nearest the exit plane in tests 143 and 146 moved out of the nozzle. The bend in the pressure ratio variation along the bottom wall indicated by A in fig 79 which corresponded to the flow region between the second and third vorticies, B in fig 75 and 76, was also not present in test 152.

The pressure ratios $p/_{pa}$ determined from the wall

Fig 79 The density and pressure ratios ρ/ρ_a and p/p_a measured on the bottom wall of the bottom reverse flow region.

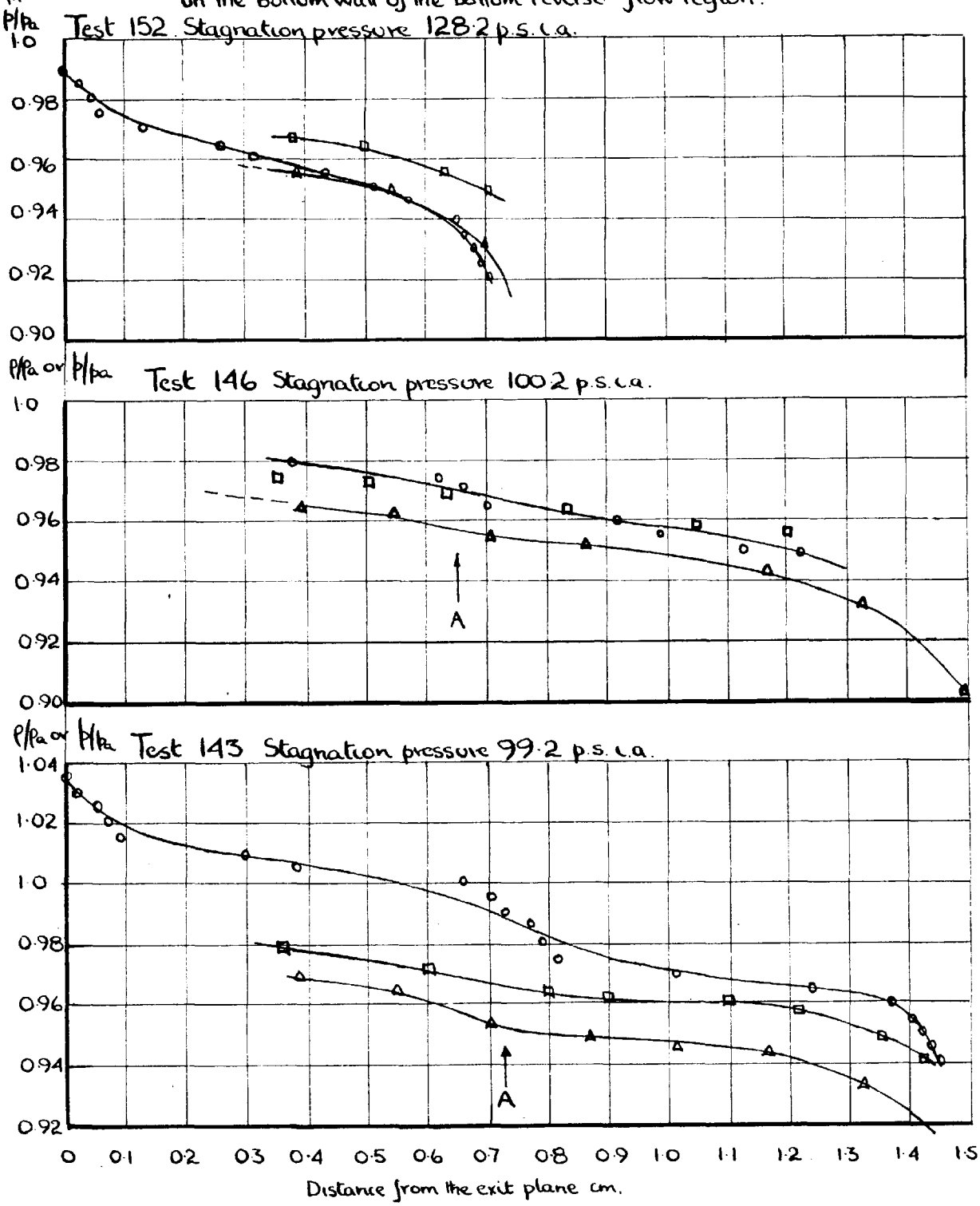

⊙ Density ratio ρ/ρ_a measured from an interferogram on bottom wall of reversed flow regi

△ Pressure ratio p/p_a " at pressure tappings " " " " " " "

□ Density ratio ρ/ρ_a calculated from the pressure ratio p/p_a assuming isentropic flow into the reversed flow region of atmospheric air.

pressure measurements, the density ratios ρ/ρ_{a_i} measured on the bottom wall, and the density ratios calculated from the pressure ratios assuming isentropic flow are plotted in fig 79. The differences between the experimental and calculated values of the density ratio were small, being approximately -3%, 0% and 1.5% of the measured density ratio for tests 143, 146 and 152 respectively.

The agreement between the density ratios obtained by the two different means, showed that the air in the reversed flow region was drawn in from the atmosphere to promote separation.

9.4. Boundary Layer Flow.

In all three types of flow photograph of the nozzle flow, namely interferometric, schlieren and shadow, the presence of the boundary layer is shown as a fairly well defined region close to the solid boundaries. By means of the interferograms it was possible to determine the density distributions at various positions in the boundary layer, and then by making certain assumptions to use them to calculate the temperature and velocity distributions.

In the interferograms of the flow shown in fig 37, the apparent width of the boundary layer increases from

practically zero at the throat to a sizable fraction of the divergence width at separation. After separation it separates the main body of the separated jet from the flow in the reversed flow region.

It has been shown in section 2 that the flow properties change in a continuous manner in moving from the free stream into the boundary layer. Any definition of boundary layer width therefore is somewhat arbitrary. The width used in this research has already been defined in section 8.2. as the distance between the nozzle wall and the sharp bend in the flow fringes at the top of the boundary layer. It can be seen from the discussion in section 8.3.2. that this width will be slightly greater than the true value due to errors caused by corner effects. The camera was focussed on a plane in the nozzle one third of the nozzle breadth from the exit window, and according to Wachtell's[66] results in section 8.3.1., refraction effects were negligible when the camera was focussed in this position.

Boundary layer widths measured in the tests 143, 146, 152 and 163, at stagnation pressures of 99.2, 100.2, 128.2 and 168.2 p.s.i.a. respectively are presented in table 25. The difference between the widths measured at corresponding positions in tests 143 and 146 was 8% in some cases. The

TABLE 25.

Boundary layer widths

Dist from exit plane cm.	Test 163 Bottom wall cm.	Test 163 Top wall cm.	Test 152 Bottom wall cm.	Test 152 Top wall cm.	Test 146 Bottom wall cm.	Test 146 Top wall cm.	Test 143 Bottom wall cm.	Test 143 Top wall cm.
0.2	0.083	0.083						
0.4	0.082	0.081						
0.6	0.078							
0.8	0.071	0.069						
1.0	0.065		0.060	0.063				
1.2	0.060		0.057	0.056				
1.4	0.056		0.055					
1.6	0.051		0.050					
1.7					0.053	0.051	0.056	0.055
1.8	0.048		0.048		0.050	0.049	0.052	0.051
2.0	0.045	0.046	0.045	0.047	0.048	0.047	0.046	0.047
2.5	0.038		0.037		0.037		0.035	
3.0	0.023		0.029	0.028	0.025	0.023	0.023	0.024
3.4					0.017	0.016	0.017	
3.5			0.019				0.015	0.015
3.9			0.006				0.006	0.006
4.1			0.005	0.005			0.006	0.005
4.3			0.005					

Position of onset point Test 152 0.995 cm from the exit plane

146 1.666 cm

143 1.684 cm

apparently large difference in these results, which were obtained at approximately the same stagnation pressure was caused by the small width of the boundary layer and the difficulty in measuring it accurately. The position of the wall on the interferogram could be estimated to $\mp$ 0.001 cms and the top of the boundary layer to $\pm$ 0.003 cms. The latter uncertaintity was reduced by plotting many measurements of the width against distance and drawing a smooth curve through the points.

The walls of the actual nozzle were not parallel to the light beam as measurement showed that the width was greater on one side of the nozzle than on the other. However examination of the nozzle dimensions presented in appendix 1 shows that the variation in nozzle width along the light beam was small upto 2.8 cms from the exit plane. Accordingly the errors caused in the measurements of boundary layer width were small, as these were all taken in the region 0 - 2.3 cms from the exit plane.

The results presented in table 25 show that the widths at corresponding positions on the top and bottom walls of the divergence were equal and independent of the stagnation pressure.

A general characteristic of the boundary layer was the high degree of shock penetration at separation (see figs

58, 72 and 73) indicating that the boundary layer was supersonic for most of its width. This was particularly so for turbulent separations that took place nearer the exit plane where the boundary layer was relatively thick. In the laminar separations (see figs 60 and 61), which took place nearer the throat, the boundary layers were too thin for the degree of shock penetration to be observed.

9.4.1. The density and velocity distributions in the boundary layer.

The main purpose of obtaining these distributions was to determine whether there was any significant changes in them as the separation position was approached. As the separation position was not measured, the position at which the distributions were obtained will be discussed relative to the onset position determined in section 9.2. It has been shown in section 3.4. that the boundary layer will be retarded upstream of this onset position, as it does not correspond to the point of furthest upstream influence of the shock wave causing separation, as it does for the results for steps and wedges discussed in sections 3.1., 3.2. and 3.3.

The density distributions measured in the boundary layer on the bottom wall of the nozzle in test 146 are plotted

in fig 80, where a marked change in shape is apparent between the distribution 0.007 cms downstream, and that 0.162 cms upstream of the onset position. At 0.006 cms upstream of the onset position, the density at the wall was below that at 0.007 cms downstream and the shape of the distribution was closer to that in the undisturbed boundary layer. On moving further upstream the distributions remained essentially the same shape, but the density increased which would be expected as that in the free stream increased. The increased density just downstream and in the vicinity of the onset point was also found to be a feature of the distributions measured in tests 152 and 163.

To calculate the temperature and hence the velocity distributions in the boundary layer, it was necessary to make the following assumptions.

(1) That the pressure was constant through the boundary layer in direction normal to the wall, and

(2) The nozzle wall temperature was equal to the stagnation temperature of the gas.

The first of these assumptions did not hold in the region close to separation, where compression of the low velocity regions of the regions of the boundary layer took place. Further upstream in the undisturbed boundary layer, the

Fig 80 The density variation in the boundary layer in test 146, stagnation pressure P_0 = 1002 p.s.i.a.

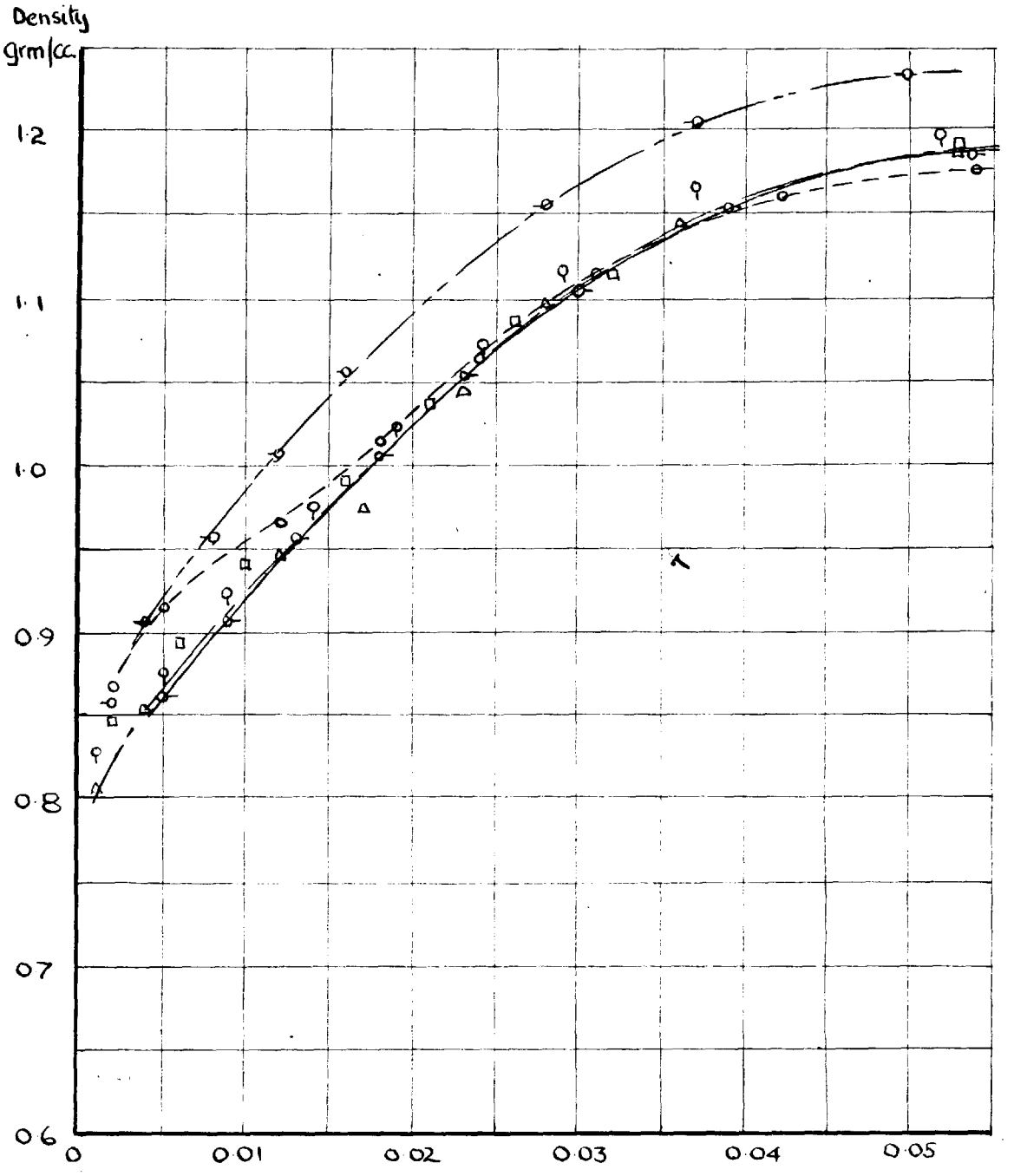

	Distance from the exit plane .cm.		Distance from the onset point .cm.
⊙	1·659	– – – – – –	– 0·007
o	1·672	———	+ 0·006
Δ	1·685	—— - —— -	+ 0·022
□	1·698		+ 0·032
♀	1·725		+ 0·059
o	1·828	——— – – ———	+ 0·162

problem of the pressure variation from the wall to the free stream has been discussed by Schlichtling,[81 Page 109] who carried out an order of magnitude analysis of the terms in the Navier-Stokes equation for the case of a laminar layer and incompressible flow. He found that the variation of pressure in the boundary layer was negligible. The application of this result to a turbulent layer has not been confirmed experimentally. There was the further complication in that the flow outside the boundary layer was two dimensional. But it was found that the pressure variation across the boundary layer was negligible, by assuming that it was the same as that calculated from the density variation across the width of the nozzle.

The second assumption was necessary because no provision could be made in the present apparatus to measure the nozzle wall temperature.

The temperature of the gas near the wall is increased by stagnation and in addition by the transfer of momentum towards the wall resulting from the velocity gradient. If the system is adiabatic no heat is transferred through the wall, but the rise in temperature at the wall causes conduction of heat from the wall back through the boundary layer into the free stream. Hence the wall assumes a

temperature Taw which is higher than that in the free stream by an amount depending primarily on the ratio of the molecular diffusivity of momentum to the molecular diffusivity of heat. The ratio, $\mu/\rho / k/c_p\rho = \frac{c_p\mu}{k} = \sigma$ which is defined as the Prandtl number.

For convenience it is usual to define a recovery factor $N_R = \frac{Taw - T}{To - T}$, so that the wall temperature can be calculated. It has been shown that $N_R \sim \sigma^{\frac{1}{3}}$ [66] for a turbulent boundary layer. The Prandtl number for air is independent of temperature[81 Page 294] and equal to 0.72, and hence the recovery factor is equal to 0.88. This means that in an adiabatic system the wall temperature is lower than the stagnation temperature.

However the flow in the nozzle was not isentropic and heat was probably conducted through the brass walls of the nozzle raising the wall temperature[82]. It has therefore been assumed that $\sigma = 1$ and Taw = To as this leads to great simplification in the calculation of velocity, because the energy equation,

$$V = \sqrt{2c_p(T_o - T)}$$

still holds in the boundary layer.[81 Page 343]

Using the assumptions discussed above the velocity distribution was calculated at a number of positions along

the wall from the density distributions measured in tests 146, 152 and 163 at stagnation pressures of 100.2, 128.2 and 168.2 p.s.i.a. respectively. The results are presented in dimensionless form in figs 81, 82 and 83. The boundary layer Reynolds numbers corresponding to positions at which the distributions were determined are tabulated in table 26. They were calculated from the free stream flow properties above the boundary layer and the axial distance from the throat.

Referring to fig 81 where the velocity distributions corresponding to the density distributions in fig 80 have been presented, it can be seen that the velocity in the region of the boundary layer close to the wall, just downstream of the onset position, appeared to be higher than that in the corresponding region upstream. The converse would be expected as the boundary layer downstream of the onset position was closer to the separation position and hence more retardation would be expected. The cause of the apparent anomally lay in the method used to calculate the velocity in the boundary layer. The temperature was first calculated from the relationship $p/\rho = RT$ and then the velocity from the energy equation. As the density rose on approaching the separation position, the value of T calculated was too low, as the pressure, which was assumed constant

Fig 81. Boundary layer velocity profiles for test 146, stagnation pressure 100·2 p.s.i.a.

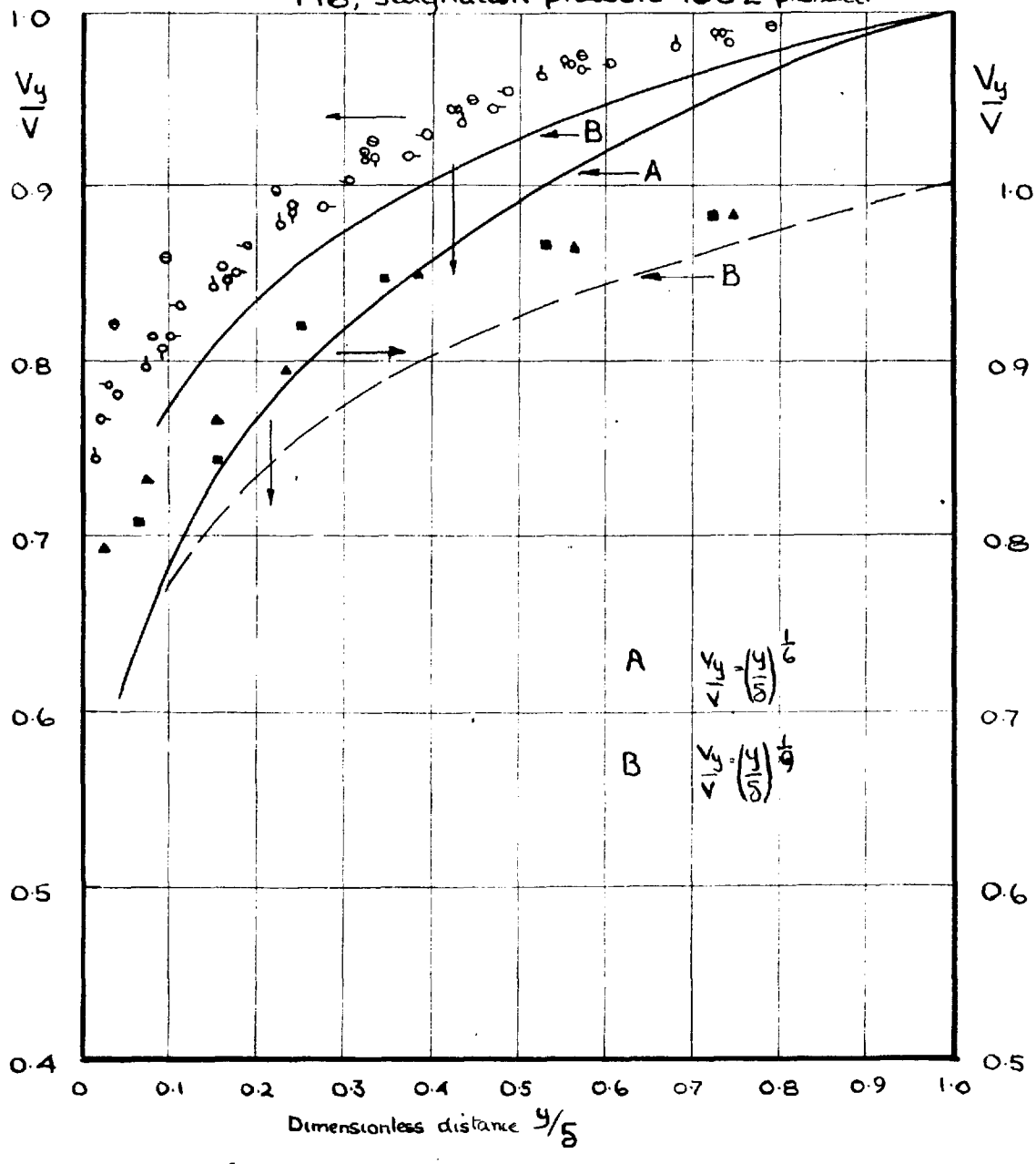

Distance from the exit plane cm.

⊖	1·659
○	1·672
◇	1·685
⊙	1·698
◎	1·725
○	1·828
△	2·300
□	2·698

Position of the onset point 1·666 cm. from the exit plane of the nozzle.

Fig 82 Boundary velocity profiles for test 152, stagnation pressure 128·2 p.s.i.a.

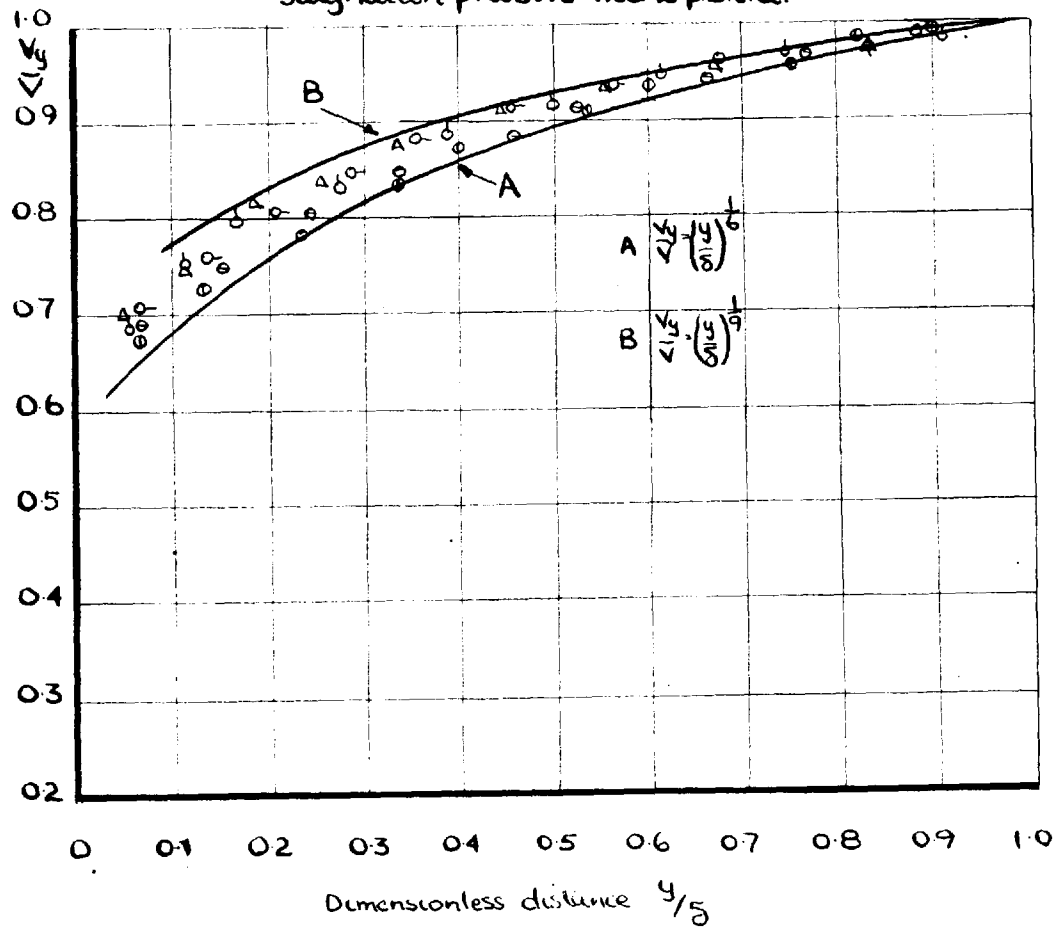

Distance from the exit plane cm.

⊕	1·001
⊖	1·029
♁	1·055
⊙	1·186
△	1·318

Position of the inset point 0·995 cm from the exit plane.

Fig 83 Boundary layer velocity profiles for test 163, stagnation pressure 1682 p.s.i.a.

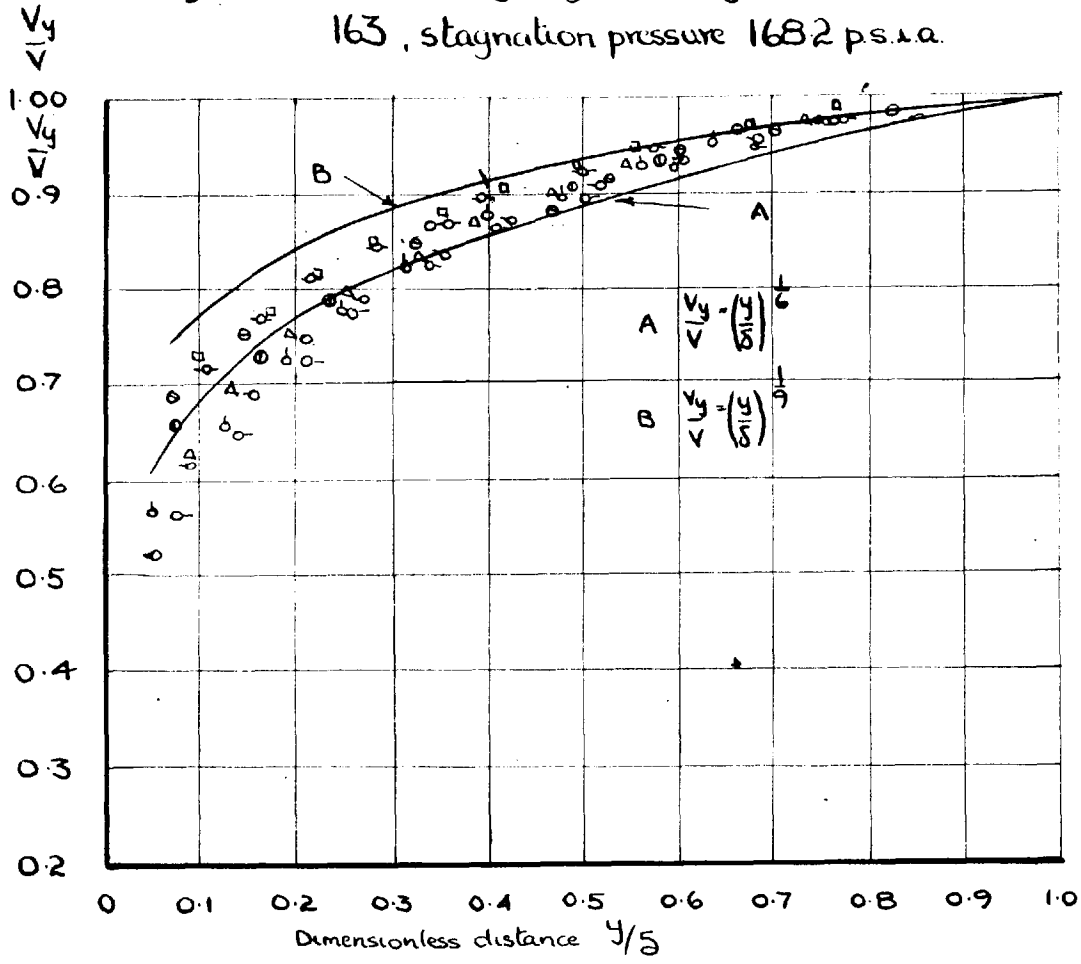

Distance from the exit plane cm.

⊖	0.334
⊖	0.360
⊖	0.427
⊖	0.493
⊖	0.652
△	0.891
□	1.181
⊖	1.421

TABLE 26.

Corresponding displacement, boundary layer thicknesses and Reynolds numbers.

Dist from the exit plane cm.	Boundary Layer thickness δ cm.	Displacement thickness δ^+ cm.	$\frac{\delta^+}{\delta}$	Reynolds Number x 10-6
Test 163. Po = 168.2 p.s.i.a.				
0.493	0.080	0.0223	0.279	2.493
0.652	0.076	0.0217	0.286	2.482
0.891	0.068	0.0186	0.273	2.432
1.181	0.064	0.0134	0.242	2.369
1.421	0.056	0.0131	0.235	2.307
Test 152. Po = 128.2 p.s.i.a.				
1.055	0.059	0.014	0.239	2.112
1.186	0.059	0.014	0.239	2.083
1.318	0.054	0.013	0.241	2.040
Test 146. Po = 100.2 p.s.i.a.				
1.698	0.053	0.009	0.1698	1.722
1.725	0.052	0.009	0.1730	1.721
1.828	0.050	0.008	0.1660	1.663
2.300	0.039	0.006	0.1462	1.533

across the boundary layer and equal to that in the free stream, must also have risen. Hence the velocity calculated from the density distributions will appear to be too high in the regions where the boundary layer was retarded.

On moving upstream away from the separation and onset positions, the dimensionless velocity in the regions of the boundary layer close to the wall fell and thereafter the distributions remained approximately the same shape. The distributions corresponding to the power law $\frac{V_Y}{V} = (\frac{Y}{\delta})^A$ where A equals $^1/_6$th and $^1/_9$th have been represented on fig 81. With reference to this figure it can be seen that the dimensionless velocity at any position on the distributions obtained in test 146 was greater than the corresponding value given by the $^1/_9$th power law. The distributions also showed a tendency to move towards curves of lower power as the Reynolds number decreased.

The results obtained in test 152 fell between the $^1/_6$th and $^1/_9$th power laws, and like those in test 146 showed a tendency to move towards curves of lower power as the Reynolds numbers increased.

In test 163 the position of the onset point could not be determined accurately as the pressure rise at separation occurred between the exit plane of the nozzle and the last

pressure tapping. However the distribution at 0.334 cms from the exit plane in fig 83 was close to the onset position. As before in test 146, the dimensionless velocity was higher in the region close to the wall than in the corresponding region of the distributions immediately upstream. On moving upstream from the profile at 0.427 cms from the exit plane, the distributions which had up to this point moved towards power law curves of higher power began to move in the opposite direction as the Reynolds number decreased. Therefore the density rise at separation was transmitted to a position 0.427 cms from the exit plane, which was at least one boundary layer thickness (0.083 cms) upstream of the onset point. Further upstream effects could occur in the very thin regions near the wall, the study of which was beyond the resolution of the optical technique used.

The effect of Reynolds number on the undisturbed boundary layer can be seen clearly in fig 84, where the velocity distributions moved towards power law curves of lower power as the Reynolds number decreased.

Calculation of the Mach number distribution in the boundary layer showed, that the flow was supersonic to within very small distances of the wall. In the case of the

Fig. 84. Comparison of the velocity profiles in tests 163 152 and 146.

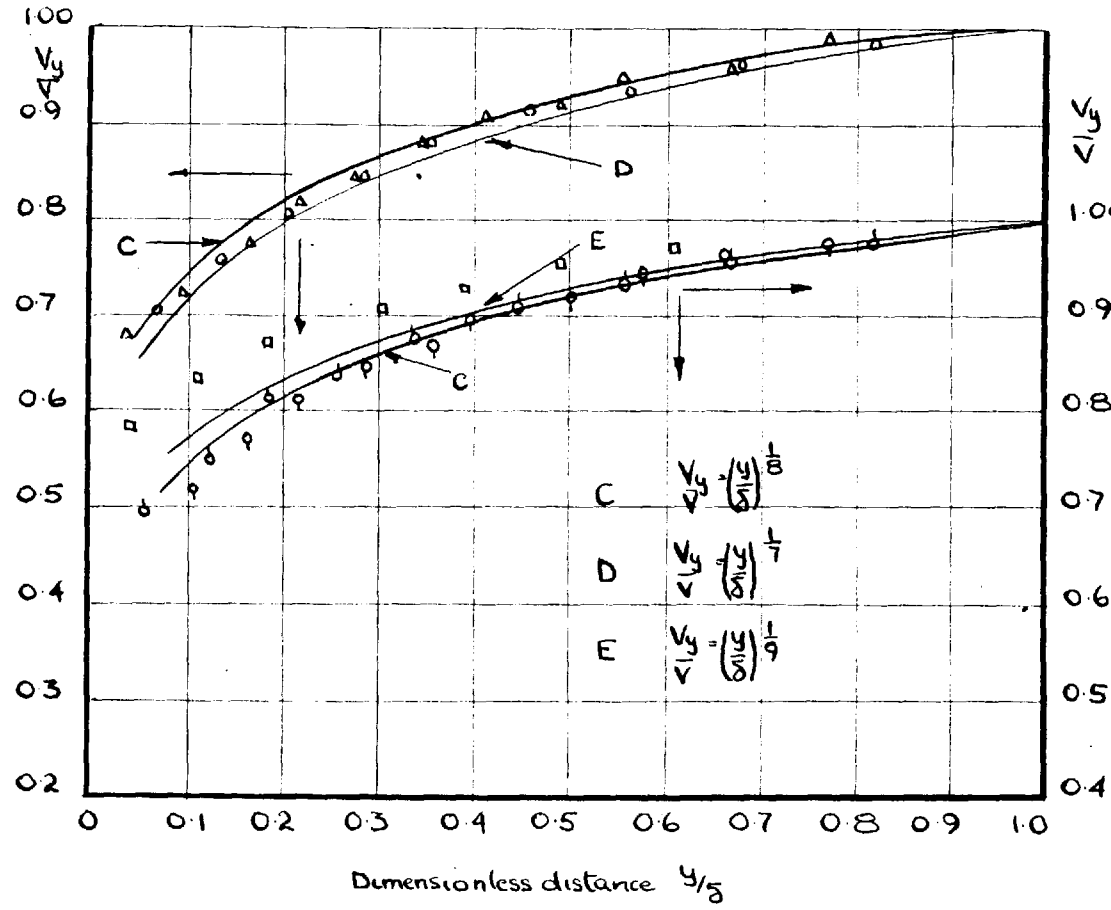

Test.		Distance from the exit plane cm.	Reynolds number.
152	○	1·186	$2·083 \times 10^6$
163	△	1·181	$2·369 \times 10^6$
152	◐	1·318	$2·040 \times 10^6$
163	♀	1·421	$2·307 \times 10^6$
146	□	1·698	$1·722 \times 10^6$

velocity distributions measured in test 163 at 0.427 and 0.493 cms from the exit plane, the flow became supersonic less than 0.004 cm from the wall.

9.4.2. The Boundary Layer Displacement Thickness.

The displacement thickness of the boundary layer defined as:-

$$\delta^* = \int_0^{\delta} \left(1 - \frac{\rho_y u_y}{\rho_v}\right) dy$$

have been calculated from the density and velocity distributions obtained for tests 146, 152 and 163 and presented in table 26 with the corresponding Reynolds numbers.

The ratio of displacement to boundary layer thickness increased as the Reynolds number increased. Therefore the Mach number at a given point in the nozzle should decrease as the stagnation pressure is increased, as the ratio is a measure of the constriction caused by the boundary layer.

9.4.3. Transition in the Boundary Layer.

A method has been described in appendix 7 by which the point of transition from a turbulent to a laminar boundary layer can be determined. The method depends on a dip

appearing, at the point of transition, in the white line representing the boundary layer on a direct shadowgraph. Examination of the shadowgraphs taken with the plate adjacent to the exit window of the nozzle, presented in fig 54, showed that there was no dip in the white line attributable to transition. However the apparent position of the wall on the shadowgraphs was displaced from that of the true wall. The white line representing the boundary layer was also tangential to the apparent wall at one point. The cause of these effects can be deduced by reference to fig 17a appendix 7.

Near the throat the boundary layer was extremly thin and the density gradients large, therefore a high degree of refraction will take place and the plate position will correspond to position XX in fig 17a(ii). On moving downstream $\frac{\partial n^2}{\partial y^2}$ decreases and the position of the plate moves towards the point of focus of the boundary layer YY. Further downstream the plate position corresponds to a position between YY and the test section. On increasing the distance of the plate from the exit window, the point at which the white line was tangential to the wall moved downstream, as would be expected from the explanation put forward above.

The optical effect associated with transition therefore occurred within the breadth of the glass exit window and as a result could not be detected.

SECTION 10. DISCUSSION.

10.1. Flow in the wetted region of the nozzle.

It has been shown in section 9.1. that the measured pressure ratios were generally above the values calculated from the theory of one dimensional isentropic flow. The difference between the theoretical and experimental values increased as the area ratio increased (see figs 50 & 51). The same observation has been made by other workers[28 31 41] and is associated with real gas effects in the nozzle.

The measured pressure ratios in the region 2.2 - 2.8 cms from the exit plane of the nozzle (see figs 49, 50 & 51) were below the one dimensional isentropic values. This result was not expected as real gas effects, such as friction tend to increase the pressure. Wilkie[28] measuring the pressure ratio in a 10^{o} axisymmetric nozzle showed that the measured and one dimensional values were coincident at a pressure ratio of 0.06, the highest pressure ratio recorded. The effect was similar to that recorded here as the values were coincident at 0.07.

The pressure variation along the bottom wall obtained by means of the method of characteristics has been drawn in fig 85 with the one dimensional and measured values. It can be seen that the results obtained from the two dimensional

Fig 85. Comparison of pressure ratios with those for one and two dimensional flow.

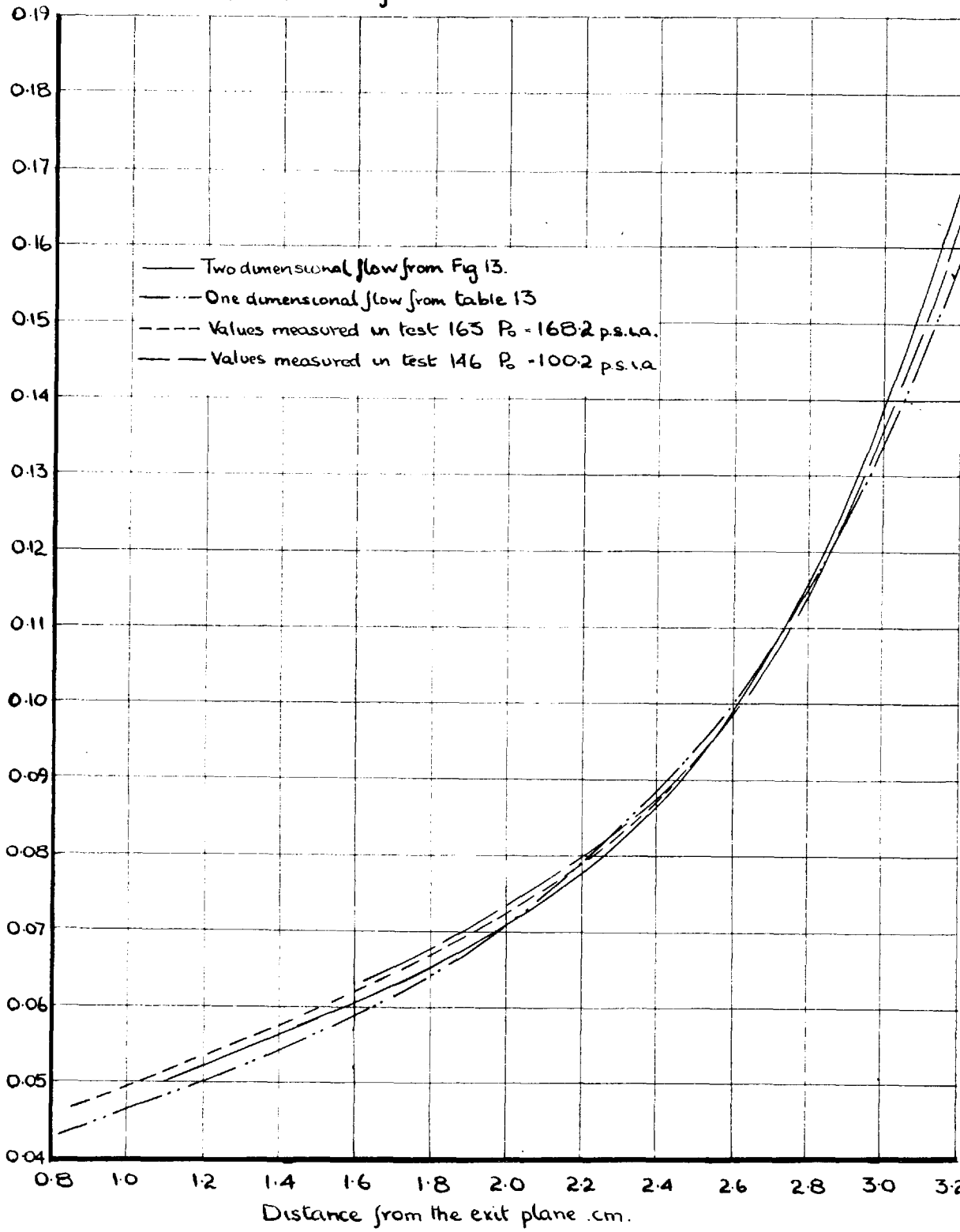

solution are a closer approximation to the experimental values than those obtained from the one dimensional theory. However there is still a region, upstream of 2.4 cms from the exit plane, where the experimental results are below the theoretical two dimensional values.

It was assumed that one of the boundary conditions for the characteristics net was a straight sonic profile, whereas the actual profile is curved (see figs 47 and 38). The effect of using the correct profile cannot be estimated without doing the actual calculation, which was not warranted in the present study. However the error in the boundary condition at the throat might account for the apparent anomally of the measured values of pressure ratio falling below theoretical.

The boundary layer reduces the area available for mainstream flow, and therefore the Mach number and pressure ratio will be high and low respectively at any given point if calculated on the basis of the area ratio defined by the solid walls.

The effective area ratio of a nozzle can be defined by means of the displacement thickness, for if W is the width of the nozzle and D the breadth, the effective area ratio is given by:-

$$A_{eff} = (w - 2\delta^*)(D - 2\delta_g^*) \qquad (1)$$

where δ^* is the displacement thickness on the nozzle walls and δ_g^* that on the glass windows.

The assumption was made that at any cross section the two displacement thicknesses were equal, this was thought to be justified in view of the discussion in section 8.3.3. Then the Mach numbers and pressure ratios corresponding to the area ratio $\frac{A_{eff}}{A_{eff\ throat}}$, were computed from the one dimensional isentropic relationships. At the throat, the boundary layer was extremely thin and therefore the displacement thickness was neglected and the measured and effective area ratios were assumed to be equal. The values of $\frac{A_{eff}}{A_{eff\ throat}}$, $\frac{p}{P_{o_{eff}}}$ and M_{eff} obtained have been tabulated in table 27.

The effective Mach numbers have been plotted in fig 87 and show a similar trend, with changing reservoir pressure to those calculated from the observed values of p/P_o and ρ/ρ_o and it can be seen that displacement thickness did not account for the difference between the one dimensional and measured values.

However it can be seen from fig 86, that the displacement thickness over compensated for the difference between the measured and one dimensional pressure ratios as the former were generally below the effective values.

TABLE 28. The Mach numbers and pressure ratios calculated from the corrected area ratios, assuming one dimensional isentropic flow.

Dist from exit plane cms.	A/A_t measured Table 1a, appendix 1.	$\frac{A_{eff}}{A_t}$	Mach number Table 13	M_{eff}	p/p_o Table 13	$p/p_{o_{eff}}$
Test 163 Po = 168.2 p.s.i.a.						
0.5	3.392	3.265	2.768	2.726	0.0390	0.0415
0.6	3.323	3.150	2.745	2.687	0.0401	0.0439
0.8	3.183	2.985	2.700	2.631	0.0438	0.0478
1.0	3.044	2.870	2.653	2.591	0.0462	0.0508
1.2	2.902	2.735	2.602	2.538	0.0499	0.0550
Test 152 Po = 128.2 p.s.i.a.						
1.0	3.044	2.901	2.653	2.602	0.0462	0.0500
1.2	2.902	2.764	2.602	2.550	0.0499	0.0542
1.4	2.765	2.637	2.551	2.449	0.0541	0.0594
Test 146 Po = 100.2 p.s.i.a.						
1.7	2.555	2.473	2.465	2.431	0.0615	0.0653
1.8	2.484	2.414	2.435	2.405	0.0647	0.0679
2.0	2.345	2.280	2.373	2.341	0.0713	0.0750
2.2	2.204	2.157	2.305	2.281	0.0807	0.0824

Fig 86. Comparison of the measured and one dimensional values of pressure ratio p/p_o with those based on one dimensional flow with correction for displacement thickness.

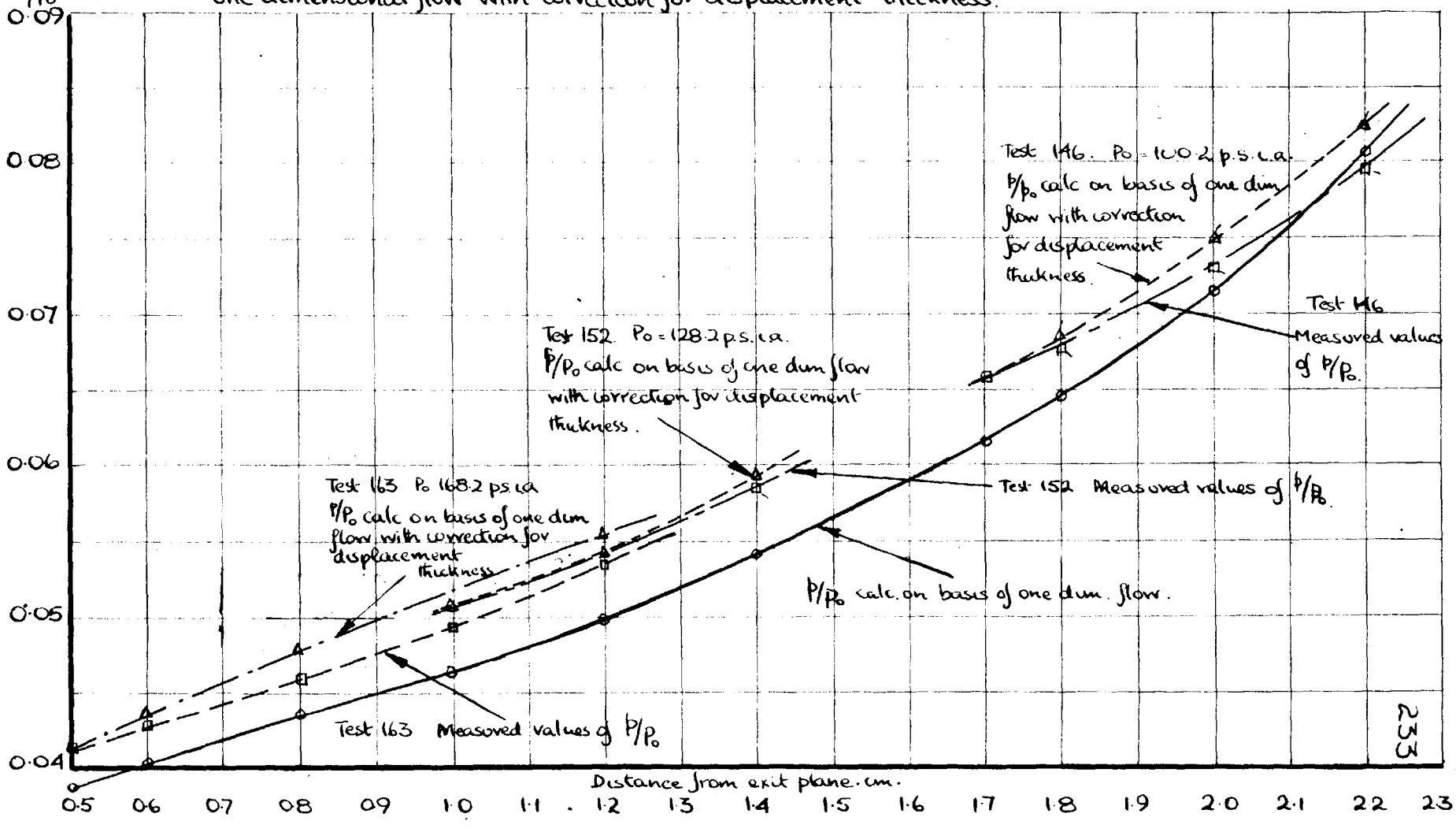

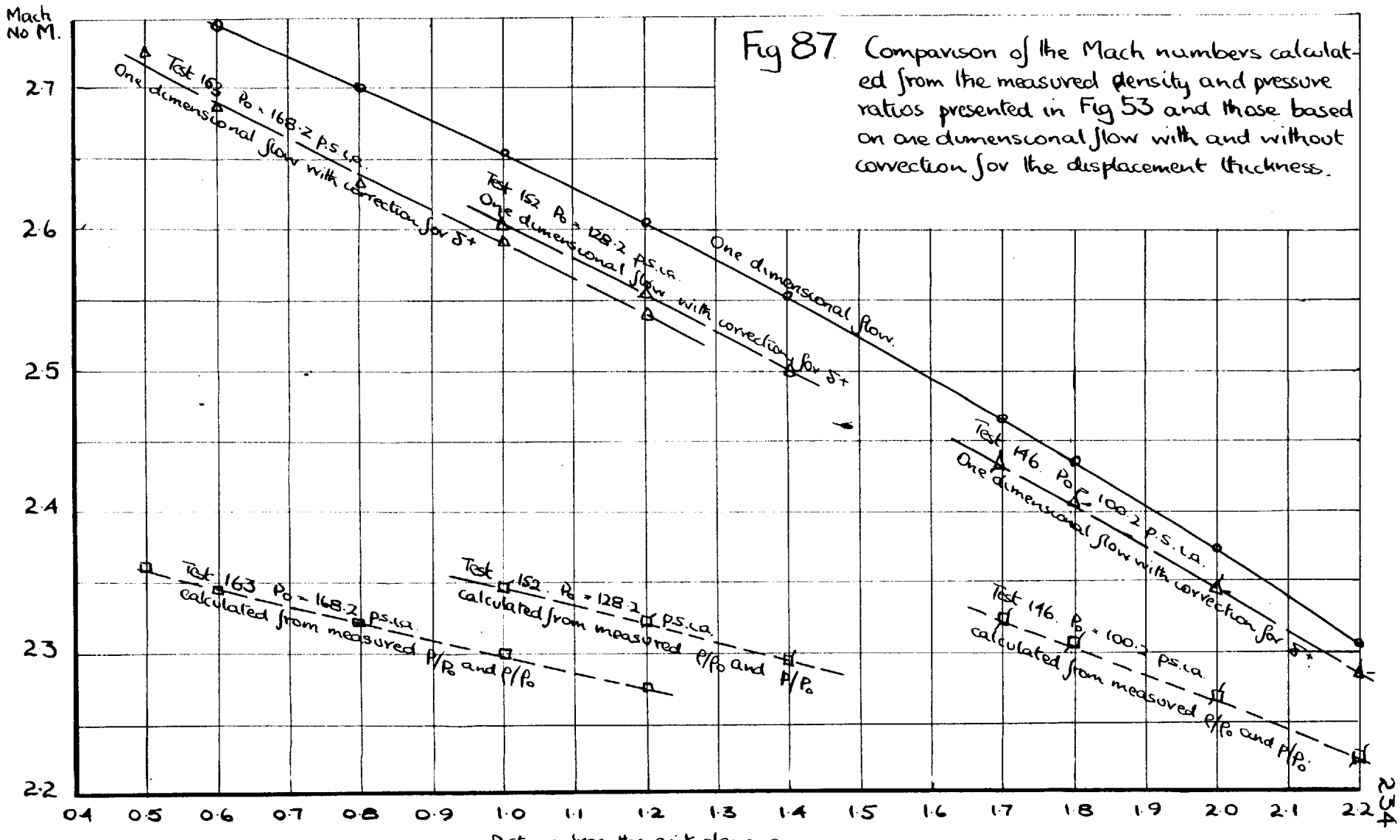

Fig 87 Comparison of the Mach numbers calculated from the measured density and pressure ratios presented in Fig 53 and those based on one dimensional flow with and without correction for the displacement thickness.

A feature of isentropic flow is that the pressure and density ratios decrease as the Mach number and area ratio increase. Therefore as the effective area ratio was always less than the measured value, the effective values of the density ratio would be expected to be always above the uncorrected values. Referring to figs 44 45 & 46 it can be seen that the measured density ratios were always below the corresponding uncorrected one dimensional values. Thus the correction for the boundary layer causes the divergence, between the theoretical and experimental values, to increase.

It is apparent therefore, that the discrepancies between the actual and the theoretical flow in the nozzle cannot be attributed to the constrictive effect of the boundary layer as calculated from the displacement thickness.

In previous interferometric work on two dimensional nozzles by Bersharder[51], a Laval nozzle and one of 4^{o} divergence half angle were used and the density only was measured. The pressure ratios and Mach numbers were then calculated from the relationships $p/P_o = \left(\rho/\rho_o\right)^{\gamma}$ and $M^2 = \frac{2}{(\gamma-1)}\left(\rho/\rho_o^{\,1-\gamma} - 1\right)$.

In the divergent nozzle, the pressure and hence the density ratios in the convergence were above the corresponding one dimensional values. The difference between the two

values reached a maximum of 3%. In contrast, the density ratios in the convergence of the nozzle used in this research were below the one dimensional values in the region 4.2 to 5.6 cms from the exit plane, the difference reaching a maximum of 5% at 5.0 cms. The convergent section walls were concave to the flow direction in Bersharder's nozzle and convex in the nozzle used in this research. The density ratio is therefore dependent on the shape of the convergence, and large errors can result by treating the subsonic flow upto the throat as one dimensional and isentropic.

The pressure ratios calculated from the density ratios in the divergence of Bersharder's nozzle were fractionally above the one dimensional values. However in this research the values of the equivalent pressure ratio fall consistently below the measured and one dimensional values (see figs 48 49 50 & 51) The difference between the one dimensional values and those calculated from the density ratio increased as the stagnation pressure increased since the density ratio at a given point in the nozzle decreased (see fig 44, 45 & 46). Bersharder only gives the results of one test in the divergent nozzle and does not indicate whether the density ratio decreased with increasing stagnation pressure. However the results obtained in his Laval nozzle show that the density ratio decreased as the stagnation pressure was increased from

4.07 to 4.8 atm, and then increased when the pressure was raised further to 6.09 atmos. In the first two tests the Mach number and hence the pressure ratio calculated from A_{eff} were respectively less and greater than the values calculated from the density ratio. In one region of the nozzle divergence the Mach number was also 2% above the value calculated from the measured area ratio. The conclusion reached by Bersharder was that the constrictive effect of the boundary layer was not as great as that calculated from the displacement thickness. If the Mach number had been calculated from the density ratios measured in the nozzle used in this research the same effect, but greater in magnitude, would have been observed. In test 163 for instance the Mach numbers at 0.5 cms from the exit plane, calculated from, the density ratio, the area ratio and the effective area ratio were 3.64, 3.39 and 3.27 respectively. Bersharders results can therefore be interpreted in the same way as those in this work, that is by assuming that the flow is not isentropic.

The subsequent increase in density ratio, shown by Bersharder's results, causing the Mach numbers to be lower at the higher stagnation pressures, was attributed by him to the strength of a system of weak shock waves present in

the nozzle increasing with stagnation pressure. The effect of these disturbances could have been sufficient to mask the effect of decreasing density ratio with increasing stagnation pressure as demonstrated in this research.

It should be noted that the Laval nozzle used in the work discussed above was made of Cedar wood, which has a low coefficient of thermal conductivity in comparison to brass. Therefore the rate at which heat could be conducted into the gas stream was much greater in the present experiments than in Bersharder's.

Naysmith[82] measured the heat transfer coefficients between a heated ramp placed on a flat plate and the gas stream flowing above it. He found that the heat transfer coefficient $h_h = \frac{q}{T_{wad} - T_w}$ increased as the Reynolds number was increased by increasing the stagnation pressure. Accordingly the large divergencies between the actual flow and isentropic flow in the nozzle could be due in part to the effects of heat transfer.

A theoretical analysis into the effects of heat transfer and friction on the one dimensional flow in the divergence of a supersonic nozzle has been carried out by Shapiro[46]. The results show that friction and heat transfer cause the

Mach number to decrease and the temperature, density, and pressure to increase, with respect to the values obtained for the corresponding one dimensional isentropic flow.

With reference to the results in section 9.1.1. it can be seen that the pressure and temperature were generally above the one dimensional values, which was in agreement with the trend predicted by the theoretical analysis given above. However the experimentally measured density was generally below the isentropic values and not above. As a result it was thought that the density measurements might have been in error.

As white light fringes could not be obtained with the optical system, no check could be made on the shift of the fringes in the reference regions. However if it is assumed that the fringes in the reference regions of the flow interferogram shifted by a further fringe shift unit, the density values throughout the flow field would have been increased by an amount corresponding to one fringe shift unit. It was found that if this was done, the entropy change became negative in some instances when calculated from the relationship given in section 9.1.1. The entropy change was negative for the complete range of the measured values in test 146 and for the initial region of the divergence in

which pressure measurements were made in tests 152 and 163. This result is in conflict with the second law of thermodynamics. Therefore in view of the excellent agreement between the density calculated from the stagnation conditions and that in the low velocity regions of the convergent section it is unlikely that the numbering of the flow fringes was in error.

Errors in the density would also be caused by bending of the glass windows during a test, as then the test section breadth D used in the calculation of the density would not be the correct value, and the fringe patterns would have been altered by the strains set up in the glass. However no detectable change of breadth was observed during a test and when the windows were loaded with a force equivalent to that exerted by the gas stream during a test at the highest stagnation pressure, no measurable fringe shift could be detected.

One of the results of Shapiro's analysis was that heat transfer through the nozzle walls, causes the Mach number to decrease with respect to the value obtained for the corresponding one dimensional isentropic flow. Since the Mach numbers obtained in section 9.1.1. exhibit the same trend, it was assumed that the areas under the temperature

entropy curves in fig.52 represented the heat transferred through the nozzle walls, and the result used to calculate the Mach number.

For instance in test 163, the heats transferred, obtained from the area under the temperature entropy chart in fig 52 were:-

$$Q\ rev_{reservoir \rightarrow 1} = 2.48 \text{ cal/gm.}$$

$$Q\ rev_{1 \rightarrow 2} = 4.12 \text{ cal/gm.}$$

then from the relationship $Q = (To_2 - To_1)\ cp.$

$To_1 = 306.7^{\circ}A$ $To_2 = 324.0^{\circ}A$ when $To = 296.3^{\circ}A.$

The relationship $T = To + \left(\frac{\gamma - 1}{2}\right) M^2$ was used to calculate the Mach numbers using the values of T corresponding to stations 1 & 2 in table 16. The values of the Mach number calculated $M_1 = 1.93$ and $M_2 = 2.54$ were greater than the corresponding values $M_1 = 1.86$ and $M_2 = 2.36$ calculated assuming adiabatic flow. The values of Mach number calculated by assuming heat transfer are too great, as they do not agree with the values measured from the Mach lines in the flow (see fig 53).

Heat transfer does not therefore account for the observed effects in the nozzle. As the Mach numbers on the bottom wall calculated from the experimental pressure and density values, assuming adiabatic flow, are in good agreement

with those measured from Mach lines, it was concluded that the flow was adiabatic and the effects observed with increasing reservoir pressure were not due to heat transfer but to some irreversible process in the nozzle.

Rowe[86] suggested that the flow in a supersonic nozzle could be treated by a relationship of the type $P/\rho^{n'} =$ constant, where n' is a fictitious expansion index less than γ. He then assumed that the flow was isentropic upto the throat and derived for the velocity the expression:-

$$V = \sqrt{2g\left(\frac{Po}{\rho o}\left\{\frac{\gamma}{\gamma-1}\,\frac{2}{\gamma+1}\left[1 - \beta\left(\frac{p}{Po}\right)^{\frac{n'-1}{n'}}\right] + \frac{\gamma}{\gamma+1}\right\}\right)}$$

where $\beta = \frac{2}{\gamma+1}^{\frac{-\gamma(n'-1)}{n'(\gamma-1)}}$

when $n' = \gamma$ the equation reduces to that for isentropic flow.

$$\text{i.e. } V_{isentropic} = \sqrt{2g\gamma\,\frac{Po}{\rho o}\left[1 - \left(\frac{p}{Po}\right)^{\frac{\gamma-1}{\gamma}}\right]}$$

The values of n' calculated from the relationship $\frac{p}{\rho^{n'}} = \frac{Po}{\rho o^{n}}$ are presented in table 28 for tests 146 and 163, where p and ρ were the measured static pressure on the bottom wall and the density on the edge of the bottom boundary layer, respectively. The velocity calculated from the equation above and the expansion index have also been tabulated in table 28, with the corresponding values calculated from the temperature ratios in table 16.

TABLE 28.

Values of the expansion index n calculated on the assumption that $p/n' = \text{constant}$, with values of the velocity V_2 calculated from the temperature ratios in table 16 and from the equation given by Rowe[86].

Test 163. Po = 168.2 p.s.i.a. To = 296.3°A				Test 146. Po = 100.2 p.s.i.a. To = 275.9°A		
Dist from exit plane cm.	n'	V_2 calc from n'^{86} cm/sec x 10^{-4}	V_2 calc from T/T_o in table 16. cm/sec x 10^{-4}	n'	V_2 calc from n'^{86} cm/sec x 10^{-4}	V_2 calc from T/T_o in table 16. cm/sec x 10^{-4}
0.4	1.313	5.71	5.62			
0.5	1.315					
0.6	1.316	5.69	5.60			
0.7	1.318					
0.8	1.319	5.66	5.58			
0.9	1.319					
1.0	1.320	5.62	5.54			
1.1	1.322					
1.2	1.322	5.59	5.50			
1.3	1.322					
1.4	1.325	5.54	5.48			
1.5	1.329					
1.6	1.333	5.51	5.46			
1.7	1.336			1.368		
1.8	1.348	5.51	5.43	1.370	5.38	5.37
1.9	1.340			1.372		
2.0	1.341	5.44	5.39	1.371	5.34	5.32
2.1	1.342			1.372		
2.2	1.342	5.39	5.34	1.372	5.26	5.26
2.3	1.346			1.373		
2.4	1.347	5.33	5.28	1.373	5.20	5.19
2.5	1.347			1.372		
2.6	1.345	5.23	5.18	1.370	5.10	5.09
2.7	1.348			1.372		
2.8	1.354	5.13	5.09	1.369	4.97	4.97
2.9	1.351			1.369		
3.0	1.356	4.98	4.94	1.373	4.84	4.83
3.1	1.377			1.380		
3.2	1.371	4.84	4.82	1.377	4.69	4.66
3.3				1.369		
3.4				1.375	4.45	4.45

The value of the expansion index n' decreased, on moving down the divergence and as the stagnation pressure increased the agreement between the two values of the velocity calculated from the expansion index and the temperature ratio in table 16 was good. The slight difference can be attributed to the incorrect assumption made by Rowe that the flow upto the throat was isentropic.

Rowe postulated that the expansion index n' relevant to the flow in a particular nozzle could be determined by measuring the pressure coefficient C_p' near the nozzle exit plane. C_p' is the ratio of theoretical one dimensional isentropic static pressure to measured wall pressure. This method does not account for the observed variation in n' as the pressure coefficient at a given point in tests 146 and 163 remains almost constant.

In the discussion above a value of n' calculated on the assumption that $p/p_o = (\rho/\rho_o)^{n'}$ has been used to calculate the velocity in an equation in the derivation of which the relationship $T/T_o = (p/p_o)^{\frac{n'-1}{n'}}$ has been assumed to be applicable. The results indicate that the assumption was correct. Therefore lines of constant density ratio in the flow are also lines of constant pressure and temperature ratio, provided the value of n' remains constant along a

line. It was not possible to check the constancy of n' along the lines of constant density ratio and therefore the temperature and pressure profiles in the flow need not necessarily correspond to the density ratio profiles shown in figs 38 - 42.

The density ratio on the edge of the bottom boundary layer and on the centreline, determined by the method of characteristics (see fig 13) have been represented in fig 88 with the corresponding measured values obtained in test 163. The theoretical and measured results do not agree. However the two dimensional solution did give a very good estimate of the extent and magnitude of the two dimensional features of the flow pattern. For instance the measured profiles were approximately straight at 1.9 and 3.0 cms from the exit as the density on the centreline was equal to that on the edge of the bottom boundary layer at these points (see fig 88). The same feature being also demonstrated by the two dimensional solution at 1.6 and 2.9 cms from the exit plane. The regions of maximum curvature were also in similar positions, 2.5 and 2.6 cms from the exit plane for the theoretical and measured density variations respectively.

Comparison of the flow patterns in figs 38 & 40 for tests 143 and 146 showed that good reproducibility was

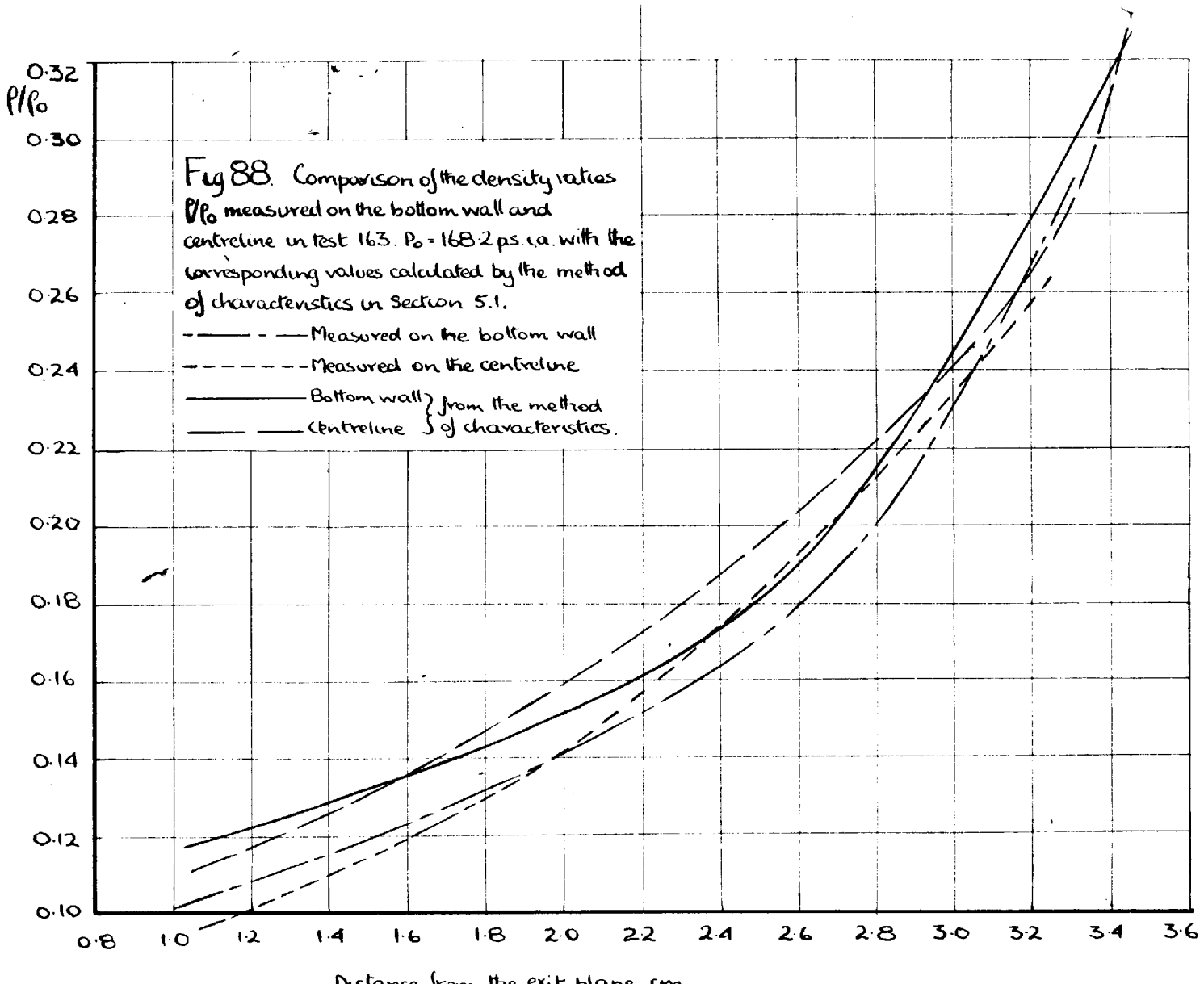
P/Po
0·32
0·30
0·28
0·26
0·24
0·22
0·20
0·18
0·16
0·14
0·12
0·10
0·8
1·0
1·2
1·4
1·6
1·8
2·0
2·2
2·4
2·6
2·8
3·0
3·2
3·4
3·6
Distance from the exit plane cm.
Fig 88. Comparison of the density ratios P/Po measured on the bottom wall and centreline in test 163. Po = 168·2 ps.ia. with the corresponding values calculated by the method of characteristics in Section 5.1.
Measured on the bottom wall
Measured on the centreline
Bottom wall
Centreline
from the method of characteristics.

obtained at a particular stagnation pressure. However the density profiles in the neighbourhood of the shock waves causing separation in tests 143 and 146 are more curved than the corresponding profiles in test 152, which are further upstream of the separation shock waves as the stagnation pressure was higher. The same feature was apparent from comparison of the density profiles in test 163. The density on the centreline of the nozzle also increased as the point of intersection of the two shock waves was approached (see figs 43,44 & 45). Hence the marked curvature of the density ratio profiles and the increased density in the vicinity of the shock waves causing separation were caused by the shock waves. These features of the flow pattern will be discussed in more detail in section 10.2.1.

10.1.2. Sonic Profile at the throat.

Values of M^+, the Mach number based on the velocity of sound at the point where M = 1 were calculated from the measured density ratios at the throat. This was done by first determining the value of $\frac{T}{To}$ corresponding to a chosen value of the Mach number. Then the entropy change corresponding to the temperature ratio was obtained from the curve in fig 52 and the density calculated from the expression $\Delta S = Cp \ln\left(\frac{T}{To}\right)^{\frac{1}{\gamma}}\left(\frac{\rho_o}{\rho}\right)^{\frac{\gamma-1}{\gamma}}$. The results tabulated in table 29 were then used to obtain the Mach number distribution across the throat plane and the profile at which sonic velocity or Mach number one was reached.

The sonic profile obtained from the density measurements and the entropy change has been plotted in fig 89 with the theoretical profile, tabulated in table 30, obtained from the solution in section 5.2. of the two dimensional flow equation in the limited throat region. The theoretical profile has been drawn about two axes, the nozzle centreline and the normal to the throat plane measured in appendix 1. The sonic profile determined from the density measured in the throat, by assuming isentropic flow from the reservoir has also been represented in fig 89.

TABLE 29.

The Density ratios corresponding to the values of the Mach number M^+ for the process in fig 52.

M^+	T/T_o	Entropy change ΔS cal/gm°C	Density ratio ρ/ρ_o
0.958	0.847	0.0017	0.645
0.966	0.844	0.0017	0.639
0.975	0.842	0.0017	0.634
0.983	0.839	0.0018	0.628
0.992	0.836	0.0018	0.623
1.000	0.833	0.0019	0.617
1.008	0.831	0.0019	0.612
1.017	0.828	0.0019	0.607
1.025	0.825	0.0020	0.601
1.033	0.822	0.0020	0.596

TABLE 30.

The theoretical throat profiles

a

Sonic profile calculated from the equation in section 5.2.

with $\frac{2h}{R} = 0.5090$

$\frac{h}{R} = 0.1111$

y cm	x cm
∓0.115	-0.0064
∓0.096	-0.0102
∓0.081	-0.0127
∓0.036	-0.0178
∓0.141	0
∓0.183	0.0127
∓0.221	0.0255
∓0.258	0.0382

b.

Variation of Mach number M^+ across the throat from the equation in section 5.2. with

$\frac{2h}{R} = 0.5090$

$\frac{h}{R} = 0.1111$

y cm	M^+
0.000	0.982
∓0.025	0.983
∓0.051	0.985
∓0.076	0.988
∓0.102	0.992
∓0.127	0.997
∓0.153	1.003
∓0.178	1.011
∓0.204	1.019
∓0.229	1.029
∓0.255	1.039

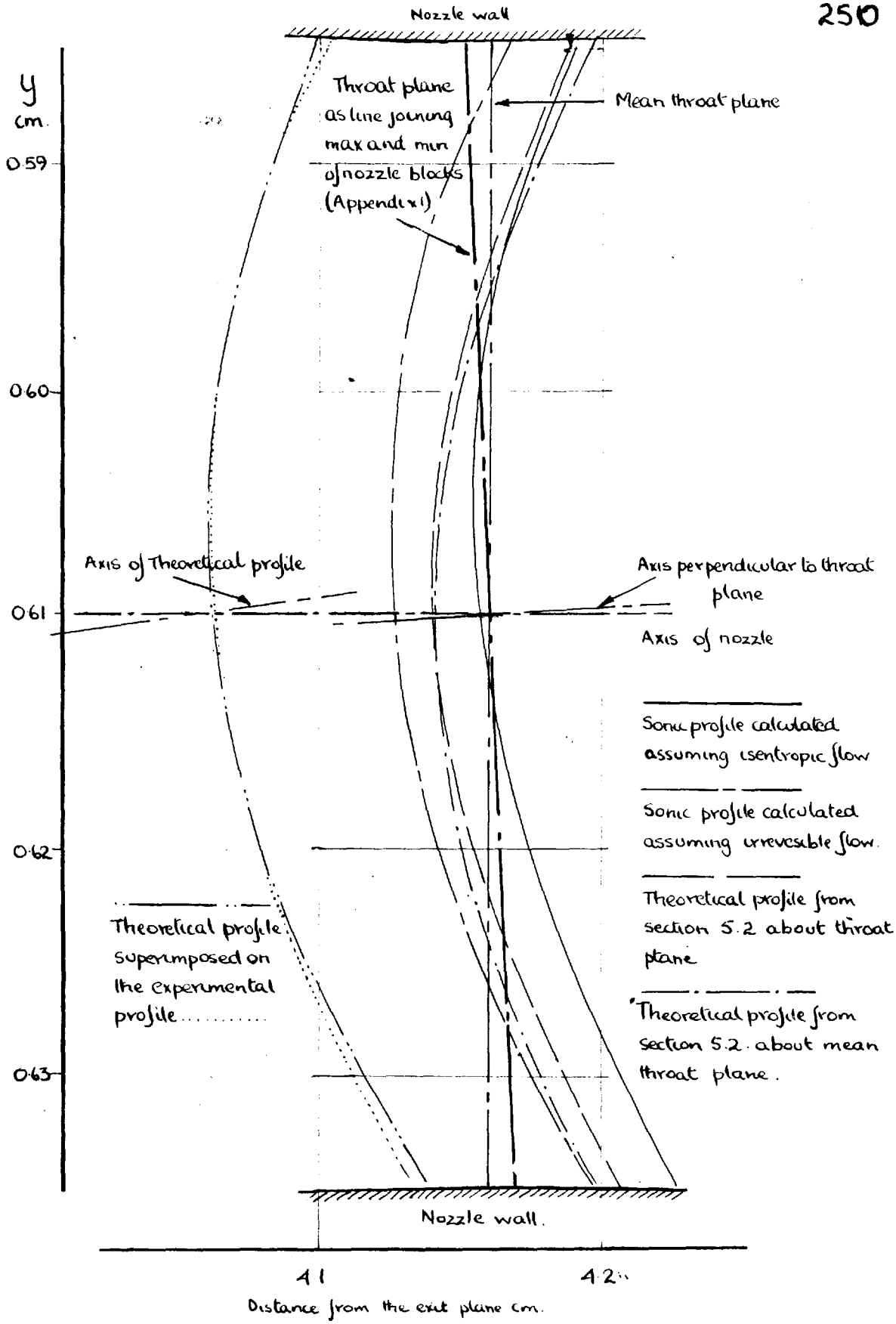

Fig 89 Theoretical and measured sonic profiles in the throat for test 152. Stagnation pressure 128·2 p.s.i.a.

It can be seen that the profiles obtained from the two dimensional solution were between the two experimental profiles, and that the theoretical profile drawn with its axis perpendicular to the measured throat plane was in better agreement with the experimental profiles. By tilting the axis of the theoretical profile and superimposing it on the experimental curve obtained from the measured density and entropy change, excellent agreement was obtained between the shape of the two curves.

A more correct approximation to the theoretical profile would have been obtained, if the entropy increase in the throat region had been assumed to be between that obtained from fig 52 and zero.

Hence although the theoretical method predicts the correct shape for the sonic profile in a real nozzle, its applicability was limited by the difficulty, in determining the actual section of minimum area and making corrections for the irreversibility of the flow. For the same reasons the experimental method was not satisfactory for determining the discharge coefficient of the nozzle from the measured Mach number profile across the throat.

10.2. Flow Separation.

In the region between the two shock waves causing boundary layer separation, two dimensional flow would be expected to extend to the shock waves. However it is apparent from the flow patterns drawn in figs 38 - 41 and the density variation in figs 44 & 45 that it did not as the density and the curvature of the density ratio profiles increased on approaching the shock waves.

Bershader[51] took interferograms of the flow above the exit plane in his divergent nozzle in a direction parallel to the glass walls which were extended for some distance above the exit plane. Examination of the interferograms showed that separation of the boundary layers on the glass walls took place at approximately 0.5 cms from the exit plane of the nozzle when the exit pressure was approximately 0.67 atmospheres. Hence it appears that recompression of an overexpanded two dimensional jet takes place in three dimensions.

There is no reason why recompression of the jet should not take place in shock waves which cause separation from the glass as well as from the nozzle walls, since in a nozzle of small divergence half angle, the boundary layer on all the walls at a given distance from the exit plane are at

approximately the same pressure and Reynolds number.

It was apparent from the photographs of the flow that the shock waves causing separation from the nozzle walls were two dimensional in that they have a plane parallel to the light beam. However shock waves causing separation from the glass walls would not be visible as the optical methods can not detect discontinuities whose plane is perpendicular to the light beam.

The density ratio measured along the centreline in Bersharder's nozzle has been plotted in fig 90 with the corresponding values obtained in test 146. Although the density ratios were not quantitatively the same, there was qualitative agreement between the two sets of results. It can be concluded therefore that the increase in density ratio as the shock intersection was approached was due to separation taking place from the glass walls of the nozzle.

Referring to figs 39,40 & 41 it can be seen that there was a marked increase in the curvature of the density ratio profiles, in the vicinity of the shock waves, when moving in the flow direction, before the minimum density ratio on the centreline was reached. If separation from the glass walls were caused by a plane shock wave, which extended from one nozzle wall to the other, the density would increase

Fig 90 A comparison of Bershardens'[51] density ratios ρ/ρ_0 measured on the nozzle axis and those measured for test 146. $P_0 = 100.2$ p.s.i.a. in the region between the two oblique shock waves causing separation from the nozzle walls.

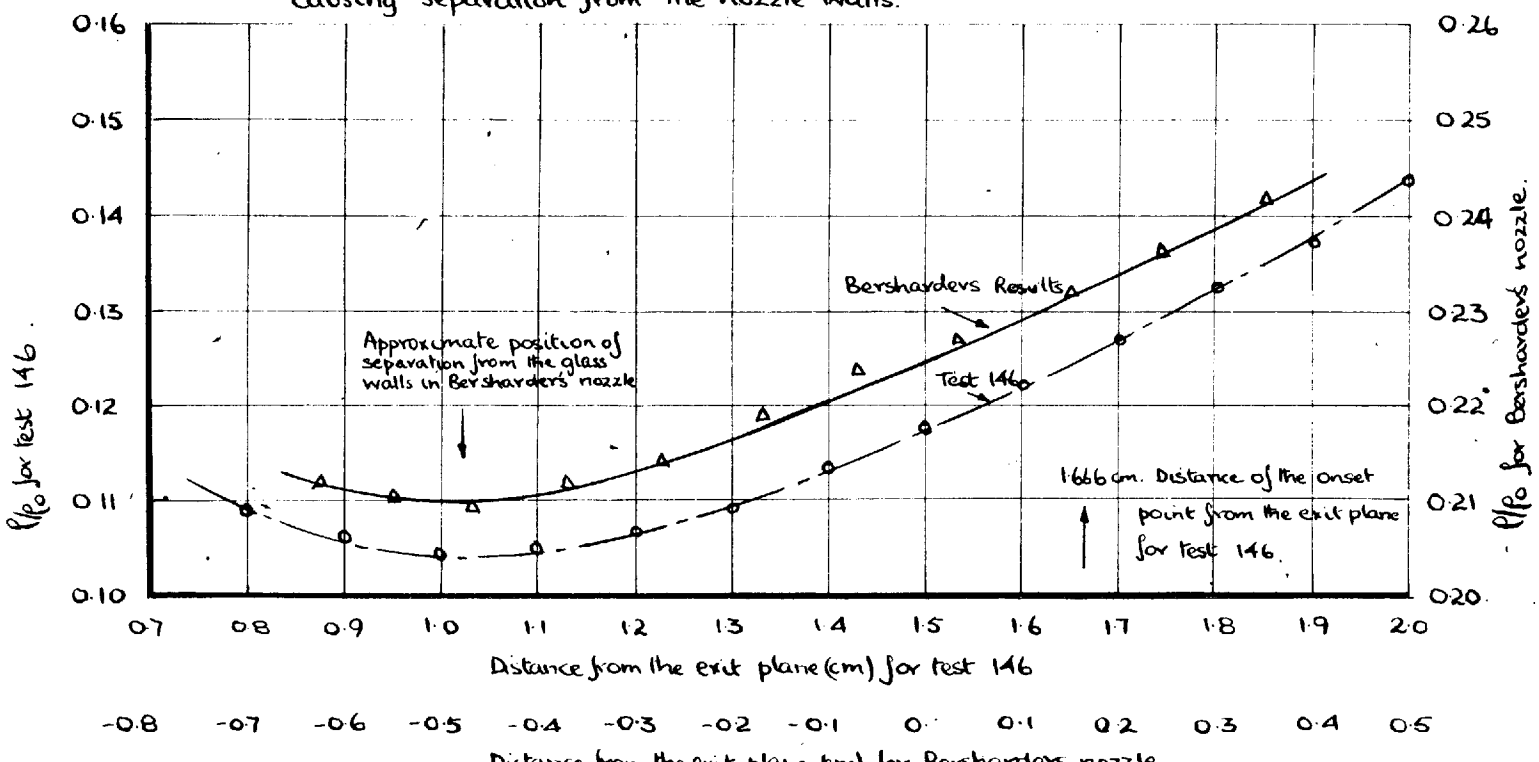

uniformly, without causing any increased curvature of the density ratio profiles. Ladenburg[66] studying the interaction of shock waves produced by a wedge, with the boundary layers on the glass walls, found that the shock waves produced by a 10^{o} half wedge appeared on interferograms to be made up of two shock waves separated by a region of varying density. The upstream shock was weak causing a small fringe shift, and diverged from the stronger shock wave on moving away from the wedge. The shock waves produced by the wedge were not strong enough to cause separation of the boundary layers on the nozzle walls. However the anomalous structure was attributed to interaction between the shock waves and the boundary layers on the glass walls. In this connection it should be noted that the incident shock waves causing boundary layer separation on flat surfaces appear as a series of lines and not as a single line (see figs 18 & 19 of ref 8 and also ref 12).

The flow pattern reproduced in fig 91 has been given by Gadd and Holder[9] for the boundary layer separation in the vicinity of a normal shock wave. The interesting feature of this flow pattern was the compression fan associated with the initial compression of the boundary layer, since it could account for the weak shock wave observed by Ladenburg.

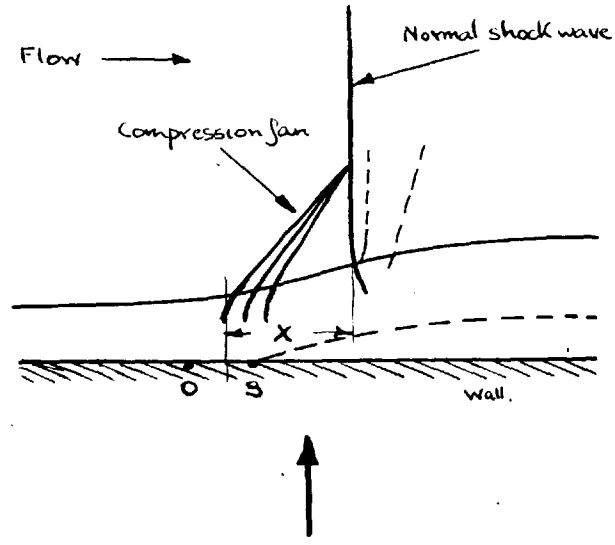

Fig 91. Flow pattern for separation caused by a normal shock wave from Gadd & Holder [9].

It can be seen from an examination of the flow photographs in figs 54 b & c, 58c and 72a, b & c, of steady turbulent separations that the weak shock wave appeared upstream of a stronger shock system in a manner similar to that observed by Ladenburg[66]. The same result would have been observed if the flow pattern in fig 91 were observed through the wall in the direction shown by the arrow. A weak shock system would appear upstream of the line representing the normal shock wave. Whether the results on the photograph will represent the full upstream spread X will depend on the density gradients in the compression fan.

It can be seen from fig 90 that the minimum in the density ratio on the centreline of Bersharder's nozzle corresponded to the observed position of separation on the glass windows. The only signs of this separation apparent from examination of the interferograms and schlieren photographs of the flow with the nozzle in the normal position were, the increased curvature of the fringes in the vicinity of the shock waves and the weak shock system immediately upstream of a stronger shock system. Hence it can be concluded that photographs of the flow in a nozzle in the normal position do not show detail of the compression fan or shock system associated with separation of the boundary

layers on the glass walls.

The shock system shown diagrammatically in fig 92 accounts for the observed results in the vicinity of the separation position. In this diagram it has been assumed that the oblique shock waves CFID and AJID causing separation from the nozzle walls look like strong normal shock waves to the boundary layers on the glass walls. Then compression fans ABE, CBE, FGH and JGH of the type shown in fig 91 would be formed as separation and compression of the boundary layers on the glass walls took place upstream of the oblique shock waves. When interferograms of this shock system are taken, the density will appear to increase on moving along the axis of the nozzle towards the shock waves. The density will be a minimum at the point B as the compression fans downstream of this point will cause the integrated density across the breadth of the nozzle to increase. The compression fans will also cause the density profiles in the vicinity of the shock waves to bend in exactly the same way as those in figs 39, 40 & 41. No calculations could be carried out to check the suggested flow pattern against the observed results as no experimental work on this type of separation is known to the author from which the upstream spread of the compression fans and the density rise through them could be determined.

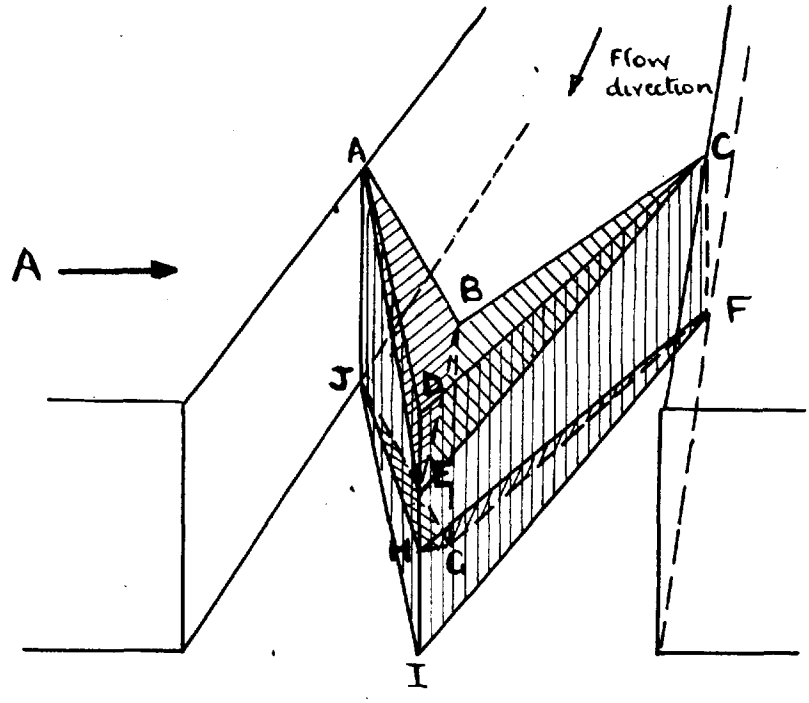

CDFI } Oblique shock waves
ADIJ } associated with separation of the boundary layer on the nozzle walls.

ABE } Planes representing the
CBE } start of the compression
FGH } fan associated with
JGH } separation promoted by a normal shock wave

Direction of light beam with which photographic observations were made.

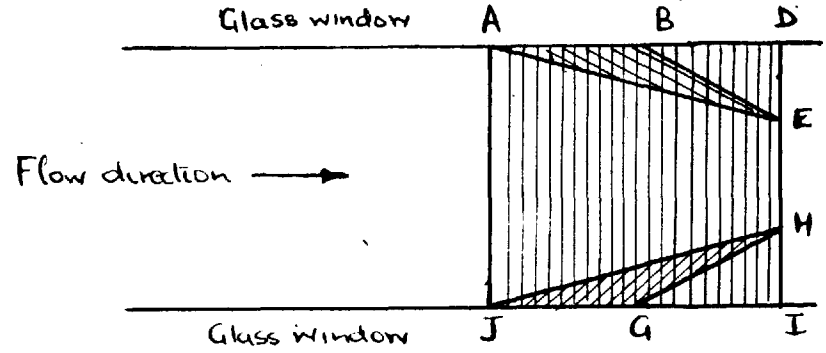

View in direction A

Fig 92 Suggested shock system at separation.

Gadd and Holder[23] pointed out that the results obtained by them at the N.P.L. for interactions between strong oblique shock waves and turbulent boundary layers indicate a greater upstream influence than that observed by Bogdonoff and Kepler[11] at Princeton. Gadd & Holder compared the different experimental details and found that the results at Princeton were obtained using models arranged so that the test boundary layer and those on the glass windows were of approximately the same thickness and Reynolds number. Conversely the N.P.L. results were obtained on models in which the test boundary layers were thinner and at lower Reynolds number than those on the glass walls.

A reasonable cause of the discrepancy between the two sets of results could be a difference in the position of separation on the glass walls relative to that on the model walls; the flow pattern at separation being analogous to that shown in fig 92. In this connection Bogdonoff[11] found that, when the model did not completely span the tunnel breadth, the results deviated considerably from those that were proved two dimensional; such as those obtained when the model completely spanned the tunnel. However patterns[8.15.] obtained in oil films on models completely spanning the tunnel demonstrate that the flow in the region

of reversed flow was not two dimensional in the vicinity of the glass walls.

In view of the present results and those observed above the question arises of whether the flow pattern in the vicinity of the separation position of a boundary layer on a two dimensional model can justifyably be assumed to be two dimensional.

The flow patterns in the reversed flow regions under the separated boundary layer have been presented in figs 75 - 78 for tests 143, 146 and 152 in the form of lines of constant ρ/ρ_a. The density was calculated on the assumption of two dimensional flow within the region, which in view of the discussion above was erroneous.

However although no great quantitative significance should be placed on the flow profiles in section 9.2.4. they show that there were a number of vorticies present in the reversed flow region. In test 152 for instance one of the vorticies present in test 143 and 146 has moved out of the nozzle. The agreement in fig 79 between the measured density ratios and those calculated from the pressure measurements on the bottom wall also showed that the air in the reversed flow region flowed in from the atmosphere. The density decreased as the shock wave was

approached which was compatible with the mechanism of separation put forward in section 2.

If isentropic flow and two dimensionality were assumed in the region of reversed flow reverse flow Mach numbers upto 0.4 were obtained; these corresponded to values of 0.4[10] and 0.3[11] measured in the reversed flow region for separations over steps.

The pressures recorded in the reversed flow region (table 18) at the pressure tapping nearest the orifice were significantly lower than atmospheric. The pressure loss was associated with the change in direction of the air flowing up the ends of the nozzle blocks into the reversed flow region. In the top region where the flow of air from the atmosphere was unobstructed by the nozzle base plate, the change in direction was rapid, as shadowographs of the flow (see fig 72c & d) showed a density change at the corner.

10.2.1. Symmetrical Turbulent Separation.

Owing to the small scale of the phenomenon studied in this research it was not possible to make sufficient wall pressure measurements in the region of interaction and so adequate wall pressure profiles were not obtained. It was not possible therefore, to determine the extent of upstream

influence and the true onset pressure. Therefore an approximation to the onset pressure was made by defining it as the pressure at the intersection of the steep pressure rise at separation, and the curve associated with the expansion of the undisturbed flow in the nozzle.

It has been shown by Gadd and Holder[10 12 18] that the upstream influence defined in terms of the undisturbed boundary layer displacement thickness, decreased with increasing Mach number for a given pressure rise across the separated boundary layer. The length taken as a measure of the upstream influence was that from the point at which the pressure first rose, to the point of intersection of the incident shock wave and the wall or to the wedge apex. Thus Gadd and Holder's results do not necessarily indicate that the difference between the actual and defined onset pressures will decrease as the Mach number increases, since they were concerned with the whole region of interaction and not the first initial pressure rise.

The results of Chapman et al[8] are not sufficiently accurate or detailed to provide any information on the first part of the pressure rise. However their results for separation over steps (see fig 93) did show that the gradient of the first steep pressure rise was independent of Mach

Fig 93. Comparison of Chapman's[8] results for the flow over steps obtained at a Reynolds number of 2.6×10^6 and those obtained in the nozzle

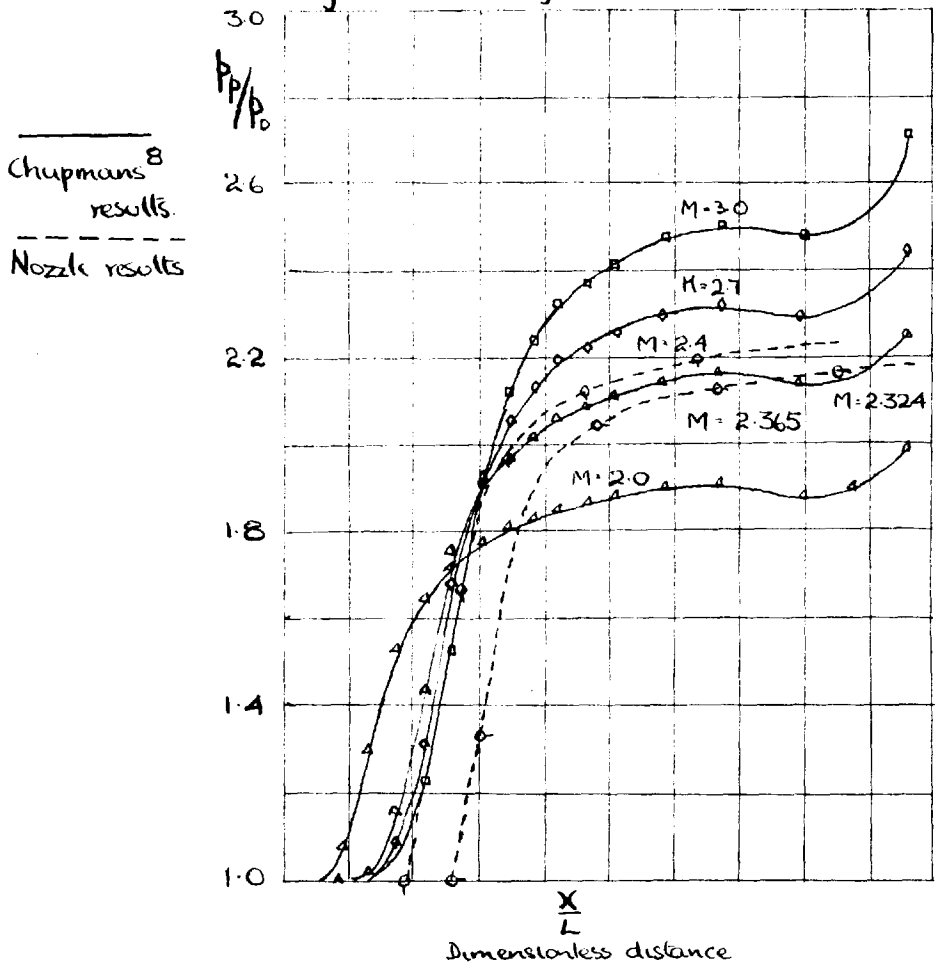

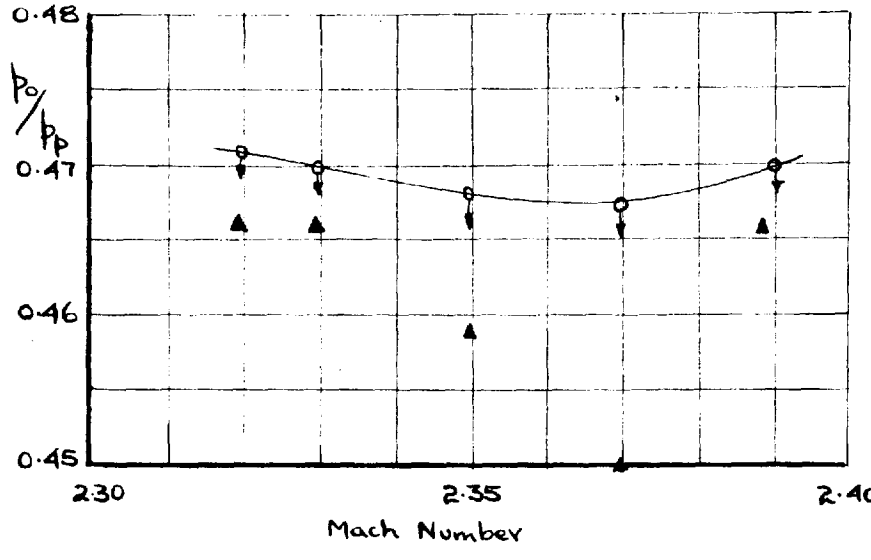

Fig 94 Comparison of Chapman's[8] results and the nozzle results presented in Table 19.

number and Reynolds number. Therefore the assumption of constant gradient for a series of tests carried out over a small range of stagnation pressure, which was made in the present investigation, should not introduce any error.

Chapman et al[8] and Bogdonoff[11] showed that turbulent separations followed a single curve only as far downstream as the separation point, further downstream the results depended on the shape of the reversed flow region. This result would be expected as it has already been shown that the velocities in the regions of reversed flow of turbulent separation were high. It is evident from comparison of the pressure distribution in fig 9 obtained for turbulent separation over steps and those in fig 56 & 57 for the separation of the boundary layer in the nozzle, that the latter correspond to separations over a step. This was not an entirely unexpected result as the shapes of the reversed flow regions were similar. The major difference was in the method by which the air 'mixed' at separation was supplied. In a nozzle it flowed in from the atmosphere, while in separations over steps it was supplied by the fluid reversed at reattachment flowing down the face of the step.

In fig 93 some results obtained by Chapman[8] have been

reproduced together with some of those obtained in the present nozzle. The dimensionless distance $\frac{X'}{L}$ used by Chapman has no exact parallel in the present work as L represented the length from the leading edge to the step face. Therefore an arbitrary value of L was chosen for the nozzle interactions so that at the onset point the dimensionless distances for the nozzle and step were approximately equal, when X' in the nozzle represented the distance from the throat plane. The values of p/p_{o}, the onset pressure ratio, were slightly greater than the corresponding values for the step. This was expected as the actual onset pressure in the nozzle was slightly greater than the value measured (see fig 6). It can be seen that the two dimensional accelerating flow in the nozzle upstream of separation did not significantly alter the shape of the wall pressure profiles in the region of interaction. Nor did differences in the means by which the air in the reversed stream was supplied. But since the pressure distributions in turbulent separations do not all lie on a single curve downstream of the separation position, it does not follow that turbulent separations in all nozzles are analogous to separations over steps, as the pressure distribution in the reversed flow region will depend on the nozzle shape downstream of the separation position.

Bogdonoff and Kepler[11] found that the peak pressure ratio for a step was independent of step height provided the step height was greater than two boundary layer thicknesses. Thus when the region of interaction was small it appeared that the mixing process which occurs downstream of separation was not established properly. The onset pressures obtained for the tests in group A and tabulated in table 19 were greater than would be expected from the trend shown by the results at lower stagnation pressures. Separation in the tests in group A took place close to the exit plane of the nozzle and therefore it appeared that the mixing process could not properly established, as the results were similar to those for steps of height less than two boundary layer thicknesses.

It can be seen from the results tabulated in table 19 that the peak pressure ratio $\frac{p_o}{p_p}$ increased as the stagnation pressure and Mach number decreased on moving from group B to group D, in a manner expected from the trend shown by the results obtained with steps. On subsequent reduction of pressure through groups E and F, the ratio remained constant. The constancy of the ratio with decreasing Mach number could be due to two factors, Reynolds number effects and the pressure at 0.6 cms from the onset point not being a true

representation of the peak pressure.

Gadd & Holder[9] plotting the results of a number of workers for the peak pressure rise over steps found that there was no significant variation of peak pressure ratio with Reynolds number, the same observation was made by Bogdonoff[11]. However Chapman et al, found a significant Reynolds number effect. The peak pressure ratio p_o/p_p was found to decrease with decreasing Reynolds number when the Mach number was held constant.

On moving down table 19 the Mach numbers and Reynolds numbers at separation progressively decrease. Therefore the peak pressure ratio would be expected to decrease as the Reynolds number decreased and increase as the Mach number at separation decreased. Hence Chapman's results show that the change of peak pressure ratio with Mach number would be offset to some extent by that with Reynolds number.

Chapman used a Reynolds number based on the length from the transition region to the onset point, while those presented in table 19, for the separations in the nozzle, were based on the distance from the throat to the onset point. The results determined in the nozzle were compared with those at corresponding Mach and Reynolds numbers obtained by extrapolating between Chapmans results for steps in fig 94.

Both sets of results showed the same trend. As transition was likely to take place downstream of the throat, in the tests at low stagnation pressure, the Reynolds numbers given for these tests in table 19 would be greater than those based on the distance from transition. Consequently the arrows attached to the points in fig 94 indicate the direction in which they would move if obtained from the true effective Reynolds number of the turbulent boundary layer.

With regard to the pressure at 0.6 cms from the onset point not being a true representation of the pressure rise in the region of interaction, Chapman[8] showed that there was little variation in the position of the peak pressure, relative to the onset point, as the Mach and Reynolds numbers were changed. It would appear therefore that the position of the pressure chosen as the peak pressure would not alter as the stagnation pressure changed.

The results in section 9.2.3. demonstrate that the boundary layer trips in the convergent section of the nozzle are effective in producing turbulent separations in the divergence. The peak pressure ratios in general increase as the reservoir pressure decreases with the exception of groups M, I and J. The latter effect was caused by a change in the downstream flow brought about by the intersection of the

shock system causing separation entering the nozzle, thereby altering the characteristics of the pressure rise downstream of the separation position slightly.

The shock systems in the tests at the low stagnation pressures were not symmetrical. The reason for this is not known, as the differences in the flow properties between the top and bottom walls as measured on the interferograms were not large enough to account for the differences in separation position. The effect also cannot be attributed to differences in the turbulence levels of the top and bottom boundary layers caused by the pressure tappings, as steady separation could be obtained with the separated jet flowing close to the top or bottom wall of the nozzle (see fig 73a & b).

A comparison has been made in fig 95, between the results obtained in this research for turbulent separations, and those for the flow over steps and other nozzles.

The agreement between the results obtained in this investigation and Crocco's theory was good over the range investigated. There was also general agreement with the results obtained for separations over steps. Therefore the results for turbulent separations over steps can be applied to nozzle separations with reasonable accuracy, provided provision is made for the pressure drop downstream of the

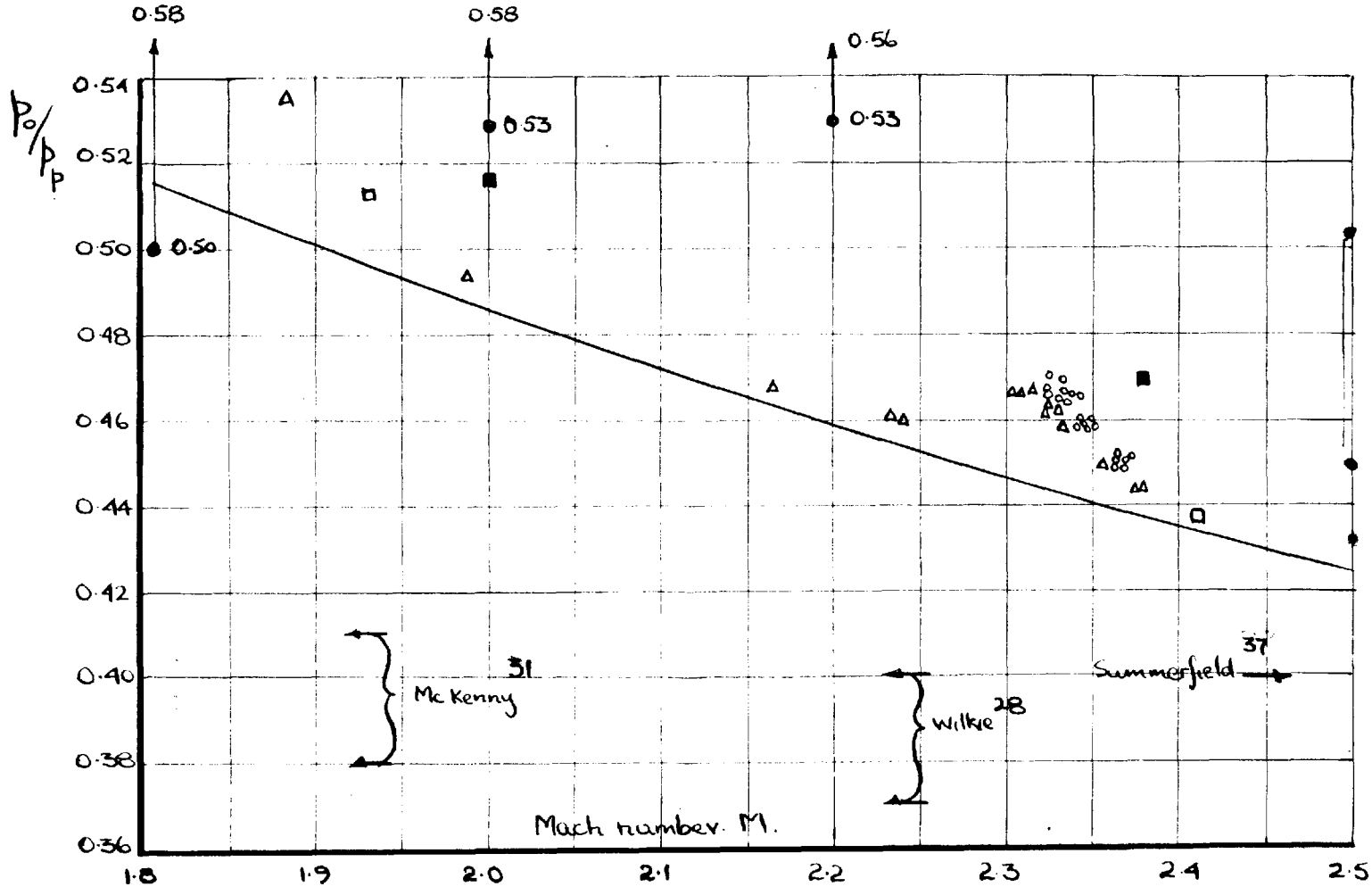

■ Data from Chapman 8
□ " " Gadd + Holder 9
● " " Arens + Spiegler 10 for the ratio p_o/p_a

△ Nozzle results with boundary layer trips fitted.
○ Nozzle results with no boundary layer trips fitted.
——— Curve obtained from Craco theoretical analysis in section 4

Fig 95. Comparison of peak pressure ratios p_o/p_p

separation position. The two dimensional accelerating flow in the nozzle, and the separation from the glass walls do not appear to affect the applicability of the results obtained on steps in wind tunnels.

10.2.2. Assymmetric Separation.

The results for separations in the low pressure range in the nozzle without trips have been presented in section 9.2.2. where it was also shown that the position of transition relative to the region of interaction was the prime factor in determining the flow pattern.

Separation did not take place uniformly across the nozzle breadth, and in certain instances the boundary layer appeared to undergo a turbulent separation on one side of the nozzle, and a transitional-type on the other. The flow pattern in this type of separation was steady and reproducible. The jet did not flip from one side of the nozzle to the other, as found by Wilkie[28] at stagnation pressures just in excess of critical.

With reference to the shadowographs of the flow pattern in the jet presented in figs 59-62, it can be seen that often the boundary layer on the bottom wall underwent a transitional-turbulent separation, while that on the top wall has the

characteristics of a laminar separation. Therefore it would appear that the pressure holes on the bottom wall raise the turbulence level of the boundary layer thereby promoting transition. No other results have come to the authors attention in which two different types of separation occured side by side. Chapman et al[8] found that pure turbulent separations could be unsteady; separations over a compression corner were found to be unsteady, as the pressure distribution was 'jagged' and the corresponding shadowgraphs were not sharp. In most instances the unsteadiness was observed in the reversed flow region only. An analogous result was observed in some of the tests in group G. However in all the other tests at low stagnation pressure, no fluctuations in the pressure recorders were observed and the results were reproducible; the pressure always 'peaking' on the same pressure hole. Chapman does not indicate whether his results were reproducible and attributed the jagged pressure distributions to differences in the connections to the pressure tappings, resulting in the pressure lines having different response times. The same argument cannot be applied to the results obtained in section 9.2.2., since it was found that changes in the pressure connections had no effect on the reproducibility of the results. It was also

found that smooth curves could be drawn through the results obtained at the odd and even numbered pressure holes respectively. It was not possible to do the same thing with Chapman's results even though a single line of holes were used.

In the process of varying the tunnel pressure Chapman observed the conversion from transitional to turbulent type separations. The conversion was observed to be unsteady and oil films did not accumulate along threadlike lines as they did in steady separations. Instead the oil wandered irregularly over the plate in a jagged random fashion. The same type of separation is apparent in fig 2.21 of reference 81, where separation over a sphere, downstream of a boundary trip, took place along a jagged line. The pressure profiles obtained by Chapman were jagged and irregular, he does not show whether these pressure profiles were reproducible, but in view of the unsteadiness it is thought that they were not. Thus, when transition took place close to the separation point in the nozzle investigated, there were points of similarity between them and separations over steps etc., particularly in the flow photographs, but there appeared to be a difference in that non oscillatory separation could take place from different points on the nozzle width at one and the same time.

In comparing the results in the nozzle with and without

boundary layer trips, it can be seen that separations that occur in the laminar transitional regime were extremely sensitive to slight differences in the flow characteristics across the nozzle width, while fully turbulent separations were not. Chapman et al[8] obtained a similar result, when non uniformity in the downstream geometry across the span of a model was found to cause laminar separation to lose two dimensionality.

In the shadowographs of the flow in which laminar type separations took place, the characteristic white line can be seen to curve away from the nozzle wall (figs 61 & 62) in some instances it appeared to do this in the absence of a shock wave, test 106 fig 62 and test 125 fig 61 for instance, but in other tests the shock wave associated with the initial compression can be seen to appear at a point remote from the wall, fig 61, test 191 bottom wall, test 192 top wall. The same results were apparent in the shadowographs of Chapman et al but only a relatively small area of the flow above the model was shown. Tucker[41] studying flow separation in a nozzle of variable divergence half angle, at very low densities, found that as the Mach number in the divergence increased, separation of an initially attached boundary layer took place without any shock wave appearing

in the schlieren photographs. When the boundary layer was made turbulent at the throat of the nozzle by means of sand paper strips, the boundary layer remained attached throughout the Mach number range. It is thought that the initially turbulent boundary layer became laminar as the Mach number increased[8 29] thereby promoting separation. The strips of sandpaper promoted turbulence throughout the whole Mach number range thereby delaying separation.

The compression fan associated with the initial compression of a laminar boundary layer can appear to be absent in shadowographs and schlieren photographs of the flow. However they are clearly shown on interferograms in fig 62.

Owing to the difficulty in defining any characteristic points on the pressure profiles of the laminar and transitional type separations, no comparison of the results with those obtained in wind tunnels could be made. However comparison of the approximate results given in fig 71 for the onset, atmospheric pressure ratio, $\frac{p_o}{p_a}$, with those in fig 94 show that laminarisation of the boundary layer is a method of reducing the pressure rise required for separation. Means by which this can be done such as by sucking or cooling warrant further study, especially in an effort towards achieving a nozzle which will work close to optimum thrust throughout a wide range of ambient pressures.

10.3.

Boundary layer velocity profiles.

The velocity distribution in turbulent boundary layers is often represented in the form[81]

$$\frac{V_y}{V} = (y/\delta)^{\frac{1}{n}}$$

It has been shown in section 9.4.1. that the experimental velocity profiles are of a type similar to that obtained from the expression above, but tend to move up the velocity axis as the Reynolds number and Mach number of the flow decrease; that is towards profiles of higher values of n.

Profiles obtained in the constant Mach number region of a Laval nozzle by Bersharder[51] showed a tendency to move towards profiles of higher n as the reservoir pressure and hence the Reynolds number increased. Other results[66] obtained interferometrically on a flat plate show the same tendency in the range of Reynolds numbers 0.88×10^6 to 1.1×10^6. The trend reversed between 1.1 and 2.9×10^6 but at increased Reynolds numbers the profiles remained substantially the same. A similar result was obtained by Monaghan[87] where the profiles obtained on a flat plate moved to lower values of n as the Reynolds numbers increased from 1.04 to 2.7×10^6. Results for the flow of an incompressible fluid in a pipe presented

in reference 81 showed the same tendency as Bershardes results, the value of n increasing as the Reynolds number increased. Experiments carried out by Wilson[88] gave agreement with a $^{1}/_{7}$th power law for a range of Mach numbers from 1.6-2.2 and Reynolds numbers from 3×10^6 to 19×10^6. The data on the variation of the shape of the turbulent compressible boundary layer on a flat plate with Mach number and Reynolds number is meagre and rather inconclusive, and therefore it is difficult to make comparisons. However the trend shown by the present results in moving towards higher values of n as the Reynolds number decreased is in agreement with the interferometric results of Landenburg[66] and with those of Monaghan[87] in the Reynolds number range 1.0 to 2.7×10^6. The experimental profiles presented in Section 9.4.1. fall within this Reynolds number range. (See table 31). Each of Ladenburg's profiles also showed a tendency to move towards higher values of n as the dimensionless distance $\frac{y}{\delta}$ increased. The same trend was shown by the results in section 9.4.1., see particularly fig 83.

The boundary layer profiles in Section 9.4.1. have been plotted in figs 96-98 using the momentum thickness instead of the boundary layer thickness as a means of making the distance plot dimensionless. The momentum thickness was calculated

TABLE 31.

Boundary Layer Results.

Dist from the exit plane cms.	Displacement thickness δ^+ cms.	Momentum thickness δ^{++} cms	Reynolds Number x 10^{-6}	Mach No.	Shape factor $H = \delta^+/\delta^{++}$	Wilson '95 Mach No.	Wilson '95 H	Monaghan '96 H
						2.0	3.1	
						2.1	3.3	
						2.2	3.5	
						2.3	3.7	
Test 163 Po = 168.2 p.s.i.a.								
0.334		0.00580						
0.360		0.00583						
0.427		0.00636						
0.493	0.0223	0.00575	2.493	2.36	3.88			3.79
0.652	0.0217	0.00588	2.482	2.34	3.69			3.75
0.891	0.0186	0.00575	2.432	2.31	3.24			3.69
1.181	0.0134	0.00387	2.369	2.28	3.46			3.63
1.421	0.0131	0.00371	2.307	2.25	3.53			3.57
Test 152 Po = 128.2 p.s.i.a.								
1.001		0.00490						
1.029		0.00435						
1.055	0.014	0.00423	2.112	2.34	3.31			3.75
1.186	0.014	0.00385	2.083	2.33	3.64			3.73
1.318	0.013	0.00350	2.040	2.31	3.72			3.69
Test 146 Po = 100.2 p.s.i.a.								
1.659		0.00223						
1.672		0.00251						
1.685		0.00252						
1.698	0.009		1.722					
1.725	0.009	0.00251	1.721	2.32	3.51			3.71
1.828	0.008	0.00226	1.663	2.30	3.54			3.67
2.300	0.006	0.00173	1.533	2.14	3.46			3.35

Fig 96. Boundary layer velocity profiles for test 146, stagnation pressure 100·2 p.s.i.a.

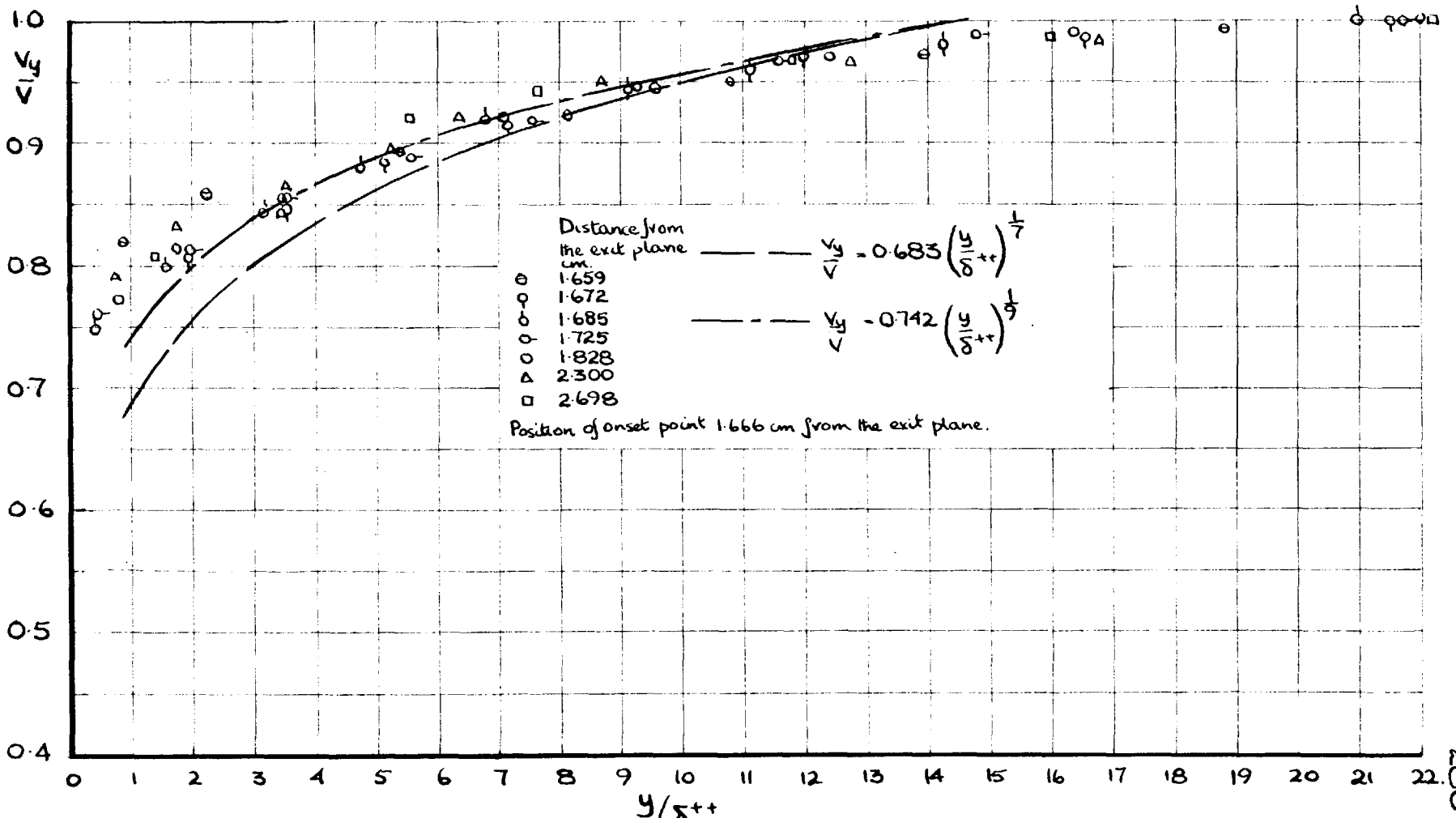

Fig 97 Boundary layer velocity profiles for test 152, stagnation pressure 128·2 p.s.i.a.

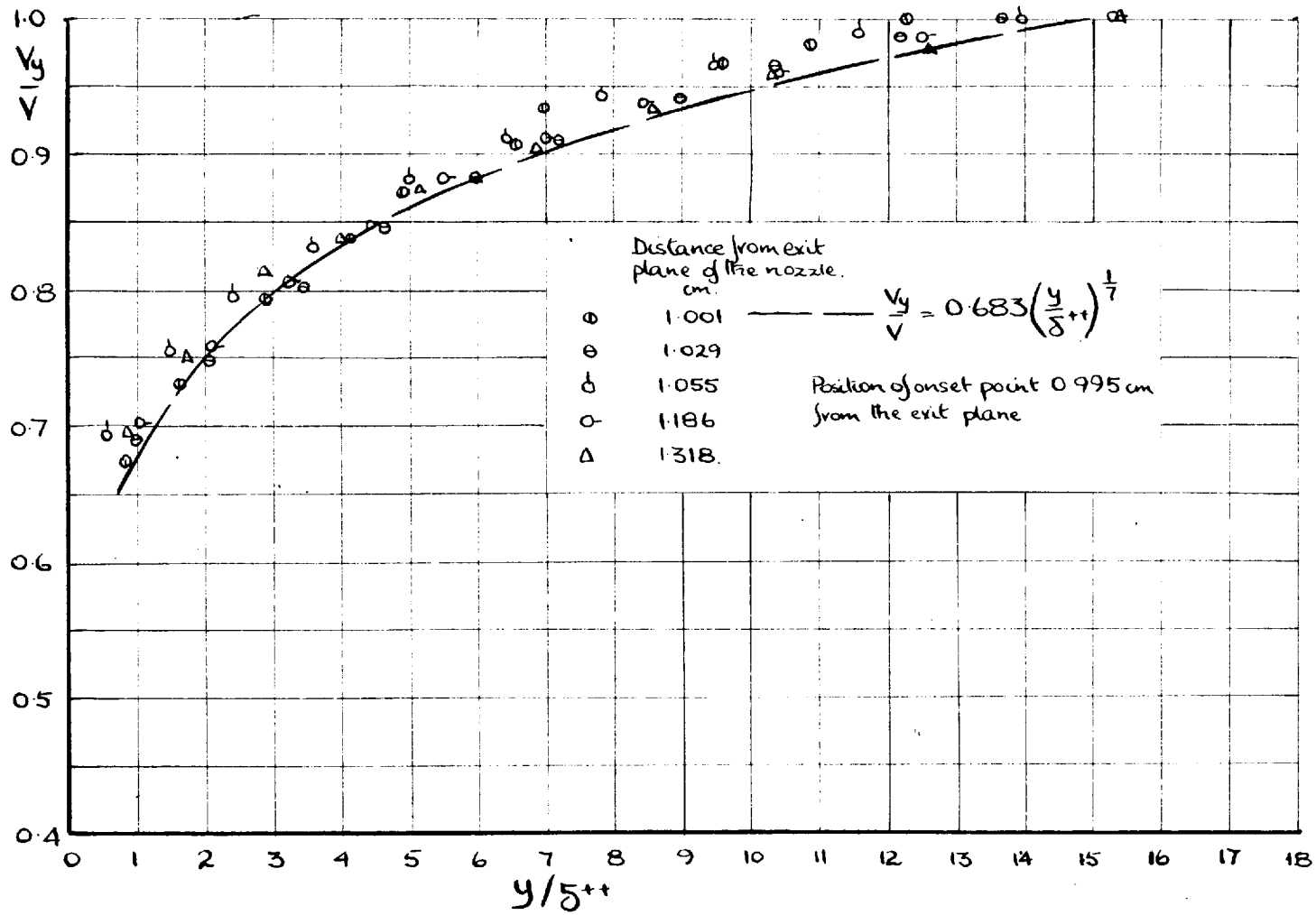

Fig 98 Boundary layer velocity profiles for test 163, stagnation pressure 168.2 p.s.i.a

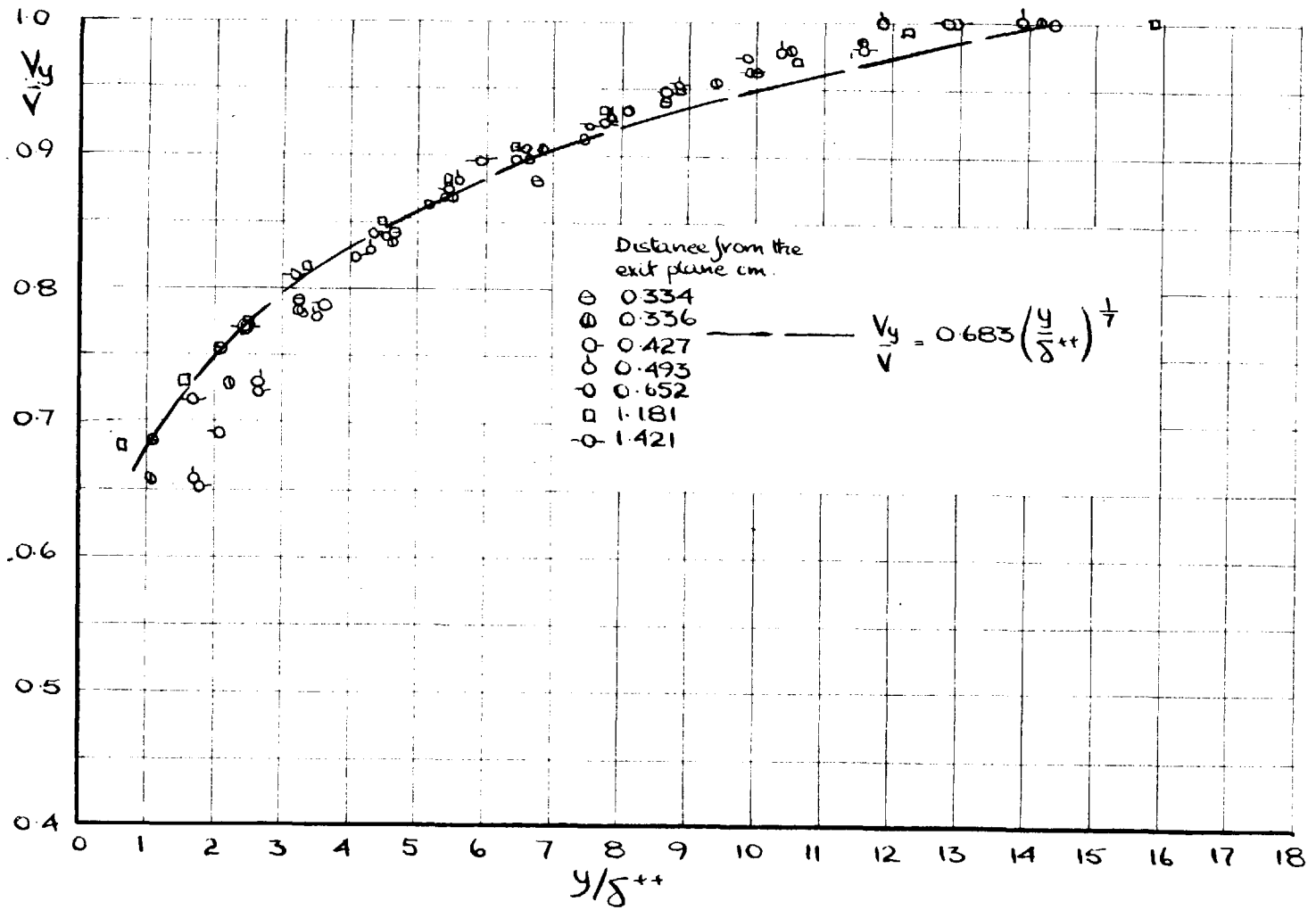

assuming that there was no pressure variation across the boundary layer and that the stagnation temperature was constant. With reference to figs 96-98 it can be seen that the spread of the profiles for any particular test is reduced, but same trend is shown with changing reservoir pressure as in section 9.4.2.

The profile $\frac{Vy}{V} = 0.683 \left(\frac{y}{\delta_{++}}\right)^{1/7}$[89] which has been found to fit the experimental results for a flat plate at a Mach number of 2.41 over the range of Reynolds numbers tested, is shown on figs 96-98. The above profile and the results of test 152 are in good agreement, while those of tests 146 and 163 lie above and below it respectively. The profile $\frac{Vy}{V} = 0.742 \left(\frac{y}{\delta_{++}}\right)^{1/9}$ obtained by Wilson[88] at M = 1.999 on the wind tunnel wall is in good agreement with those of test 146 in fig 96.

Wilson[88] defined a shape coefficient H by:-
$H = \frac{\delta^{+}_{++}}{\delta_{++}}$ and found that it increased with Mach number. The values calculated for tests 146, 152 and 162 are presented in table 31 together with results taken from Wilson and calculated from the expression $H = 1.29 + 0.45\ M_1^2$ obtained[87] from the results on a flat plate at M = 2.46. There is good agreement between the shape coefficients, even though in the case of Wilsons results, the experimental

velocity profiles are at variance.

From the discussion above it can be seen that no positive conclusions can be drawn regarding the effect of the pressure and density gradients on the turbulent boundary layer profiles, as the results for flat plates are not complete and in some cases are in conflict.

SECTION II CONCLUSIONS

II.1. Flow in the Wetted region of the Nozzle.

The main conclusions on the nature of the flow in the two dimensional nozzle are:

(1) The flow was not isentropic, the entropy change between the reservoir and a given point on the wall of the divergence increasing as the reservoir pressure was raised.

(2) Although the flow was one dimensional in the low speed flow in the convergent section of the nozzle, the variation in the density ratio did not follow that given by the one dimensional isentropic theory.

(3) The Mach numbers determined from the temperature ratios, calculated from the measured density and pressure ratios, were in agreement with those obtained from Mach angle measurements.

(4) The variation of the density ratio in the nozzle was not in agreement with that predicted by estimating the heat transfer through the nozzle walls and carrying out an analysis due to Shapiro [46].

(5) The expansion index n' [86] along the wall of the divergence was found to decrease on moving down the

divergence and also as the reservoir pressure increased.

(6) The results are incomplete in that it was not possible to determine the effect of scale, heating and cooling of the nozzle walls, and the ratio of the specific heats of the gases used on the expansion index n'. For the effects of these variables to be evaluated further work is required in which different nozzles and gases are used. Provision should be made in these nozzles to heat and cool the walls and also to measure the static pressure at points remote from the walls to determine whether the value of n' remains constant along a line of constant density ratio.

(7) The agreement between the shape of the experimental sonic profile and that obtained by solution of the two dimensional flow equation was excellent. However the position of the experimental profile could not be defined accurately owing to the difficulty in determining the section of minimum area.

(8) The displacement thickness when used as a correction term for the boundary layer in the nozzle over compensated for the difference between the one dimensional and measured pressure ratios and caused the difference between the density ratios to increase.

11.2. Flow Separation.

The conclusions on boundary layer separation in the nozzle are:-

(1) Separation of the boundary layers in a two dimensional nozzle can be divided into three different types, turbulent, transitional and laminar. Each type has a characteristic flow pattern and Reynolds number range in the same way as in separation over steps and wedges in wind tunnels.

(2) The flow patterns and the variation of the peak pressure ratio with Mach number for turbulent separations were the same as those obtained for steps.

(3) By making the boundary layers turbulent artificially in the convergent section, separation in the divergence became turbulent throughout.

(4) The variation in peak pressure ratio for the turbulent separations agreed with that predicted by Crocco's[44] theory.

(5) When turbulent separation took place close to the exit plane of the nozzle and the region of reverse flow small, the pressure rise across the separating boundary layer changed in a manner expected from results[11] obtained for very small steps.

(6) The shock waves causing separation of the turbulent boundary layers on the nozzle walls, also caused separation to take place from the glass walls of the nozzle.

(7) Insufficient evidence was obtained to make a full description of the shock pattern at separation possible. For complete analysis further work is required in which pressure surveys are taken along the glass walls and photographs of the flow taken in a direction perpendicular to the nozzle walls.

(8) The effect of separation from the glass walls on that from the nozzle walls could not be determined. To evaluate the effect experiments would have to be carried out on nozzles of different width.

(9) A number of vorticies were present in the reversed flow region under the separated turbulent layers, and the air in the region was entrained from the atmosphere.

(10) The pressure rise across the separating laminar layers was much lower than that across an equivalent turbulent layer.

(11) Separation was assymmetric and steady when laminar separation took place. The position of laminar separation also varied across the nozzle breadth.

(12) The position of transition relative to the region of interaction was the prime factor in determining the flow pattern at separation.

(13) Turbulent and transitional separation could occur side by side across the breadth of the nozzle.

(14) As the pressure rise required to cause separation of a laminar layer is low, a research programme should be carried out towards achieving complete laminarisation of the boundary layer in a nozzle either by cooling or sucking. It should then be possible to design nozzles which will work close to optimum conditions (i.e. exit pressure equal to ambient pressure) at all altitudes.

11.3. The Boundary Layer.

(1) The boundary layer velocity profiles did not correspond to the $^{1}/_{7}$th power law, that is $\frac{V_y}{V} = \left(\frac{y}{\delta}\right)^{\frac{1}{n}}$ where $n = 7$.

(2) The velocity profiles moved towards profiles of higher n as the Mach number and Reynolds number of the flow decreased.

(3) It was not possible to make a detailed analysis of the flow pattern in the boundary layer in the vicinity of separation due to the extremely small scale of the phenomenon in the nozzle. However by increasing the

scale, by carrying out experiments at low pressure in which simultanious pressure and density measurements are taken in the boundary layer close to the point of separation, it would be possible to determine the flow pattern.

REFERENCES.

1. Prandtl, L. Ueber Flüssigkeitsbe wegung bei sehr kleiner Reibung Proc III. Intern. Math Congr. Heidlburg. 1904. Translated and reprinted in N.A.C.A. TM.452.1928.
2. Ferri,A. Experimental results with aerofoils tested in the high speed tunnel at Guidonia. No. 17. 1939 Translated as N.A.C.A. TM. 946.
3. Fage, A., and Sargent,R.F. Shock wave and boundary layer phenomena near a flat surface. Proc. Roy. Soc. A. vol 190 p.1 1947.
4. Ackeret, J., Feldmann,F., and Rott,N. Investigations of compression shocks and boundary layers in fast moving gases. N.A.C.A. TM 1113 1947 .
5. Liepmann, M.W. The interaction between boundary layers and shock waves in transonic flow. J Aero. Sci. vol 13 p. 623 1946.
6. Donaldson, C.DuP. Effects of interaction between a normal shock wave and a boundary layer N.A.C.A. C.B. 4.A27. 1944.
7. Prandtl, L. Der Luftwiderstand von Kugeln Nachrichten von der Koniglichen gesselschaft der Wissenschaften zu gottingen Math Phy Klass 1914. p 170 - 190.
8. Chapman, D.R., Kuehn,D.M., and Larson,H.K. Investigation of separated flows in supersonic and subsonic streams with emphasis on the effect of transition. N.A.C.A. Report 1356. 1958.
9. Gadd, G.E., and Holder D.W. Boundary layer separation in two dimensional flow A.R.C. Technical Report. C.P. No. 270 (17,485). 1956.
10. Gadd, G.E. Holder,D.W., and Regan,J.D. Interactions between shock waves and boundary layers. Proc. Roy. Soc. Series A. vol.226. p.227, 1954
11. Bogdonoff, S.M., and Kepler,C.E. Separation of supersonic turbulent boundary layers. J. Aero. Sc. vol. 22, No.6,1955.
12. Holder, D.W., Pearcey,H.H., and Gadd,G.E. The interaction between shock waves and boundary layers. A.R.C. 16,526 - Perf. 1199 - FM 2017 1954
13. Crocco,L., and Lees,L. A mixing theory for the interaction between dissipative flows and nearly isentropic streams. J. Aero.Sc. Vol 19. p.649, 1952.
14. Honda, M. A theoretical investigation of the interaction between shock waves and boundary layers J. Aero/Space Sci. Vol 25 p. 667 - 678 1958.
15. Thomann H. Measurements of heat transfer and recovery temperature in regions of separated flow at a Mach number of 1.8. The Aeronautical Research Institute of Sweden, Report 82, 1958.

16. Kuehn, D.M. An experimental investigation of the pressure rise required for the incipient separation of turbulent boundary layers in two dimensional supersonic flow. N.A.S.A. Memo 1 - 21 - 59A. 1959.
17. Mair, W.A. Experiments on the separation of boundary layers on probes in front of blunt nosed bodies in a supersonic air stream. Phil Mag. vol 43 p. 695, 1952
18. Holder, D.W., and Gadd, G.E. The interaction between shock waves and boundary layers and its relation to base pressure in supersonic flow. Symposium on boundary layer effects in aerodynamics at the N.P.L. April 1955. Paper No. 8.
19. Lange, R.H. Present status of information relative to the prediction of shock induced boundary layer separation. N.A.C.A. TN. 3065 1954.
20. Gadd, G.E. Interactions between wholly laminar or wholly turbulent boundary layers and shock waves strong enough to cause separation J. Aero.Sci. Vol 20 p.729, 1953.
21. Ritter, A., and Kuo, Y.H. Reflection of a weak shock wave from a boundary layer along a flat plate. I. Interaction of weak shock waves with laminar and turbulent boundary layers analysed by the momentum integral method. N.A.C.A. TN. 2868. 1953.
22. Donaldson, C.Du.P. and Lange, R.H. A study of the pressure rise across shock waves required to separate laminar and turbulent boundary layers. N.A.C.A. TN. 2770 1952.
23. Gadd G.E., and Holder, D.W. The behaviour of supersonic boundary layers in the presence of shock waves. 7th Anglo-American Aero. Conference, New York 1959. I.A.S. Paper No. 59 - 138.
24. Beastall D., and Eggink, H. Some experiments on breakaway in supersonic flow. Part 1. R.A.E Tech.Note Aero. 2041, 1950; Part II R.A.E Tech. Note Aero. 2061, 1950
25. Gadd G.E. and Holder D.W. The interaction of an oblique shock wave with a boundary layer on a flate plate Part 1. Results for M = 2. A.R.C. 14,848. F.M. 1714. 1952.
26. Lighthill, M.J. On boundary layers and upstream influence Part I. A comparison between subsonic and supersonic flows. Proc. Roy. Soc. Series A. vol 217, p. 344 1953.
27. Gadd, G.E. The effects of convex surface curvature on boundary layer separation in supersonic flow. A.R.C. 18038 F.M.2335. 1955.
28. Wilkie, D. On the separation of supersonic flow in nozzles. Ph.D. Thesis London 1955. In less detail, Fraser R.P., Eisenklam P., and Wilkie D. Investigation of supersonic flow separation in nozzles. Journ. Mech. Eng. Sci. Vol 1. 1959.

29. Winter K.G., Scott-Wilson,J.B., Davies,F.V. Methods of determination and of fixing boundary layer transition on wind tunnel models at supersonic speeds. A.R.C. CP. 212, 1955.
30. Sergienko, A.A., and Gretsov, V.K. Transition from a turbulent to laminar boundary layer. Dokl. Akiad, Nauk vol 125 (4) p 746, 1959. U.S.S.R.
31. McKenny, J.D. An investigation of flow separation in an overexpanded supersonic nozzle. Thesis. Cal. Inst. Tech. U.S.A. 1949. Extract published as appendix to ref 32.
32. Summerfield, M., Foster,C.R., and Swan, W.C. Flow separation in overexpanded supersonic exhaust nozzles. J. Amer. Rocket Soc., vol 24 1954.
33. Foster, C.R., and Cowles, F.B. An experimental study of gas flow separation in overexpanded nozzles for rocket motors. Cal. Inst. Tech. U.S.A. Progress Report No 4 - 103 1949.
34. Fraser, R.P. Flow through nozzles at supersonic speeds M. O.S. D.S.R. Extra Mural Research F72/115 Interim Report No. 3. 1951.
35. Scheller, D., and Bierlein, J.A. Some experiments on flow separation in rocket nozzles. J. Amer. Rocket Soc., vol 23 p. 28. 1953.
36. Green, L.G. Flow separation in rocket nozzles. J. Amer. Rocket Soc., vol 23, p.34, 1953.
37. Summerfield, M. Fundamental problems in rocket research. J.Amer. Rocket Soc. No.81, p.79, 1950.
38. Sutton, G.P. Rocket propulsion elements. J. Wiley and Sons 1949.
39. Ashwood, P.F., Crosse, G.W., and Goddard, Jean. E. Measurements of the thrust produced by convergent-divergent nozzles at pressure ratios upto 20. A.R.C. CP. No. 326, (18.771) 1957.
40. Arens, M., and Spiegler, E. Separated flow in overexpanded nozzles at low pressure ratios. Bull. Res. Counc. of Israel Vol. 11 C. 1962.
41. Tucker, N.B. An experimental investigation of flow separation in a nozzle at high Mach numbers and low density. Inst. of Aerophysics. Univ.of Toronto. U.T.I.A. Report No. 33. 1955.
42. McKenny, J.D. An investigation of flow separation in a two dimensional transparent nozzle . Jet Propulsion Lab. Calif. Inst. Tech. Pasadena Calif. Progress Report No. 20 - 129.
43. Green, L., and Nall, K.L. Experiments on porous wall cooling and flow separation control in a supersonic nozzle. J. Aero Space Sci. Vol. 26 p. 689, 1959.

44. Crocco, L. and Probstein, R.F. The peak pressure rise across an oblique shock emerging from a turbulent boundary layer over a plane surface. Princeton University Aero. Eng. Report No. 254. 1954.
45. Stewartson, K. Correlated incompressible and compressible boundary layers. Proc. Roy. Soc A. Vol 200, p.84, 1949.
46. Shapiro, A.M. The dynamics and thermodynamics of compressible fluid flow. Vol. 1. Ronald Press Co., N.Y. 1953.
47. Erdmann, S.F. Entwurf von uberschalldusen mit zeichnerischer diskussion des Anfangswert. Nationaal Luchtvaartlaboratorium Bericht F5. 1947. Trans:- High Speed Fluid Kinetics Lab. Imperial College.
48. Harrop, R. An introduction to the method of characteristics R.A.E. Report Aero. 2275. 1948.
49. Harrop, R. The design of supersonic nozzles R.A.E., Report, Tech. Memo No. Aero, 42, 1949.
50. Herbert, P.J., and Older S.J. Tables for use in the investigation of supersonic fields of flow by the method of characteristics. R.A.E., TN. No. C.W.1., Nov. 1946.
51. Bersharder, D. Interferometric analysis of supersonic flow through rectangular nozzles at M = 1.7. Ph.D. Thesis 1948 Princeton, U.S.A.
52. Sauer, R. General characteristics of the flow through nozzles at near critical speeds. N.A.C.A. T.M. 1147, 1947.
53. Taylor, G.I. The flow of air at high speeds past curved surfaces. A.R.C. No. T. 2904 (1930) and R. and M. 1,381, 1930.
54. Mach, L. Ober ein interferenzrefractometer. Wierner Berichte 101, 5, (1892). 102, 1035, (1893).
55. Zehnder, L. Ein neuer interferenzrefracktor. Zeit fur Instrumentkunde vol. 11. p. 275, 1891.
56. Winkler, E.H. Analytical studies of the Mach Zehnder interferometer. Part I Navord, Lab. Report 1077, 1947: Part II Navord Lab. Report 1099 1950.
57. Kinder, W. Theorie des Mach-Zehnder interferometer und Beschriebung einer Gerates nait Einspiegeleinstellung. Optik Vol. 1, p. 413, 1946.
58. Tanner, L.H. The Optics of the Mach-Zehnder interferometer. A.R.C. R. and M. 3069, 18733. 1959.
59. Ladenburg, R., and Bersharder, D. Art. A3. Volume 1X of High speed aerodynamics and jet propulsion. Physical Measurements in gas dynamics and combustion. Editors Von Karmen. T., Dryden, L.L., and Taylor, M. Oxford University Press 1955.
60. Weyl. F.J. Analytical methods in optical examination of supersonic flow Navord 211 - 45. 1945.

61. Winkler, J. The Mach Zehnder interferometer applied to studying an axially symmetric supersonic air jet. Rev. Sci. Inst. Vol. 19, p. 307 1948.
62. Schardin, H. Theorie und Anwendung des Mach-Zehnderschen interferenz - refractometers. Zeit. fur Instruementenkunde Part I. Vol. 53 p. 396, 1933.
63. Winkler, J.R., Van Voorhis, C.C., Panofsky R., and Ladenburg R. A study of shock waves by interferometry N.D.R. C. Rep No. A - 332 or O.S.R.D. Rep No. 52 D4 1949.
64. Ladenburg, R., Winkler, J., and Van Voorhis, C.C. Interferometric studies of faster than sound phenomena. Part I. The gas flow around various objects in a free homogeneous supersonic air stream Phy. Rev. Vol. 73 p. 662, 1948.
65. Ladenburg, R., Van Voorhis, C.C., and Winkler, J. Interferometric study of supersonic phenomena. Part I. A supersonic air jet at 60 p.s.i. tank pressure. Navord Rep 69 46 1949. Part II Navord Rep 93 - 46. Condensed in Physical Review Vol. 76. 1947.
66. Ladenburg R., and Bersharder, D. Optical studies of boundary layer phenomena on a flat plate at Mach number 2.35. Princeton Univ. Report NR061-20 N6 ori - 105 Task II. 1952.
67. Crede, C.E. Vibration and shock isolation. Wiley and Sons 1951 Page 38.
68. Tanner, L.H. Light scource requirements for high speed gas flow. A.R.C. 18165 F.M. 2357.
69. Bowman, J. Private communication. A.R.D.E. Fort Halstead Kent.
70. Pack, D.C., and Groth, E. Investigation of the flow past finite wedges of 20° and 40° apex angle at subsonic and supersonic speeds using a Mach Zehnder interferometer. A.R.C. R and M 2321 1949.
71. Wood, G.P. Optical methods for examining the flow in a high speed wind tunnel. Part II. Interferometer methods. Agardograph 23. 1956.
72. Looms, J.S.T., and North R.J. Short duration spark light scources for photography of high speed airflow. 3rd International Congress on High Speed Photography 1956. Butterworths 1957.
73. Ladenburg, R., and Bersharder, D. Interferometric studies on laminar and turbulent boundary layers along a plane surface at supersonic velocities. Symposium on Experimental Compressible flow. U.S. Naval Ord. Lab. NOLR. 1133. 1949
74. Chemical Engineers Handbook. Editor Perry, J.H. 3rd Edition, 1950. McGraw-Hill.
75. Lukasiewiez J., and Royle, J.K. Effects of air humidity in supersonic wind tunnels. A.R.C. R and M 2563 (10977) 1953.

76. Fraser, R.P., Rowe, P.N., and Coulter, M.O. The efficiency of supersonic nozzles for rockets and some unusual designs. Proc. Inst. Mech. Eng. Vol. 171. No. 16. 1957.
77. Kafka, F. An experimental study of some problems in the design of supersonic nozzles. Ph.D. Thesis. University of London, 1949.
78. Hower, W.L., and Buchele, D.R. Practical considerations in specific applications of gas flow interferometry N.A.C.A. 3507. 1955.
79. Hower, W.L., and Buchele, D.R. A theory and method for applying interferometry to the measurement of certain two dimensional gaseous density fields. N.A.C.A. TN 2693 1952.
80. Gadd, G.E. Holder, D.W., and Regan, J.D. An experimental investigation of the interaction between shock waves and boundary layers. A.R.C. 16.680 F.M. 2054.
81. Schlichting, H. Boundary layer theory. McGraw Hill 4th Edition 1960.
82. Naysmith, A. Heat transfer and boundary layer measurements in a region of supersonic flow separation and reattachment. R.A.E. TN Aero 2558 1958.
83. Ferri, A. The elements of aerodynamics of supersonic flow. MacMillan. N.Y. 1949.
84. Hooker, S.G. The flow of compressible fluid in a circular wind channel. Proc. Roy. Soc. Series A. vol 135. p. 498. 1932.
85. Munday, G. The rapid discharge of gases through bursting disc valves and similar pressure release mechanisms. Ph.D. Thesis London 1961.
86. Rowe, P.N. The trust of a supersonic conical nozzle with non-isentropic flow Proc. Inst. Mech. Eng. Vol. 172 p. 877, 1958.
87. Monaghan R.J., and Johnson J.E. The measurement of heat transfer and skin friction at supersonic speeds Part II. Boundary layer measurements on a flat plate at M = 2.5 and zero heat transfer. A.R.C. CP. No. 64 1952.
88. Wilson R.E. The turbulent boundary layer characteristics at supersonic speeds. Theory and experiment. J.Aero.Sci. Vol. 17 p. 585. 1950.
89. O'Donnell. R.M. Experimental investigation at a Mach number of 2.41 of average skin friction coefficients and velocity profiles for laminar and turbulent boundary layers and an assessment of probe effects. N.A.C.A. TN. 3122 1954.

APPENDIX 1. Measurement of the nozzle.

(1) Measurement of the nozzle profile

The nozzle blocks, described in section 7.2. were measured fitted into the nozzle holder (see fig 25) with manometer leads etc. attached, on a two dimensional microscope accurate to $\pm$ 0.0005 cms. The measurement was carried out once only as it was not necessary to dismantle the nozzle after measurement.

The nozzle holder containing the nozzle blocks was mounted on the table of the microscope, with the windows removed so that the nozzle was in the x, y, plane, with its walls parallel to the z axis, (see fig 1a). The final polishing process of the nozzle walls caused the edges to be rounded off slightly, therefore the microscope (25x) was adjusted until there was no parallex between the cross wires and the nozzle wall zz. (see Fig 2a).

Each side of the nozzle was measured twice. The maximum deviation from the mean value for either side was $\mp$0.00 cms. The mean values for each side are presented in table 1a together with the mean of all the measurements. As the machining and polishing operations used in the manufacture of the nozzle blocks could only be carried out between

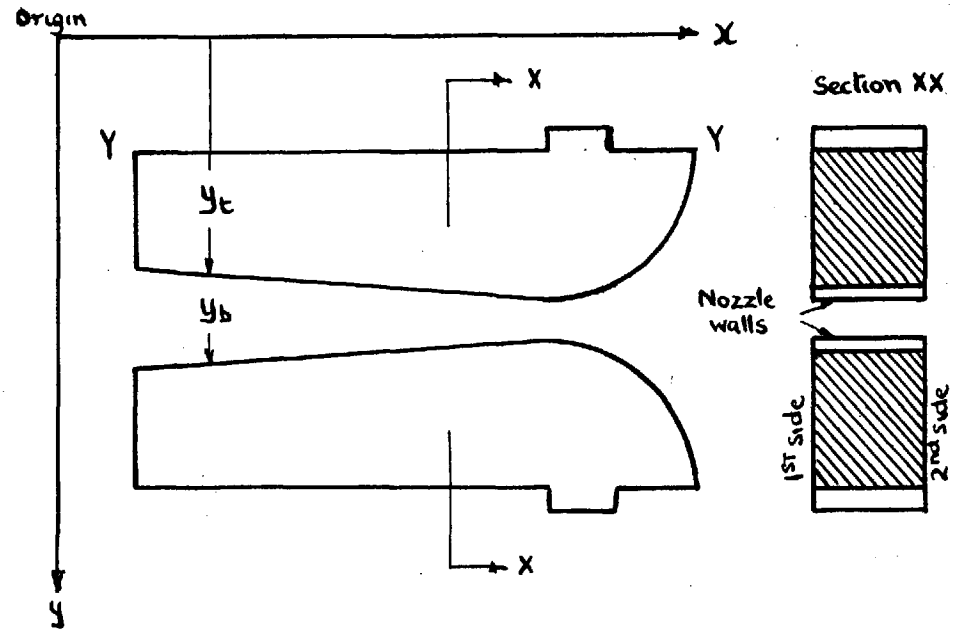

Fig 1a. Frame of reference for measurement of nozzle profile

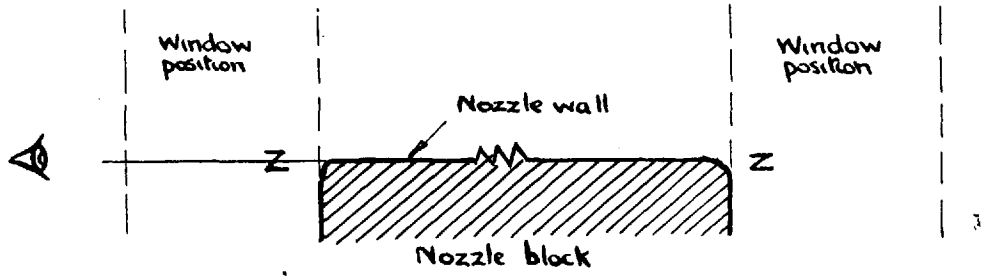

Fig 2a Plane of focus for measurent of nozzle profile.

tolerances, there were slight differences in the dimensions measured on the two sides of the nozzle. The width on one side at any particular x value was upto 1.7% greater than that on the other; at the throat the differences were small 0.2% (see table 1a).

The position of the throat plane or section of minimum area was determined by plotting the mean profile at the throat with an expanded y scale (as in fig 3a) to increase the curvature. In this way the throat plane was found to be slightly skewed, being 4.17 cms and 4.15 cms from the exit plane on the bottom and top walls of the nozzle respectively.

(2) Measurement of the pressure holes.

As the holes were in the central region of the nozzle wall and the axial distance from the exit plane only was required, the nozzle was tipped up 30° (fig 4a) so that the holes could be brought into focus. The tilted nozzle was lined up by means of the edge YY which was found to be parallel to the x axis of measurement.

The distances of the hole axes from the exit plane were determined twice and the mean distances are tabulated in table 2a.

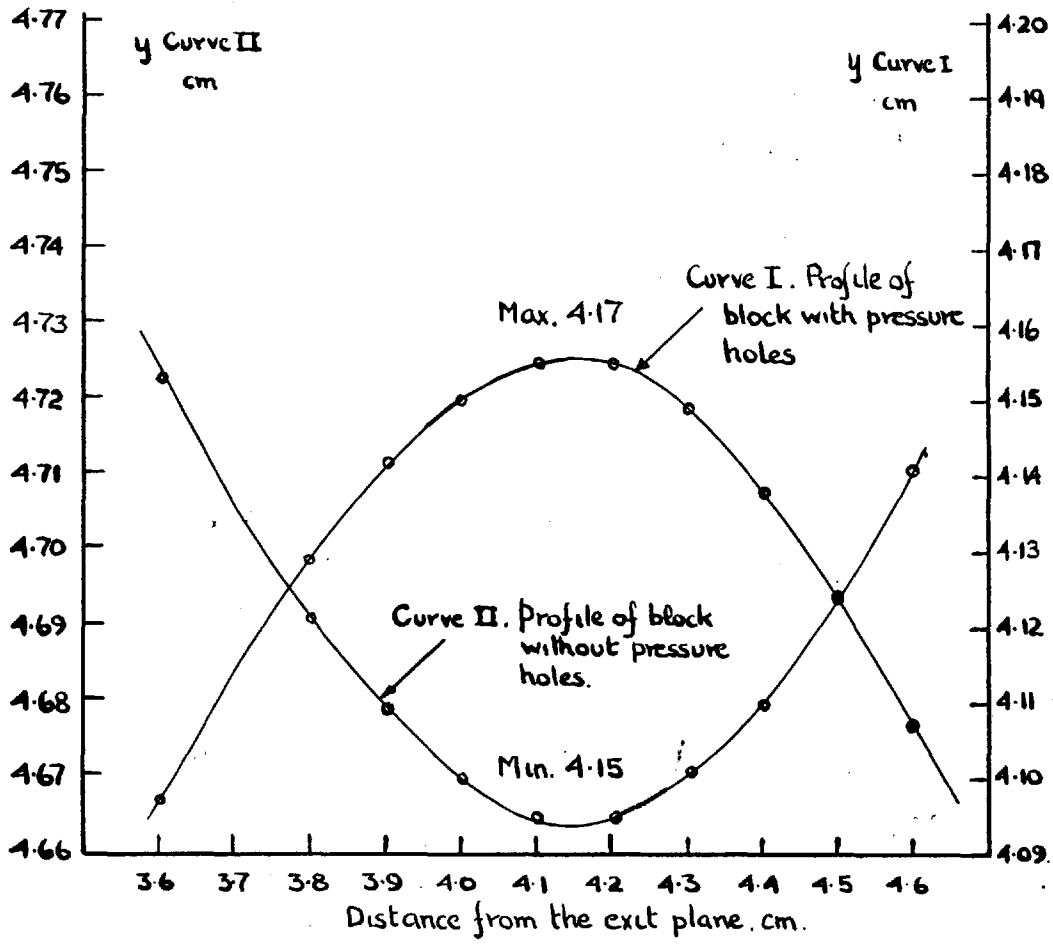

Mean throat width = 4·664 - 4·155 = 0·509.

Fig. 3a. Determination of throat position and width

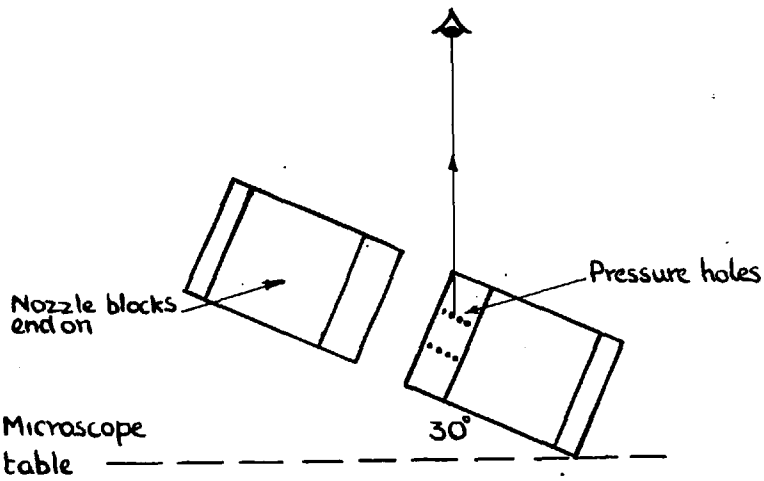

Fig. 4a. Method of measuring position of the pressure holes.

TABLE 1a. Nozzle Profile Measurements (All dimensions in cms.)

Distance from End	First side mean of 2 Measurements		Mean width first side	Second side Mean of 2 Measurements corrected so that 1st and 2nd ℄ coincident		Mean width second side	Mean of 1st & 2nd side measurements		Mean width	Difference between 1st & 2nd widths	Percentage difference	Area ratio based on throat width of 0.509 cm.
	yb	yt		yb	yt		yb	yt				
0	5.366	3.454	1.912	5.366	3.455	1.911	5.366	3.454	1.912	0.001	0.05	3.756
0.2	5.328	3.492	1.836	5.326	3.495	1.832	5.327	3.493	1.833	0.005	0.3	3.601
0.4	5.293	3.527	1.766	5.289	3.531	1.758	5.291	3.529	1.762	0.008	0.5	3.462
0.8	5.221	3.599	1.622	5.219	3.601	1.618	5.220	3.600	1.620	0.004	0.2	3.183
1.2	5.149	3.670	1.479	5.147	3 672	1.475	5.148	3.671	1.477	0.004	0.3	2.902
1.6	5.081	3.740	1.341	5.076	3.744	1.332	5.079	3.742	1.337	0.009	0.7	2.627
2.0	5.007	3.813	1.194	5.005	3.816	1.189	5.006	3.814	1.192	0.005	0.4	2.345
2.3				4.952	3.868							
2.4	4.936	3.884										
2.8	4.866	3.954	0.912	4.863	3.957	0.906	4.865	3.956	0.909	0.006	0.7	1.786
3.0	4.831	3.989	0.842	4.826	3.994	0.832	4.829	3.992	0.837	0.010	1.7	1.644
3.2	4.796	4.023	0.773	4.793	4.027	0.766	4.794	4.025	0.769	0.007	0.9	1.511
3.4	4.760	4.060	0.700	4.757	4.063	0.694	4.759	4.062	0.697	0.006	0.4	1.369
3.5	4.743	4.077										
3.6	4.726	4.095	0.631	4.721	4.098	0.623	4.724	4.097	0.627	0.008	1.3	1.232
3.7	4.708	4.112										
3.8	4.692	4.128	0.564	4.689	4.130	0.559	4.691	4.129	0.562	0.005	0.9	1.104
3.9	4.680	4.140	0.540	4.677	4.143	0.534	4.679	4.142	0.537	0.006	1.1	1.055
4.0	4.671	4.149	0.522	4.669	4.151	0.518	4.670	4.150	0.520	0.004	0.8	1.022
4.1	4.664	4.155	0.509	4.665	4.155	0.510	4.664	5.155	0.509	0.001	0.2	1.000
4.2	4.665	4.155	0.510	4.665	4.155	0.510	4.663	4.155	0.510	0.000	0.0	1.002
4.3	4.672	4.149	0.523	4.671	4.150	0.521	4.671	4.149	0.522	0.002	0.3	1.026
4.4	4.682	4.138	0.544	4.679	4.139	0.540	4.680	4.138	0.542	0.004	0.7	1.065
4.5	4.696	4.124	0.572	4.692	4.128	0.564	4.694	4.126	0.568	0.008	1.4	1.108
4.6	4.714	4.106	0.608	4.709	4.111	0.598	4.711	4.107	0.604	0.010	1.6	1.187
4.7	4.762	4.058	0.704	4.756	4.064	0.692	4.759	4.061	0.698	0.012	1.7	1.371
4.8	4.826	3.994	0.832	4.822	3.999	0.823	4.824	3.997	0.827	0.009	1.1	1.625

TABLE 2a.

Distance of pressure holes from exit plane of nozzle.

Hole	Distance from exit plane cms. Mean of 2 measurements	Hole	Distance from exit plane cms. Mean of 2 measurements.
1	3.506	11	1.953
2	3.357	12	1.797
3	3.190	13	1.639
4	3.042	14	1.486
5	2.886	15	1.329
6	2.729	16	1.169
7	2.574	17	1.019
8	2.423	18	0.861
9	2.261	19	0.701
10	2.108	20	0.544
		21	0.386

TABLE 3a

Nozzle width

1st Measurement. inches.	20 tests after 1st. 2nd Measurement. inches.
0.9596	0.9592
0.9594	0.9595
0.9598	0.9595
0.9598	0.9592
0.9599	0.9595
0.9599	0.9593
0.9601	0.9595
0.9590	0.9592
0.9594	0.9598
0.9597	0.9592
Mean 0.9597	Mean 0.9595

Mean 0.9596

(3) Measurement of nozzle width.

The gaskets described in section 7.2. were fitted and the windows replaced. After 20 tests the windows were removed, leaving the gaskets adherring to the nozzle blocks. The width was measured at randomly chosen points and the test section reassembled. The measurement was repeated after a further 20 tests. The results of the two measurements presented in table 3a showed that the effects due to gasket compression were small.

APPENDIX 2. Solution of the two dimensional irrotational flow equation by the method of characteristics.

It can be shown that when a stream of fluid flows past a small point disturbance with velocity greater than sound, the regions influenced are in the cone whose apex coincides with the disturbance and whose generators are Mach lines. Therefore the effect of a deviation at A in the wall, fig 5a, is transmitted into the stream along the Mach line AB.

The deviation at A is in accordance with the stipulation that the flow is isentropic, as expansion takes place gradually, therefore if the flow is isentropic before A it remains so after. As the flow has expanded in the zone ABD the velocity must be greater than that in CAB. Therefore the value of the velocity potential in ABC ϕ_2, will be different from that in CAB ϕ_1. But as the flow is continuous the functions ϕ_1 and ϕ_2 must have the same values along AB, the values of the first derivatives (the velocity components) of these functions must also have the same value. Thus two solutions corresponding to ϕ_1 & ϕ_2 must exist for the potential flow equation:-

$$\left(1 - \frac{\phi_x^2}{a^2}\right)\phi_{xx} + \left(1 - \frac{\phi^2_y}{a^2}\right)\phi_{yy} - \frac{2\phi_y\phi_x}{a^2}\phi_{xy} = 0 \qquad (1)$$

The solutions must be coincident for all the points on the line AB and the values of the first derivatives must also

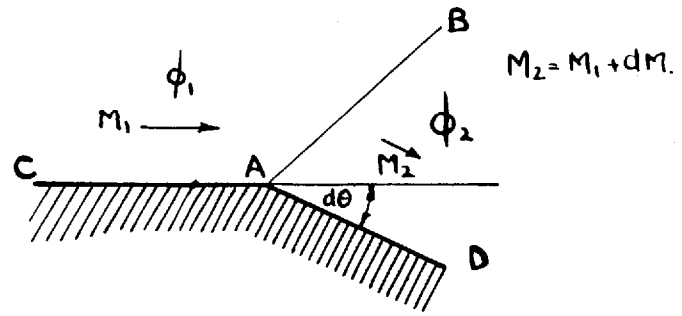

Fig 5a.

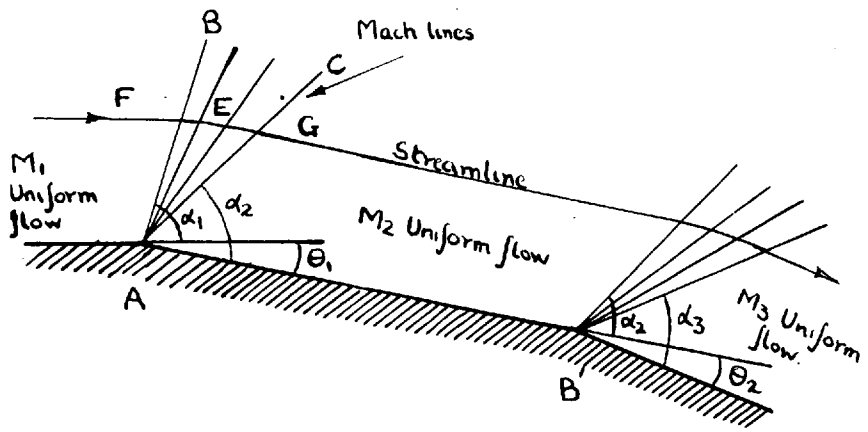

Fig 6a

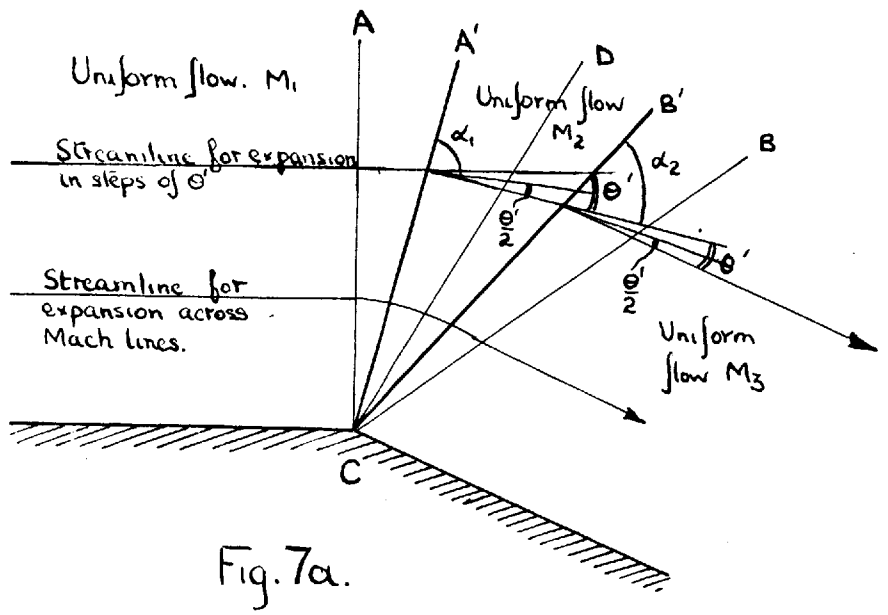

Fig. 7a.

be coincident. The Mach line AB for which these conditions apply is a characteristic line of the differential equation above.

In references[46.48.83] the equations to the characteristics at a point in a fluid have been found and used to find the relationship between the Mach number and the direction of the velocity sector at all points along a characteristic line namely:-

$$\frac{dv}{d\theta}\frac{1}{v} = -\frac{1}{\sqrt{(M^2-1)}} \qquad (2)$$ which when integrated becomes

$$\theta = -\sqrt{\frac{\gamma+1}{\gamma-1}}\arctan\sqrt{\frac{\gamma-1}{\gamma+1}(M^2-1)} + \arctan\sqrt{M^2-1} + \text{constant} \qquad (3)$$

Prandtl Mayer Expansion.

Consider the deflection of a stream round a corner with reference to fig 6a. The expansion can be considered to be made up of an infinite number of small steps, each step generating a Mach line e.g AB, AC etc. The first mach line will make an angle α_1 with the initial direction and on crossing this the Mach number will have increased by dM and the flow deflected $d\theta$ in accordance with equation 2. The Mach angle for the next Mach line will correspond to the Mach number $M_1 + dM$ etc. Finally a point will be reached when the total deflection will correspond to Θ, and the Mach number M_2, and the Mach angle $\alpha_2 = \sin^{-1}\frac{1}{M_2}$. The uniform

stream at Mach number M_2 can undergo an expansion at the corner B' in the same way. The result can be extended to an infinite number of corners and in the limit the wall can be replaced by a continuous curve. As the final Mach number depends only on the initial Mach number and the angle between the initial and final velocity occtors (equation 3), any Mach number can be expressed as a function of the angle through which it is required to turn a sonic stream to reach that Mach number. The function to be used is:-

$$P = 1000 - \Theta \qquad (4)$$

where P is the pressure number corresponding to the Mach number M obtained by turning a sonic stream through angle Θ .

Approximate Method for the Prandtl Meyer Expansion.

In the preceeding sections it was shown that the potential flow equation could be solved by a step procedure using the artifice that two regions of uniform flow are separated by Mach lines. The shape of the streamline FG in fig 6a was found by considering that the expansion took place over an infinite number of small steps ie. Mach lines. In practical computations it is not possible to carry out an itterative process with an infinite number of small steps. Therefore the solution is obtained by assuming that the expansion takes place in a finite number of steps. The

procedure used is described below.

Consider the expansion at corner C in fig 7a, strictly the expansion takes place in the envelope of Mach lines ACB and equations 2 and 3 apply. However an approximation to the expansion can be carried out along the finite disturbances A'C and B'C provided the correct average values are used. Let the flow deviation at the lines A'C and B'C be Θ'. Then A'C can be described as the sum of all the Mach lines in the expansion fan ACD required to turn the flow by Θ'. Provided the initial Mach number is known the Mach number M_2 downstream of A'C can be found from equation 3 and the pressure numbers P_1 and P_2 from equation 4. Then the Mach angle α_1 corresponding to the mean pressure numbers $\frac{P_1 + P_2}{2}$ can be found and the characteristic A'C drawn at an angle of $\alpha_1 + \frac{\Theta'}{2}$ to the initial flow direction. In the same way the characteristic CB' corresponding to the expansion fan DCB can be drawn at angle $\alpha_2 + \frac{\Theta'}{2}$ to the flow direction in region A'CB', where α_2 is the Mach angle corresponding to $\frac{P_2 + P_3}{2}$. It can be seen that as $\Theta' \to 0$ and the number of characteristics increase, the representation of the flow becomes more exact, and in the limit when $\Theta' = 0$ the characteristic lines will become Mach lines and the representation will be exact.

The direction numbers A and B will now be introduced so that $A + B = P$ (5) and $A - B = D$ (6).

D is the direction of the stream measured from an arbitrary datum and is positive when measured in an anticlockwise direction.

Then if $M_1 = 1$ and AC' and B'C correspond to turning angles of 1° in fig 7a

$P_1 = 1000$ $P_2 = 999$ $P_3 = 998$

$D_1 = 0$ $D_2 = -1$ $D_3 = -2$

$A = 500$ $A = 499$ $A = 498$

$B = 500$ $B = 500$ $B = 500$.

Thus A decreases and B remains unchanged in the bottom wall expansion of fig 7a. In the same way it can be shown that a top wall expansion as at A in fig 8a will cause B to decrease and leave A unchanged.

Simultaneous Expansion at both Walls.

With reference to fig 8a, let the characteristics AD, AC etc correspond to turning angles of 1°, then the numbers P, A, B and D can be determined by the method shown below.

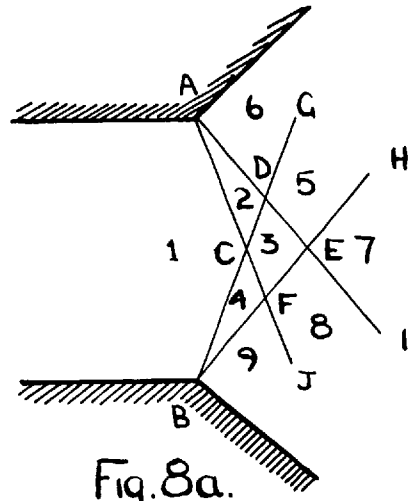
A
6
G
D
H
2
5
1
C
3
E
7
4
F
8
I
9
J
B

Fig. 8a.

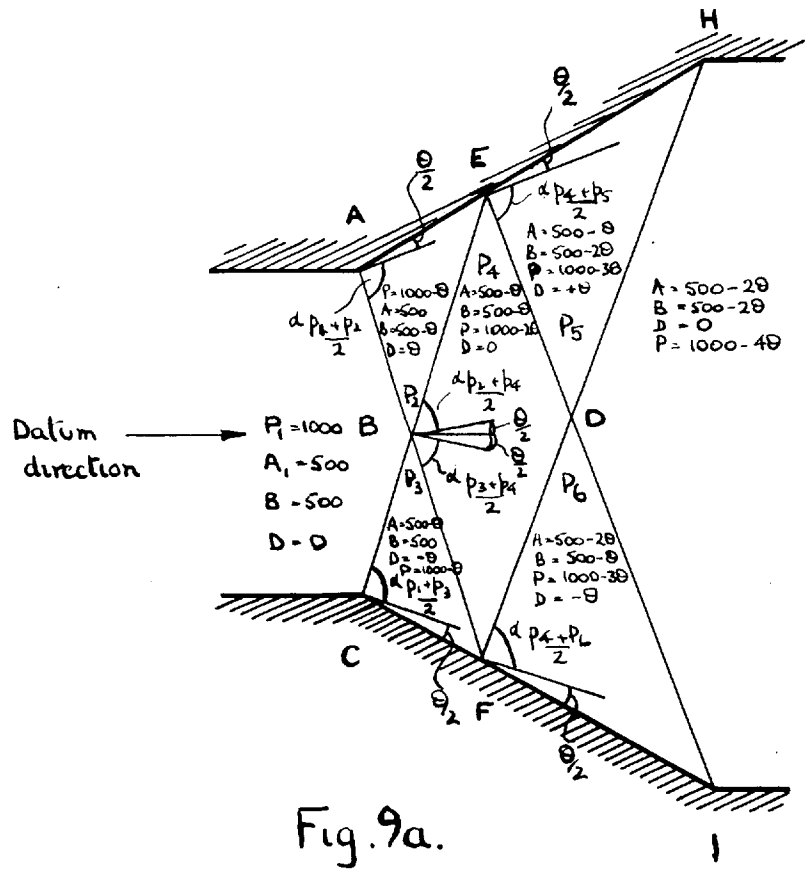
H
θ/2
θ/2
E
A
α P4+P5 / 2
A = 500 - θ
B = 500 - 2θ
P = 1000 - 3θ
D = + θ
P4
P5
A = 500 - 2θ
B = 500 - 2θ
D = 0
P = 1000 - 4θ
P = 1000 - θ
A = 500
B = 500 - θ
D = θ
α P6+P2 / 2
A = 500 - θ
B = 500 - θ
P = 1000 - 2θ
D = 0
P2
α P2+P4 / 2
θ/2
θ/2
D
Datum direction
P1 = 1000 B
A1 = 500
B = 500
D = 0
P3
α P3+P4 / 2
P6
A = 500 - θ
B = 500
D = - θ
P = 1000 - θ
α P1+P3 / 2
A = 500 - 2θ
B = 500 - θ
P = 1000 - 3θ
D = - θ
α P4+P6 / 2
C
θ/2
F
θ/2
I

Fig. 9a.

Space	Method	P	A	B	D
1	Data	1000	500	500	0
2	Top wall expansion of 1^{o} from Space 1	999	500	499	+1
3	Bottom wall expansion of 1^{o} from Space 2	998	499	499	0
4	Bottom wall expansion of 1^{o} from Space 1	999	499	500	-1
6	Top wall expansion of 1^{o} from Space 2	998	500	498	+2
5	Top wall expansion of 1^{o} from Space 3	997	499	498	+1
5	Bottom wall expansion of 1^{o} from Space 6	997	499	498	+1

Hence the flow can be divided easily into regions of uniform flow by means of a characteristic net and values of P,A,B and D assigned to them. These numbers define uniquely the direction and Mach number etc. of the flow in any region.

Graphical construction of a characteristic net.

It has been shown how the direction and pressure numbers can be determined for a characteristics net. The method by which the coordinates of the flow C,D,E,F and G in fig 9a are found will now be demonstrated.

Consider the simultaneous expansions at corners A and C. Let the angle turned through be θ, and let the characteristics AB and CB also turn the flow through this angle.

The Mach angle corresponding to the mean pressure number for AB is $\alpha \frac{p_1 + p_2}{2}$. Then AB can be constructed by drawing this angle to the mean direction of flow. In a similar manner the characteristic CB can be drawn and the point B obtained and hence E,F and D. The method can be extended for any number of characteristics through the points A and C.

The method presented above divides the flow into regions of uniform flow. This method is very convenient when it is required to find the wall shape to obtain a given uniform Mach number. At H for instance in fig 9a the wall can be turned through angle $-\Theta$, where Θ is the direction number in EDH cancelling the characteristic DH. The flow in the quadrilateral HDI then becomes uniform and parallel. If however the object of constructing the net is to find the approximate shape of the velocity profiles for a given wall shape, it can be seen that the method above using squares does not give good results. A more satisfactory method is that using points.

Method of Characteristics using Points.

Suppose the coordinates of each quadrilateral of a characteristic net are taken as the coordinates of the flow at the centre, where the centre is defined as the intersection of the lines joining the bisectors of the opposite sides (see fig 10a).

The inclination of the characteristics to the datum are given approximately by:-

$$AD_1 \propto (p + \frac{\Theta}{2}) + (D + \frac{\Theta}{2})$$

$$DE_1 \propto (p - \frac{\Theta}{2}) + (D + \frac{3}{2}\Theta)$$

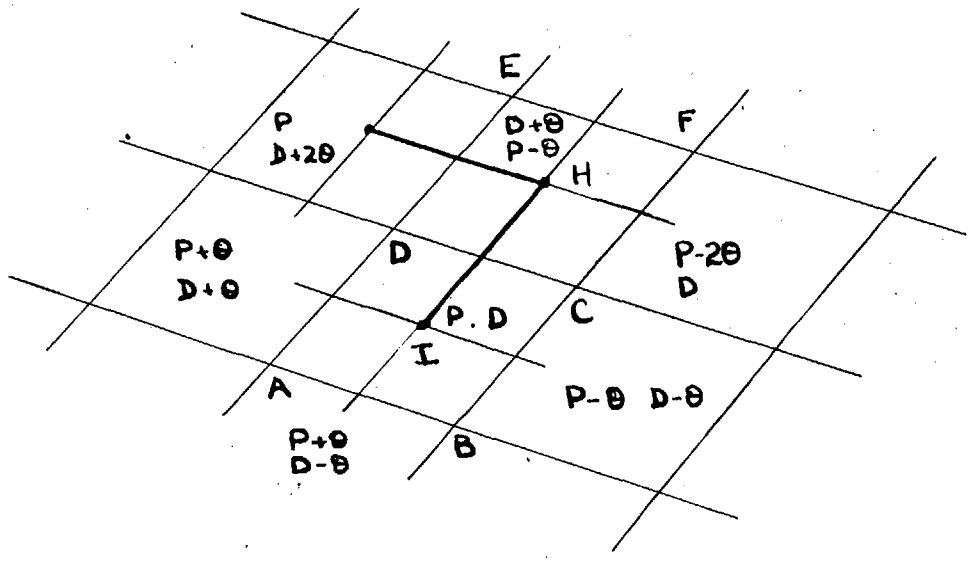

Fig 10a.

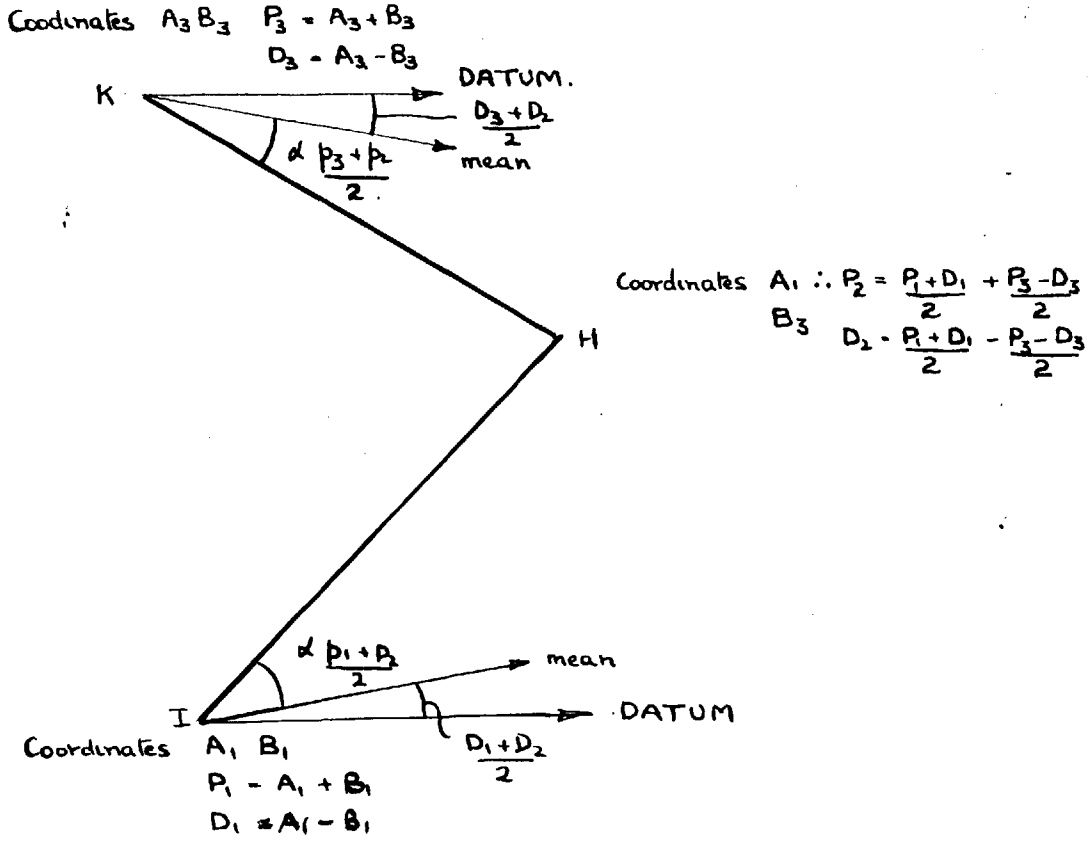

Fig. 11a.

the mean inclination to the datum of AE is then given approximately by:-

$$\alpha_p \div (D + \Theta) \quad (7)$$

In the same way the mean inclination of BF is given approximately by:-

$$\alpha (p - \frac{\Theta}{2}) \div (D + \frac{\Theta}{2}) \quad (8)$$

and the inclination of IH by the mean of 7 and 8 namely:-

$$\alpha (p - \frac{\Theta}{2}) + (D + \frac{\Theta}{2}) \quad (9)$$

The expressions are approximate and like the method using squares the representation of the flow becomes more exact as the size of the disturbances is reduced, and the two methods approach each other, until in the limiting case of Mach lines they are coincident.

The scheme by which the method using points is used graphically is demonstrated in fig 11a. The numbers are obtained by the same methods used in the method using squares and the angles by the use of equation 9. But now the numbers apply to points in the flow and can be regarded as continuous variables.

APPENDIX 3. Solution of the two dimensional irrotational flow equation in the throat of a nozzle.

Solutions of this type have previously been obtained by Hooker[84] and Mundy[85] for three dimensional flow and by Taylor[53] for two dimensional flow. However some of the values given for the constants in the latter paper are in error due to printers errors. Therefore it was necessary to carry out the complete solution here.

It has been shown for two dimensional flow that:-

$$\phi_{yy} + \phi_{xx} = \frac{1}{2-(\gamma-1)(M^{*2}-1)} \left(\frac{\partial M^{*2}}{\partial x} \phi_x + \frac{\partial M^{*2}}{\partial y} \phi_y \right)$$

where $a^{*2}.\ M^{*2} = \phi_x^2 + \phi_y^2$

and that the solution must be of the form

$$\phi = a_1x + a_2x^2 + a_3x^3 + a_4x^4 + c_2y^2 + c_3y^2x + c_4x^2y^2 + \text{[illegible]}\,y^4$$

This series is convergent for $-1 < x$ and $y < 1$ and therefore is only applicable to the throat region bounded by the lines $y<1$ $y>-1$ $x<1$ $x>-1$. As with all series of this type the accuracy is improved by taking an increasing number of terms in the polynomial. But if the series is extended to the 6th degree the number of constants increases to 14 and the equations become unmanageable. The solution therefore has been obtained for a polynomial of the 4th degree in ϕ. The errors involved is difficult to estimate

but it will be a function of x^5 and y^6. However there is evidence that the error is small in the throat in the vicinity of $M^{+2} = 1$, as good agreement has been obtained between theory and experiment by Harrop[49] who used a method of solution due to Sauer[52].

Substitution of ϕ into the equation of motion yields for the terms:-

$$\left(\frac{\partial M^{+2}}{\partial x}\phi x + \frac{\partial M^{+2}}{\partial y}\phi y\right) = 4a_1^2a_2 + (12a_1^2a_3 + 16a_2^2a_1)x$$

$$+(24a_4a_1^2+72a_1a_2a_3+16a_2^3)x^2+(4a_1^2c_4+8a_1a_2c_3+16a_1c_2c_3+16c_2^3)y^2$$

$$2-(\gamma-1)(M^{+2}-1) = 2-(\gamma-1)\left(a_1^2-1+4a_1a_2x + (6a_3a_1 + 4a_2^2)x^2\right.$$

$$\left.+(4c_2^2 + 2c_3a_1)y^2\right)$$

$$\phi xx+\phi yy = (2a_2+2c_2)+(2c_3+6a_3)x + (2c_4+12a_4)x^2 +(12l_5 + 2c_4)y^2$$

By simplifying this equation and equating the coefficients of x and y upto the seccnd power four equations are obtained:-

1st equation equating constant terms

$$c_2(\overline{\gamma+1} - \overline{\gamma-1}a_1^2) + a_2(\overline{\gamma+1}\,.\,\overline{1-a_1^2}) = o$$

2nd equation equating coefficients of x

$$2c_3(\overline{\gamma+1} - \overline{\gamma-1}\,a_1^2) + 6a_3(\overline{\gamma+1}.1-a_1^2) - 8a_1a_2^2(\gamma+1)$$

$$- 3(\gamma-1)\,a_1a_2c_2 = o$$

3rd equation equating coefficients of x^2

$$2c_4(\overline{\gamma+1} - \overline{\gamma-1}a_1^2) + 12a_4(\overline{\gamma+1}.1-a_1^2) - 36a_1a_2a_3.\overline{\gamma+1}$$

$$- 8\overline{\gamma-1}.a_1a_2c_3 - 12\overline{\gamma-1}\,c_2a_3a_1 - 8\overline{\gamma-1}a_2^2c_2 - 8a_2^3\overline{\gamma+1} = 0$$

4th equation equating coefficients of y^2

$$12\,15(\overline{\gamma+1} - \overline{\gamma-1}a_1^2) + 2c_4(\overline{\gamma+1}.\overline{1-a_1^2}) - 8\overline{\gamma-1}c_2^2a_2 - 8c_2^3(\gamma+1)$$

$$- 4a_1a_2c_3.\overline{\gamma+1} - 4c_3c_2a_1.\overline{\gamma+3} = 0$$

If h is the half width the throat then

$$y = h + R - (R^2 - x^2)^{\frac{1}{2}}$$

expanding $y = h + R - R\left(1 - \frac{x^2}{2R^2} + \frac{x^4}{8R^4} \ldots\right)$

But as $R > x$

$$y \approx h + \frac{x^2}{2R^2} \quad (-1 < x < 1)$$

Then from the boundary conditions $\frac{\partial y}{\partial x} = \frac{x}{R} + \frac{x^3}{2R^3}$

and $y = h + \frac{x^2}{2R}$ the following equation is obtained

$$\frac{x}{R} + \frac{1}{2}\frac{x^3}{R^3} = \left(2c_3hx + \frac{2c_3x^3}{2R} + 2c_4x^2h + \frac{c_4x^4}{R} + 41_5h^3 + \frac{15h^2x^2}{R}\right.$$

$$\left. + 2c_2h + \frac{c_2x^2}{R}\right)\left(a_1 + 2a_2x + 3a_3x^2 + 4a_4x^3 + c_3h^2 + \frac{hx^2c_3}{R}\right.$$

$$\left. + 2c_4xh^2 + \frac{2c_4\,hx^3}{R}\right)^{-1}$$

By simplyfing this equation and equating the coefficients of x upto the third power four equations are obtained:-

5th equation equating constant terms

$$21_5h^3 + c_2h = 0$$

6th equation equating coefficients of x

$$\frac{2c_3h^2}{a_1+c_3h^2} = \frac{h}{R}$$

7th equation equating coefficients of x^2

$$\frac{2c_3h}{a_1+c_3h^2}\left(2a_2 + 2c_4h^2\right) = \frac{c_2}{R} + 2c_4h + 61_5h^2$$

8th equation equating coefficients of x^3.

$$\frac{1}{2R^3}(a_1 + h^2c_3)^2 = \frac{c_3}{R}(a_1 + h^2c_3) - 2c_3h\left(\frac{c_3h}{R} + 3a_3\right)$$

The eight equations were solved by the method set out in the table 4.

The solution produces after the 6th step a relationship between a_1^2 and $x' = \frac{h}{R}$ given by:-

$$\frac{\frac{1}{2x'-x'^2} - \frac{1}{2-x'}}{(\gamma+1)A-(\gamma-1)} = \frac{\frac{3A}{x'^2} + \frac{1}{x'-x'^2}(A-B) + \frac{2a_1^2}{(2x'-x'^2)}\left(\gamma(1-\frac{A}{B}) + (3 - \frac{A}{B})\right)}{2(\gamma - 1)A - 2(\gamma + 1)B}$$

where $A = \sqrt{\gamma + 1} - \sqrt{\gamma - 1}a_1^2$

$B = \sqrt{\gamma + 1} - \gamma\sqrt{\gamma + 1}a_1^2$

This equation was solved graphically for a value of $\frac{h}{R}$ corresponding to the measured nozzle. The coefficients were found subsequently by substitution of the values of a_1 and

TABLE 4a

Equation	7	3	4	8	2	1	5	6	Step of solution
1st	a_1	a_2			c_2				3
2nd	a_1	a_2	a_3		c_2	c_3			7
3rd	a_1	a_2	a_3	a_4	c_2	c_3	c_4		8
4th	a_1	a_2			c_2	c_3	c_4	l_5	5
5th					c_2			l_5	2
6th	a_1					c_3			1
7th	a_1	a_2			c_2	c_3	c_4	l_5	6
8th	a_1		a_3			c_3			4
coefficient eliminated	a_1	a_2	a_3	a_4	c_2	c_3	c_4	l_5	

Method of using table

For instance in step 1 c_3 is eliminated from 2nd 3rd, 4th, 7th, 8th equations by using the 6th equation.

$\frac{h}{R}$ in the 1st to 8th equations, and are tabulated below.

$x' = \frac{h}{R} = 0.1111$ $\quad a_1 = 0.9823 \quad a_2h = -0.1138$
$a_3h^2 = 0.01927 \quad a_4h^3 = -0.1983$
$c_2h = 0.00475 \quad c_3h^2 = 0.05724$
$c_4h^3 = -0.01541 \quad l_5h^3 = -0.00237$

But as $M^{+2} = a_1^2 + 4a_1a_2\,x + (6a_3a_1 + 4a_2^2)x^2 + (8a_4a_1 + 12a_3a_2)x^3$

$+ (4c_2^2 + 2c_3a_1)y^2 + (8c_2c_3 + 4a_1c_4 + 4a_2c_3)xy^2$

an expression for M^{+2} can be obtained by substitution of the coefficients namely:-

$$M^{+2} = 0.9650 - 0.4471\,\frac{x}{h} + 0.1654\,\frac{x^2}{h^2} - 1.584\,\frac{x^3}{h^3} + 0.1144\,\frac{y^2}{h^2} - 0.0847\,\frac{xy^2}{h^3}$$

APPENDIX 4. Adjustments to the Interferometer Plates.

The purpose of the adjustments are:-

(1) To produce fringes of the desired spacing and orientation

(2) To bring the fringes of maximum contrast or any desired fringe to the centre of the field of view

(3) To focus the fringes in the chosen position.

It can be shown[58] that of the twelve possible adjustments on a four mirror interferometer, only five are needed to carry out the operations stipulated above. There were seven possible adjustments on the instrument used, these have been summarised in fig 12a.

The function of each individual adjustment was:-

(1) Rotation of Mirror 1 about an axis perpendicular to the plane containing the optical axes, altered the position and angle of intersection of the two beams in the vertical plane, giving rise to horizontal fringes of different spacing and orientation.

(2) Rotation of semi reflecting plate 4, about an axis lying in the plane containing the optical axes, altered the angle and position of intersection in the horizontal plane giving rise to vertical fringes.

(3) Movement of Mirror 3 in a direction normal to its optical

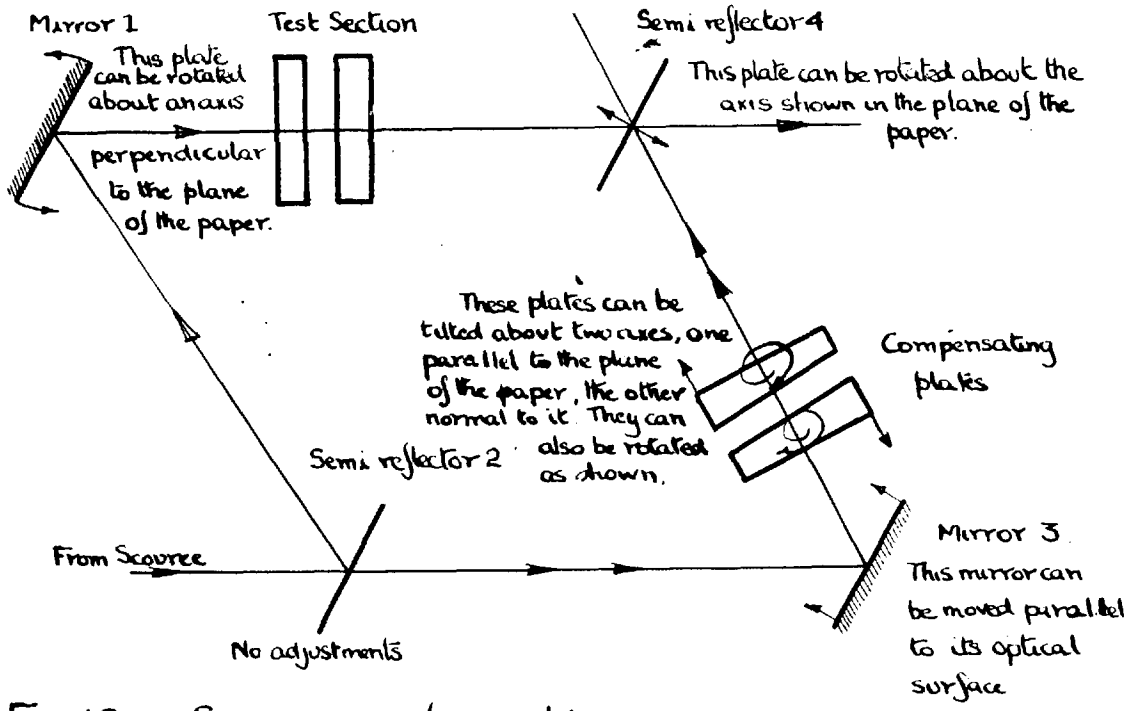

Fig. 12a Summary of possible adjustments to the optical plates of the interferometer

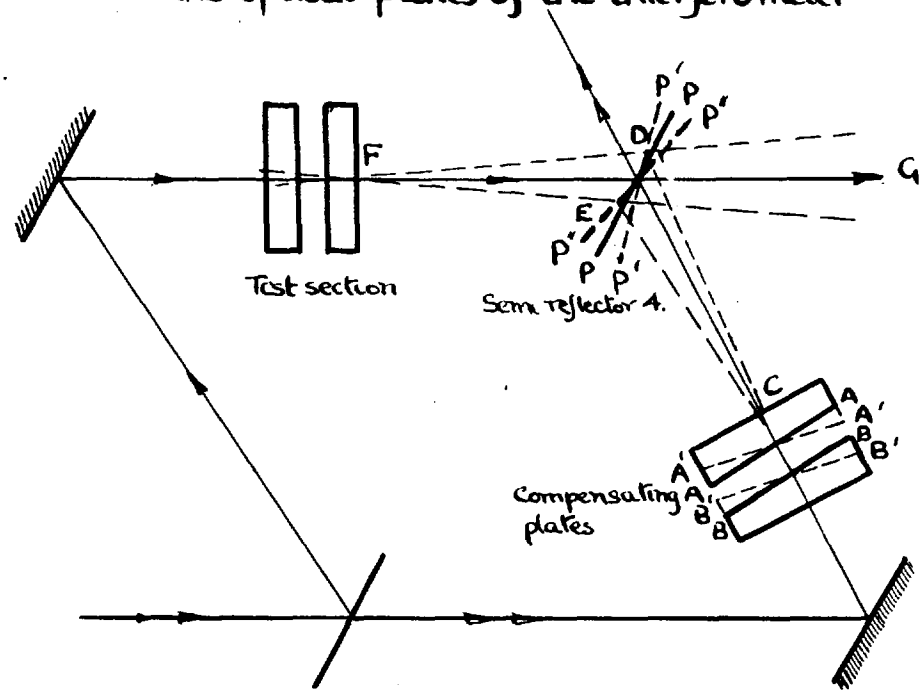

Fig. 13a. Fringe formation by manipulation of the compensating plates.

surface changed the optical path length difference between the two beams, whereby any desired fringe could be brought into the centre of the field of view.

(4) Tilting the compensating plates as a whole about, the two axes perpendicular to the light beam altered the plane of intersection of the two beams, while altering the path length difference between the two beams. Rotation of each wedged shaped plate about an axis parallel to the light beam altered the angle and plane of intersection.

The adjustments to the compensating plates were equivalent to four independent adjustments of a mirror.

APPENDIX 5. Method of Increasing the density range covered by the available fringes.

It was stated in section 6.7. that the normal fringe shift technique could only be used upto a pressure of approximately 50 p.s.i.g. As the tests in the nozzle were usually carried out at higher pressures, a method of utilizing the available fringes more effectively was developed using the compensating plates to set up the fringes.

Consider the interferometer shown in fig 13a adjusted so that the path difference between the two beams is zero and all the plates parallel. Then fringes can be formed at any desired plane in the test section by rotation of one of the compensating plates through 180°. If compensating plate AA is rotated to position A'A' the beam is deflected to path DC. By rotation of the semi reflector PP to position P'P' fringes can be formed at a plane in the test section. By returning the compensating plate AA to its original position and rotating BB through 180° to B'B', the beam is deflected to path CE and fringes once again formed in the test section by rotation of the semi reflector PP to P"P". During both operations the direction of the beam FG passing through the test section has remained unchanged. This method of setting up the fringes has been explained with reference to the

vertical plane for convenience of graphical representation only. Vertical fringes were set up by using the same method, when the two beams intersect in the horizontal plane.

With reference to fig 14a, let the wavetrain CC represent the beam FG in fig 13a and the wavetrains AA and BB, the two beams corresponding to the two positions of the compensating plates. Let the line XYZW represent the wavefront of the beam passing through the disturbance. Then the position of the fringes formed in the presence of the disturbance depends on whether the unretarded beam is AA or BB. The fringes formed when AA is used are shifted in logical sequence. But if the undisturbed beam is BB, the fringes are displaced in the opposite direction and at each island the fringe sequence reverses, with the result that the density change has been covered by 10 fringes when beams BB and CC interfereas opposed to 19 when beams AA and CC interfere. The fringe shifts however at any point are the same in both cases but opposite in sign.

The density profile which caused the retardation of the beam CC in fig 14a is similar to that found in the expansion of air in a supersonic convergent divergent nozzle. Where XY corresponds to the convergent section, YZ the throat region, and ZW the divergent section.

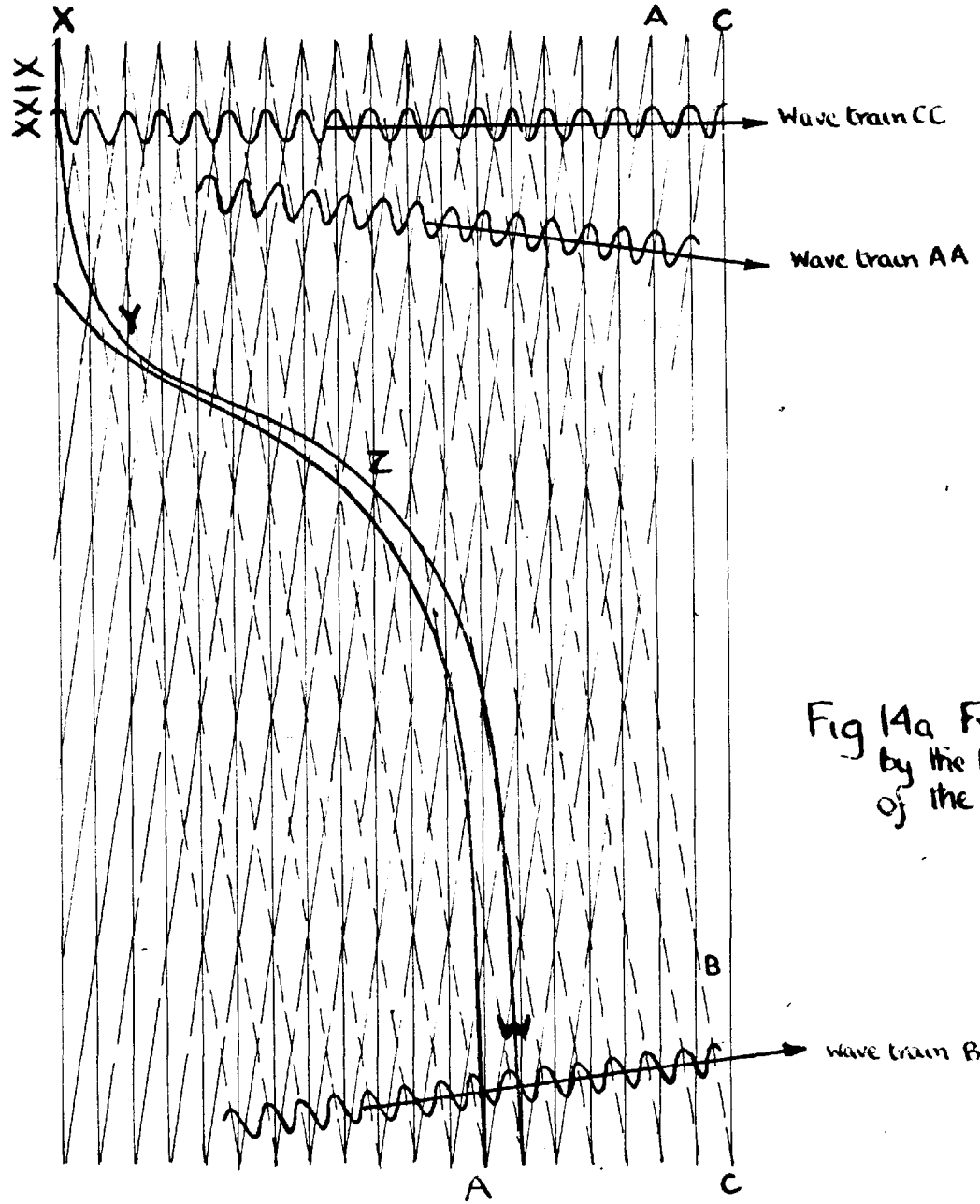

When AA and CC interfer fringes move ↓ for density increase

When BB and CC interfer fringes move ↑ for density increase

Fig 14a Fringes produced by the two different positions of the compensating plates

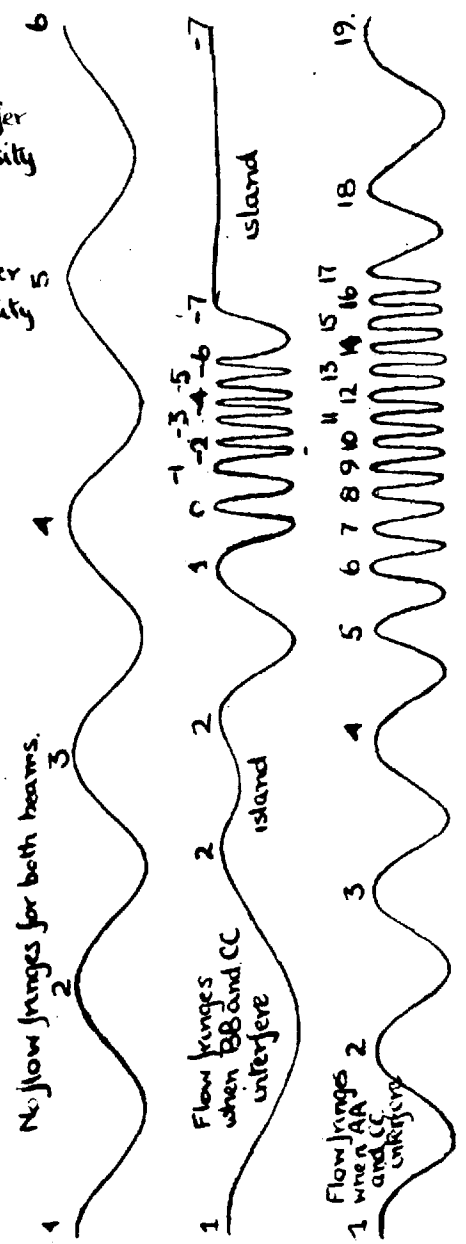

The fringe patterns corresponding to the two positions of the plates A'A' and B'B' are shown in figs 21 and 22 with the corresponding no flow patterns.

By using the compensating plates in this way, fringe shifts of 90 were obtained, so that the complete flow pattern could be studied upto reservoir pressures of 85 psig.

APPENDIX 6. The Method of Determining the Magnification of the interferograms.

The magnification of the interferograms was determined from measurements of the nozzle outline. At the orifice plane the axial coordinates of the actual profile and those on the interferogram coincide, hence by determining the width of the profile on the interferogram and that of the actual nozzle at the orifice plane, the magnification could be determined.

The profile measured on the no flow interferogram was used as it was free from refraction effects caused by the flow. It can be seen in appendix 1 that the mean profile on the second side is slightly narrower than that on the first side at the end of the divergence. Therefore in this region the second side measurements correspond to the profile observed by the camera, accordingly they were used in the calculation of magnification.

The widths of the actual profile and that on the no flow interferogram were determined for test 143 by means of fig 16a. Where, using the coordinates defined by fig 15a

$$y_2 = 5.364 - 3.457 = 1.907$$

$$y_1 = 3.376 - 1.934 = 1.442$$

$$\therefore \text{ Magnification} = \frac{y_1}{y_2} = 0.7563$$

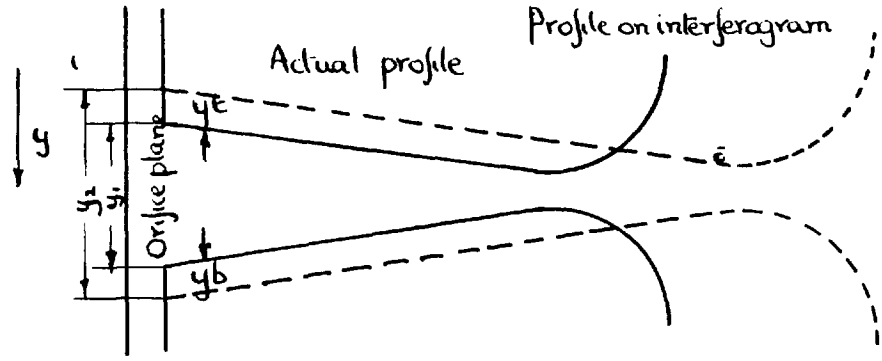

Fig.15a. Coordinates used in the measurement of magnification

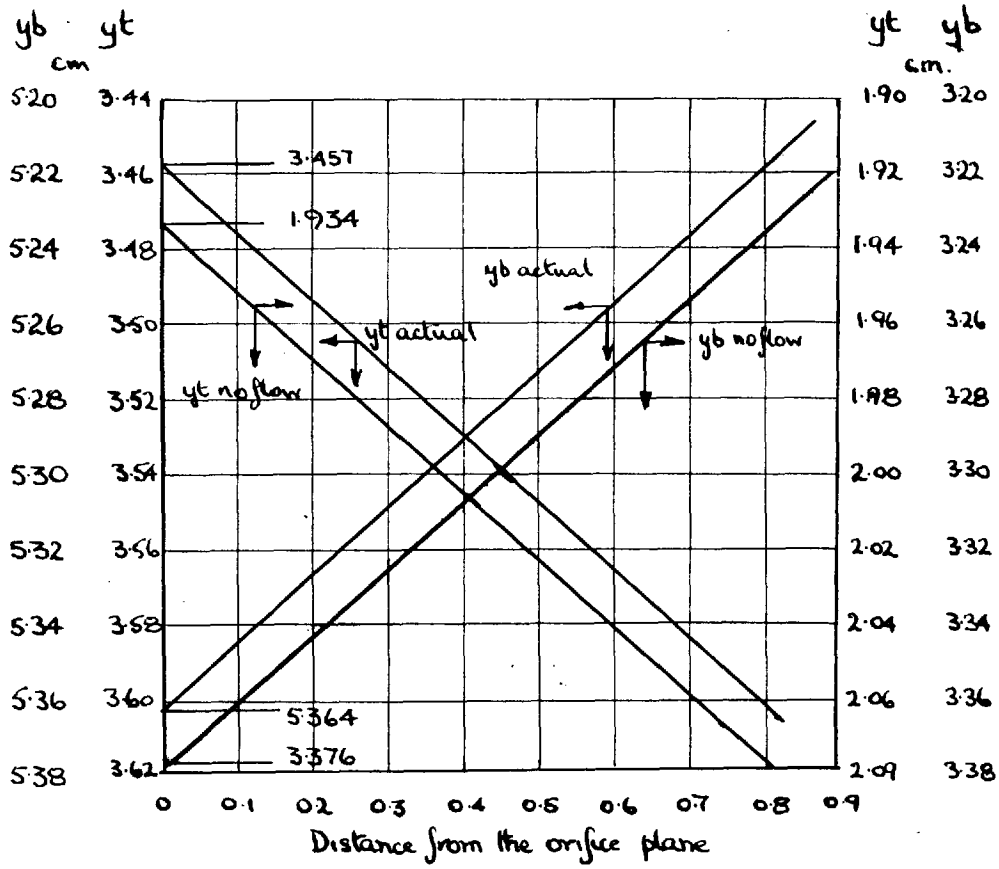

Fig.16a. Calculation of magnification

APPENDIX 7. A Method of determining the point of transition in the boundary layer.

Consider the laminar and turbulent boundary layers shown in fig 17a, through which a parallel beam of light passes onto a photographic plate. In a laminar layer the density gradient increases initially on moving away from the wall and therefore the rays close to the surface will diverge and the illumination of the photographic plate will be low at the wall. Near the outer edge of the boundary layer the density gradient falls causing the light rays to converge, with the result that a white line appears on the plate at YY in fig 17a(i) separated from the surface by a dark band.

The density gradient, in a turbulent boundary layer, decreases rapidly at first on moving away from the wall, and continues to do so, but at an increasingly gradual rate as the top edge is approached. Hence the light rays converge in the regions close to the wall and produce a white line adjacent to it, if the photographic plate is placed in position YY in fig 17a(ii).

Chapman et al[8] used the technique described above to determine the point of transition in the boundary layer. At the transition point the white line representing the laminar boundary layer, suddenly turns towards the wall and becomes established as a white line adjacent to the surface,

representing a fully developed turbulent boundary layer.

It is apparent from fig 17a, that there is an optimum position of the photographic plate YY where the white line can be observed. Chapman et al[8] adjusted the position of the plate by means of an adjustable camera back.

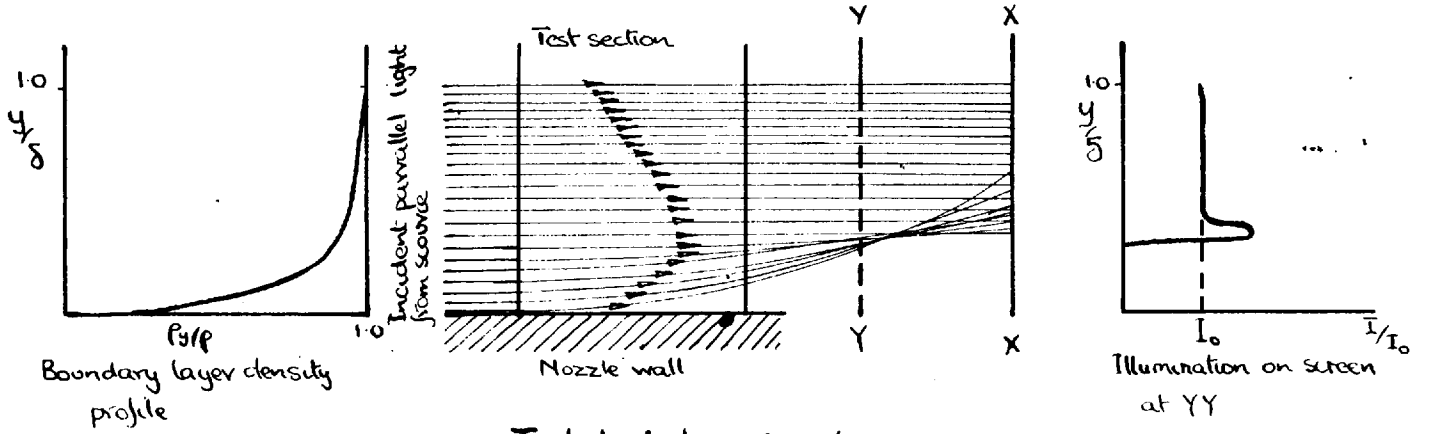

Fig 1.7a The formation of shadow photographs of a turbulent and a laminar two dimensional boundary layer.